

An Experimental Study  
of the Hydraulic Characteristics  
beneath a Partial Ice Cover

By  
Mitchel R. Peters

A thesis submitted to the Faculty of Graduate Studies of  
The University of Manitoba  
in partial fulfilment of the requirements for the degree of

MASTER OF SCIENCE

Department of Civil Engineering  
Faculty of Engineering  
University of Manitoba  
Winnipeg, Manitoba

Copyright © 2015, Mitchel R. Peters

## **Abstract**

While many studies have been conducted in channels that are fully open or entirely covered with ice, little has been examined in channels with border ice. To begin filling in this gap in knowledge, experiments were conducted in the Hydraulics Research Testing Facility at the University of Manitoba in a 1.2m wide, 14m long flume to assess the impact of Froude number, coverage ratio and bed-to-ice roughness ratio on the hydraulic characteristics of channels with border ice cover. Acoustic Doppler velocimetry was used to collect detailed 3D velocity data over a cross section of the flume which facilitated the analysis of velocity and turbulence intensity fields as well as the shear stress distribution. The data collected thus far represents the most complete experimental dataset of measured water velocities in a channel with a border ice cover.

## **Acknowledgements**

I am thankful for the support of my thesis advisors, Dr. Shawn Clark and Dr. Karen Dow. Your advice and guidance was invaluable.

I would like to acknowledge the financial contributions of the Natural Science and Engineering Research Council of Canada, Manitoba Hydro, the University of Manitoba, and the Government of Manitoba. I am grateful of the support you have provided me.

Thank you to Alex Wall and Hoda Pahlavan, whose assistance constructing the flume, obtaining necessary materials and equipment, and conducting preliminary testing was greatly appreciated.

To my family and friends, your support and encouragement kept me moving forward, and for that I cannot thank you enough.

## Contents

List of Tables .....	vii
List of Figures.....	viii
List of Symbols .....	xxi
1. Introduction .....	1
1.1. Objectives.....	2
1.2. Overview .....	3
2. Literature Review .....	4
2.1. Border Ice Formation.....	4
2.2. Flow Characteristics of Open Channels .....	7
2.2.1. Velocity.....	7
2.2.2. Turbulence Intensities.....	10
2.2.3. Shear Stress.....	12
2.3. Flow Characteristics of Channels with Full Ice Cover .....	14
2.3.1. Velocity Distribution.....	15
2.3.2. Turbulence Intensities.....	17
2.3.3. Shear Stress.....	18
2.3.4. Composite Roughness .....	20
2.4. Flow Characteristics of Channels with Border Ice Cover .....	22
3. Physical Model and Methodology .....	26
3.1. Physical Model .....	26

3.2.	Data Collection.....	28
3.3.	Post-Processing of ADV Data .....	34
3.4.	Preliminary Testing.....	35
3.5.	Experiment Parameters .....	37
4.	Results and Analysis.....	42
4.1.	Channel Resistance.....	42
4.2.	Average Velocity Components .....	55
4.2.1.	Streamwise Velocity .....	55
4.2.2.	Secondary Circulation .....	81
4.3.	Discharge Distribution .....	85
4.4.	Boundary Shear Stress Distribution.....	91
4.5.	Turbulence Intensities.....	102
5.	Conclusions and Recommendations .....	115
5.1.	Conclusions .....	116
5.2.	Recommendations for Future Work .....	121
6.	Works Cited.....	123
Appendix A: Rationale behind ADV Settings .....		130
A.1	Ping Algorithm.....	131
A.2	Frequency.....	132
A.3	Time to convergence (for 100 Hz Adaptive Interval) .....	134
A.3.1	Free Stream .....	134

A.3.2	Near Boundary.....	135
A.4	Summary.....	138
Appendix B:	Symmetry Analysis .....	139
Appendix C:	Supplemental Results Figures.....	152
C.1	Water Surface Profiles.....	152
C.2	Secondary Circulation.....	160
C.3	Discharge Distribution - Cumulative .....	164
C.4	Discharge Distribution – Transverse .....	167
C.5	Log-law Velocity Profiles .....	170
C.6	Shear Stress Distributions .....	191
C.7	Streamwise Turbulence Intensity Distributions.....	195

## List of Tables

Table 3-1: Experiment Conditions .....	38
Table 4-1: Composite roughness values calculated using the standard step method. ....	45
Table 4-2: Composite roughness estimation results. ....	54
Table 4-3: Velocity profile classification over a cross section for the base partial cover case of $F = 0.25$ and 67% coverage.....	70
Table 4-4: Impact of Froude number on velocity profile characterization in a cross section for channels with 67% coverage.....	71
Table 4-5: Impact of coverage ratio on velocity profile characterization in a cross section for channels with $F = 0.25$ . ....	72
Table 4-6: Impact of coverage ratio on velocity profile characterization in the open water section (normalized). ....	72
Table 4-7: Impact of relative roughness on velocity profile characterization in a cross section for channels with $F = 0.25$ and 67% coverage .....	74
Table 4-8: Average Shear Stresses (Pa).....	93
Table A-1: Percent error for flow statistics in the free stream region. ....	135
Table A-2: Percent error for flow statistics in cells near a boundary. ....	137

## List of Figures

Figure 2-1: Velocity contours in open channels.....	8
Figure 2-2: Typical open channel bed shear stress distribution.....	13
Figure 2-3: Typical covered channel bed shear stress distribution. ....	19
Figure 3-1: Headwater box components.....	27
Figure 3-2: Installed border ice. ....	28
Figure 3-3: Vectrino II Profiling ADV (left) and Vectrino + ADV (right). ....	29
Figure 3-4: Sample locations and ADV orientations for the Open Channel Experiment. Orientations indicate the direction of the ADV probe head while data was collected.....	30
Figure 3-5: Traversing Mechanism .....	31
Figure 3-6: Convergence test results for selected flow statistics.....	32
Figure 3-7: Vectrino Profiler sampling range.....	33
Figure 3-8: Preliminary assessment of channel's developing length.....	35
Figure 3-9: Symmetry assessment of mean flow velocity components for two distances from the centerline of the channel: 150mm (top) and 400mm (bottom).....	37
Figure 3-10: Roughness element orientation. ....	40
Figure 4-1: Water surface profiles from the Base Experiment showing a) bed included, b) water surface profiles only. ....	43
Figure 4-2: The effect on composite roughness of a) coverage, and b) Froude number.....	47

Figure 4-3: Sample division of wetted perimeter .....	48
Figure 4-4: Sabaneev Equation Implementation .....	50
Figure 4-5: Alpha-Method Implementation .....	51
Figure 4-6: Division of cross section into sub areas assuming: a) no wall influence, max velocity at mid-depth; b) no wall influence, max velocity offset from mid-depth; c) wall influence included, max velocity assumed at mid- depth; and d) wall influence included, max velocity offset from mid-depth. ....	52
Figure 4-7: Streamwise velocity maxima, as indicated by red circles, at the centreline of the Open Channel Experiment. ....	56
Figure 4-8: $U / U_{\text{bulk}}$ contours for the Open Channel Experiment. ....	57
Figure 4-9: $U / U_{\text{bulk}}$ contours for the Covered Channel Experiment.....	57
Figure 4-10: $U / U_{\text{bulk}}$ contours for the Base Experiment ( $F = 0.25$ with 67% coverage).....	58
Figure 4-11: $U / U_{\text{bulk}}$ contours for the Low Froude ( $F = 0.10$ ) Experiment.....	59
Figure 4-12: Percent difference in $U / U_{\text{bulk}}$ contours between the Base and Low Froude Experiments ( $(\text{Exp. 4} - \text{Exp. 3}) / \text{Exp. 3}$ ). ....	59
Figure 4-13: $U / U_{\text{bulk}}$ contours for the High Froude ( $F = 0.50$ ) Experiment. ....	60
Figure 4-14: Percent difference in $U / U_{\text{bulk}}$ contours between the Base and High Froude Experiments ( $(\text{Exp. 5} - \text{Exp. 3}) / \text{Exp. 3}$ ). ....	60
Figure 4-15: $U / U_{\text{bulk}}$ contours for the 25% Coverage Experiment.....	61
Figure 4-16: Percent difference in $U / U_{\text{bulk}}$ contours between the Base and 25% Coverage Experiments ( $(\text{Exp. 6} - \text{Exp. 3}) / \text{Exp. 3}$ ).....	61
Figure 4-17: $U / U_{\text{bulk}}$ contours for the 50% Coverage Experiment.....	62
Figure 4-18: Percent difference in $U / U_{\text{bulk}}$ contours between the Base and 50% Coverage Experiments ( $(\text{Exp. 7} - \text{Exp. 3}) / \text{Exp. 3}$ ).....	62

Figure 4-19: $U / U_{\text{bulk}}$ contours for the Rough Bed – Smooth Ice Experiment.....	63
Figure 4-20: Percent difference in $U / U_{\text{bulk}}$ contours between the Base and Rough Bed – Smooth Ice Experiments ((Exp. 8 – Exp. 3) / Exp. 3).....	63
Figure 4-21: $U / U_{\text{bulk}}$ contours for the Smooth Bed – Rough Ice Experiment.....	64
Figure 4-22: Percent difference in $U / U_{\text{bulk}}$ contours between the Base and Smooth Bed – Rough Ice Experiments ((Exp. 9 – Exp. 3) / Exp. 3).....	64
Figure 4-23: $U / U_{\text{bulk}}$ contours for the Rough Bed – Rough Ice Experiment.....	65
Figure 4-24: Percent difference in $U / U_{\text{bulk}}$ contours between the Base and Rough Bed – Rough Ice Experiments ((Exp. 10 – Exp. 3) / Exp. 3).....	65
Figure 4-25: Streamwise velocity profiles normalized by their respective average velocity are shown where the profile from the partial cover experiment can be characterized as: a) similar to the open channel profile, b) transitional, and c) similar to the fully covered profile. ....	67
Figure 4-26: Streamwise velocity profiles normalized by their respective average cross sectional velocity are shown where the profile from the partial cover experiment can be characterized as: a) similar to the open channel profile, b) transitional, and c) similar to the fully covered profile. ....	69
Figure 4-27: Streamwise velocity profiles beneath the cover of the Rough Bed Experiment. ....	73
Figure 4-28: Relative average velocity distributions for the Open Channel, Covered Channel, and Base Experiments. Vertical line indicates edge of partial ice cover. ....	75
Figure 4-29: Relative average velocity distributions for the Froude Number Experiments. Vertical line indicates edge of ice cover. ....	77

Figure 4-30: Relative average velocity distributions for the Coverage Experiments. Vertical lines indicate the respective edges of the partial ice covers. ....	79
Figure 4-31: Relative average velocity distributions for the relative roughness Experiments. Vertical line indicates the edge of the partial ice cover. ....	80
Figure 4-32: Secondary circulation vectors for the 50% Coverage Experiment. ....	83
Figure 4-33: Secondary circulation vectors for the High Froude Experiment. ....	84
Figure 4-34: Progression of partial area for computing cumulative discharge. ....	87
Figure 4-35: Cumulative discharge distribution for the Base Experiment. Vertical line indicates edge of ice cover. ....	88
Figure 4-36: Differences between experimental and theoretical cumulative discharge distributions as a percent of the total cross-sectional discharge for: a) the Froude experiments, b) the coverage experiments, and c) the roughness experiments. Vertical lines indicate edge of ice cover. ....	89
Figure 4-37: Relative unit discharge for a) the Base Experiment, and b) the Smooth Bed – Rough Ice Experiment. Vertical line indicates edge of ice cover. ...	91
Figure 4-38: Dimensionless shear stress distributions for the a) Open Channel, b) Covered Channel, and c) Base Experiments. ....	94
Figure 4-39: Dimensionless shear stress distribution comparison Experiments 3 (F = 0.25), 4 (F = 0.10), and 5 (F = 0.50) along a) the underside of the ice, b) the vertical side wall, and c) the bed. Vertical line indicates edge of ice cover above the bed. ....	96
Figure 4-40: Dimensionless shear stress distribution comparison Experiments 3 (67% coverage), 6 (25% coverage), and 7 (50% coverage) along a) the	

underside of the ice, b) the vertical side wall, and c) the bed. Vertical lines indicate respective edges of ice cover above the bed.....	98
Figure 4-41: Dimensionless shear stress distribution comparison Experiments 3 (smooth bed – smooth ice), 8 (rough bed – smooth ice), 9 (smooth bed – rough ice), and 10 (rough bed – rough ice) along a) the underside of the ice, b) the vertical side wall, and c) the bed. Vertical line indicates edge of ice cover above the bed. ....	99
Figure 4-42: Streamwise turbulence intensity distribution for the Open Channel Experiment. ....	104
Figure 4-43: Turbulence intensity profiles for the Open Channel Experiment at $Y = 0$ . ....	105
Figure 4-44: Streamwise turbulence intensity distribution for the Covered Channel Experiment. ....	106
Figure 4-45: Streamwise turbulence intensity profile for the Covered Channel Experiment at $Y = 0$ . ....	107
Figure 4-46: Streamwise turbulence intensity distribution for the a) Base, b) Rough Bed – Rough Ice, c) 50% Coverage, and d) High Froude Experiments. ....	108
Figure 4-47: Streamwise turbulence intensity profiles for the a) Base, b) Rough Bed – Rough Ice, c) 50% Coverage, and d) High Froude Experiments under the partial ice cover at $Y = 400$ .....	110
Figure 4-48: Streamwise Turbulence intensity profiles for the a) Rough Ice, and b) Rough Bed Experiments beneath the partial ice cover at $Y = 400$ .....	111
Figure 4-49: Turbulence intensity profiles from the transition zone ( $Y = 250$ ) of the 50% Coverage Experiment. ....	112

Figure 4-50: Streamwise turbulence intensity profiles for the a) Base, b) Rough Bed - Rough Ice, c) 50% Coverage, and d) High Froude Experiments at $Y = 0$ ..	113
Figure 4-51: Streamwise turbulence intensity near border ice: Experiment 3. ....	114
Figure A-1: Comparison of the effect of sampling frequency on convergence in the free stream velocity region.....	133
Figure A-2: Convergence test in free stream (a) including -uv ; (b) excluding -uv...	134
Figure A-3: Convergence test (a) 7 mm, (b) 6 mm, (c) 5 mm, and (d) 4 mm from the bed .....	136
Figure B-1: Open Channel Symmetry Analysis: Streamwise Velocity.....	140
Figure B-2: Open Channel Symmetry Analysis: Spanwise Velocity .....	141
Figure B-3: Open Channel Symmetry Analysis: Vertical Velocity .....	142
Figure B-4: Open Channel Symmetry Analysis: Streamwise Turbulence Intensity.....	143
Figure B-5: Open Channel Symmetry Analysis: Spanwise Turbulence Intensity ...	144
Figure B-6: Open Channel Symmetry Analysis: Vertical Turbulence Intensity .....	145
Figure B-7: Covered Channel Symmetry Analysis: Streamwise Velocity .....	146
Figure B-8: Covered Channel Symmetry Analysis: Spanwise Velocity .....	147
Figure B-9: Covered Channel Symmetry Analysis: Vertical Velocity .....	148
Figure B-10: Covered Channel Symmetry Analysis: Streamwise Turbulence Intensity.....	149
Figure B-11: Covered Channel Symmetry Analysis: Spanwise Turbulence Intensity.....	150

Figure B-12: Covered Channel Symmetry Analysis: Vertical Turbulence	
Intensity.....	151
Figure C-1: Water surface profiles from the Base Experiment showing a) bed included, b) water surface profiles only. ....	152
Figure C-2: Water surface profiles from the Low Froude Experiment showing a) bed included, b) water surface profiles only. ....	153
Figure C-3: Water surface profiles from the High Froude Experiment showing a) bed included, b) water surface profiles only. ....	154
Figure C-4: Water surface profiles from the 25% Coverage Experiment showing a) bed included, b) water surface profiles only. ....	155
Figure C-5: Water surface profiles from the 50% Coverage Experiment showing a) bed included, b) water surface profiles only. ....	156
Figure C-6: Water surface profiles from the Rough Bed Experiment showing a) bed included, b) water surface profiles only. ....	157
Figure C-7: Water surface profiles from the Rough Ice Experiment showing a) bed included, b) water surface profiles only. ....	158
Figure C-8: Water surface profiles from the Rough Bed – Rough Ice Experiment showing a) bed included, b) water surface profiles only. ....	159
Figure C-9: Secondary circulation vectors for the Open Channel Experiment. ....	160
Figure C-10: Secondary circulation vectors for the Covered Channel Experiment..	160
Figure C-11: Secondary circulation vectors for the Base Experiment.....	161
Figure C-12: Secondary circulation vectors for the Low Froude Experiment. ....	161
Figure C-13: Secondary circulation vectors for the High Froude Experiment. ....	161
Figure C-14: Secondary circulation vectors for the 25% Coverage Experiment.....	162

Figure C-15: Secondary circulation vectors for the 50% Coverage Experiment.....	162
Figure C-16: Secondary circulation vectors for the Rough Bed Experiment.....	162
Figure C-17: Secondary circulation vectors for the Rough Ice Experiment. ....	163
Figure C-18: Secondary circulation vectors for the Rough Bed - Rough Ice Experiment. ....	163
Figure C-19: Cumulative discharge distribution for the Base Experiment. ....	164
Figure C-20: Cumulative discharge distribution for the Low Froude Experiment..	164
Figure C-21: Cumulative discharge distribution for the High Froude Experiment. ....	165
Figure C-22: Cumulative discharge distribution for the 25% Coverage Experiment. ....	165
Figure C-23: Cumulative discharge distribution for the 50% Coverage Experiment. ....	165
Figure C-24: Cumulative discharge distribution for the Rough Bed Experiment....	166
Figure C-25: Cumulative discharge distribution for the Rough Ice Experiment. ....	166
Figure C-26: Cumulative discharge distribution for the Rough Bed - Rough Ice Experiment. ....	166
Figure C-27: Transverse discharge distribution for the Base Experiment. ....	167
Figure C-28: Transverse discharge distribution for the Low Froude Experiment. ...	167
Figure C-29: Transverse discharge distribution for the High Froude Experiment...	168
Figure C-30: Transverse discharge distribution for the 25% Coverage Experiment. ....	168
Figure C-31: Transverse discharge distribution for the 50% Coverage Experiment. ....	168
Figure C-32: Transverse discharge distribution for the Rough Bed Experiment.....	169

Figure C33: Transverse discharge distribution for the Rough Ice Experiment. ....	169
Figure C34: Transverse discharge distribution for the Rough Bed - Rough Ice Experiment. ....	169
Figure C-35: Fit of experimental data in the bed affected zone to the log-law at Y = 0 mm for the Base Experiment with $u_* = 0.019 \text{ m/s}$ . ....	170
Figure C-36: Fit of experimental data in the bed affected zone to the log-law at Y = 50 mm for the Base Experiment with $u_* = 0.01875 \text{ m/s}$ . ....	171
Figure C-37: Fit of experimental data in the bed affected zone to the log-law at Y = 100 mm for the Base Experiment with $u_* = 0.0185 \text{ m/s}$ . ....	171
Figure C-38: Fit of experimental data in the bed affected zone to the log-law at Y = 150 mm for the Base Experiment with $u_* = 0.01825 \text{ m/s}$ . ....	172
Figure C-39: Fit of experimental data in the bed affected zone to the log-law at Y = 200 mm for the Base Experiment with $u_* = 0.01825 \text{ m/s}$ . ....	172
Figure C-40: Fit of experimental data in the ice affected zone to the log-law at Y = 200 mm for the Base Experiment with $u_* = 0.02 \text{ m/s}$ . ....	173
Figure C-41: Fit of experimental data in the bed affected zone to the log-law at Y = 250 mm for the Base Experiment with $u_* = 0.018 \text{ m/s}$ . ....	173
Figure C-42: Fit of experimental data in the ice affected zone to the log-law at Y = 250 mm for the Base Experiment with $u_* = 0.02 \text{ m/s}$ . ....	174
Figure C-43: Fit of experimental data in the bed affected zone to the log-law at Y = 300 mm for the Base Experiment with $u_* = 0.018 \text{ m/s}$ . ....	174
Figure C-44: Fit of experimental data in the ice affected zone to the log-law at Y = 300 mm for the Base Experiment with $u_* = 0.019 \text{ m/s}$ . ....	175

Figure C-45: Fit of experimental data in the bed affected zone to the log-law at Y = 350 mm for the Base Experiment with $u_* = 0.018 \text{ m/s}$ .....	175
Figure C-46: Fit of experimental data in the ice affected zone to the log-law at Y = 350 mm for the Base Experiment with $u_* = 0.018 \text{ m/s}$ .....	176
Figure C-47: Fit of experimental data in the bed affected zone to the log-law at Y = 400 mm for the Base Experiment with $u_* = 0.01775 \text{ m/s}$ .....	176
Figure C-48: Fit of experimental data in the ice affected zone to the log-law at Y = 400 mm for the Base Experiment with $u_* = 0.01775 \text{ m/s}$ .....	177
Figure C-49: Fit of experimental data in the bed affected zone to the log-law at Y = 450 mm for the Base Experiment with $u_* = 0.01725 \text{ m/s}$ .....	177
Figure C-50: Fit of experimental data in the ice affected zone to the log-law at Y = 450 mm for the Base Experiment with $u_* = 0.0175 \text{ m/s}$ .....	178
Figure C-51: Fit of experimental data in the bed affected zone to the log-law at Y = 500 mm for the Base Experiment with $u_* = 0.01625 \text{ m/s}$ .....	178
Figure C-52: Fit of experimental data in the ice affected zone to the log-law at Y = 500 mm for the Base Experiment with $u_* = 0.0175 \text{ m/s}$ .....	179
Figure C-53: Fit of experimental data in the bed affected zone to the log-law at Y = 535 mm for the Base Experiment with $u_* = 0.01625 \text{ m/s}$ .....	179
Figure C-54: Fit of experimental data in the ice affected zone to the log-law at Y = 535 mm for the Base Experiment with $u_* = 0.0175 \text{ m/s}$ .....	180
Figure C-55: Fit of experimental data in the bed affected zone to the log-law at Y = 550 mm for the Base Experiment with $u_* = 0.01625 \text{ m/s}$ .....	180
Figure C-56: Fit of experimental data in the ice affected zone to the log-law at Y = 550 mm for the Base Experiment with $u_* = 0.018 \text{ m/s}$ .....	181

Figure C-57: Fit of experimental data in the bed affected zone to the log-law at Y = 565 mm for the Base Experiment with $u_* = 0.0155 \text{ m/s}$ .....	181
Figure C-58: Fit of experimental data in the ice affected zone to the log-law at Y = 565 mm for the Base Experiment with $u_* = 0.017 \text{ m/s}$ .....	182
Figure C-59: Fit of experimental data in the bed affected zone to the log-law at Y = 575 mm for the Base Experiment with $u_* = 0.01515 \text{ m/s}$ .....	182
Figure C-60: Fit of experimental data in the ice affected zone to the log-law at Y = 575 mm for the Base Experiment with $u_* = 0.017 \text{ m/s}$ .....	183
Figure C-61: Fit of experimental data in the bed affected zone to the log-law at Y = 585 mm for the Base Experiment with $u_* = 0.01425 \text{ m/s}$ .....	183
Figure C-62: Fit of experimental data in the ice affected zone to the log-law at Y = 585 mm for the Base Experiment with $u_* = 0.016 \text{ m/s}$ .....	184
Figure C-63: Fit of experimental data in the bed affected zone to the log-law at Y = 595 mm for the Base Experiment with $u_* = 0.0125 \text{ m/s}$ .....	184
Figure C-64: Fit of experimental data in the ice affected zone to the log-law at Y = 595 mm for the Base Experiment with $u_* = 0.013 \text{ m/s}$ .....	185
Figure C-65: Fit of experimental data in the wall affected zone to the log-law at Z = 45 mm for the Base Experiment with $u_* = 0.016 \text{ m/s}$ .....	185
Figure C-66: Fit of experimental data in the wall affected zone to the log-law at Z = 60 mm for the Base Experiment with $u_* = 0.0165 \text{ m/s}$ .....	186
Figure C-67: Fit of experimental data in the wall affected zone to the log-law at Z = 75 mm for the Base Experiment with $u_* = 0.0165 \text{ m/s}$ .....	186
Figure C-68: Fit of experimental data in the wall affected zone to the log-law at Z = 90 mm for the Base Experiment with $u_* = 0.01675 \text{ m/s}$ .....	187

Figure C-69: Fit of experimental data in the wall affected zone to the log-law at Z = 105 mm for the Base Experiment with $u^* = 0.0165 \text{ m/s}$ .....	187
Figure C-70: Fit of experimental data in the wall affected zone to the log-law at Z = 120 mm for the Base Experiment with $u^* = 0.01625 \text{ m/s}$ .....	188
Figure C-71: Fit of experimental data in the wall affected zone to the log-law at Z = 130 mm for the Base Experiment with $u^* = 0.01625 \text{ m/s}$ .....	188
Figure C-72: Fit of experimental data in the wall affected zone to the log-law at Z = 140 mm for the Base Experiment with $u^* = 0.016 \text{ m/s}$ .....	189
Figure C-73: Fit of experimental data in the wall affected zone to the log-law at Z = 150 mm for the Base Experiment with $u^* = 0.016 \text{ m/s}$ .....	189
Figure C-74: Fit of experimental data in the wall affected zone to the log-law at Z = 165 mm for the Base Experiment with $u^* = 0.01575 \text{ m/s}$ .....	190
Figure C-75: Fit of experimental data in the wall affected zone to the log-law at Z = 175 mm for the Base Experiment with $u^* = 0.015 \text{ m/s}$ .....	190
Figure C-76: Shear stress distribution for the Open Channel Experiment. ....	191
Figure C-77: Shear stress distribution for the Covered Channel Experiment. ....	191
Figure C-78: Shear stress distribution for the Base Experiment. ....	191
Figure C-79: Shear stress distribution for the Low Froude Experiment.....	192
Figure C-80: Shear stress distribution for the High Froude Experiment. ....	192
Figure C-81: Shear stress distribution for the 25% Coverage Experiment.....	192
Figure C-82: Shear stress distribution for the 50% Coverage Experiment.....	193
Figure C-83: Shear stress distribution for the Rough Bed Experiment. ....	193
Figure C-84: Shear stress distribution for the Rough Ice Experiment.....	193

Figure C-85: Shear stress distribution for the Rough Bed - Rough Ice	
Experiment. ....	194
Figure C-86: Streamwise turbulence intensity distribution for the Open Channel	
Experiment. ....	195
Figure C-87: Streamwise turbulence intensity distribution for the Covered	
Channel Experiment. ....	195
Figure C-88: Streamwise turbulence intensity distribution for the Base	
Experiment. ....	195
Figure C-89: Streamwise turbulence intensity distribution for the Low Froude	
Experiment. ....	196
Figure C-90: Streamwise turbulence intensity distribution for the High Froude	
Experiment. ....	196
Figure C-91: Streamwise turbulence intensity distribution of the 25% Coverage	
Experiment. ....	196
Figure C-92: Streamwise turbulence intensity distribution for the 50% Coverage	
Experiment. ....	197
Figure C-93: Streamwise turbulence intensity distribution for the Rough Bed	
Experiment. ....	197
Figure C-94: Streamwise turbulence intensity distribution for the Rough Ice	
Experiment. ....	197
Figure C-95: Streamwise turbulence intensity distribution for the Rough Bed -	
Rough Ice Experiment. ....	198

## List of Symbols

<u>Symbol</u>	<u>Definition</u>	<u>Units [MLT]</u>
$A$	= cross sectional area	[ L <sup>2</sup> ]
$A_{cover}$	= area of the cross section that is covered	[ L <sup>2</sup> ]
$A_{open}$	= area of the cross section that is uncovered	[ L <sup>2</sup> ]
$A_p$	= partial area	[ L <sup>2</sup> ]
$b$	= bottom width	[ L ]
$B$	= maximum width of flow area	[ L ]
$C_{u,v,w}$	= coefficients from Eqns. (2-4), (2-5), and (2-6)	[ - ]
$d\bar{u}/dz$	= mean streamwise velocity gradient	[ 1 / T ]
$D$	= depth	[ L ]
$g$	= gravity	[ L / T <sup>2</sup> ]
$k_n$	= unit conversion factor	[ - ]
$k_s$	= equivalent sand grain roughness	[ L ]
$K_{covered}$	= conveyance in the covered area of the channel	[ - ]
$K_{open}$	= conveyance in the open area of the channel	[ - ]
$K_{total}$	= total conveyance for the channel	[ - ]
$K_0$	= a constant for a given flow rate	[ - ]
$L$	= reach length between locations $i$ and $i + 1$	[ L ]
$m_b$	= parameter related to bed roughness	[ - ]
$m_i$	= parameter related to ice roughness	[ - ]
$n$	= Manning's roughness coefficient	[ T / L <sup>0.33</sup> ]
$n_{bed}$	= Manning's roughness value of the bed	[ T / L <sup>0.33</sup> ]
$n_c$	= Manning's composite roughness value	[ T / L <sup>0.33</sup> ]

$n_i$	=	Manning's roughness value of location i	[ T / L <sup>0.33</sup> ]
$n_{ice}$	=	Manning's roughness value of the ice	[ T / L <sup>0.33</sup> ]
$P_i$	=	wetted perimeter of location i	[ L ]
$q$	=	unit discharge at y	[ L <sup>2</sup> / T ]
$\bar{q}$	=	average unit discharge of the cross section	[ L ]
$Q$	=	discharge	[ L <sup>3</sup> / T ]
$Q_p$	=	discharge in partial area of cross section	[ L <sup>3</sup> / T ]
$R$	=	hydraulic radius	[ L ]
$R_{covered}$	=	hydraulic radius of the covered area of cross section	[ L ]
$R_{open}$	=	hydraulic radius of the open area of cross section	[ L ]
$R_p$	=	hydraulic radius of partial area of cross section	[ L ]
$S$	=	slope	[ L / L ]
$\bar{S}_e$	=	average energy grade line slope	[ L / L ]
$TKE$	=	turbulent kinetic energy	[ L <sup>2</sup> / T <sup>2</sup> ]
$U$	=	instantaneous streamwise velocity	[ L / T ]
$\bar{u}$	=	average streamwise velocity	[ L / T ]
$u'$	=	streamwise turbulence intensity	[L/T]
$u_*$	=	shear velocity	[ L / T ]
$\overline{uv}$	=	time average of product of fluctuating velocity components	[ L <sup>2</sup> / T <sup>2</sup> ]
$U_{avg}$	=	average streamwise velocity of a vertical transect	
$U_{bulk}$	=	bulk average cross sectional streamwise velocity	[ L / T ]
$V$	=	instantaneous spanwise velocity	[ L / T ]
$\bar{v}$	=	average spanwise velocity	[ L / T ]

$v'$	=	spanwise turbulence intensity	[L/T]
$V_{avg}$	=	average velocity	[ L / T ]
$W$	=	instantaneous vertical velocity	[ L / T ]
$\bar{w}$	=	average vertical velocity	[ L / T ]
$w'$	=	vertical turbulence intensity	[L/T]
$WSE_i$	=	water surface elevation at location i	[ L ]
$y$	=	spanwise cross section coordinate	[ L ]
$z$	=	distance from bed	[ L ]
$Z_{bed}$	=	depth of flow affected by bed	[ L ]
$Z_{ice}$	=	depth of flow affected by ice	[ L ]
$z_0$	=	height from bed of zero Reynolds shear stress	[ L ]
$\alpha$	=	fraction of water depth affected by ice cover	[ - ]
$\alpha_e$	=	kinetic energy flux correction coefficient	[ - ]
$\gamma$	=	specific weight	[ M / L <sup>2</sup> T <sup>2</sup> ]
$\Delta B$	=	roughness shift	[ - ]
$\theta$	=	angle of misalignment	[ - ]
$\kappa$	=	von Karman constant	[ - ]
$\mu$	=	dynamic viscosity	[ M / L T ]
$\nu$	=	kinematic viscosity	[ L <sup>2</sup> / T ]
$\rho$	=	density	[ M / L <sup>3</sup> ]
$\tau$	=	shear stress	[ M / L T <sup>2</sup> ]
$\tau_a$	=	average shear stress	[ M / L T <sup>2</sup> ]
$\tau_b$	=	boundary shear stress	[ M / L T <sup>2</sup> ]
$\phi$	=	arbitrary exponent	[ - ]

## 1. Introduction

In northern climates where water bodies are subjected to sub-freezing temperatures for part of the year it is important to know how the presence of ice impacts the flow characteristics of channels. While many studies have been conducted in channels that are fully open or completely covered with ice, little is known about the hydraulic characteristics of channels with only a partial cover, such as when border ice is present. Acoustic Doppler velocimetry was utilized to enhance our understanding of how channels are affected by border ice. Specifically, the ability of acoustic Doppler velocimeters (ADV) to record high frequency, three-dimensional velocity time series was used to characterize both the mean velocity components in all three dimensions as well as explore the impact on the turbulence intensities and boundary shear stress distributions.

Understanding border ice formation and the impact of its presence on discharge, velocity, and turbulence intensity patterns can help to fill current knowledge gaps and improve existing numerical models, especially since comprehensive, two dimensional river ice models now exist. The improved capability to model river ice processes can help to reduce the impact of large spring floods through better planning and management of river ice as well as to reduce ice related energy losses, and ensuing financial losses experienced at northern hydroelectric generating stations.

Attempting to study natural processes, such as border ice formation, through the construction of numerical models based on data collected from field monitoring is complicated by the fact that the geometry and roughness of natural rivers are highly

three dimensional and constantly evolving. As a result, calibration parameters may change over time and models that were valid for one type of scenario are invalidated when a new situation arises. To avoid the need to deal with the variability of natural conditions a physical model can be built. This provides the researcher with a simplified platform to collect data from and greater control over variables, as well as ensuring a degree of uniformity/consistency between tests.

### **1.1. Objectives**

The main objective of this research is to fill existing knowledge gaps regarding the impact of border ice on the hydraulic characteristics of a channel including the velocity and turbulence intensity distributions. The specific technical objectives of this research are to:

- Collect detailed measurements of three-dimensional water velocities in a cross-section of fully developed flow for a channel with varying degrees of discharge, border ice encroachment, and bed-to-ice roughness ratios.
- Quantify the effect of border ice on the composite roughness of a channel and determine a suitable means of estimating it.
- Quantify and examine the structure of the three-dimensional velocity fields in channels subjected to border ice.
- Examine the effect of border ice on the shear stress distribution along the wetted perimeter of a channel.
- Quantify and examine the turbulent flow characteristics of a channel with border ice.
- Provide data for the future development and calibration of numerical models of partial ice cover.

## **1.2. Overview**

Chapter Two contains a literature review looking at: the types of border ice and factors influencing formation and growth; velocity distribution and turbulence intensity profiles of open channels; velocity distribution and turbulence intensity profiles for channels with full ice cover; and the velocity distribution of channels affected by partial ice cover. The laboratory set-up, including the flume and apparatus used for the research, in addition to a description of the testing procedure are found in Chapter Three. Chapter Four presents the results of the experiments along with a detailed analysis. Lastly, a summary of findings and conclusions with recommendations for future work are included in Chapter Five.

## **2. Literature Review**

This chapter will first provide an introduction into the types of border ice and the factors that influence their formation. Then, the velocity distribution and selected turbulence characteristics of open and fully ice-covered channels will be introduced. Lastly, the current literature relating specifically to the impact of border ice on the velocity distribution in a channel will be discussed.

### **2.1. Border Ice Formation**

Border ice, as the name suggests, is ice that forms along the banks, or border, of a river. It can grow out toward the center where it may or may not eventually close over the channel. Two general categories of border ice growth have been identified in the literature and are characterized by the conditions under which they form, i.e. whether it forms thermally or mechanically.

Thermal border ice forms in low velocity areas near the bank of a channel. Under the right conditions, the border ice will continue to grow outward from the bank towards the centre of the channel. Eventually, thermal growth may become hindered or even halt as a result of increasing velocities at the leading edge. Matousek (1984) conducted studies on watercourses in the former Czechoslovakia dealing with the factors that influence static ice formation. The basis of his theoretical analysis was that ice forms on the supercooled surface layer and border ice will form in the parts of the cross section with mean vertical water velocities less than a threshold value. This value is primarily a function of heat transfer, water temperature at the edge of the ice, wind velocity and fetch. Relating the formation of a thermal border ice cover to the vertical component of water velocity is similar to the conditions for the

formation of skim ice on lakes; the surface is supercooled and the vertical turbulence at the surface must be less than the rise velocity of the ice particles that are forming (Beltaos, 2013). This makes sense if thermally-grown border ice is thought of as skim ice that began growing from the shore.

The second means of border ice formation/growth is that which occurs mechanically. Mechanical border ice formation is primarily a function of the accretion of many tiny disk shaped ice particles, called frazil ice, rather than through thermal growth. Groups of frazil particles, called flocs, can accumulate by collecting in the outside of meanders and other low velocity regions at the banks. It is important to note that mechanisms of border ice growth are not mutually exclusive on a given channel in a given season. For example, the border ice regime can start off as thermal in the early season and turn to mechanical as conditions for frazil formation become favorable. In that situation, frazil would adhere to the leading edge of the thermally grown border ice in a process that is sometimes referred to as “buttering” (Beltaos, 2013). Newbury (1968) identified that mechanical “border ice growth is dependent on the heat loss to the atmosphere and the local flow condition for a given concentration of slush ice.” He went on to develop a model describing mechanical border ice growth relating it to heat loss, number of boundaries ice can grow from, and an adhesion parameter that is a function of the cross sectional area and water surface slope of the channel, modified by empirical coefficients.

Michel et al. (1982), performed research on the Saint Anne River in Quebec, and presented five principal factors that would affect border ice progression: heat exchange, velocity at the leading edge of the border ice, frazil production, the geometry of the local reach, and the depth of the reach. Each of these factors has a

different relative importance at different periods through freeze-up. Postulating that geometry and depth were of indirect importance and could be related through velocity and frazil concentration, Michel et al. developed a model of border ice growth that related border ice growth to heat flux, surface velocity along the leading edge of the border ice, and frazil concentration.

Miles (1993), through review of the available literature and his own study of border ice cover on the Burntwood River in Manitoba, agreed that the three main components that influence border ice growth are heat loss, velocity at the ice edge, and the concentration of frazil ice. However, Miles sought to create a model that “uses easily obtainable information, is not computationally intensive, and provides good border ice growth predictions” so frazil was eliminated as a parameter due to the difficulty in obtaining/estimating frazil concentrations. Miles concluded that the incremental border ice growth was best related to the fraction of the channel already covered (as a surrogate for edge velocity) and degree-days of freezing (as a surrogate for heat loss) in his study area.

Conclusions in the literature (Haresign, Toews, & Clark, 2011; Miles, 1993) indicate care should be taken when applying border ice models to situations outside those for which they were determined. It is important to understand the means by which border ice is known to form in the specific area of interest prior to choosing a model. For example, if it is known that frazil is regularly produced in a reach, it would not be advised to use the model proposed by Matousek (1984).

## 2.2. Flow Characteristics of Open Channels

Open channel hydraulics is covered in many textbooks and papers, each of which may use its own convention for discussing velocity. Hereafter, the convention used for referring to velocities will be to separate the velocity vector into its three orthogonal components, labeled  $U$  (representing the main streamwise direction),  $V$  (spanwise), and  $W$  (vertical). Each of these components can be decomposed into its mean value ( $\bar{u}, \bar{v}$  and  $\bar{w}$  respectively) and a fluctuating component ( $u, v$ , and  $w$  respectively) such that the instantaneous velocity is given by  $U = \bar{u} + u$ .

### 2.2.1. Velocity

When examining channel flow, often the simplest place to begin is by looking at simple parameters such as the depth and average velocity during uniform flow. One of the most famous equations for describing the average velocity of a channel is the empirically based Manning equation. Manning analyzed the results of a series of existing experiments, primarily those of Darcy and Bazin, and arrived at the conclusion that the relationship between velocity and hydraulic radius was better described by a two-thirds power relationship rather than one-half as suggested by others (Munson, Young, & Okiishi, 2006; Sturm, 2010). Manning's equation as it is used today is as follows:

$$V_{avg} = \frac{k_n}{n} R^{2/3} \sqrt{S} \quad (2-1)$$

where

$V_{avg}$	=	average velocity	[ L / T ]
$k_n$	=	unit conversion factor	[ - ]
$n$	=	Manning's roughness coefficient	[ T / L <sup>0.33</sup> ]

$R$	=	hydraulic radius	[ L ]
$S$	=	slope	[ L / L ]

Manning's roughness coefficient is intended to account for the effect of the resistance of the channel on the depth and velocity. Typical values of Manning's  $n$  for various materials and surfaces have been determined experimentally. Alternately, the bulk average velocity of the cross section,  $U_{\text{bulk}}$ , can be determined by dividing the discharge,  $Q$ , by the cross sectional area,  $A$ .

In reality, the velocity in a channel is not the same for all locations. Chow (1959) provides a high level description of the two dimensional velocity distribution of an open channel. He attributes the non-uniform distribution of velocity in a cross section to the presence of the free surface and shear forces along the boundaries. Chow also states that other factors such as geometry of the cross section, bends in the channel, and bed roughness will affect the velocity distribution. Generally, lower velocities are found near the solid boundaries and increase toward the centre of the channel and inertia will carry the position of maximum velocity to the outside of bends. Figure 2-1 illustrates how streamwise velocity contours might look in two different types of channels.

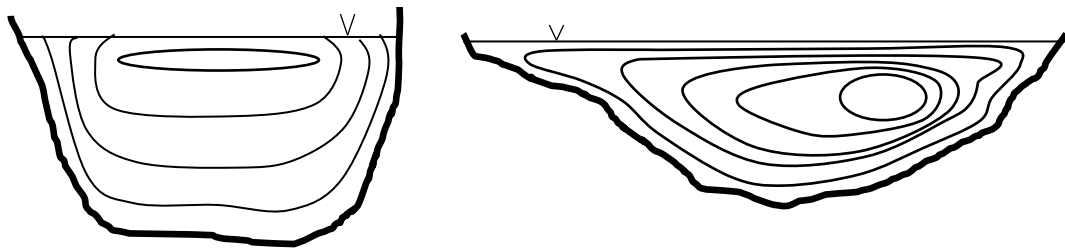


**Figure 2-1: Velocity contours in open channels**

Over the depth of flow, the velocity profile at a particular location is often described by either a logarithmic or power relationship. Some of the most common expressions are the log-law, the velocity-defect law, and Cole's law of the wake. While theoretically these equations are each applicable only within a certain region of the velocity profile, experimental data shows that practically these expressions can be used to describe the velocity over nearly the full depth of flow (Nezu & Nakagawa, 1993; Sturm, 2010). The equation for the log-law is given below for rough channels. To obtain the relationship for smooth channels, set the roughness shift equal to zero.

$$\bar{u}/u_* = \frac{1}{\kappa} \ln(u_* z / \nu) + 5 - \Delta B \quad (2-2)$$

where

$\bar{u}$	=	average streamwise velocity	[ L / T ]
$u_*$	=	shear velocity	[ L / T ]
$\nu$	=	kinematic viscosity	[ L <sup>2</sup> / T ]
$\kappa$	=	von Karman constant (0.41)	[ - ]
$z$	=	distance from bed	[ L ]
$\Delta B$	=	roughness shift	[ - ]

This relationship suggests that the maximum velocity will always occur at the surface, as it increases monotonically with distance from the bed. However, in open water flow, the maximum velocity is usually located between 5% and 25% of the depth from the surface (Chow, 1959). This has been attributed by some to secondary currents (Absi, 2011; Nezu & Nakagawa, 1993). Attempts have been made at developing equations that account for the dip-phenomenon including modifications

to the log-wake law (Absi, 2011; Guo & Julien, 2008; Guo, 2014) or through incorporating the Reynolds Averaged Navier Stokes (RANS) equation in the derivation (Lassabatere, Pu, Bonakdari, Joannis, & Larrarte, 2012; Pu, 2013; Yang, Tan, & Lim, 2004).

### 2.2.2. Turbulence Intensities

Flow in natural channels is inherently turbulent. The complex nature of the environment gives rise to small random fluctuations in flow field characteristics, such as velocity, through space and time over a wide range of scales (Sturm, 2010). It is important to consider turbulence in natural channels because of its strong connection to mass, momentum and heat transfer as well as its efficient mixing properties. This efficient mixing has implications that influence the velocity distribution, shear stress near boundaries, sediment transport, energy losses, etc. (Nezu & Nakagawa, 1993; Sturm, 2010).

The degree by which the velocity fluctuates can be characterized by the turbulence intensity, calculated as the (square) root of the mean of the squares of the fluctuating component of the velocity. As an equation it is expressed:

$$u' = \sqrt{\overline{(U - \bar{u})^2}} \quad (2-3)$$

where  $u'$  denotes the turbulence intensity, or root-mean-square (RMS) velocity and an overbar signifies a time average. While the equation given above represents the turbulence intensity in the streamwise direction  $u$ ,  $v$  and  $w$  can be substituted to obtain the spanwise and vertical values, respectively. It can be seen that larger

turbulence intensities are a result of larger and more frequent fluctuations from the mean velocity.

Nezu and Nakagawa (1993) derived semi-theoretical, exponential relationships between turbulence intensity when normalized by shear velocity, and the relative position from the bed. Analysis of existing experimental data allowed for the evaluation of the empirical constants and found that they are independent of both the Reynolds number and Froude number when the Reynolds number is sufficiently high in magnitude. The equations are given as follows:

$$u'/u_* = 2.30\exp(-z/D) \quad (2-4)$$

$$v'/u_* = 1.63\exp(-z/D) \quad (2-5)$$

$$w'/u_* = 1.27\exp(-z/D) \quad (2-6)$$

where

$$u', v', w' = \text{streamwise, spanwise, and vertical} \quad [\text{L/T}]$$

turbulence intensities respectively

$$D = \text{depth} \quad [\text{L}]$$

While equations (2-4), (2-5), and (2-6) were developed for the intermediate region, ( $\sim 0.1 < z/D < \sim 0.6$ ) where production and dissipative forces equal and an energy equilibrium occurs, practically they can be applied throughout nearly the entire depth of flow regardless of Froude or Reynolds number, with exception of the region very near the wall (Nezu & Nakagawa, 1993). At the wall, the no-slip boundary condition causes the turbulence intensities to go to zero and thus Equations (2-4), (2-5), and (2-6) will not accurately depict the profile in this near-wall region.

### 2.2.3. Shear Stress

Immediately adjacent to a boundary, the velocity of a fluid is the same as that of the boundary; this is called the no-slip condition. By virtue of this condition, a shear force is exerted on the boundary of a channel by the movement of the water above (Munson et al., 2006). A force balance performed on a reach of a channel under uniform flow reveals that the average value of shear stress in the channel can be calculated as:

$$\tau_a = \gamma RS \quad (2-7)$$

where

$$\begin{aligned} \tau_a &= \text{average shear stress} && [ \text{M} / \text{L T}^2 ] \\ \gamma &= \text{specific weight} && [ \text{M} / \text{L}^2 \text{T}^2 ] \end{aligned}$$

However, the shear stress distribution is not uniform throughout the channel. There are areas where it will be higher or lower than average. One method for determining the shear stress at a particular point on the bed is to calculate it from fitting the velocity profile at that location to the log-law. In the log-law, the shear velocity,  $u_*$ , is used as a fitting parameter to make the measured and theoretical profiles overlap. Once  $u_*$  is known, it can be used to obtain the boundary shear stress at that location with the following equation:

$$\tau_b = \rho u_*^2 \quad (2-8)$$

where

$$\tau_b = \text{boundary shear stress} \quad [ M / L T^2 ]$$

$$\rho = \text{density} \quad [ M / L^3 ]$$

Performing this analysis for several locations along the wetted perimeter of a cross section of a channel yields the shear stress distribution. The exact shape of the shear stress distribution will differ from channel to channel but has been found to be influenced by cross-sectional shape, sinuosity of the channel, the boundary roughness distribution, and secondary flows (Khodashenas, Abderrezzak, & Paquier, 2008). Knight, Demetriou, & Hamed (1984) conducted a series of experiments to determine the shear stress distribution along the bed and side walls of rectangular channels. Their results are presented with others in Nezu and Nakagawa (1993). The findings for open channel flow indicate that the distribution of shear stress along the bed is highest in the centre of the channel and lowest in the corners, where it decreases rapidly to zero. It was also observed that near the wall there was a local peak followed by a slight trough before the shear stress increased again to its maximum. A typical shear stress distribution is shown in Figure 2-2. Figure 2-2 is not intended to be shown to scale nor is the location of  $\tau_a$  intended to represent the actual relative magnitude of the average shear stress.

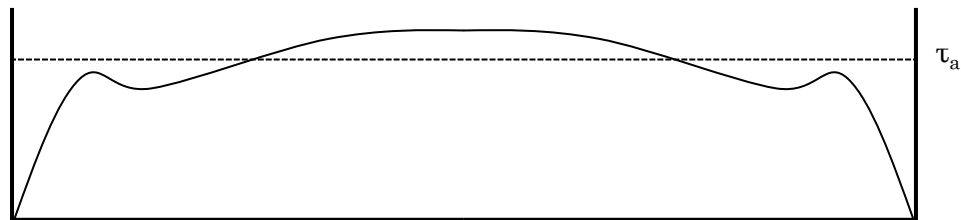


**Figure 2-2: Typical open channel bed shear stress distribution.**

Once the shear stress along the boundary is known, the distribution through the depth of the channel can be determined. Shear stress is known to decrease linearly

from the bed until it reaches a value of zero at the free surface. Where detailed measurements can be taken, the shear stress at a point can also be calculated using

$$\tau = \mu d\bar{u}/dz - \rho\bar{u}\bar{v} \quad (2-9)$$

where

$\tau$	=	shear stress	[ M / L T <sup>2</sup> ]
$\mu$	=	dynamic viscosity	[ M / L T ]
$d\bar{u}/dz$	=	mean streamwise velocity gradient	[ 1 / T ]
$\bar{u}\bar{v}$	=	time average of product of fluctuating velocity components	[ L <sup>2</sup> / T <sup>2</sup> ]

On the right hand side of the equation the first term represents the laminar, or viscous, shear stress and the second term represents the turbulent, or Reynolds, shear stress. Practically, the Reynolds shear stress will be much larger than the viscous shear stress in fully turbulent flow and thus the viscous shear stress is often ignored. The exception to this case is in a small layer of flow near the boundary where viscous forces dominate.

### **2.3. Flow Characteristics of Channels with Full Ice Cover**

When the free surface is replaced by an ice cover, this new boundary imposes the no-slip condition on the flow, changes the roughness coefficient, increases the wetted perimeter, and increases the overall resistance to flow. The most extreme example would be on a very wide channel, where the wetted perimeter is essentially doubled. The result of this increase in resistance is a decrease in discharge for the same stage, or conversely, an increase in stage for the same discharge. This means rating

curves that have been developed for open water conditions may over predict the discharge a reach is experiencing if ice is not accounted for. This is complicated by the intrinsic spatial and temporal variability of ice covers. For the increase in flow depth, and thus cross sectional area, resulting from the presence of the ice cover, continuity demands that the average velocity decrease for the same discharge. In addition to decreasing the mean velocity of the flow, the replacement of the free surface with a solid boundary will have an effect on the velocity distribution.

### 2.3.1. Velocity Distribution

The no-slip condition imposed by the cover forces the velocity on the underside of the ice to go to zero. This acts to shift the location of the maximum velocity down toward the bed. The relative roughness of the ice with respect to the channel bottom will determine approximately where the maximum velocity will be; the rougher the ice, the deeper the maximum velocity. In theory, an ice cover with the same roughness as the channel bed will have the maximum velocity located equidistant to the bed and the underside of the ice.

One method common in the literature for determining the velocity distribution of ice covered channels is the concept of two-layer flow (Arisz, Davar, & Tang, 1988; Gogus & Tatinclaux, 1980; Larsen, 1969; Majewski, 1990, 1994; Sukhodolov, Thiele, Bungartz, & Engelhardt, 1999). This concept assumes the velocity profile extending from each of the boundaries follows an open channel velocity profile, such as the log-law or the power-law. The position of maximum velocity in the channel as a whole is located at the intersection of the two profiles describing the regions influenced by the roughness of the underside of the ice and of the bed. As a result, the channel is

effectively divided into two regions separated by the plane of maximum velocity. Each of these regions can be treated as their own open channel in other calculations. One of the assumptions required to separate the flow at the maximum velocity is that it is also the location of zero shear stress, as it would be if it were a truly open channel. In reality this is only the case when the maximum velocity occurs at mid-depth. For cases of asymmetric distributions there is a small difference in the location of these two planes which, for practical purposes, can be neglected (Gogus & Tatinclaux, 1980; Hanjalic & Launder, 1972; Parthasarathy & Muste, 1994). Both the log-law and power-law have been found to represent the velocity distribution equally well by Dolgoplova (1998), however, they comment that the power-law expression produces a profile without discontinuities as opposed to the log-law which is discontinuous at the location of maximum velocity.

Some researchers (Teal, Ettema, & Walker, 1994; Tsai & Ettema, 1994) prefer the use of a two parameter power law to describe the vertical streamwise velocity profile. They argue that it allows the entire distribution to be represented by a single expression producing a continuous profile as opposed to the piecewise function created by the two layer flow method which may be discontinuous at the maximum velocity. It is also no longer bound by the assumption that the plane of maximum velocity coincides with the plane of zero shear stress (Tsai & Ettema, 1994). The two-parameter power law given by Tsai and Ettema (1994) is written as

$$\bar{u} = K_0 \left(\frac{z}{D}\right)^{1/m_b} \left(1 - \frac{z}{D}\right)^{1/m_i} \quad (2-10)$$

where

$K_0$	=	a constant for a given flow rate	[ - ]
$m_i$	=	parameter related to ice roughness	[ - ]
$m_b$	=	parameter related to bed roughness	[ - ]

The above equation was shown by Teal, Ettema, and Walker (1994) to provide good fit with field measurements and  $R^2$  values ranging from 0.961 to 0.994 when fitted to data measured from flume experiments. Engel et al. (1996) express that the convenience of this equation is contingent on knowledge of the values of the  $K_0$ ,  $m_i$ , and  $m_b$  parameters and go on to provide a means of estimating  $m_b$  based on the bed roughness and flow depth. Otherwise  $m_i$ , and  $m_b$  for a given location need to be estimated from nonlinear regression of velocity profiles. No mention is provided for the determination of  $K_0$ .

Regardless of the method employed, the end result is the same general description; for a given discharge, ice cover will increase stage and decrease mean velocity. Further, the maximum velocity will no longer be near the surface of the channel but instead depressed into the channel, displaced towards the smoother boundary.

### 2.3.2. Turbulence Intensities

As shown previously by Equations (2-4), (2-5), and (2-6), in open channels dimensionless turbulence intensity decreases monotonically in the central region with increasing distance from the bed. It has been found though, that in ice-covered channels the dimensionless turbulence intensities have local maxima near the boundaries and decrease to a minimum value near the location of zero shear stress (Muste, Braileanu, & Ettema, 2000; Parthasarathy & Muste, 1994; Robert & Tran, 2012; Sukhodolov et al., 1999). Additionally, rougher surfaces will produce greater turbulence intensities than if that surface were smooth (Muste et al., 2000;

Parthasarathy & Muste, 1994). In the same manner that the location of maximum velocity is displaced towards the smoother boundary, so is the location of minimum turbulence intensity. As a result, the shape of the dimensionless turbulence intensity profile will depend in part on the relative roughnesses of the bed and ice.

The concept of two-layer flow has been applied to estimating the mean streamwise velocity profile with a piecewise application of the log-law; similarly, a piecewise application of the general form of equations (2-4), (2-5), and (2-6) has been used with good results to estimate the distribution of dimensionless turbulence intensities under a floating cover both in nature and in the lab (Parthasarathy & Muste, 1994; Sukhodolov et al., 1999). Notably though, Sukhodolov et al. (1999) changed the coefficients to produce the best fit for their data. In the centre of the channel away from the boundaries, the coefficients were similar to those proposed by Nezu and Nakagawa (1993) in both the ice and bed affected layers. The exception was in the vertical component coefficients which, even in the core flow region, were 20% smaller than the values recorded in laboratory settings. This suggests a lesser exchange of turbulent energy in the vertical direction which the authors suggest may be a result of possible flow stratification in their experiment (Sukhodolov et al., 1999).

### **2.3.3. Shear Stress**

The same methods used for determining the average shear stress and local bed shear stress in open channels also apply to covered channels. However, the distribution of shear stress through a cross section is not necessarily the same. The distribution provided by Nezu and Nakagawa (1993) does not have a maximum value at the centre of the channel. Rather, the centre of the channel is a local minimum and there are two maxima, each located approximately half the distance

from the wall to the centre as illustrated in Figure 2-3. Not all distributions follow this pattern though. In several of the figures presented by Knight et al (1984) the bed shear stress distributions for the covered channel flow are similar to the distributions for open channel flow. There are still differences in magnitude and positioning of local maxima, but many experiments still displayed global maximum shear stresses at the centre of the channel as previously shown in Figure 2-2.

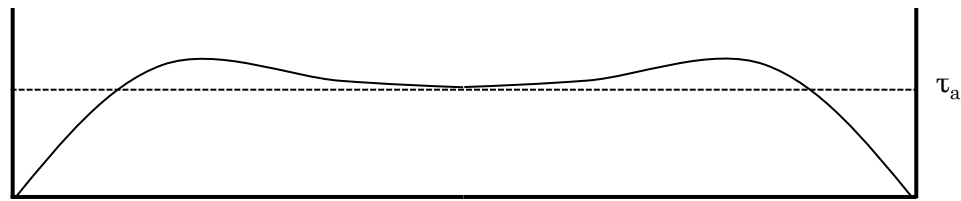


**Figure 2-3: Typical covered channel bed shear stress distribution.**

The shear stress distribution through the depth of flow is also similar to that of open channels. Parthasarathy & Muste (1994) performed a series of experiments building off the works of Hanjalic & Launder (1972) analyzing flow characteristics in asymmetrically rough, turbulent channels. The experiments were conducted in a flume with a sand bed and floating cover so as to be analogous to an ice-covered river. From analysis of the streamwise momentum equation they produced an equation demonstrating a linear distribution of shear stress through the channel still exists. However, instead of a value of zero at the surface, each boundary had its own independent bed shear stress with a linear distribution between them. This analysis was confirmed by results from lab experiments (Parthasarathy & Muste, 1994). Observations in other research from both field and lab studies support this conclusion (Robert & Tran, 2012; Sukhodolov et al., 1999). As mentioned previously, the locations of zero shear stress and maximum velocity are not the same in asymmetrically rough channels. Further, neither the absolute location nor distance

from the maximum velocity can be known without collecting measurements.

However, the plane of zero shear stress was found to always be displaced toward the smoother boundary (Hanjalic & Launder, 1972; Parthasarathy & Muste, 1994).

#### 2.3.4. Composite Roughness

Manning's  $n$  is impacted by many factors, including but not limited to: bed roughness, presence of vegetation, and changes in cross section and slope (Ashton, 1986). Furthermore, as is often the case in natural channels, Manning's  $n$  can be spatially and temporally variable. This can especially be the situation during the winter when channels may be subject to an ice cover.

As ice forms over a channel, it replaces the free surface with an additional boundary with its own unique roughness. The roughness of ice can be highly variable, ranging from smooth, continuous skim ice to the large, irregular blocks that make up an ice jam. To account for spatial variability when using Manning's equation, a composite value of the roughness coefficient is needed. Different methods have been proposed for calculating the composite roughness of an ice-covered channel. Several methods have been reviewed by Uzunur (1975) and Pratte (1979) and summarized by Ashton (1986). One method presented by Ashton (1986) is that of Larsen (1969) given below:

$$\frac{1}{n_c} = \frac{(1/n_{ice})Z_{ice}^{5/3} + (1/n_{bed})Z_{bed}^{5/3}}{D^{5/3}} \quad (2-11)$$

where

$$n_c = \text{composite roughness value} \quad [ T / L^{0.33} ]$$

$$n_{bed} = \text{roughness value of the bed} \quad [ T / L^{0.33} ]$$

$$n_{ice} = \text{roughness value of the ice} \quad [ T / L^{0.33} ]$$

$$Z_{bed} = \text{depth of flow affected by bed} \quad [L]$$

$$Z_{ice} = \text{depth of flow affected by ice} \quad [L]$$

Larsen used the principle of two-layer flow that divides the flow into an ice-affected region and a bed-affected region in conjunction with the application of flow continuity and the Manning equation to solve for the composite roughness. A simple re-arrangement of Equation (2-11) and substitution of  $\alpha = Z_{ice}/D$  yields the so-called  $\alpha$ -method:

$$n_c = \frac{1}{2^{2/3}} \frac{n_{bed} n_{ice}}{n_{bed} \alpha^{5/3} + n_{ice} (1 - \alpha)^{5/3}} \quad (2-12)$$

Use of equations (2-11) and (2-12) requires prior knowledge of, or at least the willingness to assume, the location of the maximum velocity. To facilitate reasonable estimation, Ashton (1986) provides a figure that shows a relationship between the relative position of the maximum velocity and the ratio of bed and ice roughness coefficient values. Assuming  $Z_{ice} = Z_{bed}$  the above equations can be reduced to

$$n_c = \left( \frac{n_{ice}^{3/2} + n_{bed}^{3/2}}{2} \right)^{2/3} \quad (2-13)$$

Equation (2-13) is also known as the Sabaneev Equation and is commonly used in practice. Even though it is less comprehensive than other formulas, it still performs adequately and is simpler to use (Ashton, 1986; Pratte, 1979).

Normally, the  $n$  value of ice needs to be estimated or assumed based on the type and condition of the ice to use one of the above equations. However, if observed discharge or average velocity data for a channel is available, calculating  $n$  using Manning's

equation already accounts for the heterogeneity of the bed and ice cover, providing  $n_c$ . In this case, one of the above composite roughness equations can be used to calculate the roughness value of ice using the known bed and composite roughnesses.

#### **2.4. Flow Characteristics of Channels with Border Ice Cover**

Tsang (1970) states, “as ice cover forms at the banks, the extra resistance causes a reduction in flow in the ice covered part and an increase in flow in the open channel part of a river. ... Once a complete surface ice cover is formed, the resistance in the central portion is also increased. This in turn causes a reduction in flow in the central part and an increase in flow at the sides. Thus as the surface of a river is being frozen, there is a gradual change in velocity distribution in the cross-section of the river” which shows we have observed that border ice has a dynamic effect on the flow distribution of the channel throughout freeze-up.

The depth-averaged velocity distribution of a channel under a known encroachment of border ice can be estimated using the principle of conveyance in divided channels. It states the total conveyance of the channel is the sum of the conveyances in each subsection. For a channel with border ice this amounts to dividing the channel into sections that are covered and open, then calculating the conveyance of each of these sections to determine the flow distribution in the channel. Hirayama (1986) utilized this method when distributing flow on the Yubetsu River in Japan and found that as the border ice grew a higher percentage of the total flow was found in the open water section. It was also observed by Majewski and Baginska (1988) during an ice jam event on an estuarine section of the Vistula River in Poland, that upstream of the

jam there were very low velocities beneath the border ice while the velocities in the open water section had increased.

Miles (1993) looked at border ice growth on the Burntwood River in northern Manitoba. Velocity was measured at 20% and 80% of the depth and averaged to obtain a depth-averaged velocity. Measurements were taken at multiple points along a cross section to construct a velocity profile across the river. However, because of safety concerns and the remoteness of the location, Miles was only able to collect velocity measurements beneath competent border ice and therefore the velocity distribution in the open water section of the channel had to be estimated. This was accomplished by removing the calculated discharge beneath the border ice from the total estimated discharge of the river (obtained from a routing model) and matching the general shape of the open water velocity distribution while preserving the average velocity of both the open water section and cross section as a whole. By comparing the depth averaged velocity profiles at the same cross section for two different dates in winter, the impact of border ice could clearly be seen. The larger wetted perimeter in the areas of border ice increased the resistance to flow and decreased the conveyance capacity of those regions. This forced some of the flow into the open water section of the channel. Consequently, the velocity in the open water section increased for the same discharge. These results agree with the statement made by Tsang (1970).

Tsang (1970) conducted field studies on the Nottawasaga River in southern Ontario examining how the freezing over of a river changes the velocity distribution. He gathered velocity measurements every 5 feet to 10 feet across the river at vertical intervals ranging between 2 to 6 inches with a propeller style current meter. A

cableway was used to enable the safe collection of velocity measurements in the open water section. On one of the days that velocity measurements were collected, the river had not completely frozen over, and so, a cross section of velocities in a channel of border ice was obtained. The velocity profiles at the 15 foot and 25 foot verticals are presented in the paper for each of the dates Tsang collected velocity data. In the case of the partially covered channel these verticals correspond to both an open water and covered section of the channel, respectively. At the 25 foot vertical, beneath the ice, the velocity profile had the same appearance as the profile for an ice covered channel where it is zero at both of the boundaries, increasing to a maximum value somewhere in-between. In the open water section the velocity profile had the same shape as a regular open channel where it began at zero at the bed and increased to a maximum value somewhere near the surface.

Majewski (1992) conducted laboratory experiments to measure the velocity distribution of a channel with varying encroachments of simulated border ice cover and ice-to-bed roughness ratios. Tests were conducted under three different amounts of coverage: open channel flow, 67% coverage, and 80% coverage. Each surface was subjected to two different roughness regimes, smooth and roughened. Bed roughness was simulated with 12 mm diameter stones placed every 10 cm while roughness on the underside of the ice was simulated with 1 cm by 1 cm bars placed every 10 cm. Both sets of roughness elements were oriented perpendicular to the flow. Data was collected for every combination of surface roughness and coverage amount for a total of ten experiments.

Experiments were conducted in a 20 m long by 2 m wide flume under steady flow conditions. Discharge for all tests was 100 L/s. When ice cover was applied, the

depth of the open section of the channel where velocity measurements were taken was maintained at 0.20 m by adjusting the tailwater condition. Time averaged velocity measurements were taken with a miniature current meter. Data was collected for nine vertical profiles throughout the cross section with six to eight measurements on each vertical.

The results of his experiments showed that as the cover encroached farther into the channel, the location of the maximum velocity depressed and the isovels along the surface became pinched together indicating a higher velocity gradient across the surface of the open water section. Majewski also examined the effect of coverage and roughness on the discharge distribution in the channel. He conducted an analysis where he split the cross section into three areas: one area under each covered section and the open area in the middle. The discharge in each area that was calculated from velocity measurements was compared to a predicted discharge that was calculated using the principle of conveyance in divided channels, as discussed above. He found that the values were similar, but, differences between observed and predicted were sometimes as high as 25%. Furthermore, he found that the measured under-ice discharge was always higher than the predicted values and that flow in the open water area could be up to 50% greater than beneath the cover.

### **3. Physical Model and Methodology**

Modeling was conducted in the Hydraulics Research and Testing Facility (HRTF) at the University of Manitoba. The facility has a recirculating flow system where water is drawn from an underground cistern by one or both of two pumps (60 and 75 horsepower) to a constant head tank. From there water is distributed through 350 mm diameter PVC pipes to one or more of several flumes in the HRTF. After running through the flume(s), the water returns to the underground cistern via collection channels in the floor. The experiments described herein were all conducted in one flume, described below in Section 3.1.

#### **3.1. Physical Model**

The flume was designed and built to use all of the available space in the lab. The channel of the flume was 14 m long by 1.2 m wide with a bed slope of 0.25%. The base of the flume was supported by joists spaced approximately 0.3 m apart which rested on joist hangers. The joist hangers were attached to a series of 2x10s that ran the length of the flume. A transit level was used to establish the position of key joist hangers and a chalk line was used to interpolate the position of the remainders. The channel bed and walls were constructed of high density overlay (HDO) plywood and all seams were sealed with a waterproof polyurethane adhesive sealant.

Before entering the channel, water from the recirculating system entered a 2.4 m by 3.6 m headwater box. This acted as a reservoir where the water velocity was reduced and the flow underwent an initial conditioning process. After emerging from the distribution pipe into the headwater box (Figure 3-1A), the water passed through a furnace filter (Figure 3-1B) covering a wall of 38 mm diameter 30 cm long PVC tubes

(Figure 3-1C) in order to straighten the flow. Immediately after the PVC flow straighteners, the flow entered a projecting inlet with the same dimensions as the channel (Figure 3-1D). The presence of the inlet reduced any recirculation effect that the headwater box had on the flow. Lastly, the flow passed over a 13 mm by 13 mm acrylic bar positioned along the perimeter of the flume entrance (Figure 3-1E) that tripped the flow to promote early development of the velocity profile in the channel.

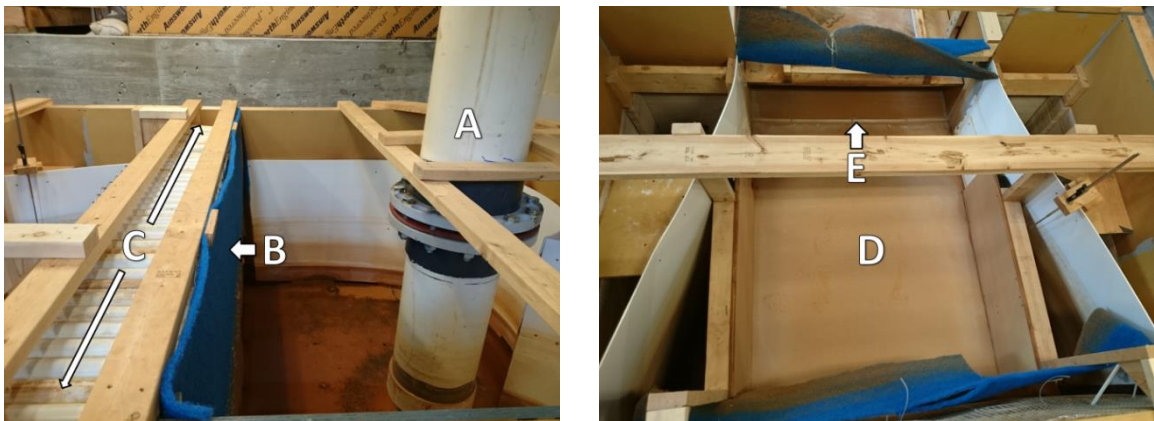


**Figure 3-1: Headwater box components.**

The water level in the channel was controlled by adjusting a gate at the end of the flume that rotated about the base of the outlet, functioning as a weir. From there, the water spilled into the lab's main collection channel and returned to the cistern. A box was built around the end of the flume to contain the splashing from the overflow and to direct the water into the collection channel but did not provide any storage or influence the water level in the channel.

Ice was simulated with HDO plywood. Strips were cut from 1.2 x 2.4 m sheets and supported from above by three legs. The legs were installed 30 cm from either end and in the middle to ensure the HDO did not sag. For some pieces it was necessary to add an additional bracing member to each leg in order to properly support the width of the ice. Individual strips were joined together along the length and across

the width of the channel to create a stable raft of border ice. Neither the lengthwise or widthwise connections interfered with the flow. The ice was installed for each experiment after the water level in the channel had already reached a steady state. The ice was lowered into the water and allowed to float freely while the water level adjusted to the additional resistance. Once steady state was reobtained the ice was fixed into position by fastening the support legs to the top of the channel walls, with close attention paid to ensure that the ice was level across the width of the channel. Figure 3-2 shows fully installed border ice for one of the experiments.



**Figure 3-2: Installed border ice.**

### **3.2. Data Collection**

Velocity data was collected over a cross section to facilitate the analysis of 2D streamwise velocity and turbulence intensity distributions, secondary circulation patterns, and bed shear stresses. Using a Nortek Vectrino II profiling acoustic Doppler velocimeter (ADV) and a Nortek Vectrino+ side-looking ADV, (shown in Figure 3-3), velocity data was able to be collected for all three dimensions of flow simultaneously. The side-looking ADV was capable of measuring data at a single point approximately 5 cm from the transducer while the down-looking ADV could measure up to 30, 1 mm thick, cells in the range from 4 to 7 cm from the transducer.



**Figure 3-3: Vectrino II Profiling ADV (left) and Vectrino + ADV (right).**

The probe heads of the ADVs were connected to their respective main bodies by a flexible cable rather than a rigid stem. This allowed the ADVs to be oriented in different directions using custom-built mounting mechanisms which facilitated sampling throughout most of the channel cross section. However, one region in each of the lower corners, approximately 45 mm high and 65 mm wide, could not be sampled. Figure 3-4 illustrates the sampling locations used for the open channel experiment as well as the corresponding ADV orientation. The down-looking ADV was found to be the most reliable, so it was used whenever possible. The points labelled “Down” were acquired using the Vectrino II ADV oriented normal to the bed. The points labelled “Side” and “Side – Reversed” were acquired using the Vectrino II ADV turned 90 degrees, so that it was normal to the wall. The points labeled “Up” and “Up – Reversed” were collected with the Vectrino+ side-looking ADV oriented to look upwards. For consistency in alignment between tests, the distance from the wall of the flume and two opposing receiver arms on the ADVs were set equal each time a new ADV was mounted. A small level was used to ensure plumbness of the probe head once it had been aligned.

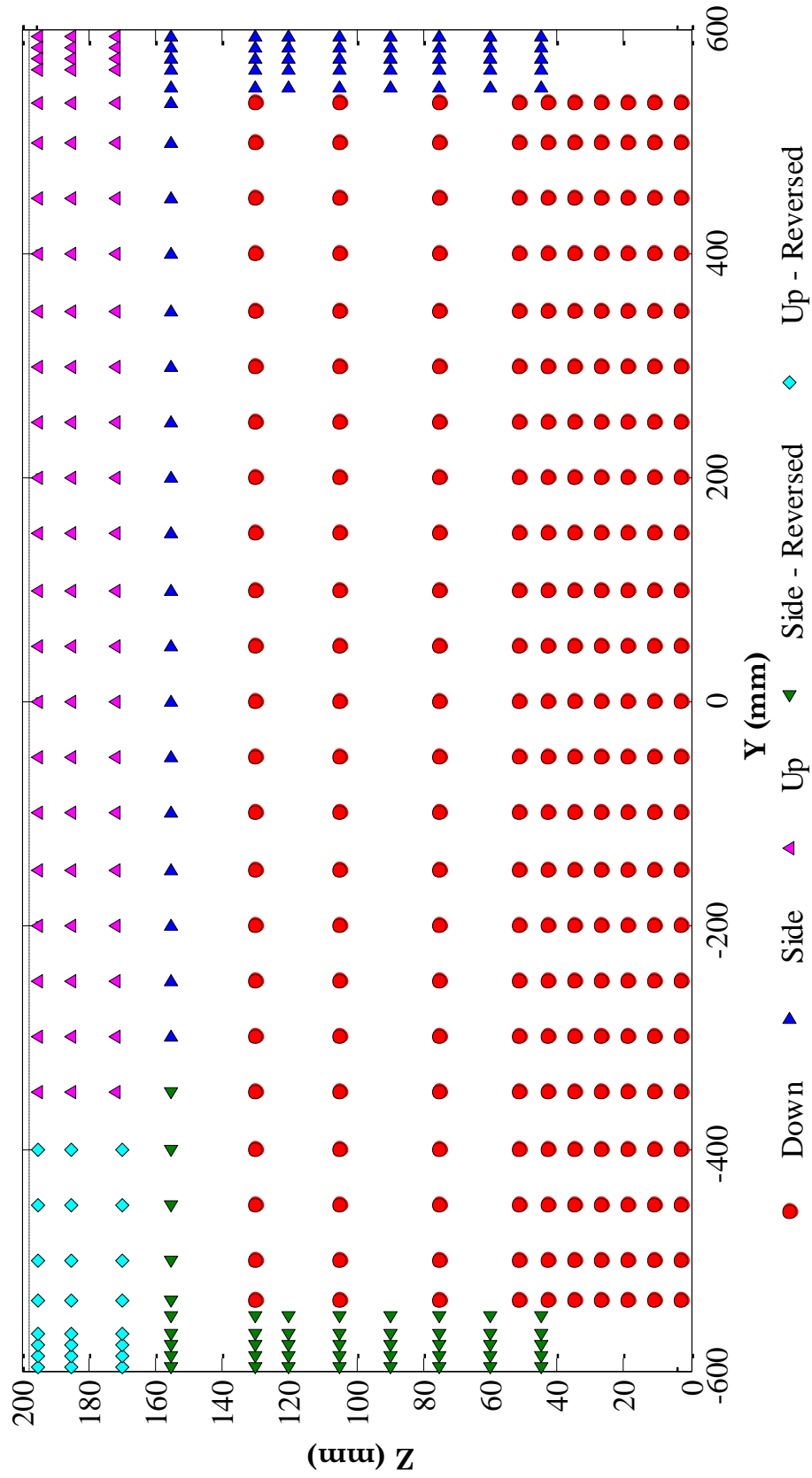


Figure 3-4: Sample locations and ADV orientations for the Open Channel Experiment. Orientations indicate the direction of the ADV probe head while data was collected.

These instruments were moved through the 2D grid of points semi-autonomously by a computer-controlled traversing mechanism capable of movement in the vertical-spanwise plane. A photo of the traversing mechanism can be found in Figure 3-5. A custom computer code was written to move the ADV through a series of predefined points automatically. Upon arriving at the destination point, the traversing mechanism was coded to send a signal to the ADV which initiated sampling. The program would then pause for the duration of data collection before moving on to the next point in the list.



**Figure 3-5: Traversing Mechanism**

Tests were conducted initially to determine which ADV settings would be used during data acquisition. Convergence testing indicated there was no appreciable decrease in error by sampling for longer than 3 minutes (Figure 3-6). Additionally, no time savings were realized by altering the sampling frequency. However, sampling at the maximum rate, 100Hz for the Vectrino Profiler and 200Hz for the Vectrino+, reduced the size of the confidence intervals since more points could be

included in the sample. Therefore each ADV collected data at its highest frequency. Figure 3-7a shows the velocity profile when acquired using the full sampling range of the Vectrino II profiling ADV with some cells overlapping at the ends of each profile. The velocities did not match at the overlapping ends of the sampling ranges, which produced an incorrect saw-tooth profile. This demonstrates that while the instrument is purported to be capable of sampling over a 30 mm range, the data quality drops off at points located farther away from the centre cell and becomes less reliable. The number of cells from which data was collected was therefore limited to the 7 central cells to eliminate the overlap issue (Figure 3-7b). A more detailed explanation of the rationale behind these values is outlined in Appendix A.

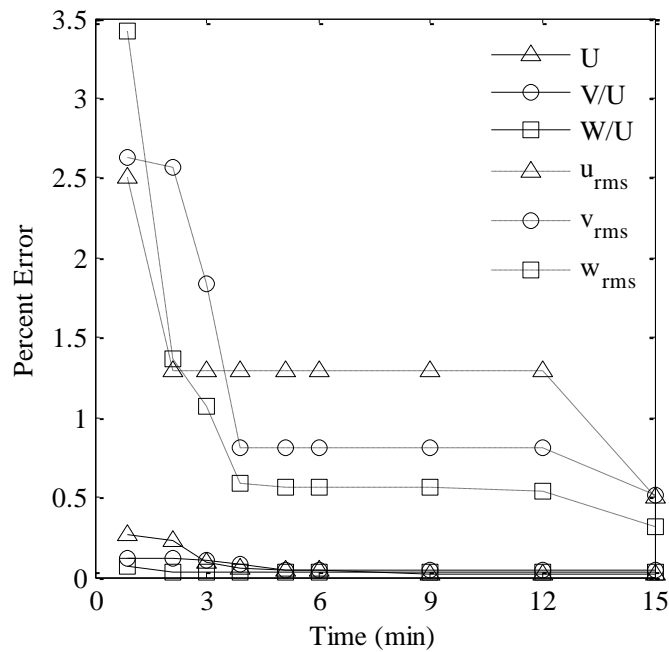
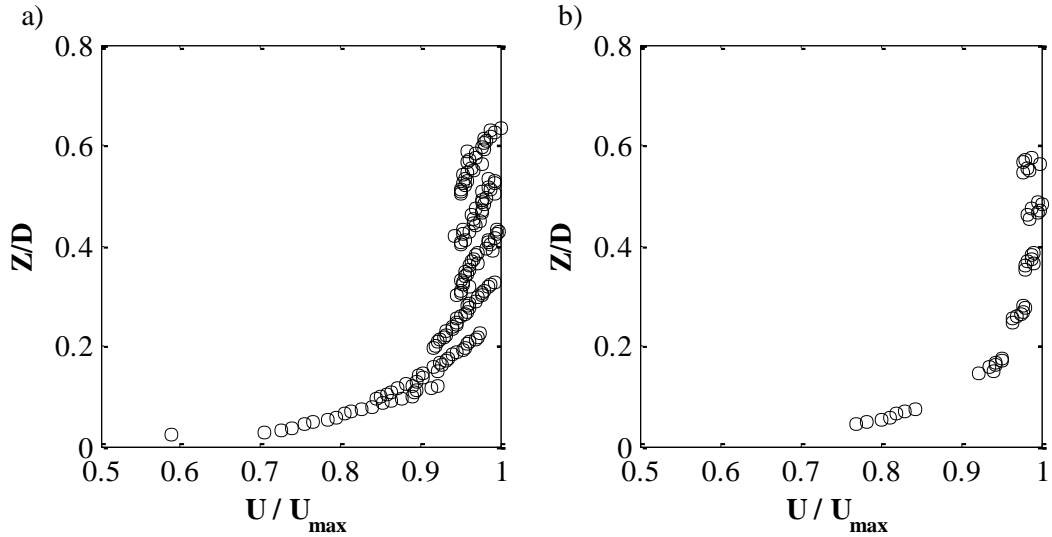


Figure 3-6: Convergence test results for selected flow statistics.



**Figure 3-7: Vectrino Profiler sampling range.**

Although not an instrument setting, signal-to-noise ratio (SNR) is an important parameter for consideration when collecting data with ADVs. SNR is a measure of how strong the signal is compared to the background noise level and is expressed in log scale with units of dB. Low values of SNR can lead to unreliable velocity data (Durand (2014)). One method to increase the signal is adding more material to the water for the sound to reflect off of. This material is often called seeding material. The seeding material used for this study was 10  $\mu\text{m}$  diameter neutrally buoyant glass spheres. If the SNR of the data being collected fell below 15 dB, seeding material was added to the lab's water supply until it returned to that level.

Discharge was measured using volumetric calculations prior to the commencement of each testing day. An ultrasonic flowmeter was connected to the feeder pipe but produced inaccurate flow readings when compared to volumetric calculations. However, the ultrasonic flowmeter provided a steady instantaneous reading that, while incorrect by as much as 25%, was consistent for a given discharge. For this reason, the ultrasonic flowmeter was used to return the discharge to the proper

magnitude faster at the beginning of a testing day and to ensure that it remained relatively constant over the day. The value of the discharge obtained from integration of the velocity data over the cross section was assumed to be the most correct and used in any subsequent calculations.

Water surface profiles were also collected for each of the experiments to provide insight into how the presence of border ice affects the hydraulic grade line of a channel. Manometers tapped into the wall near the base, approximately every 2 meters, were used to measure the hydraulic head at seven points along the length of the flume as well as in the headwater box. Using a transit level, the manometer board was tied in to the same pre-established lab datum as the channel bed. A spreadsheet was used to determine the hydraulic grade line and water depth at any point along the length of the flume.

### **3.3. Post-Processing of ADV Data**

After data was collected, it went through a multiple step post-processing procedure. The steps for this procedure were as follows. First, the data collected was converted from its native format into one that could be manipulated easily using Matlab. Then the local co-ordinate system of the up and side-looking data was adjusted to match the global coordinate system. A first pass through the data identified and removed bad cells using weak spots and minimum thresholds for SNR and correlation as criteria. The thresholds used for SNR and correlation were 15 dB and 30% respectively using values recommended by the manufacturer through personal communications described in Durand (2014). Cells with more than 10% of the data below these thresholds were removed. Following that, the data was de-spiked using the method of Goring & Nikora (2002). In this method the velocity was plotted in

three dimensional phase space against its first and second derivatives. The resulting plot formed a cloud of points in an ellipsoid. Points that fell beyond the expected absolute maximum extents of the main body of the ellipsoid were flagged as spikes and were replaced with the mean of the time series. The process iterated until no new spikes were identified. Generally, 1% to 3% of the points in a time series were identified as spikes. The results for all of the files in an experiment were compiled into a useable format. Lastly, each profile was examined individually and compared to the log-law to identify any anomalous data that may have been missed by the earlier steps. The removal of bad cells, de-spiking, and compilation was accomplished using Matlab programs adapted from those used in Durand (2014).

### 3.4. Preliminary Testing

Prior to conducting the primary experiments, tests were conducted to assess the developing length of the channel. A single vertical profile was collected at the centre of the channel at distances 1, 2, 4, and 8 m from the channel inlet. It can be seen in Figure 3-8 that the flow became self-similar, or fully developed, 2 m from the inlet.

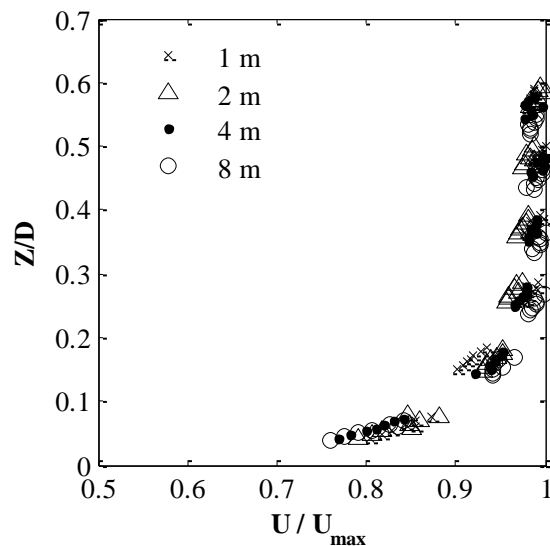


Figure 3-8: Preliminary assessment of channel's developing length.

The two initial experiments that examined the fully open and fully covered channel flow were designed such that the entire cross section of the channel was sampled. In collecting data for the full cross section it was possible to determine whether the velocity field was symmetric about the centerline. An assumption of symmetry would allow for a reduction in the time required to run each additional test by a factor of two. The up-looking and side-looking ADV configurations were not split at the centerline in order to eliminate the possibility that any asymmetry in that region was from switching instrument configurations rather than actual asymmetry in the flow. Figure 3-9 shows select results of the symmetry assessment for the open channel test at two locations for the three mean velocity components. The symmetrical shape of the plots is apparent, where the right hand side and left hand side (looking upstream) values overlapped reasonably well with differences in velocity less than 5% on average near the centre of the channel. In the case of the spanwise velocity the profiles were equal and opposite as expected. The streamwise velocity profiles farther from the center did not overlap as well as the profiles closer to the center with differences in velocity up to 12% but less than 10% on average. However, the profiles were deemed to be sufficiently close to warrant measuring flow in only half of the channel for the partial ice cover tests. Similar analysis also demonstrated that the mean flow components in the fully covered flow and the turbulence intensities for both tests were symmetric and is shown in Appendix B.

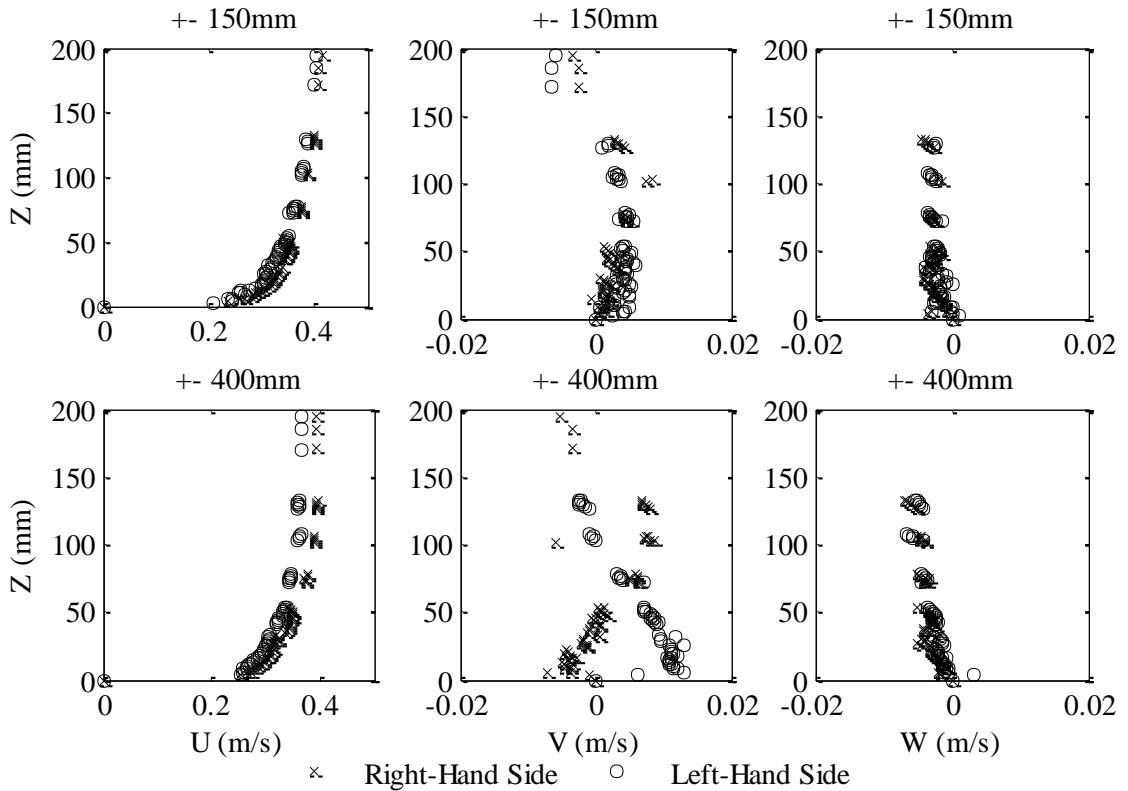


Figure 3-9: Symmetry assessment of mean flow velocity components for two distances from the centerline of the channel: 150mm (top) and 400mm (bottom).

### 3.5. Experiment Parameters

A total of ten experiments were designed to examine the impact of Froude number, the percent of the channel that was covered (coverage ratio), and the bed-to-ice roughness ratio on the velocity, turbulence intensity, and bed shear stress distributions of a channel cross-section. Two experiments that looked at a fully open and fully covered channel flow were used for comparison to the partial cover experiments. Of the remaining eight experiments, one was chosen as the base condition from which one parameter was varied at a time to achieve the remaining seven tests. Table 3-1 outlines the parameters used for each of the experiments. Froude number, coverage ratio, and bed-to-ice roughness ratio were chosen to be parameters as a first step in filling existing knowledge gaps and building a basic understanding of the impact of border ice on a channel.

Table 3-1: Experiment Conditions

Condition												
Exp.	Froude Number			Channel Coverage					Roughness			
	0.1	0.25	0.5	0%	25%	50%	67%	100%	Bed is rough	Ice is rough	Bed is smooth	Ice is smooth
1		X		X							X	
2		X						X			X	X
3		X					X				X	X
4	X						X				X	X
5			X				X				X	X
6		X			X						X	X
7		X				X					X	X
8		X					X			X		X
9		X					X				X	
10		X					X			X		

The values chosen for the Froude number experiments cover a range of conditions that may be present on a channel with border ice but were limited by experimental constraints. A value of 0.1 was chosen as a lower bound. At this level, the SNR of the data had decreased sufficiently to begin affecting the quality of the data without the constant addition of seeding material; lower values were not explored. A Froude number of 0.5 was chosen as the upper limit for practical reasons as well. Flows that produced Froude numbers greater than 0.5 created a series of relatively large standing waves along the entire length of the flume which was deemed undesirable for testing. The base value of 0.25 was chosen because it falls roughly midway between the two other cases. The change in Froude number was accomplished by adjusting the discharge up or down while maintaining the same open water depth of 0.2 m prior to the addition of the ice cover. In this manner, the Froude number is effectively being used as a dimensionless proxy for the average velocity. The average velocities that correspond to the three levels of Froude number examined in increasing order are 0.14 m/s, 0.35 m/s and 0.7 m/s. Under these conditions, the Reynolds numbers of each of the experiments are approximately 28000, 70000, and 140000, respectively. These were deemed large enough to assume that any changes would be independent of differences in Reynolds number and solely as a consequence to changing Froude number.

Coverage ratios were selected to be 25%, 50% and 67%. The base case was selected to be 67% coverage to allow for a greater number of experiments to be compared with the results of Majewski (1992). The other two values were chosen to assess lower coverage ratios as would be the case during border ice formation.

Two levels of roughness were examined to establish a base of comparison for the effect on the flow when either both the bed and the underside of the ice are the same roughness, the bed is rougher than the underside of the ice, or vice-versa. Roughness was simulated on both surfaces using 13 mm by 13 mm acrylic rods spaced 130 mm apart, perpendicular to the direction of the flow as illustrated in Figure 3-10. The spacing was chosen to maximize the effect of the roughness elements on the flow. Measurements were taken approximately mid-way between two rods.

While in nature, bed and under ice roughness is three-dimensional, a two-dimensional arrangement of roughness elements was chosen to speed up the implementation process. Granular bed material was intentionally excluded as a roughness simulator to eliminate the possibility of sediment transport and a mobile bed from confounding the results. This also ensured that the system's recirculating pump system was not exposed to any sediment that may have been transported out of the flume.

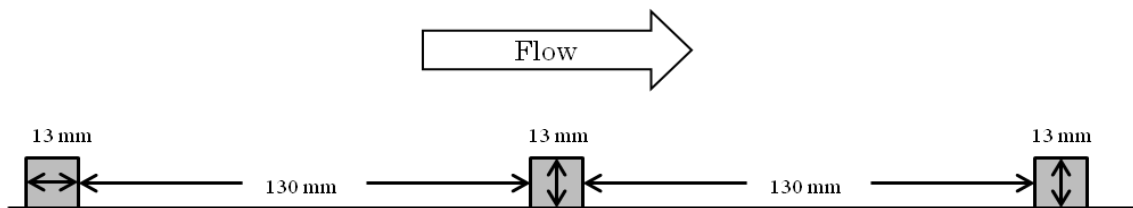


**Figure 3-10: Roughness element orientation.**

Leonardi, Orlandi, Smalley, Djenidi, & Antonia, (2003) show that the maximum effect of uniformly spaced, transverse, square bars occurred at a spacing-to-height ratio of approximately 7. However, in the range between 5.5 and 10 there was only a slight change. Therefore, a spacing of 10:1 was chosen for constructability. There was no way to directly determine what approximate Manning's n this corresponded

to. It was necessary to first determine the equivalent sand grain roughness,  $k_s$ , then, approximate Manning's  $n$  with the equations below (Sturm, 2010). The value of  $k_s$  can be determined from the log-law, but in design, parameters such as shear velocity and the roughness shift are not known ahead of time and need to be estimated. Leonardi et al., (2003) present a relationship where the roughness shift can be determined from the spacing of transverse square bars and Leonardi, Orlandi, & Antonia, (2005) present a relationship that relates the spacing to the ratio of shear velocity to average free stream velocity,  $u_* / \bar{u}$ . Using the information from the sources above with the chosen spacing, an approximate, theoretical Manning's  $n$  was calculated as 0.019. This compares to the theoretical Manning's  $n$  of the smooth surface which is approximately 0.010 – 0.012.

$$\frac{n}{k_s^{1/6}} = \frac{\frac{k_n}{\sqrt{8g}} \left(\frac{R}{k_s}\right)^{1/6}}{2.03 \log\left(\xi \frac{R}{k_s}\right)} \quad (3-1)$$

$$\xi = \exp\left(\ln\left(1 + 2\frac{D}{b}\right) - \frac{D}{b} + 2.4\right) \quad (3-2)$$

where

$k_s$	=	equivalent sand grain roughness	[ L ]
$g$	=	gravity	[ L / T <sup>2</sup> ]
$b$	=	bottom width	[ L ]

## **4. Results and Analysis**

This chapter examines several aspects of flow in channels with border ice and presents corresponding results. First, methods for calculating the composite roughness of the channel are introduced and evaluated. This is followed by presentation of the mean streamwise velocity distribution for each experiment and an analysis of both its distribution and characterization. Observations of secondary circulation cells and some of the challenges with their analysis will also be discussed. Following that, the observed discharge distributions are compared to those produced by the equations of Shen & Ackermann (1980). Lastly, the shear stress distributions along the wetted perimeter of the channel are shown and discussed before examining the impact of a partial cover on all three components of turbulence intensity.

### **4.1. Channel Resistance**

Numerical models such as HEC-RAS, developed by the U.S. Army Corps of Engineers, and CRISSP2D, developed out of Clarkson University, are important tools for the design and analysis of waterways and their interaction with our manmade landscape. Being able to accurately quantify the resistance of a channel and how it changes under different conditions is necessary for producing useful results. The correct prediction of flood extents is just one example of where it is imperative to have a well calibrated model.

Observed water surface profiles (WSPs) were used to quantify the resistance of the channel. By collecting the WSPs both before and after installing the cover, an analysis of how border ice affected the resistance could be performed. Figure 4-1

provides an illustration of the WSPs for Experiment 3 in both the scales of the water depth and of the change in water surface elevation. It should be noted that the elevation is with respect to an arbitrary datum and not intended to coincide with any measured point. WSPs for all experiments are given in Appendix C. For Experiment 3, it can be seen that the effect of adding the border ice on the WSP did not become measureable until approximately 4 m upstream of the outlet. Even at the most upstream measurement, located approximately 2 m from the inlet, the difference was only 3 mm which represents less than a 2% change to the flow depth at that location.

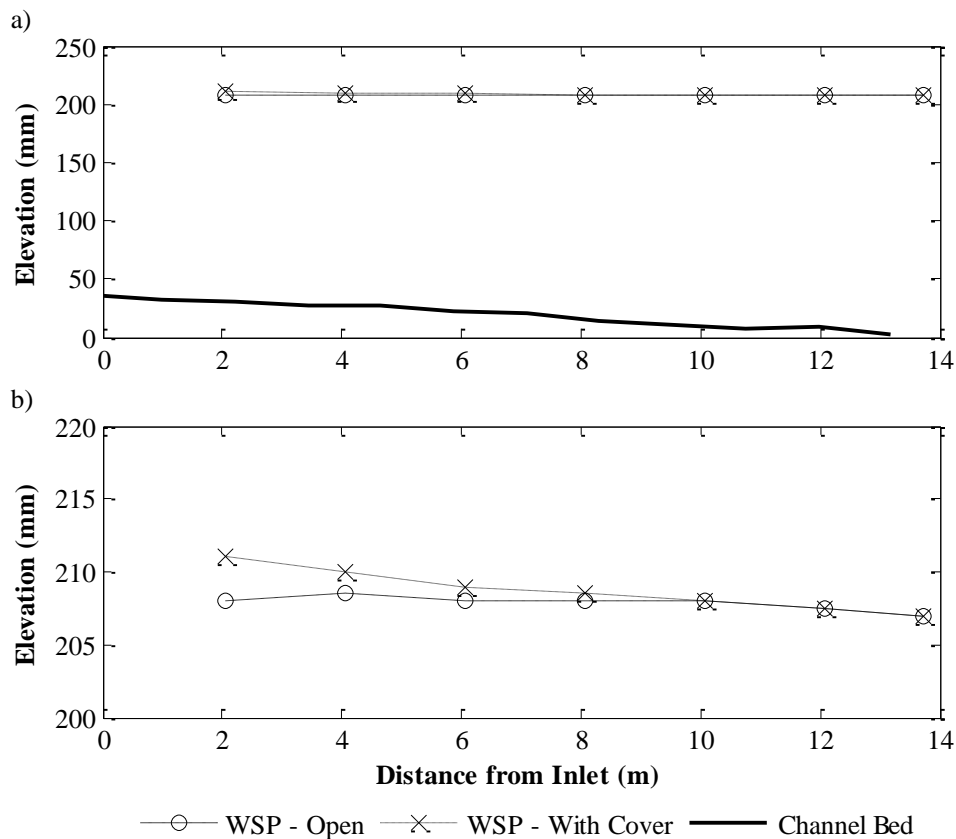


**Figure 4-1: Water surface profiles from the Base Experiment showing a) bed included, b) water surface profiles only.**

One way to evaluate the resistance of a channel is to calculate a roughness coefficient. For the purposes of this analysis, Manning's n was chosen. The channel

was not divided into reaches or the cross section into different regions, e.g. open water and covered. Thus, a single composite roughness was calculated for the entire channel. As can be seen in Figure 4-1a, the channel was backwatered with an M1 profile (i.e. the water depth downstream was greater than that upstream). This precluded the direct calculation of a composite n value,  $n_c$ , from Manning's equation (Equation 2-2) since the flow was not uniform. However, knowing the water surface profiles and geometry of the channel, the standard step method was used to determine the composite roughness of the channel for each experiment. The standard step method when there are no minor losses can be written as:

$$WSE_{i+1} + \alpha_{e,i+1} \frac{V_{avg,i+1}^2}{2g} = WSE_i + \alpha_{e,i} \frac{V_{avg,i}^2}{2g} + \bar{S}_e L \quad (4-1)$$

where

$WSE_i$	=	water surface elevation at location i	[ L ]
$\alpha_e$	=	kinetic energy flux correction coefficient	[ - ]
$\bar{S}_e$	=	average energy grade line slope	[ L / L ]
$L$	=	reach length between locations i and i + 1	[ L ]

and

$$\alpha_e = \frac{\sum Q_i^3 / A_i^2}{Q^3 A^2} \quad (4-2)$$

and

$$\bar{S}_e = \left( \frac{2Q}{\frac{1}{n_c} (A_i R_i^{2/3} + A_{i+1} R_{i+1}^{2/3})} \right)^2 \quad (4-3)$$

Since the cross section was not divided into different regions the value of  $\alpha_e$  always reduced to one. Values of  $n_c$  were optimized by iterating to minimize the root mean squared error between the calculated depths and those calculated using measurements from the manometer board. No roughness for the Covered Channel Experiment before the cover was added is presented because the data for that water surface profile was lost. Composite roughnesses for all of the experiments, rounded to the nearest 0.001, are listed in Table 4-1 below:

**Table 4-1: Composite roughness values calculated using the standard step method.**

<b>Experiment</b>	<b>Open Water <math>n_c</math></b>	<b>Covered <math>n_c</math></b>	<b>Difference</b>
<b>1 – Open Channel</b>	0.008	N/A	N/A
<b>2 – Fully Covered</b>	ND	0.011	N/A
<b>3 – Base Partial Cover</b>	0.013	0.013	0.000
<b>4 – F = 0.10</b>	0.016	0.016	0.000
<b>5 – F = 0.50</b>	0.011	0.010	-0.001
<b>6 – 25% Coverage</b>	0.012	0.012	0.000
<b>7 – 50% Coverage</b>	0.011	0.011	0.000
<b>8 – Bed is Rough</b>	0.027	0.023	-0.004
<b>9 – Ice is Rough</b>	0.013	0.018	0.005
<b>10 – All Rough</b>	0.027	0.030	0.003

ND – No Data; N/A – Not Applicable

The roughness obtained for the Open Channel Experiment was much lower than the open water roughnesses obtained for any other experiment so it was excluded from further analysis. For the remaining open water profiles from the experiments with a Froude number of 0.25 and a smooth bed, the average Manning’s  $n$  was 0.012. In Experiments 2 – 7, where the bed and underside of the ice were both smooth, there was no significant change (<5%) to the roughness from adding the cover. In fact, the net effect was more often a slight decrease in roughness, approximately 0.0004 on average. It was therefore assumed that the smooth boundaries in the channel had a

Manning's roughness of 0.012, whether they were bed, side-wall or underside of the ice cover. The increase in upstream water surface elevation had therefore resulted from the increase in wetted perimeter added by the partial ice cover, rather than an increase in Manning's roughness.

For the open water profiles of the experiments where the bed had been roughened, the average Manning's roughness of the channel was 0.027. Unlike when both surfaces were smooth, when both surfaces were rough the value of Manning's roughness changed significantly (>10%). The reason for this is unknown but suggests that the roughened ice had a higher Manning's roughness than the roughened bed despite the same implementation of roughness elements. Moving forward it was assumed that the same Manning's  $n$  for roughened surfaces (0.027) could be used for both the underside of the ice and the flume bed.

Examining the composite roughnesses from Experiments 3, 6, 7, and 10 in Figure 4-2a it is evident that the amount of coverage in the channel does not affect  $n_c$ . The data points do not possess any trend and are scattered randomly about a roughness of approximately 0.012. There is, however, an apparent effect on composite roughness from altering the Froude number (Experiments 3 - 5). Figure 4-2b shows decreasing composite roughness with increasing Froude number. This is likely an artifact from the design of the experiments. As mentioned in Chapter 3, all experiments were conducted such that the open water depth at the cross section where velocity data was collected, before the partial ice cover was installed, would be approximately 0.2 m and different Froude numbers were attained by increasing or decreasing the discharge and adjusting the tailgate. Since a given tailgate setting would naturally produce greater depths for higher flows and vice-versa, the net

effect of adjusting the tailgate would be to create an apparent increase in roughness for lower discharges and an apparent decrease in roughness for higher discharges.

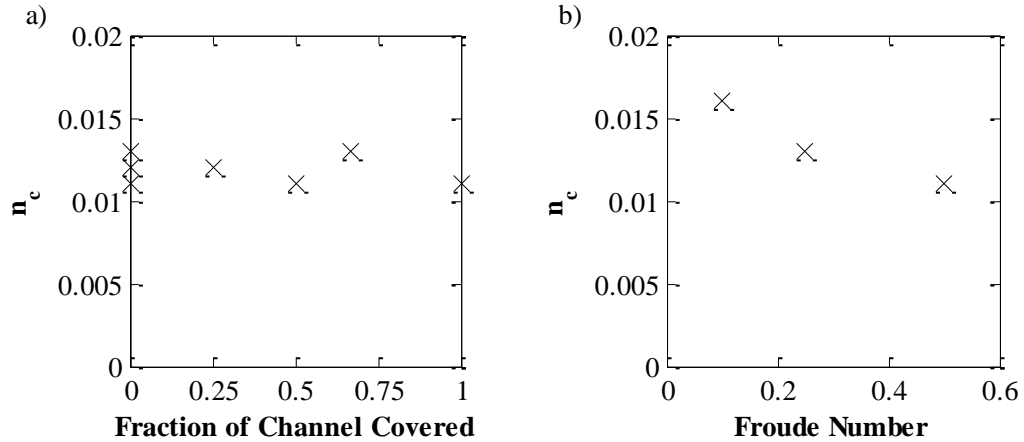


**Figure 4-2: The effect on composite roughness of a) coverage, and b) Froude number.**

For Experiments 8 and 9 where the bed and ice roughnesses were not equal, several methods of calculating a composite roughness from the established smooth and rough surface values were explored. This was done to assess which method could best predict the composite roughness value obtained from the measured WSP. These methods can be categorized into two main groups: those where only knowledge of the wetted perimeter is needed, and those that require knowledge, or an assumption, of the zones of influence for each of the boundaries. Most methods were assessed both with and without the assumption that the effect of the vertical side wall could be ignored. Each of the methods used are outlined in the text that follows.

The general form of the methods where only knowledge of the wetted perimeter is required is similar from method to method and is given by Equation (4-4). They all involve weighting the component roughnesses, raised to a given exponent,  $\phi$ , by their respective perimetric distances. The values of the exponents for each equation are based on different assumptions. These will be discussed later in the text.

$$n_c = \left( \frac{\sum (n_i^\phi P_i)}{P} \right)^{1/\phi} \quad (4-4)$$

Figure 4-3 illustrates how the wetted perimeter would be divided, over half of the cross section, for Experiment 9. The underside of the ice, the side wall, and the bed would each be their own components with wetted perimeters of  $P_1$ ,  $P_2$ , and  $P_3$  respectively. The roughness of the ice was assumed to be 0.027 and the roughness of the bed and side wall (if it was included) was 0.012.

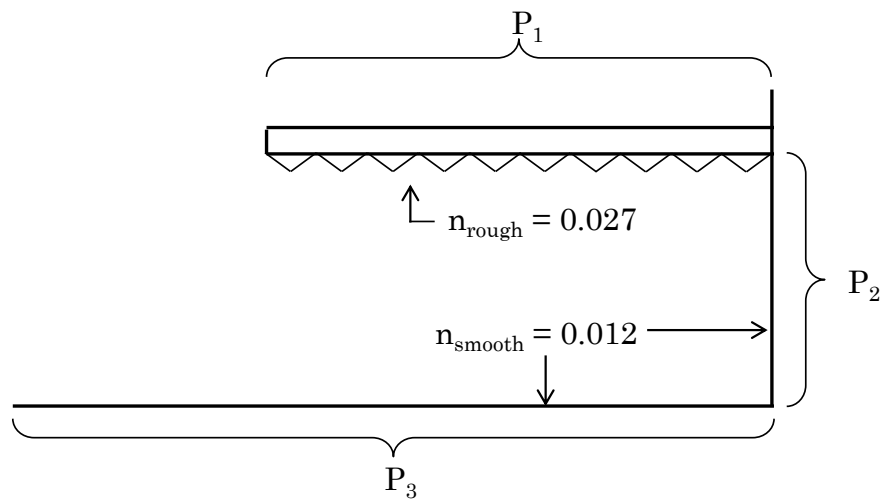


**Figure 4-3: Sample division of wetted perimeter**

The first, and simplest, method used was to weight the roughnesses linearly by the fraction of the wetted perimeter they occupied using Equation (4-5). This method represents using an exponent of one in the general form.

$$n_c = \frac{\sum n_i P_i}{P} \quad (4-5)$$

The Horton method (Equation (4-6)) was also used. It is based on the assumption that the mean velocities in each section of the wetted perimeter are equal to each

other and therefore the mean. This is the method HEC-RAS uses to calculate the composite roughness for the main body of the channel in open channel flow (Brunner, 2010).

$$n_c = \left( \frac{\sum (n_i^{3/2} P_i)}{P} \right)^{2/3} \quad (4-6)$$

The Einstein-Banks method (Equation (4-7)) assumes the total resisting force of the cross section is equal to the sum of the resisting forces of each individual section.

$$n_c = \left( \frac{\sum (n_i^2 P_i)}{P} \right)^{1/2} \quad (4-7)$$

The Sabaneev equation (Equation (2-13)) is used by HEC-RAS for calculating the composite roughness of ice covered channels (Brunner, 2010). Since it is implicit in the equation that the wetted perimeter of the ice and bed are equal, in this analysis the Sabaneev equation was only applied to the parts of the cross section with a cover to obtain a composite roughness for that section, as illustrated in Figure 4-4. The composite roughness of the channel as a whole was obtained assuming that the conveyance of the channel was equal to the sum of the conveyances from each of the sub sections and solving for  $n_c$  as outlined in Equations (4-8) and (4-9).

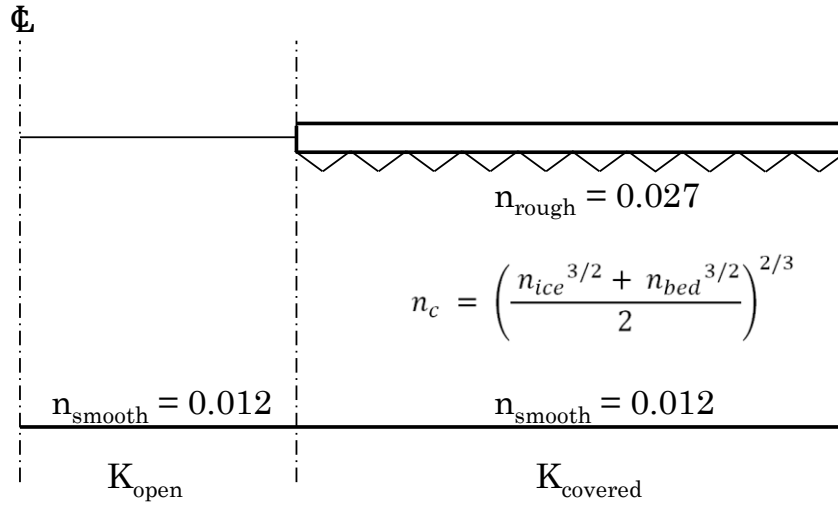


**Figure 4-4: Sabaneev Equation Implementation**

$$K_{Total} = K_{Open} + K_{Covered} \quad (4-8)$$

$$\frac{1}{n_c} AR^{2/3} = \frac{1}{n_{bed}} A_{Open} R^{2/3}_{Open} + \frac{1}{n_{Sabaneev}} A_{Covered} R^{2/3}_{Covered} \quad (4-9)$$

As stated in Chapter 2, the Sabaneev method assumes that the ice-affected and bed-affected regions of the channel have an equal depth. Using the  $\alpha$ -method (Equation (2-12)) this assumption is no longer required. The  $\alpha$ -method was implemented in the same manner as the Sabaneev equation, i.e. the composite roughness was determined for the covered region (Figure 4-5) and the composite roughness of the channel solved from Equations (4-8) and (4-9).

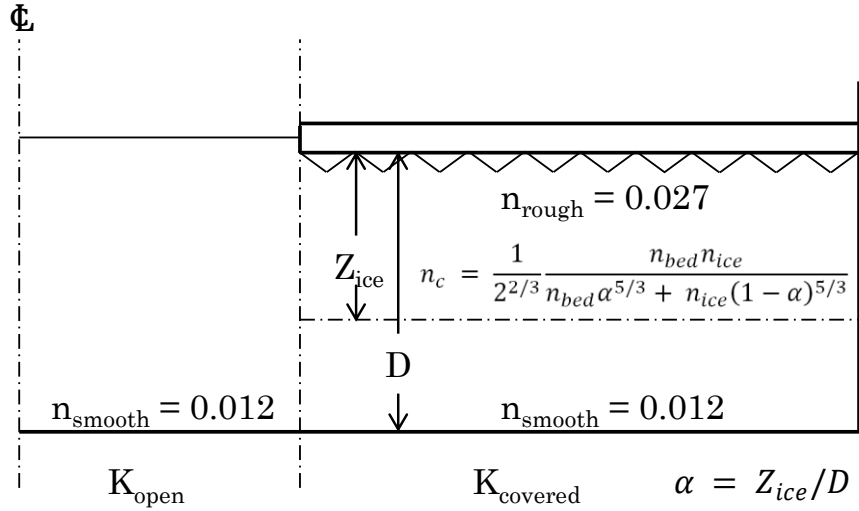


**Figure 4-5: Alpha-Method Implementation**

Another method that was examined which required knowledge of the depth of each region was the Krishnamurthy and Christensen formula (Equation (4-10)). This equation had been derived assuming a logarithmic velocity distribution over the flow depth, and that the channel was wide. For analyzing the results of this study, two cases were considered: one where the flow was assumed to be split at mid-depth and another where the location of the maximum velocity was known. The cross section was then split into five regions; one ice and one bed affected region under each piece of border ice, and one bed affected region in the open water section of the channel as shown in Figure 4-6a and Figure 4-6b. The effect of the side wall was not included due to the nature of the formula. Since it was assumed in its derivation that the channel was wide it would be inappropriate to include the wall as a separate zone.

$$\ln(n_c) = \frac{\sum(P_i z_i^{3/2} \ln(n_i))}{\sum(P_i z_i^{3/2})} \quad (4-10)$$

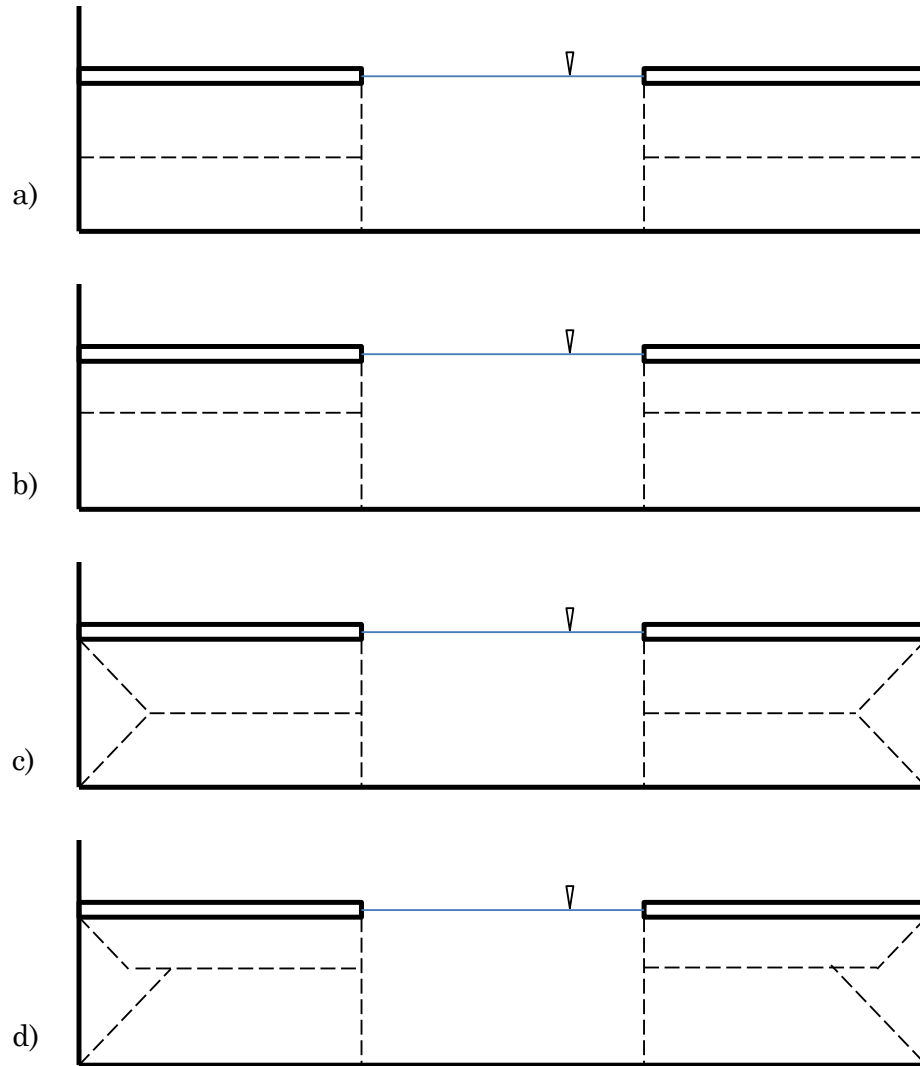


**Figure 4-6: Division of cross section into sub areas assuming: a) no wall influence, max velocity at mid-depth; b) no wall influence, max velocity offset from mid-depth; c) wall influence included, max velocity assumed at mid-depth; and d) wall influence included, max velocity offset from mid-depth.**

The last method used to estimate the composite roughness was Lotter's formula (Equation (4-11)). Lotter's formula is based on the concept that the total discharge in the channel is the sum of the discharges from each subsection. As with the Krishnamurthy and Christensen formula, Lotter's formula was evaluated with the flow in the covered section split at both mid depth and at the known location of maximum velocity. Additionally, with Lotter's formula the effect of including the

vertical side wall was explored. The division of sub areas for these cases are illustrated in Figure 4-6c and Figure 4-6d. The boundary of the wall affected zone was assumed to extend from each corner at 45° until it intersected the plane of maximum velocity. This means that when the maximum velocity was not located at mid-depth there was a sudden shift in the width of the zone. The sensitivity of this method to the manner of subdividing the cross section was not explored.

$$n_c = \frac{PR^{5/3}}{\sum(P_i R_i^{5/3}/n_i)} \quad (4-11)$$

The results of the composite roughness estimations for each of the different methods are presented in Table 4-2. The methods that best estimated the  $n_c$  values for the Rough Bed Experiment ( $n_c = 0.023$ ) and the Rough Ice Experiment ( $n_c = 0.018$ ) are at the top of the list and the methods that produced the worst estimate are at the bottom. All values have been rounded to the nearest 0.001. The best results were produced by the Krishnamurthy and Christensen method when the location of maximum velocity was known. The simple linear weighting also produced good results when the vertical side walls were ignored. Lotter's formula produced the worst results of the methods examined with differences consistently more than 10%. Estimates for both Lotter's formula and the Krishnamurthy and Christensen method improved when the location of maximum velocity was known rather than assumed to occur at mid-depth. However, the Sabaneev equation performed as well as the  $\alpha$ -method but did not require the additional knowledge of the location of maximum velocity. Generally, adding the influence of the wall decreased the performance of a given method. It was detrimental to the estimates for the rough

bed experiment because all methods underestimated the composite roughness and adding the additional smooth boundary of the wall only served to lower them further. The effect was neutral overall for the Rough Ice Experiment. This was because these estimates were scattered on both sides of the value obtained from the standard step method rather than biased to one side as with the Rough Bed Experiment. While the Krishnamurthy and Christensen method had the best overall performance, it required knowledge of the location of the maximum velocity. The simple perimeter weighted methods performed nearly as well using less information and therefore represent a more practical approach to estimating  $n_c$  in channels with border ice.

**Table 4-2: Composite roughness estimation results.**

Method	Wall Included?	Exp. 8		Exp. 9		RMS Diff.
		$n_c$	% Diff.	$n_c$	% Diff.	
<b>Krishnamurthy and Christensen <math>U_{\max}</math> at known depth</b>	No	0.022	-2.6%	0.017	-1.1%	2.0%
<b>Horton</b>	No	0.022	-5.7%	0.019	6.9%	6.3%
<b>Linear</b>	No	0.021	-8.7%	0.018	2.9%	6.5%
<b>Einstein-Banks</b>	Yes	0.021	-9.1%	0.018	5.1%	7.4%
<b>Einstein-Banks</b>	No	0.022	-3.5%	0.019	10.9%	8.1%
<b>Horton</b>	Yes	0.020	-11.7%	0.018	1.1%	8.3%
<b>Krishnamurthy and Christensen <math>U_{\max}</math> at mid-depth</b>	No	0.020	-12.2%	0.016	-8.6%	10.6%
<b>Linear</b>	Yes	0.020	-14.8%	0.017	-2.9%	10.7%
<b>Lotter - <math>U_{\max}</math> at known depth</b>	No	0.021	-7.0%	0.014	-18.3%	13.9%
<b>Sabaneev</b>	No	0.021	-10.0%	0.014	-22.9%	17.7%
<b><math>\alpha</math> Method</b>	No	0.021	-10.0%	0.014	-22.9%	17.7%
<b>Lotter - <math>U_{\max}</math> at known depth</b>	Yes	0.020	-14.8%	0.013	-25.7%	21.0%
<b>Lotter - <math>U_{\max}</math> at mid-depth</b>	No	0.019	-17.8%	0.013	-24.6%	21.5%
<b>Lotter - <math>U_{\max}</math> at mid-depth</b>	Yes	0.018	-22.6%	0.012	-30.3%	26.7%

## 4.2. Average Velocity Components

The average velocity components were broken into two sets for analysis. First, streamwise velocity was analyzed on its own, ignoring the other two components. Then, the spanwise and vertical velocity components were analyzed together in vector plots for the impact of varying the parameters on secondary circulation patterns in the cross section.

### 4.2.1. Streamwise Velocity

A number of analyses were conducted on the streamwise velocity component. First, contour plots were produced showing the streamwise velocities in each experiment normalized by their respective  $U_{\text{bulk}}$ , (recall  $U_{\text{bulk}} = Q/A$ ). This was done to facilitate the comparison of results from different experiments. For the individual contour plots, the Open Channel and Covered Channel figures will be compared to the descriptions given in Chapter 2. The velocity distribution of the Base Experiment (Exp. 3) will be compared to the results of the Open Channel and Covered Channel Experiments. For Experiments 4 – 10, figures illustrating the percent differences between each experiment and the Base Experiment will be presented and discussed along with the contour plots. Following that, the velocity profiles across the cross section of each experiment will be characterized based on whether their shape is similar to open channel flow, covered channel flow, or something in between. Lastly, the depth-averaged velocity distribution across the cross section for each experiment will be compared to the other experiments in their respective parameter group and analyzed for any trends that may be present.

## Velocity Contours

The streamwise velocity profiles for the Open Channel Experiment show two local maxima (Figure 4-7). One was located at the surface, while the other one was depressed into the channel. Near the centreline the depression was approximately 20-25% of the depth. Both locations are reasonable and are consistent with what was stated in Chapter 2. This ambiguity likely arose from the use of multiple ADVs to sample the cross section. The streamwise velocity distribution for the Open Channel Experiment (Figure 4-8) looked as one would expect. There was a nearly monotonic increase from the bed and side wall towards the free surface and centre of the channel, respectively. The magnitude of the maximum velocity did not exceed  $U_{\text{bulk}}$  by more than 15%.

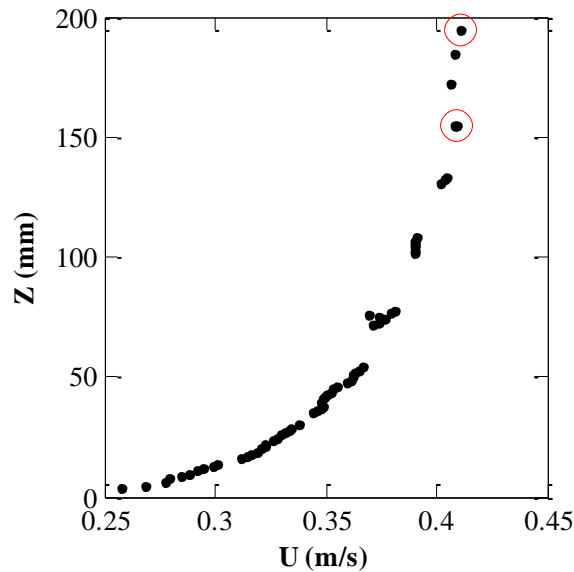
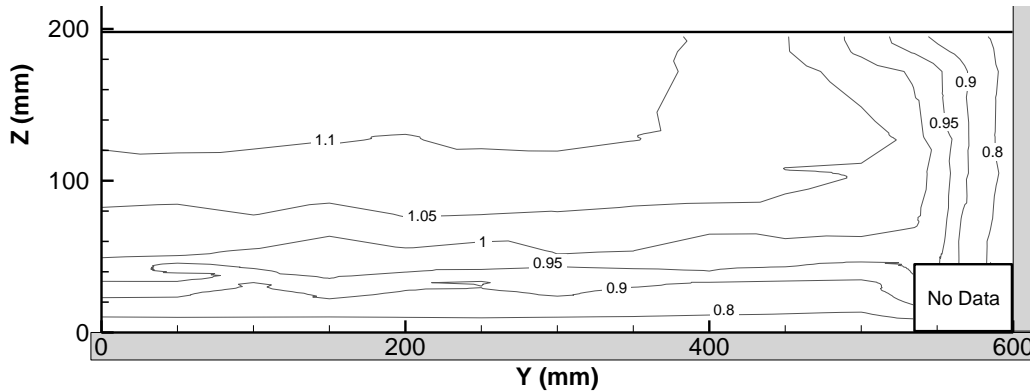
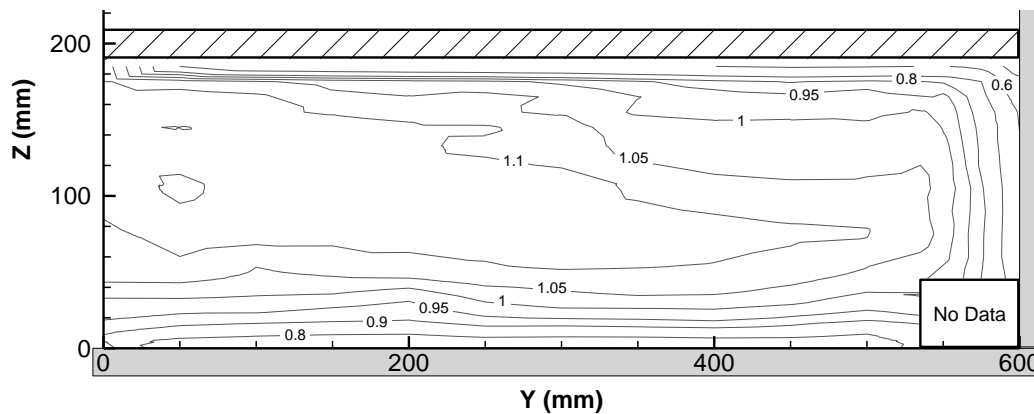


Figure 4-7: Streamwise velocity maxima, as indicated by red circles, at the centreline of the Open Channel Experiment.



**Figure 4-8:  $U / U_{\text{bulk}}$  contours for the Open Channel Experiment.**

The velocity distribution of the Covered Channel Experiment (Figure 4-9) looked similar to what would be expected of a covered channel. Streamwise velocity increased from the bed, surface cover, and side wall toward the centre of the channel. The maximum velocity was located within  $\pm 20$  mm ( $\pm 10\%$ ) from mid-depth throughout the cross section. Similar to the Open Channel Experiment, the highest streamwise velocity was approximately 15% greater than  $U_{\text{bulk}}$ .



**Figure 4-9:  $U / U_{\text{bulk}}$  contours for the Covered Channel Experiment.**

The velocity distribution of the Base Experiment (67% covered), illustrated in Figure 4-10, exhibited characteristics from both the completely open and completely covered distributions. In the covered section, the velocity increased from the boundaries and reached a maximum value approximately at mid-depth. Simultaneously, in the open

water section near the centerline, the velocity increased monotonically from the bed to a maximum near the surface. At the centreline the velocity became as much as 25% higher than  $U_{\text{bulk}}$ , compared to 15% for the Open and Covered Channel experiments. The higher relative velocity in the centre demonstrates that flow had been redistributed from beneath the ice cover into the open water section.

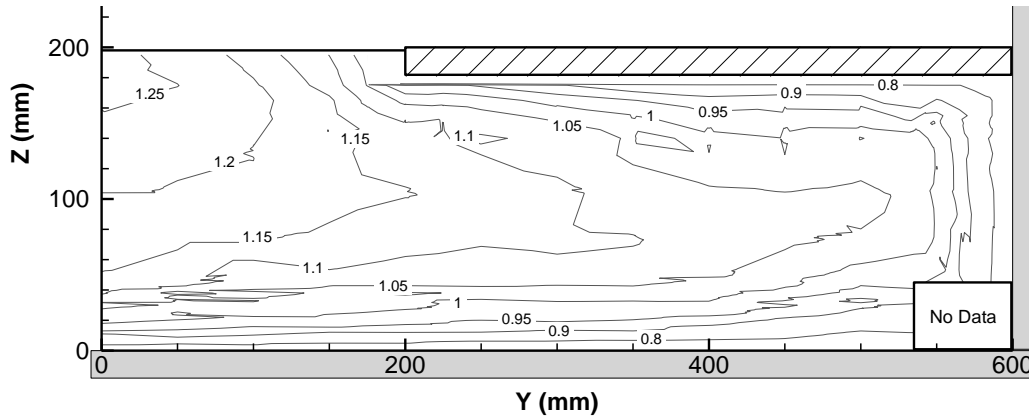


Figure 4-10:  $U / U_{\text{bulk}}$  contours for the Base Experiment ( $F = 0.25$  with 67% coverage).

The general appearance of the streamwise velocity contours for the Low Froude Experiment (Figure 4-11) was the same as The Base Experiment. This is supported by Figure 4-12 which shows that most of the cross section was within  $\pm 5\%$  of the normalized velocity of the Base Experiment ( $F = 0.25$ ). Areas with the largest variance were located near the side wall and the edge of the simulated ice cover where the normalized velocities were up to 10% and 25% lower, respectively. There were no coherent regions where the normalized velocity was significantly higher for the Low Froude Experiment. The exception was the area immediately beneath the cover since the underside of the ice was farther from the bed than in the Base Experiment.

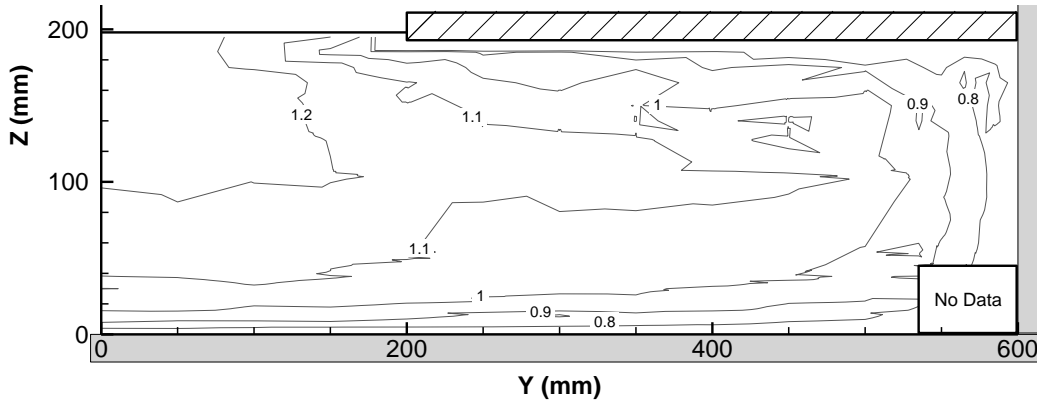


Figure 4-11:  $U / U_{bulk}$  contours for the Low Froude ( $F = 0.10$ ) Experiment.

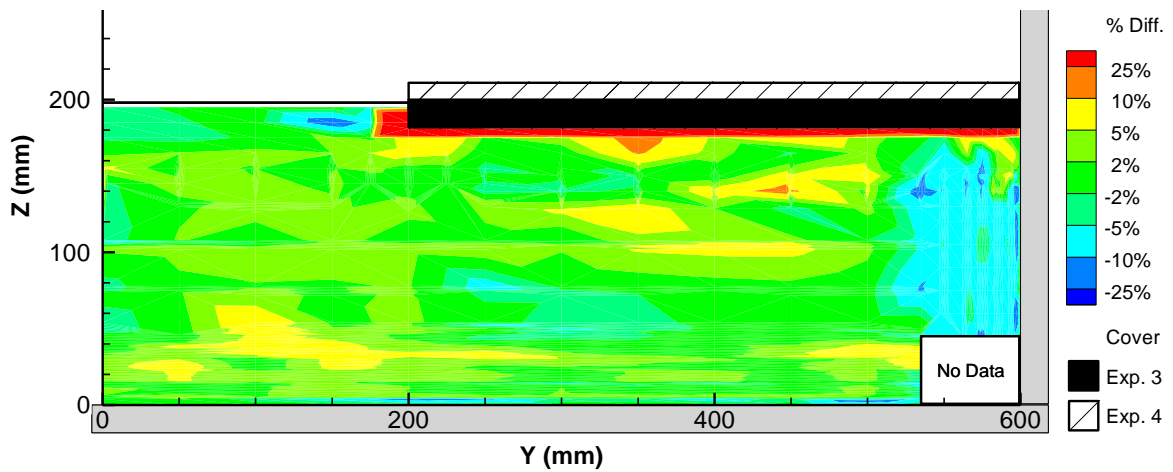


Figure 4-12: Percent difference in  $U / U_{bulk}$  contours between the Base and Low Froude Experiments ( $(Exp. 4 - Exp. 3) / Exp. 3$ ).

The High Froude Experiment, pictured in Figure 4-13, though still similar to the distribution from the Base Experiment in some respects, exhibited a slightly different flow distribution. The change is more clear when examining Figure 4-14. It can be seen that in the open water region the normalized velocity was more than 10% lower than the  $F = 0.25$  (base) condition. This flow was redistributed primarily around the perimeter of the covered section of the channel. Overall, most of the covered section saw an increase in normalized velocity, though there were still areas, particularly near mid depth beneath the edge of the ice cover, which underwent insignificant change.

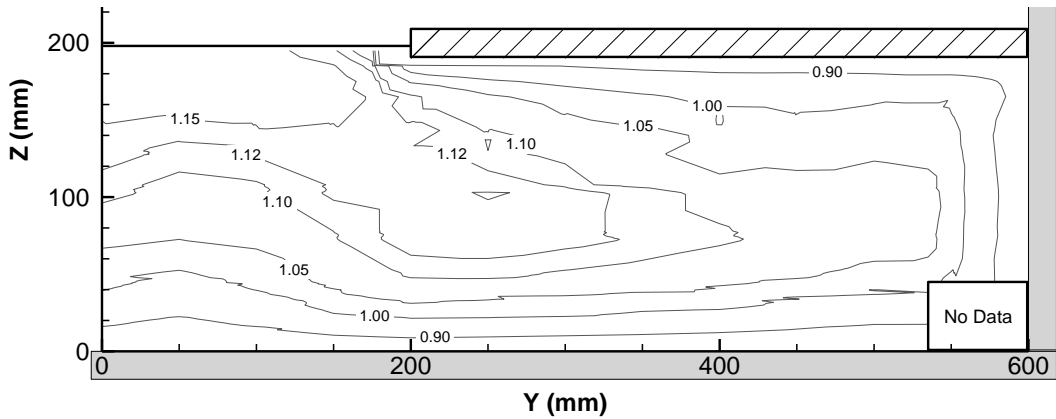


Figure 4-13:  $U / U_{bulk}$  contours for the High Froude ( $F = 0.50$ ) Experiment.

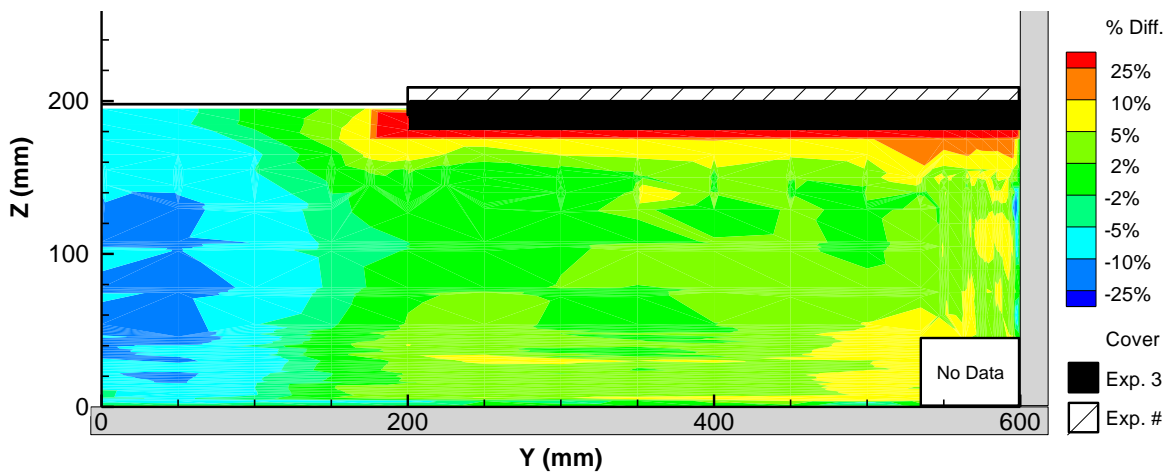
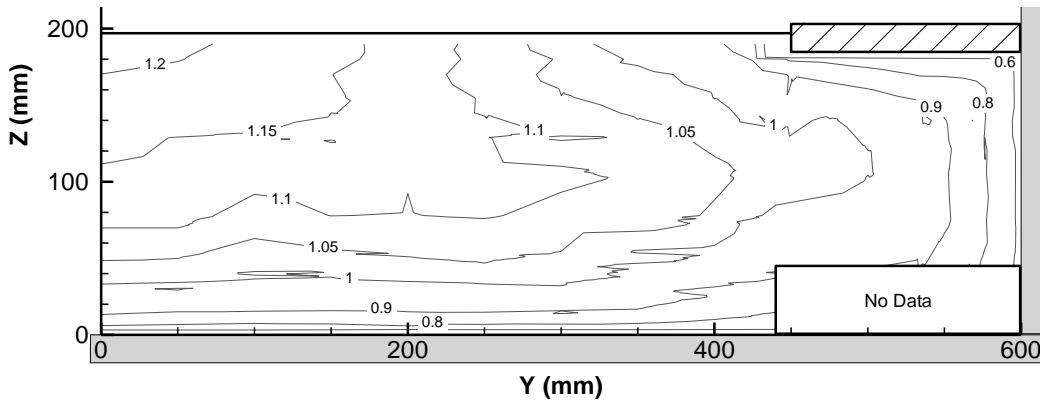


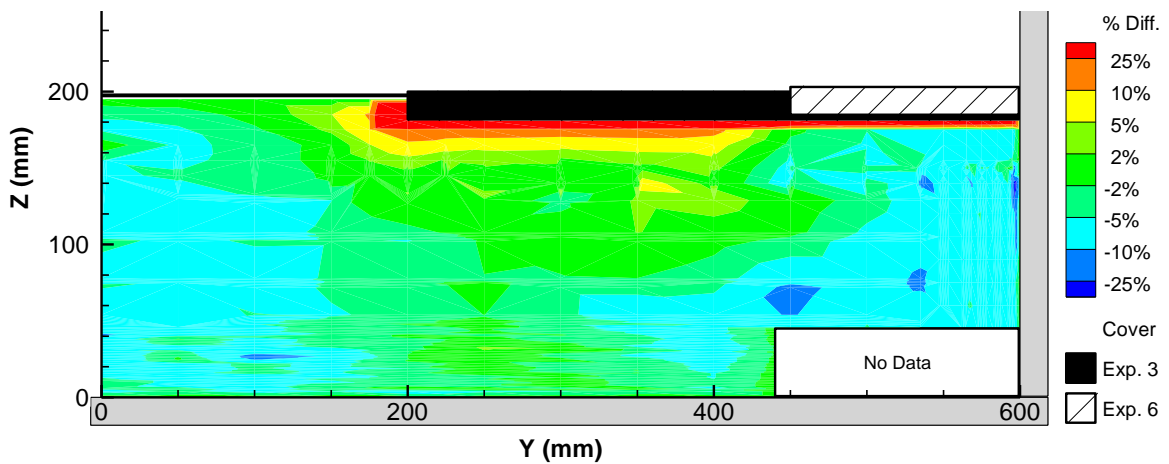
Figure 4-14: Percent difference in  $U / U_{bulk}$  contours between the Base and High Froude Experiments ( $(Exp. 5 - Exp. 3) / Exp. 3$ ).

Even at 25% coverage, the streamwise velocity contours still showed characteristics of both the Open Channel and Covered Channel experiments as can be seen in Figure 4-15. The maximum velocity was just over 20% higher than  $U_{bulk}$  which represents an increase from the Open Channel Experiment but a decrease from the Base Experiment (67% coverage). This suggests that less flow is redistributed, which makes sense given that less of the channel is covered. The large increase in normalized velocity along the surface, shown in Figure 4-16, was expected as there was no longer cover in that location to displace or restrict the flow. It can be seen that the increase in velocity in this region is compensated for by decreases in

normalized velocity in the open water region near the centreline and beneath what remained of the cover.



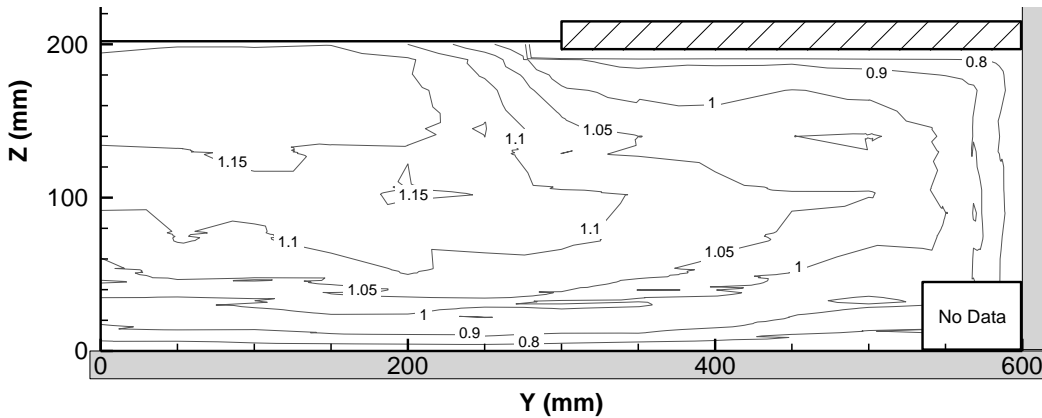
**Figure 4-15:  $U / U_{bulk}$  contours for the 25% Coverage Experiment.**



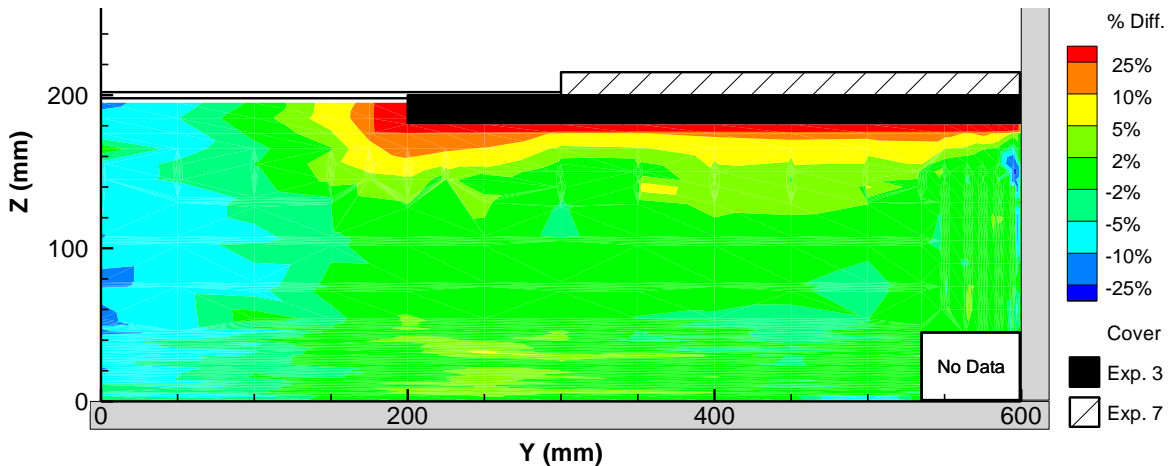
**Figure 4-16: Percent difference in  $U / U_{bulk}$  contours between the Base and 25% Coverage Experiments ( $(Exp. 6 - Exp. 3) / Exp. 3$ ).**

Figure 4-17 shows that when the channel was only 50% covered the maximum velocity had not exceeded the mean by more than 20%. This was a reduction from both the 25% and 67% (Base) coverage experiments but still an increase from the Open Channel Experiment. It is unclear why the maximum velocity relative to the average did not end up being between the 25% Coverage and Base Experiment (67% coverage) in magnitude. Much of the normalized velocity distribution did not change significantly from the Base Experiment to the 50% Coverage Experiment, as can be

seen in Figure 4-18. As expected, increases in normalized velocity occurred at the surface and immediately beneath the cover where it had previously obstructed flow in the Base Experiment. The corresponding decrease occurred in the open water region near the centreline where the normalized velocity decreased 5-10%.



**Figure 4-17:  $U / U_{\text{bulk}}$  contours for the 50% Coverage Experiment.**



**Figure 4-18: Percent difference in  $U / U_{\text{bulk}}$  contours between the Base and 50% Coverage Experiments ( $(\text{Exp. 7} - \text{Exp. 3}) / \text{Exp. 3}$ ).**

As was expected, roughening the bed while maintaining 67% coverage caused a shift in the velocity contours. This is illustrated in Figure 4-19. In the covered portion of the cross section, the lower half of the channel underwent a drastic reduction in the normalized velocity, more than 25%, while the top half increased. Figure 4-20 illustrates that beneath the cover this change occurred in a manner parallel to the

bed, up to approximately 75% of the depth. Above this depth the velocity was higher near the edge of the ice than towards the wall. This “extra” flow may have come from the open water region. In the open water region, there was a larger area with reduced normalized velocity near the centreline than the edge of the ice. Discharge would have been forced up and away from the bed and centre of the channel by the roughness elements.

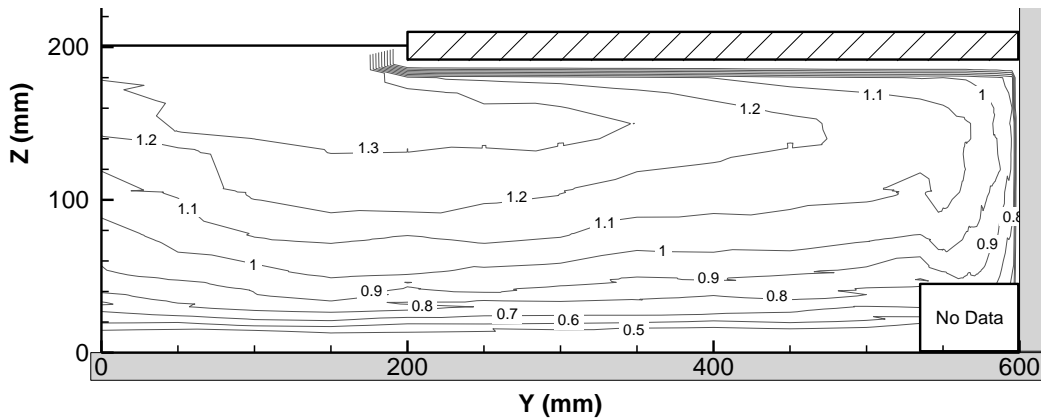


Figure 4-19:  $U / U_{\text{bulk}}$  contours for the Rough Bed – Smooth Ice Experiment.

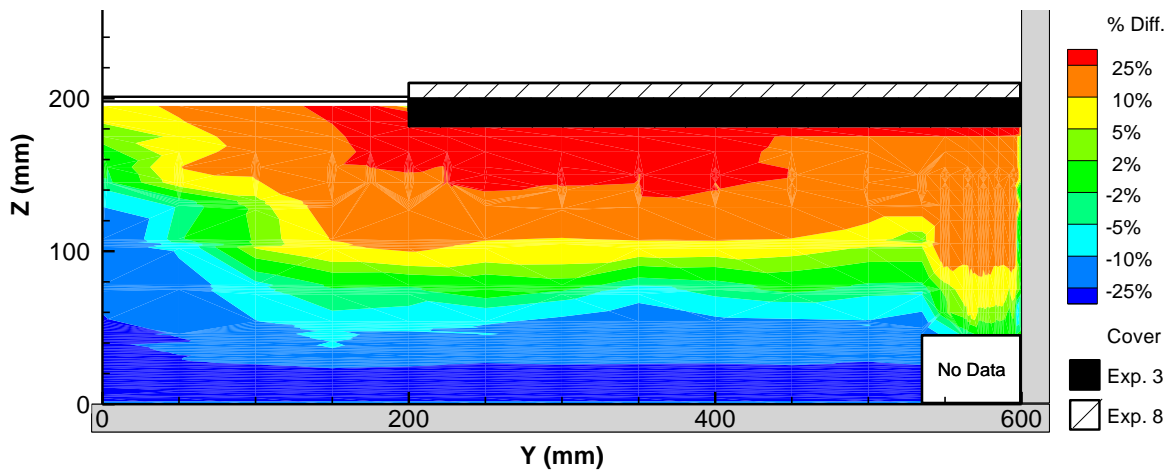


Figure 4-20: Percent difference in  $U / U_{\text{bulk}}$  contours between the Base and Rough Bed – Smooth Ice Experiments ((Exp. 8 – Exp. 3) / Exp. 3).

It was expected for the Rough Ice Experiment that the velocity near the underside of the ice would decrease for the same reason that velocities near the bed decreased for Rough Bed Experiment. Unlike the Rough Bed Experiment, however, the decrease

in velocity did not occur in a manner parallel to the bed / ice. There was a greater reduction in normalized velocity near the side wall than near the edge of the ice. This may be a result of the incomplete ice cover creating a preferential flow path in the open water section of the channel. Roughening the cover enhanced the lateral redistribution more than roughening the bed since the change to bed roughness occurred uniformly across the width of the channel. Figure 4-21 shows the maximum velocity in the central open water section of the channel had been depressed severely into the bottom half of the channel. Despite less of the wetted perimeter subjected to roughening, the Rough Ice Experiment had velocities in greater exceedance of the mean than the Rough Bed Experiment at nearly 45% compared to 40%.

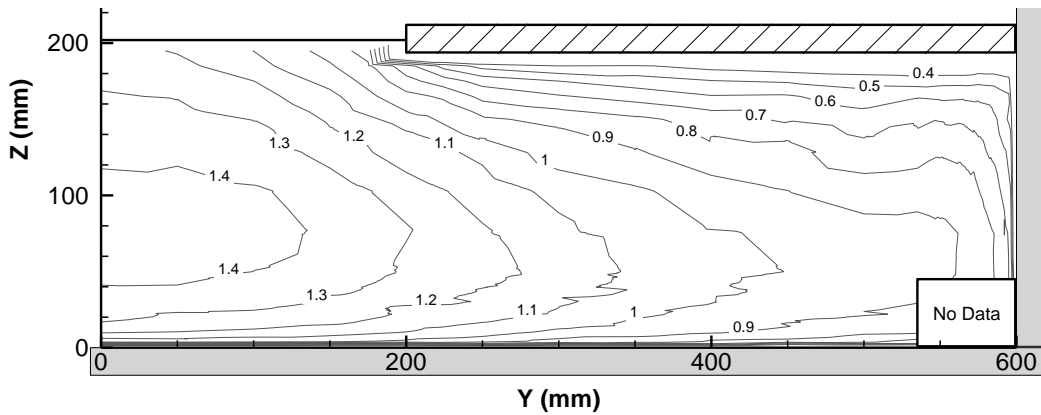


Figure 4-21:  $U / U_{bulk}$  contours for the Smooth Bed – Rough Ice Experiment.

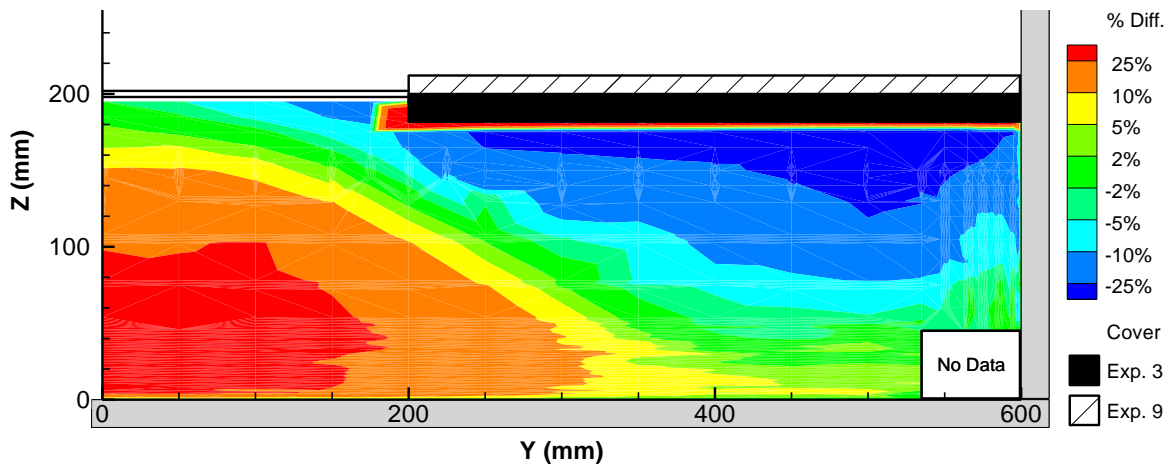


Figure 4-22: Percent difference in  $U / U_{bulk}$  contours between the Base and Smooth Bed – Rough Ice Experiments  $((Exp. 9 - Exp. 3) / Exp. 3)$ .

When both the bed and underside of the ice were roughened, normalized velocities in the vicinity of those boundaries decreased, as seen in Figure 4-23 and Figure 4-24. Beneath the cover, near mid-depth, the change to the velocity was neither significantly higher nor lower than when neither boundary was roughened. The excess flow was displaced primarily into the open water section near the surface with a smaller amount displaced toward the side wall. This experiment produced the largest exceedance of the mean than any other experiment at nearly 70%.

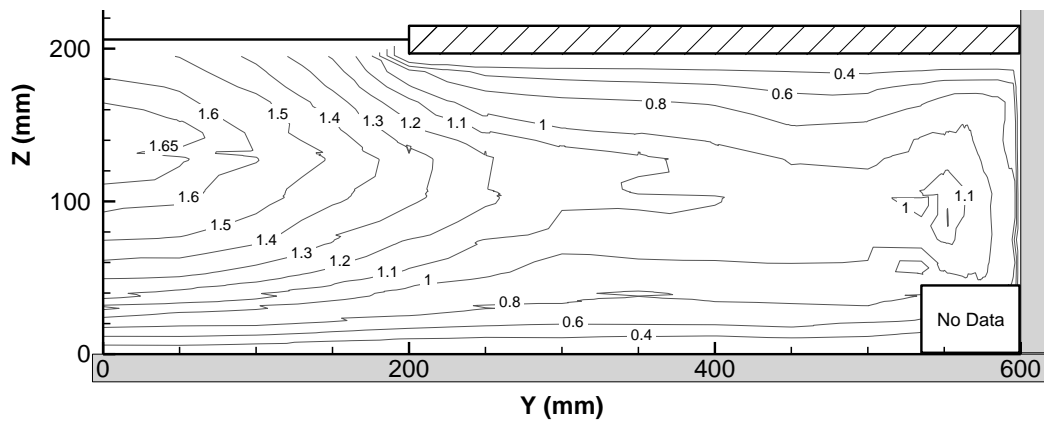


Figure 4-23:  $U / U_{\text{bulk}}$  contours for the Rough Bed – Rough Ice Experiment.

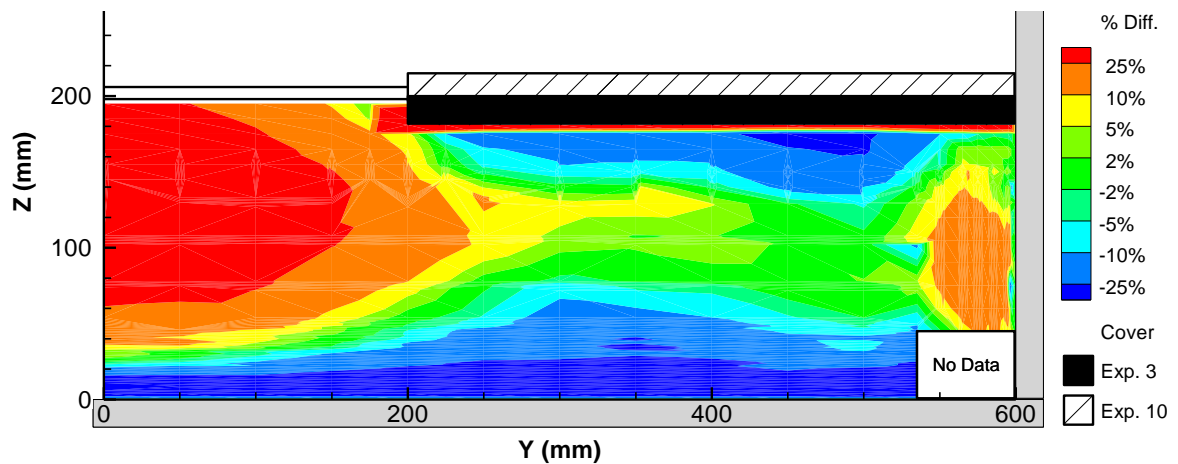
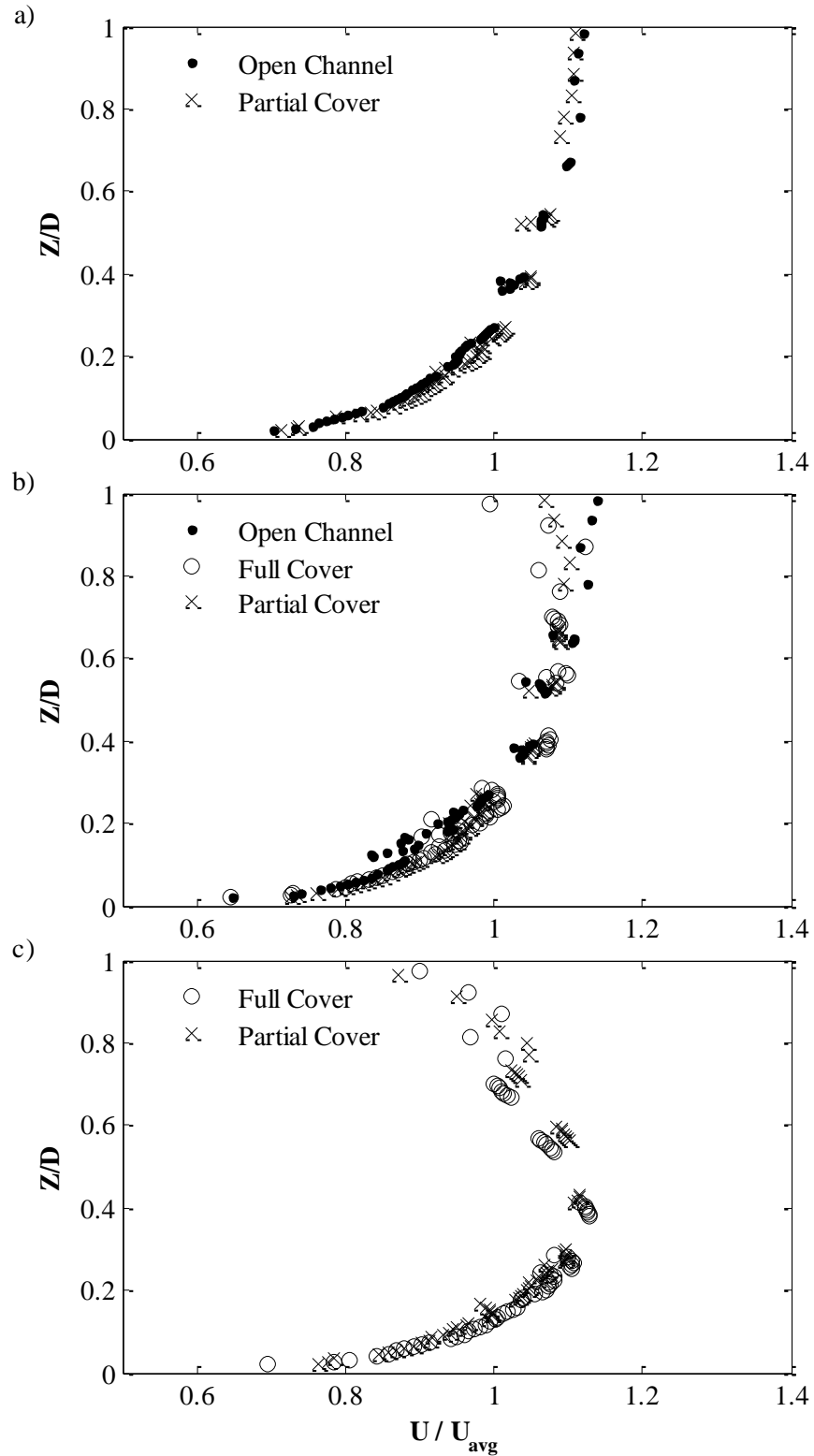


Figure 4-24: Percent difference in  $U / U_{\text{bulk}}$  contours between the Base and Rough Bed – Rough Ice Experiments  $((\text{Exp. 10} - \text{Exp. 3}) / \text{Exp. 3})$ .

## Velocity Profile Characterization

An underlying assumption when using the compound channel method is that along the interface of the sections there is no mixing and no internal stresses. This implies that the characteristics in one section do not affect the other. However, intuitively there will not be a sharp discontinuity in the velocity distribution where the streamwise velocity profiles suddenly change from the covered channel shape to an open channel shape. Certain profiles in the open water section may not strictly follow the empirical equations of an entirely open channel and certain profiles in the covered section may not strictly follow the empirical equations of a fully covered channel. A different approach is required.

Based on observations from this study, channels with a partial ice cover contain regions where the streamwise velocity profiles exhibit the same characteristics as if the channel was fully covered, regions where the profiles are the same as if the channel was open, as well as a transition region between the two where the profiles are neither the same as fully covered nor open channel flow. Figure 4-25 illustrates an example of each of these conditions. Each of the panels in the figure show a streamwise velocity profile, normalized by its average velocity, taken at the same location for three different experiments: the Open Channel Experiment (Experiment 1), the Covered Channel Experiment (Experiment 2), and the Base Experiment (Experiment 3). By comparing the shape of the partial cover profile to the other profiles, the velocity at that location in the channel was characterized.



**Figure 4-25: Streamwise velocity profiles normalized by their respective average velocity are shown where the profile from the partial cover experiment can be characterized as: a) similar to the open channel profile, b) transitional, and c) similar to the fully covered profile.**

Figure 4-25a demonstrates where the partially covered channel velocity profile exhibits the same shape as the profile of an open channel. Under this normalization the two profiles overlapped over the entire depth of flow. If, instead of their average velocity, each profile had been normalized by the average velocity of their respective cross section, the profiles would not have overlapped. As seen in Figure 4-26a, the partial cover velocity profile had a greater magnitude than the open channel profile. This difference was a result of the flow redistribution that occurred in the presence of border ice. Since some flow was transferred from beneath the cover to the open water section, the streamwise velocity profiles in the open water section had a higher value when normalized by the average velocity of the cross section.

Similar observations can be made of panel c). However, instead of the partial cover profile in Figure 4-26c having a greater normalized velocity than the fully covered profile, it had a lower value. This agrees with the observations of Hirayama (1986), Majewski & Baginska (1988), Majewski (1992), and Miles (1993) that in channels with partial cover, areas beneath the cover have a lower than average velocity and the open section is higher than average indicating a transfer of discharge from beneath the cover to the open section.

Unlike the previous two panels, in panel b), the velocity profile from the partial cover dataset was not similar to either the open channel or the fully covered data. The profile exhibited a transitional shape. Over the lower half of the depth the three profiles developed similarly, but towards the top of the profile the difference was apparent. The profile from the partially covered experiment continued to increase along with that of the open channel data until a relative distance from the bed of approximately  $Z/D = 0.8$  where it began to decrease. The decrease was caused by

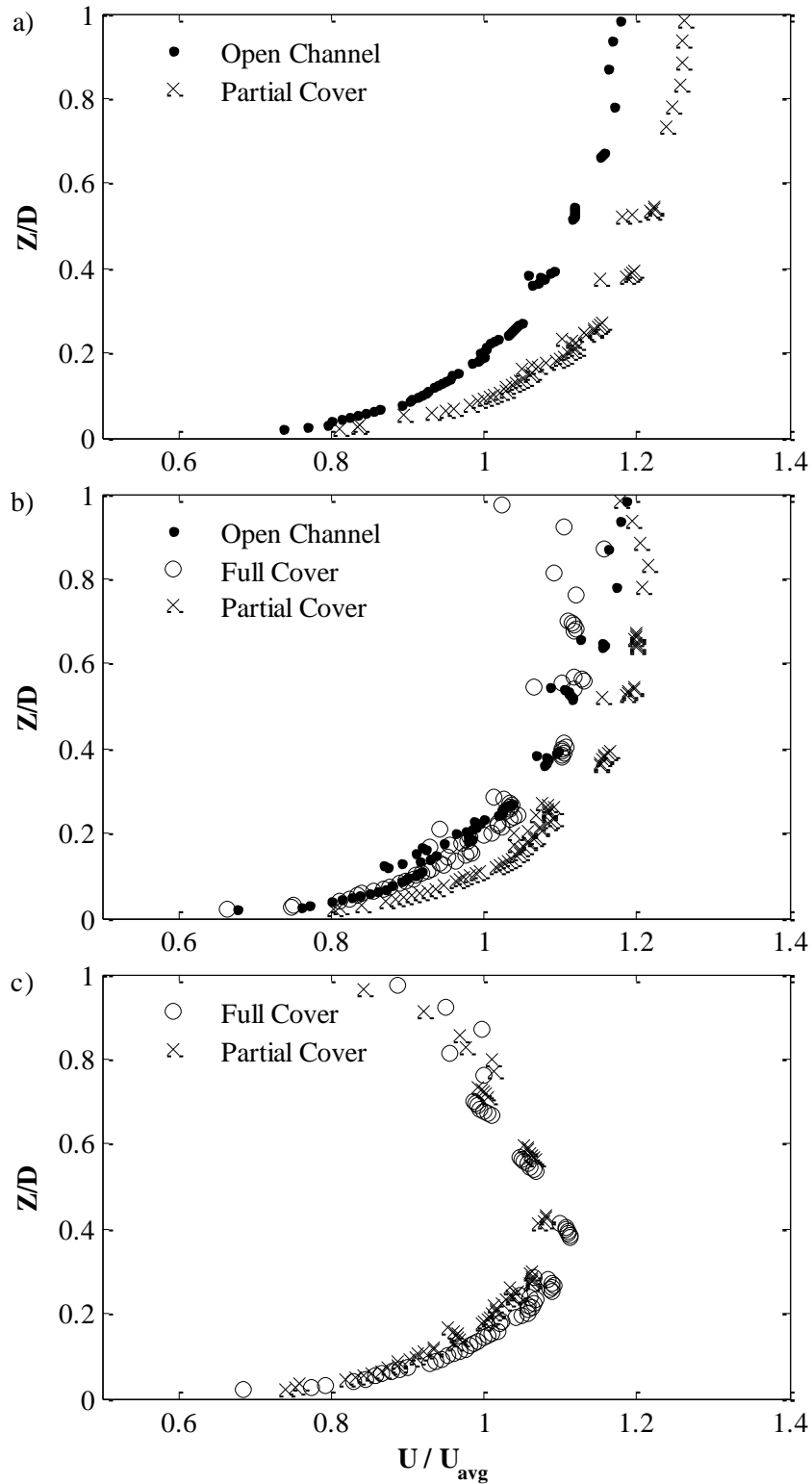


**Figure 4-26: Streamwise velocity profiles normalized by their respective average cross sectional velocity are shown where the profile from the partial cover experiment can be characterized as: a) similar to the open channel profile, b) transitional, and c) similar to the fully covered profile.**

lower surface velocities which resulted from resistance at the leading edge of the ice. When each profile was normalized by its respective average velocity, (Figure 4-25b), the velocities near the surface exhibited a fan shape with the values for the open channel greater than the partially covered channel, both of which were greater than the fully covered channel.

A summary of the characterization for each vertical profile from Experiment 3 is shown in Table 4-3 where “O” indicates the profile has a similar shape as an open channel, “C” as similar to a covered channel, “T” as a transitional shape, and “W” meaning the velocity profile is most dominated by effects from the wall. The grey cell indicates the profile located directly beneath the edge of the ice cover. The dominance of the cover is shown extending up to and including the ice edge where the velocity profile still exhibited the same shape as the profile from the fully covered channel data. In the open water section was a region near the center where the velocity profiles exhibited the same characteristics as an open channel. Between these two regions was the transitional zone where the velocity profile could not be characterized as covered or open, and instead developed from one to the other.

**Table 4-3: Velocity profile classification over a cross section for the base partial cover case of  $F = 0.25$  and 67% coverage.**

Y (mm)	ϕ	50	100	150	200	250	300	350	400	450	500	550	600
<b>Classification</b>	O	O	T	T	C	C	C	C	C	C	C	W	W

The results of Experiments 3 – 5 in Table 4-4, demonstrate that the Froude number does have an impact on the characterization of some of the velocity profiles.

Generally, for the higher Froude condition, the transition zone was smaller and closer to the edge of the ice. As the Froude number decreased, the transition region

extended farther into the open area of the flow. Under the lowest tested value, the velocity profiles in the open water section all exhibited transitional shapes rather than returning to fit the open channel profile. Interestingly, under all three tests, the cover maintains its influence up to the profile located directly beneath the edge of the ice.

**Table 4-4: Impact of Froude number on velocity profile characterization in a cross section for channels with 67% coverage.**

<b>Y (mm)</b>	<b><math>\Phi</math></b>	<b>50</b>	<b>100</b>	<b>150</b>	<b>200</b>	<b>250</b>	<b>300</b>	<b>350</b>	<b>400</b>	<b>450</b>	<b>500</b>	<b>550</b>	<b>600</b>
<b>F = 0.10</b>	T	T	T	T	C	C	C	C	C	C	C	W	W
<b>F = 0.25</b>	O	O	T	T	C	C	C	C	C	C	C	W	W
<b>F = 0.50</b>	O	O	O	T	C	C	C	C	C	C	C	W	W

Comparing the results of Experiments 3, 6 and 7 in Table 4-5, the velocity profiles beneath the cover are all characterized as if the entire channel was covered, up to and including the edge of the ice. This agrees with the previous results examining the impact of Froude number. As the cover encroached farther into the channel the size of the transition zone reduced. However, focusing on only the open water section and normalizing its width to be the same for each experiment, (Table 4-6), the relative size of the transitional area remained essentially constant at approximately 50% of the open water width, even though the absolute amount of the channel that was in transition decreased.

**Table 4-5: Impact of coverage ratio on velocity profile characterization in a cross section for channels with  $F = 0.25$ .**

Y (mm)	$\zeta$	50	100	150	200	250	300	350	400	450	500	550	600
25%	O	O	O	O	T	T	T	T	T	C	C	W	W
50%	O	O	O	T	T	T	C	C	C	C	C	W	W
67%	O	O	T	T	C	C	C	C	C	C	C	W	W

**Table 4-6: Impact of coverage ratio on velocity profile characterization in the open water section (normalized).**

$\zeta$	Open Water Section									Edge
25%	O	O	O	O	T	T	T	T	T	C
50%	O	O	O	T	T	T				C
67%	O		O	T	T					C

Classification of profiles from Experiments 8 – 10 was more difficult and subjective than Experiments 3 – 7 because baseline experiments were not conducted to obtain velocity profiles for an open-water-rough-bed condition, a smooth-bed-with-full-rough-cover condition, or a rough-bed-with-full-rough-cover condition. This is reflected in the dual classification of several of the profiles. The decision whether profiles beneath the cover in a given experiment could be classified as covered or not was inferred from the amount of change in the topmost part of the profile. Lack of significant change, as shown in Figure 4-27, suggested that the profile should be classified as covered, otherwise it may be transitional. Similarly, in the open water section, the change in shape of the profile was examined from location to location. This was done in addition to looking at the general shape of the velocity profile. Dual classification occurred when the shape of the profile suggested one classification but the change, or absence thereof, suggested another.

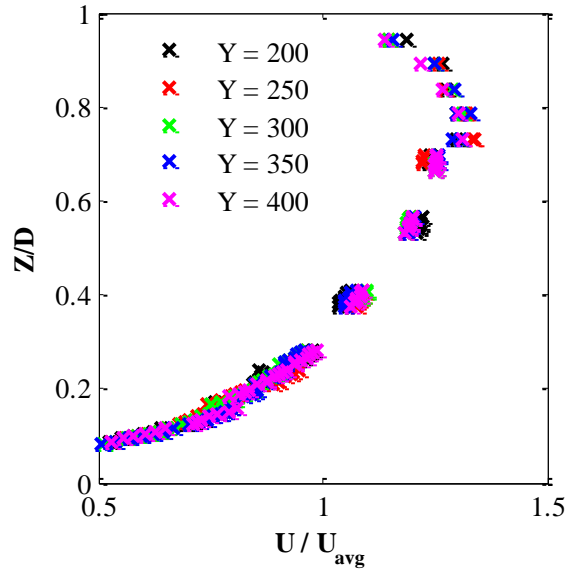


**Figure 4-27: Streamwise velocity profiles beneath the cover of the Rough Bed Experiment.**

The results of Experiments 3, 8, 9, and 10 in Table 4-7 demonstrate the effect of relative bed-to-ice roughness on velocity profile classification in a channel. When the bed was rougher than the ice, as before, the region beneath the cover, up to and including the edge, was classified as if the entire channel were covered. The ambiguity in the characterization of this cross section was in the open water section where, for several profiles, it was unclear whether or not they were transitional. When only the ice was roughened, the entire open water section was in a transitional state with the maximum velocity submerged over the entire cross section. Beneath the cover, up to and including the leading edge, the velocity profiles were classified as covered. For the experiment where both the ice and bed were roughened, the entire open water section was again in transition. Compared to the experiment where only the ice was roughened (Figure 4-21), the location of the maximum velocity in the experiment where both surfaces were roughened (Figure 4-23) approached the surface of the open water section at a faster rate when moving out from beneath the cover. This suggests that the roughened bed was reducing the

distance that would have been required for the transition zone if the open water section had been wider. As with all other tests, beneath the cover the profiles could all be classified as if the entire channel was covered. However, there was some uncertainty in the classification of the profile located directly beneath the edge. It is recommended that further research be conducted to better define the boundaries of these zones and to develop relationships where the extents of each zone may be predicted.

**Table 4-7: Impact of relative roughness on velocity profile characterization in a cross section for channels with  $F = 0.25$  and 67% coverage**

<b>Y (mm)</b>	<b>℄</b>	<b>50</b>	<b>100</b>	<b>150</b>	<b>200</b>	<b>250</b>	<b>300</b>	<b>350</b>	<b>400</b>	<b>450</b>	<b>500</b>	<b>550</b>	<b>600</b>
<b>Both Smooth</b>	O	O	T	T	C	C	C	C	C	C	C	W	W
<b>Bed Rough</b>	O	O/T	O/T	O/T	C	C	C	C	C	C	C	C	W/C
<b>Ice Rough</b>	T	T	T	T	C	C	C	C	C	C	C	C	W/C
<b>Both Rough</b>	T	T	T	T	T/C	C	C	C	C	C	C	C	W/C

### **Depth-Averaged Velocity Distribution**

Many two dimensional models, such as MIKE21 and CRISSP2D, take a depth-averaged approach to modeling velocities in a channel. In order to accurately model border ice in models such as these, understanding how the depth-averaged velocity distribution is influenced by border ice is required. In this study, the depth-averaged velocity of a vertical profile was calculated by numerically integrating the streamwise velocity over the depth of flow and dividing by that depth. The depth-averaged velocity distributions for each experiment were then all normalized by

$U_{\text{bulk}}$  of their cross section. This was done to facilitate comparison among them. From this point forward, this will be referred to as the relative average velocity distribution, since the depth-averaged velocity distributions are shown relative to  $U_{\text{bulk}}$  of their cross section.

Figure 4-28 shows the relative average velocity distributions for the Open Channel, Covered Channel, and Base ( $F = 0.25$ , 67% coverage) Experiments. The Open Channel and Covered Channel distributions were similar, with the Open Channel approximately 2.5% greater than the Covered overall. Both approached a plateau by approximately  $Y = 500$  mm but continued with a slight rise towards the center where each profile had an average velocity roughly 5% greater than their respective  $U_{\text{bulk}}$ . The similarity in the profiles makes sense, given that in both experiments the depth and resistance were constant across the cross section.

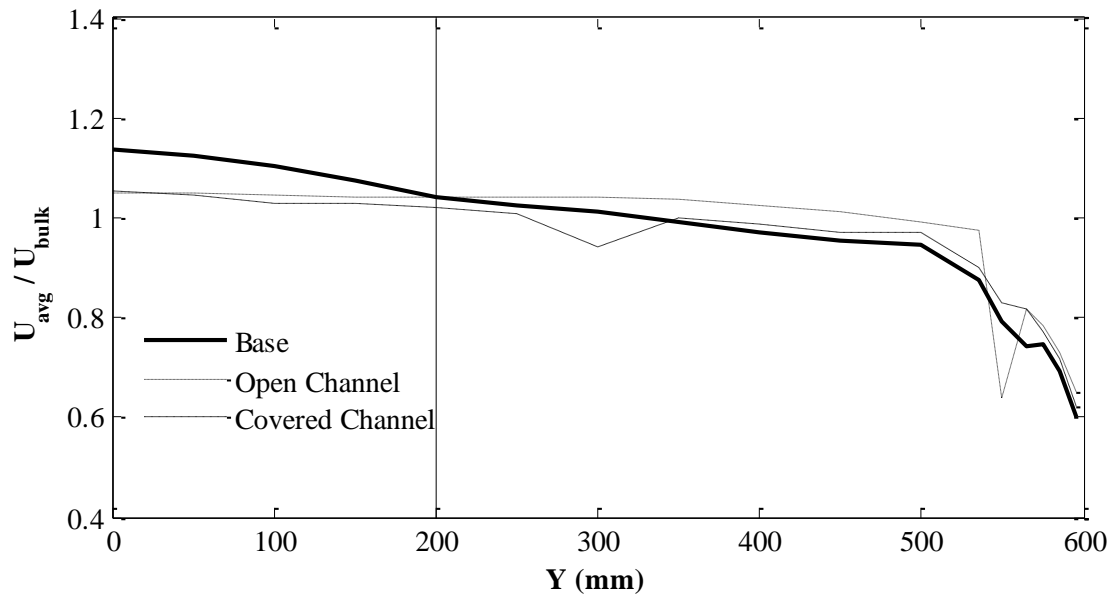


**Figure 4-28: Relative average velocity distributions for the Open Channel, Covered Channel, and Base Experiments. Vertical line indicates edge of partial ice cover.**

The relative average velocity distribution for the Base Experiment was an exaggerated combination of the Open Channel and Covered Channel distributions. There was a noticeable slope break at the edge of the ice cover where the magnitude of the Base profile became higher than the Open Channel. Since a free surface offers less resistance to flow this increase in relative average velocity was expected. In the open water region, the profile from the Base Experiment had a higher magnitude than the Open Channel Experiment, 4.8% greater on average. At the centerline, the average velocity was 14% higher than  $U_{\text{bulk}}$  compared to 5% for the Open Channel Experiment. Beneath the cover the Base profile was generally lower than the Covered Channel profile. The maximum deviation occurred in what was previously identified as the wall affected zone. The smaller absolute magnitudes of the velocity in this region caused differences to become exaggerated when expressed as a percent. Excluding the wall affected zone, the Base profile was on average 1.5% lower than the Covered profile. The fact that the relative average velocity was lower than the Covered Channel Experiment beneath the cover and higher than the Open Channel Experiment in the open water region supports previous observations and demonstrates the flow redistribution that occurs as a result of only a fraction of the channel being covered.

Figure 4-29 demonstrates the effect of the Froude number on the relative average velocity distribution. There is a trend in the open water section where increasing the Froude number decreased the relative average velocity. The relative average velocity of the High Froude Experiment was approximately 6% lower than the Base Experiment and the Low Froude experiment was approximately 1.5% higher, on average. At the centreline, the Low Froude and Base Experiments had a depth-

averaged velocity that was 14% higher than their respective  $U_{\text{bulk}}$  while the High Froude Experiment was only 4% higher. Interestingly, for the High Froude Experiment, the highest relative average velocity occurred at the ice edge with a value of 6%. The reason for the decrease in average velocity in the open water section is unknown. Beneath the cover, the High Froude Experiment had a higher relative average velocity than the other two experiments. The trend from the open water section was not strictly reversed, as the  $F = 0.10$  and  $F = 0.25$  experiments crossed over one another for much of the covered section. However, in the wall affected zone, there was a clear trend where higher Froude numbers produced higher relative average velocities. Overall, a higher Froude number produced a more muted average velocity profile with values closer to  $U_{\text{bulk}}$  throughout, suggesting less flow redistribution occurred for higher Froude numbers.

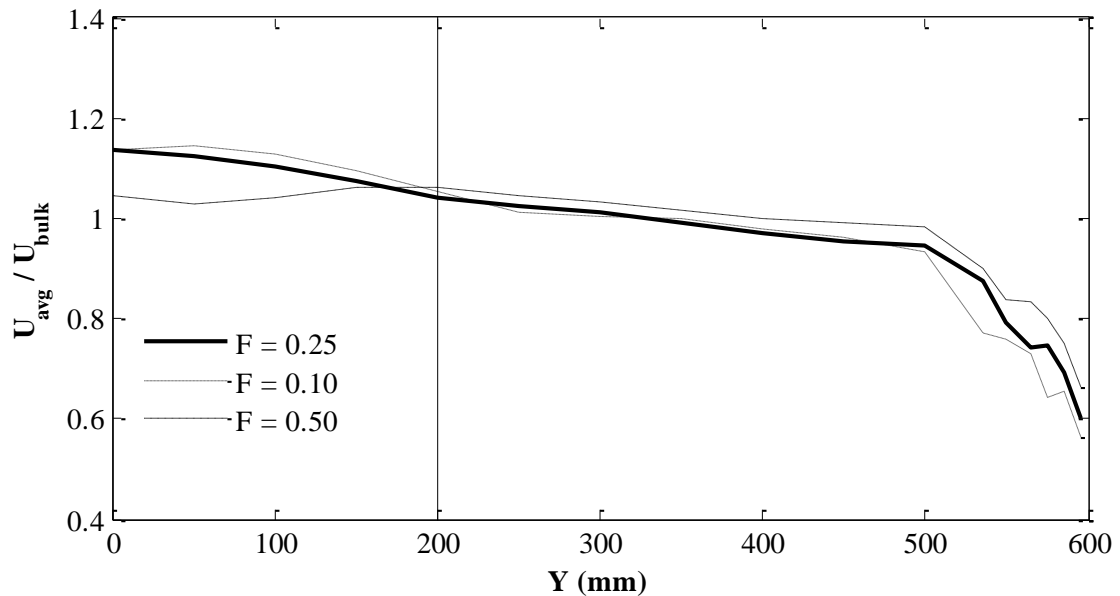


**Figure 4-29: Relative average velocity distributions for the Froude Number Experiments. Vertical line indicates edge of ice cover.**

It was expected that increasing amounts of cover would increase the relative average velocity in the centre from flow redistribution into a smaller open water section as observed by Hirayama (1986), Miles (1993), and Tsang (1970). However, this trend did not manifest itself. As shown in Figure 4-30, when the channel was 25% covered, the average velocity profile at the centreline was 8% higher than  $U_{\text{bulk}}$ . This represents an almost 50% reduction from the Base Experiment when the channel was 67% covered. It is also where the maximum relative average velocity occurred for the 25% Coverage Experiment. However, the average velocity at the centreline was only 6% higher than  $U_{\text{bulk}}$  when the channel was 50% covered. This was a larger increase than both the Open Channel and Covered Channel experiments, suggesting some flow redistribution did still occur, but smaller than the 67% coverage and 25% Coverage Experiments. Additionally, in the 50% Coverage Experiment, the maximum relative average velocity occurred beneath the edge of the ice at 8% above  $U_{\text{bulk}}$ . The reason for the decrease in average velocity in the open water region is unknown, but caused the 50% Coverage distribution to become lower than that of the 25% Coverage Experiment. It was also expected that at the ice edge, the relative average velocity distributions would initially increase at a more rapid rate in the direction of the centerline because of the sudden decrease in resistance to flow caused by the termination of the cover. For the 67% coverage and 50% coverage experiments this increase occurred as expected while for the 25% coverage experiment the increase began beneath the cover. The reason for this discrepancy is unknown. It is possible that the ice edge of the 25% Coverage Experiment was too close to the wall affected zone which may have had some influence in the progression of the depth-averaged velocity distribution.

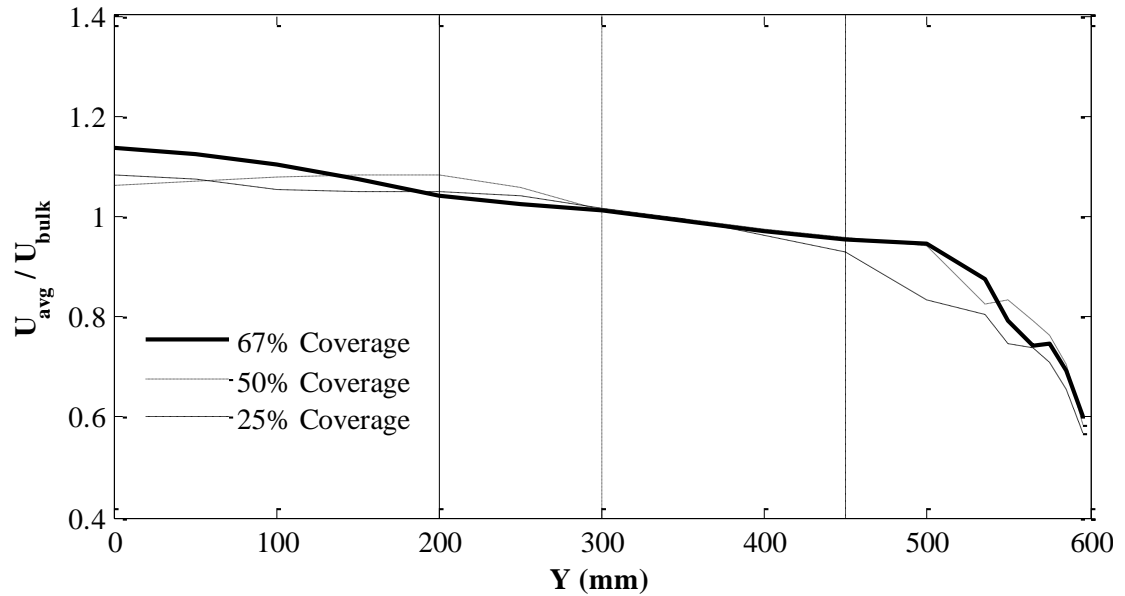


**Figure 4-30: Relative average velocity distributions for the Coverage Experiments. Vertical lines indicate the respective edges of the partial ice covers.**

The effects of bed and under-ice roughness are illustrated in Figure 4-31. Both Experiments 9 and 10, where the ice had been roughened, displayed exaggerated velocity distributions compared to those where the ice had been smooth. This suggests that the roughness of the ice had a greater influence over flow redistribution than the roughness of the bed. As mentioned previously, this may be a result of the incomplete ice cover creating a stronger preferential flow path in the open water section of the channel. Roughening the cover enhanced the redistribution more than roughening the bed since the change to bed roughness occurred uniformly across the width of the channel. Consequently, when only the ice had been roughened, the general shape of the relative average velocity distribution was different than for the other experiments. Compared to the other distributions, a greater amount of flow was redistributed away from the wall region. The area beneath the cover also lacked the distinctive plateau in the relative average velocity distribution possessed by all the other experiments. However, when both surfaces

had been roughened, there was a clearer distinction between the covered and open areas of the cross section than when only the ice had been roughened, and the distribution more closely resembled that of the Base Experiment. This combined with the similarity between the distributions of the Base and Rough Bed Experiments indicated that the roughness of the bed was more a factor in flow redistribution from the bed to the surface, rather than from beneath the cover to the open water section. It should be noted that there was a portion of the open water region where the magnitude of the relative average velocity of the Rough Bed Experiment decreased until, at the centerline, the average velocity was 5% lower than  $U_{\text{bulk}}$ . The reason for the decrease in average velocity in the open water section is unknown.

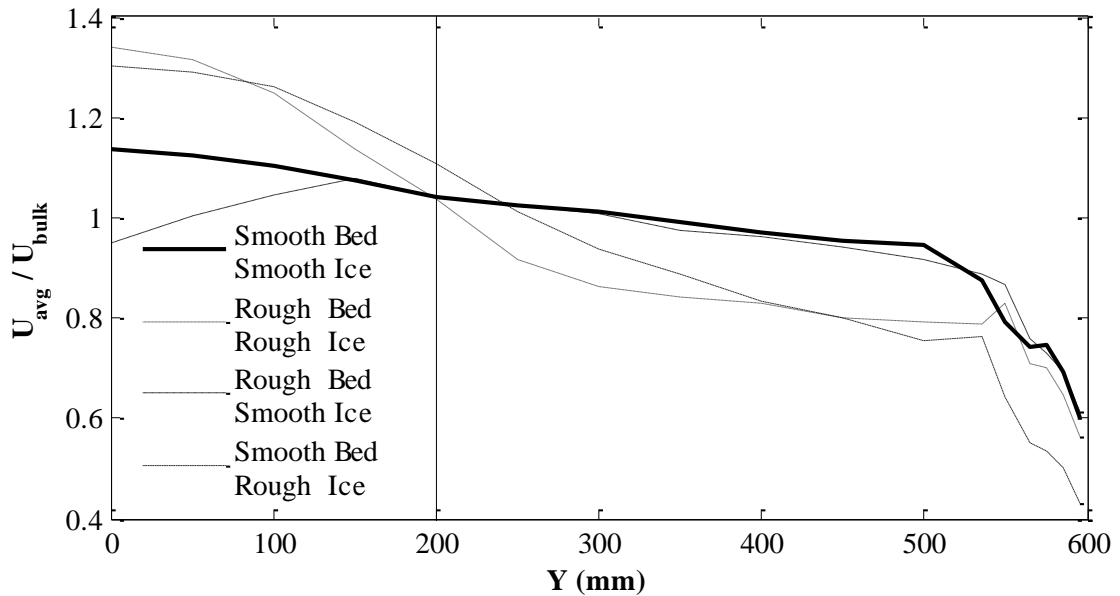


**Figure 4-31: Relative average velocity distributions for the relative roughness Experiments. Vertical line indicates the edge of the partial ice cover.**

#### 4.2.2. Secondary Circulation

With computers becoming increasingly powerful the ability to model complex, 3D flows is becoming a more viable option. However, before something can be meaningfully modeled, it first needs to be understood and little is known about the secondary circulation characteristics in channels with border ice. 3D velocity measurements were collected in the hope of shedding light on this phenomenon. Unfortunately, there is still little that can be stated with confidence. This section will outline some of the difficulties in measuring and analyzing secondary flows and provide a brief discussion of select results.

Further post processing was required to clean up the spanwise and vertical velocity components for analysis. First, the spanwise velocity was corrected for any rotation of the ADV probe head. Misalignment of as little as  $1^\circ$  can introduce a bias of nearly 2% of the streamwise velocity. The assumption was made that at the centreline the average spanwise velocity was zero. Therefore the misalignment,  $\theta$ , was calculated as  $\theta = \tan^{-1}(\bar{v}/\bar{u})$ . A single value of  $\theta$  was determined for the entire vertical profile since the ADV did not rotate from point to point. Once  $\theta$  had been calculated, the spanwise velocity was corrected for each point using:  $\bar{v}_{new} = \bar{v}_{old} - \bar{u} \tan \theta$ . The vertical velocity was corrected by assuming the ADV probe head was installed perpendicular to the horizontal, rather than perpendicular to the flume bed, since a level was used for this process. The adjustment required was therefore the average bed slope of 0.25%. Each point was corrected using the equation:  $\bar{w}_{new} = \bar{w}_{old} + \bar{u} \tan 0.0025$ . Only the data collected from the Vectrino Profiler in the down looking orientation was analysed for secondary circulation. The magnitude and direction of

flow from the other orientations did not match the boundaries of the down-looking data and there was no satisfactory means of objectively transforming the data.

Due to the low magnitude of the spanwise and vertical velocities, it is important to consider how accurately the ADV can sample data. The Nortek Vectrino Profiler User Guide gives the accuracy for a Vectrino Profiler as “a fraction of 1 cm/s” (Nortek, 2012). Another manual for a non-profiling Nortek Vectrino states the accuracy as  $\pm 0.5\%$  of the velocity  $\pm 1$  mm/s (Nortek, 2004). This is in line with the accuracy given for other ADVs as well (SonTek, 2001). Therefore, it was assumed to apply to the data collected for these experiments. Consequently, for the majority of experiments with a Froude number of 0.25 and an average velocity of 0.35 m/s the uncertainty would be approximately  $\pm 3$  mm/s on average. This range encompasses most spanwise and vertical velocity measurements which presents a challenge when analyzing secondary circulation patterns. Since both the spanwise and vertical velocities are on the order of millimeters per second, the measurement uncertainty on its own is large enough to cast doubt on both the magnitude and direction of the measurements. This poses a challenge in analyzing the data. It can be seen in Figure 4-32 that there is almost no upward velocity in most of the channel. This makes it impossible to trace a complete secondary circulation cell from the vectors. However, even though the velocity is shown to be mostly in the direction of the bed, it could very well be in the upward direction in parts of the channel because of the magnitude of the flow and the accuracy of the Vectrino. Caution and good judgement need to be exercised when conducting analyses of results with magnitudes close to the measurement error. Figures illustrating the secondary flow of only two

experiments will be presented and discussed in this section. However, all figures can be found in Appendix C.

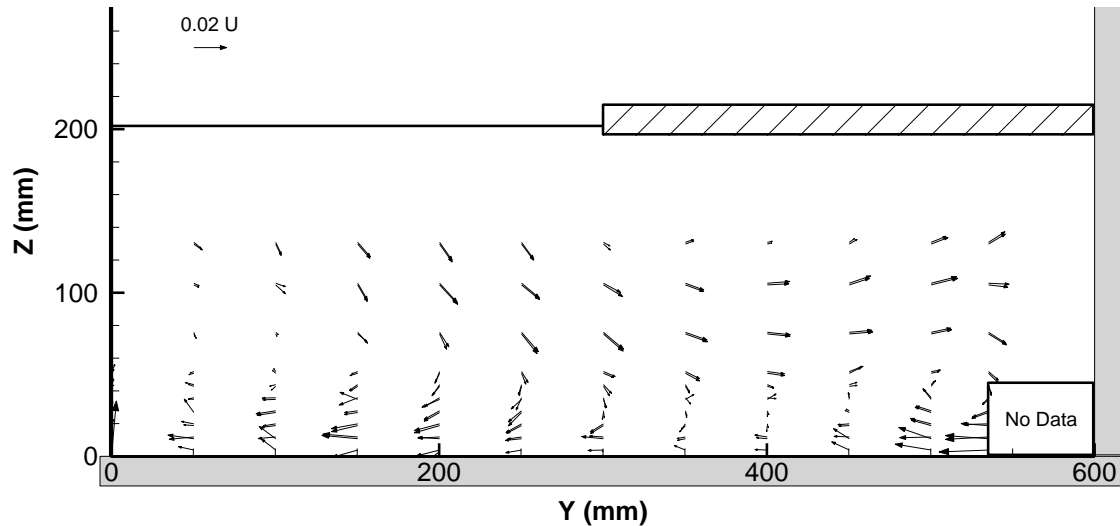


**Figure 4-32: Secondary circulation vectors for the 50% Coverage Experiment.**

The results of several numerical simulations of secondary currents in open and covered channels conducted by various authors are given in Nezu & Nakagawa (1993). For covered channels, each quadrant was comprised of two cells that flowed into the corner, then around and back toward the centre of the channel and were about equal in magnitude. In open channel flow the configuration is slightly different. Each half channel possessed two cells that were divided into a top cell, called the “free-surface vortex”, and a bottom cell. These cells were separated by a horizontal plane where flow went in the direction of the wall and returned to the centre along the surface and bed of the channel. In open channel flow it was found that the magnitude of the free-surface vortex was much higher than the cell at the bottom.

There were some similarities in the secondary circulation cells in this study and those presented by Nezu & Nakagawa (1993) for open channel flow. The most

noticeable was that each half cross section had two secondary circulation cells, though not always in the same configuration. Most, however, had the same general pattern that is displayed in Figure 4-32 and Figure 4-33 for the 50% Coverage and High Froude Experiments, respectively. There was a cell located in the upper corner that extended along the underside of the cover. For the 50% Coverage Experiment, the cell extended somewhat into the open water section while for the High Froude Experiment it appears to have been confined beneath the cover. This seems to correspond to the location of the “free-surface vortex”, although, in this study, it was not located at the free surface due to the partial cover. Unlike the results presented in Nezu & Nakagawa (1993), the second, bottom cell was larger than the previously described cell. It was located, in part, beneath the top cell but also extended into the open water section where it expanded to encompass more than just the lower half of the channel. Beneath the cover, the top and bottom cell were often divided by lateral flow in the direction of the wall as stated in the literature for open channel flow. In contrast, the top cell was not always the stronger of the two. One possible explanation for this is the lack of a free surface.

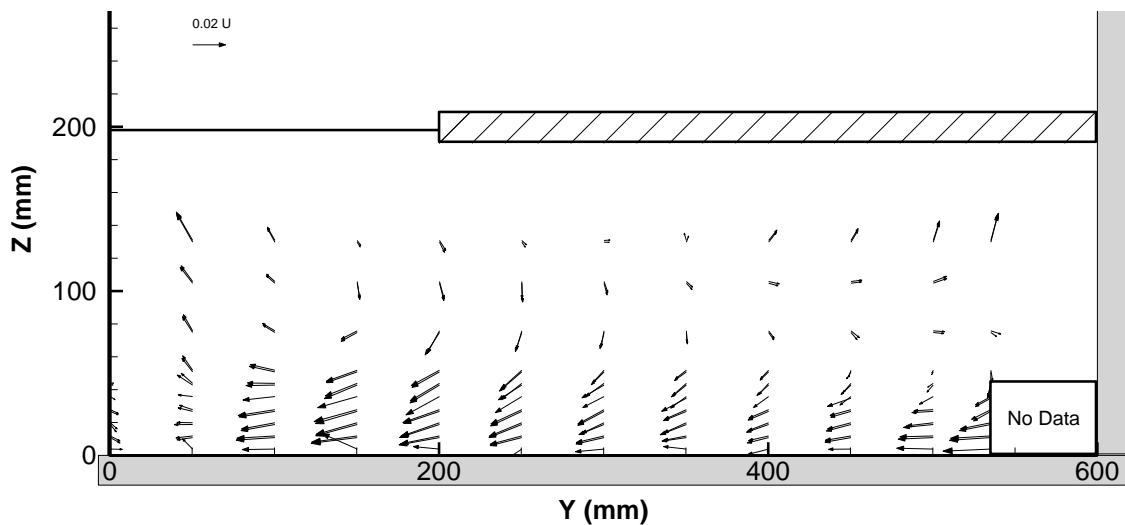


Figure 4-33: Secondary circulation vectors for the High Froude Experiment.

### 4.3. Discharge Distribution

Shen & Ackermann (1980) developed a simple set of equations to predict the cumulative discharge distribution (Equation (4-12)) and transverse discharge distribution (Equation (4-13)) in a channel. These equations do not require a complicated numerical model to be used and have been shown to work in the field for open channels, ice covered channels, and channels with border ice. Shen & Ackermann (1980) suggest using these equations to aid in the determination of discharge in a channel. In the context of border ice this could be especially advantageous. Safety is a primary concern with field work, perhaps even more so when working on border ice when the strength and thickness of the cover is low. The ability to measure a single velocity profile to obtain an approximate discharge and velocity distribution of the whole cross section would both increase safety and save time. Equation (4-12) and (4-13) are presented below. The distributions they produce are compared with the current data set to assess their accuracy.

$$\frac{Q_p}{Q} = \frac{A_p R_p^{2/3}}{AR^{2/3}} \quad (4-12)$$

where

$Q_p$  = discharge in partial area of cross section [ L<sup>3</sup> / T ]

$A_p$  = partial area of cross section being examined [ L<sup>2</sup> ]

$R_p$  = hydraulic radius of partial area [ L ]

and

$$\frac{q}{\bar{q}} = \frac{d(Q_p/Q)}{d(y/B)} \quad (4-13)$$

where

$q$	=	unit discharge at $y$	[ L <sup>2</sup> / T ]
$\bar{q}$	=	average unit discharge of the cross section	[ L <sup>2</sup> / T ]
$y$	=	spanwise cross section coordinate	[ L ]
$B$	=	maximum width of the flow area	[ L ]

To use Equation (4-12), the cross section was first subdivided into a number of stations in the spanwise direction. The vertical transects where points were sampled were selected for use as stations.  $Q_p$ ,  $A_p$ , and  $R_p$  were then calculated for each station. Figure 4-34 illustrates the progression of using Equation (4-12) across the channel. In Figure 4-34a, the partial area under consideration is the shaded grey region beginning at the wall and extending out into the channel.  $A_p$ , and  $R_p$  are determined for this geometry and the theoretical  $Q_p/Q$  is calculated for this station. For comparative purposes, the observed  $Q_p$  for this area was calculated using only the velocity measurements in the shaded region, represented in the figure as solid black dots. The process was then repeated for the next station (Figure 4-34b), and so on to the centreline of the channel. Equation (4-13) was evaluated by numerically differentiating the results of Equation (4-12).

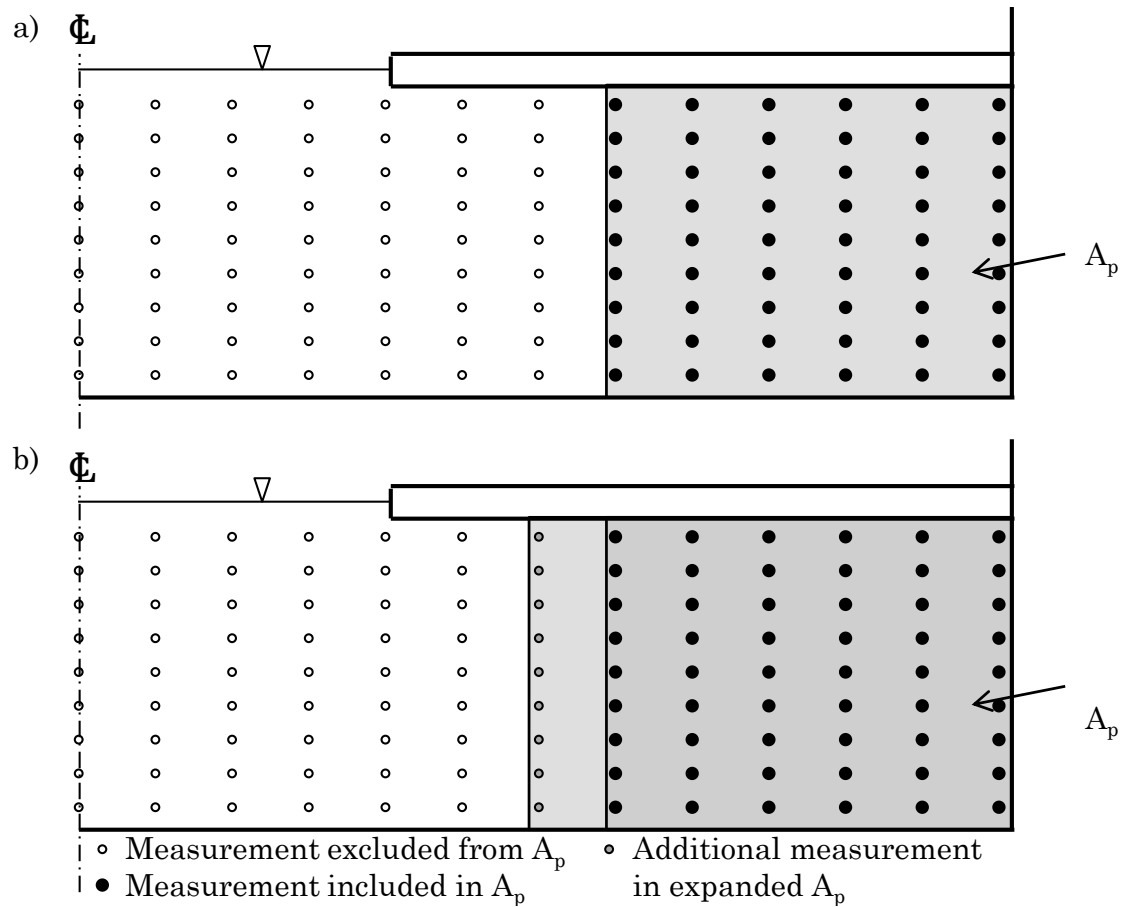


**Figure 4-34: Progression of partial area for computing cumulative discharge.**

When compared with the results of Experiments 3 to 10, Equation (4-12) consistently underpredicted the cumulative discharge of the channel but captured the approximate shape of the profile. A typical comparison between measured and calculated profiles is shown in Figure 4-35. Figures showing comparisons of the other experiments can be found in Appendix C.

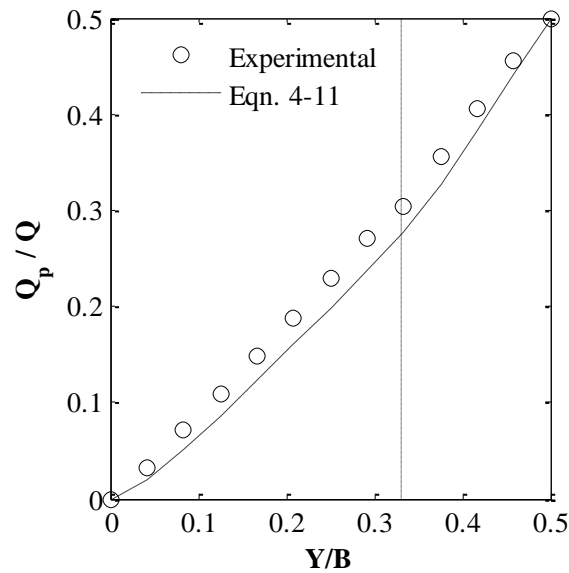


**Figure 4-35: Cumulative discharge distribution for the Base Experiment. Vertical line indicates edge of ice cover.**

Figure 4-36 illustrates the differences between the calculated and predicted cumulative discharge distributions as a percent of the total flow. On average the differences were 2% to 2.5%. This is the same magnitude as the accuracy of the streamwise velocity measurements of  $\pm 0.5\% \pm 1$  mm/s. Using the average velocity of most experiments this simplifies to approximately  $\pm 3\%$ . Given the similarity, Equation (4-12) produced a good estimate of the cumulative discharge distribution. The experiments with the best fit had roughness on the ice cover which produced deviations that were only 0.5% on average. The greatest percent difference observed in any vertical profile over all experiments was 4%. For each individual experiment, the maximum difference between measured and predicted was located at the vertical profile located under the edge of the ice cover, or in the cases of the two experiments with roughened ice cover, near the wall. Additionally, for the same coverage and roughness regime, higher Froude numbers produce greater deviations than lower Froude numbers.

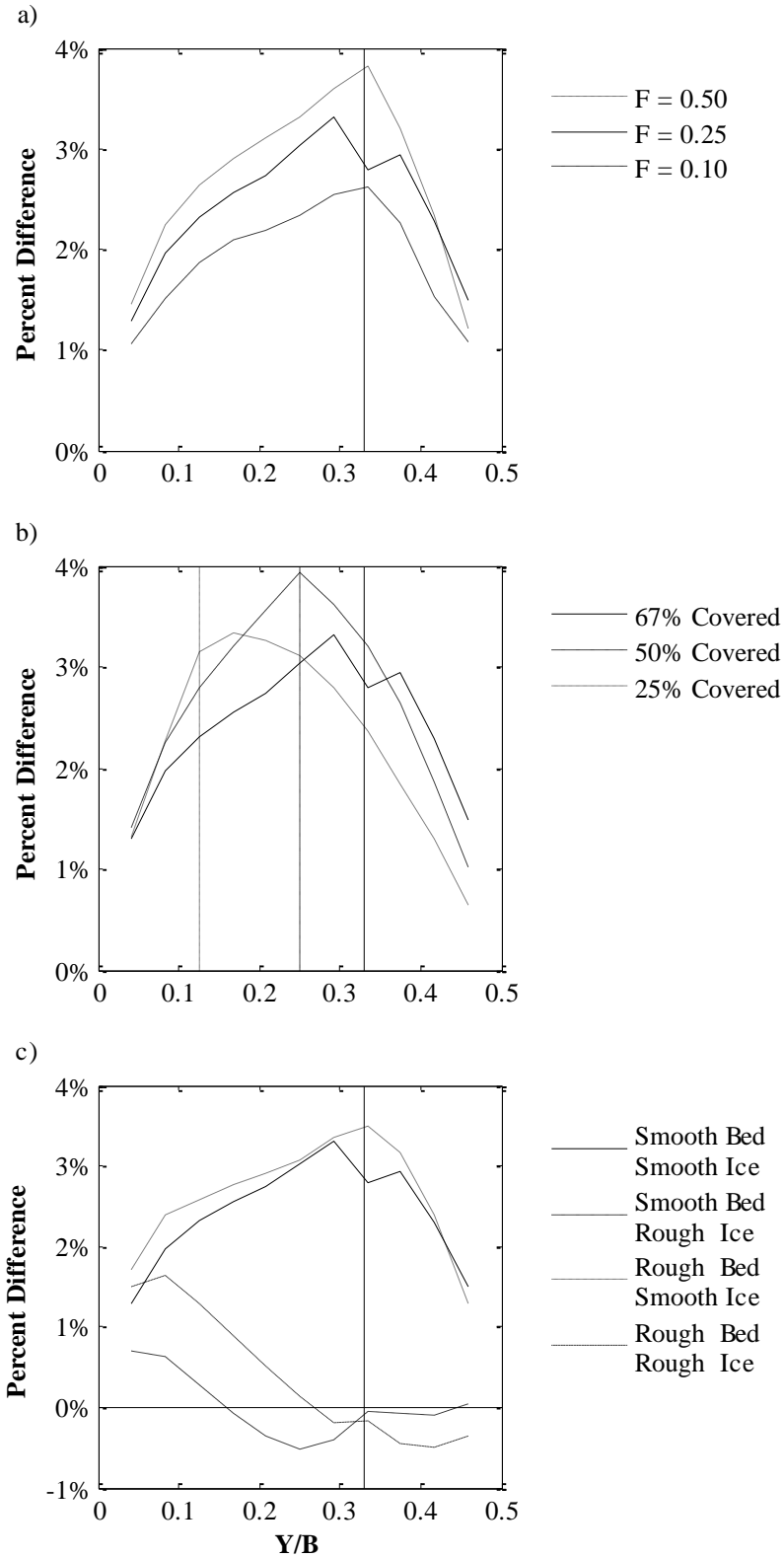


**Figure 4-36: Differences between experimental and theoretical cumulative discharge distributions as a percent of the total cross-sectional discharge for: a) the Froude experiments, b) the coverage experiments, and c) the roughness experiments. Vertical lines indicate edge of ice cover.**

Equation (4-13) captured the general shape of the relative unit discharge distribution, i.e. increased rapidly from the wall, approached a plateau beneath the cover, and increased again in open water. However, instead of a consistent underestimation as with Equation (4-12), Equation (4-13) exhibited a tendency to underpredict discharges near the wall and overpredict discharges in the open water section as demonstrated in Figure 4-37a below. The result was an exaggerated distribution compared to what was observed. Since Equation (4-13) is the derivative of Equation (4-12), the difference between the shapes of the two profiles is a result of the different slopes in the cumulative discharge distribution. The experimental data was generally steeper sloping beneath the cover than the predicted distribution which caused the overestimation in Equation (4-13) with the reverse true in the open water section. The percent difference from the measured value was, on average, a 40% overestimation near the wall and an 18% underestimation near the centre, with maximum differences of 46% and 34% respectively. The most accurate region for predicting the unit discharge was beneath the ice cover where the error was within  $\pm 10\%$ . The experiments with roughened surface cover had the best fit with the predicted distribution as shown in Figure 4-37b. This was unsurprising since those two experiments also provided the best fit to the distribution described by Equation (4-12). Figures showing discharge distributions for all experiments can be found in Appendix C.

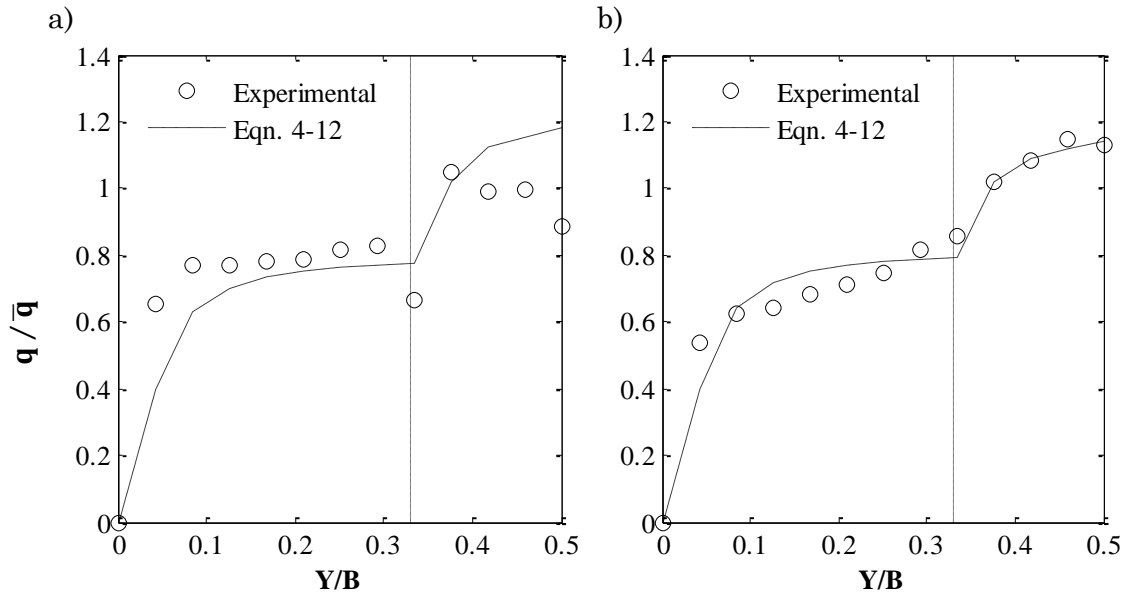


Figure 4-37: Relative unit discharge for a) the Base Experiment, and b) the Smooth Bed – Rough Ice Experiment. Vertical line indicates edge of ice cover.

#### 4.4. Boundary Shear Stress Distribution

Understanding how border ice affects the shear stress distribution in a channel is necessary for the analysis of other factors such as sediment transport. Being able to describe sediment transport is important for analyzing scour and bank stability, impact on aquatic habitat, and concentration of suspended sediment, to name a few (Sturm, 2010). In river ice engineering specifically, knowing how the shear stress distribution changes along the underside of the ice cover has significance in understanding the transport or accumulation of frazil ice.

Several steps were required to calculate the shear stress distribution around the wetted perimeter. First, streamwise velocity profiles were extracted from the data sets along the entire length of the wetted perimeter for each experiment, normal to each boundary. For the bed and underside of the ice, the profiles were taken over the entire depth of flow while from the side wall the profiles extended approximately 5

cm into the flow. Each profile was then fit to the log-law (Equation (2-2)) by adjusting the shear velocity,  $u_*$ , until a visual best fit was attained. For the profiles in the covered section, the log law was applied twice to each profile, once using the bed as  $Z = 0$ , and once using the underside of the ice. In this way, the shear velocity for both surfaces could be determined. For experiments where one or both surfaces had been roughened, it was also necessary to adjust the roughness shift parameter,  $\Delta B$ . The roughness shift and shear velocity were adjusted iteratively to obtain the best visual fit to the data. Samples of the experimental data fit to the log-law are located in Appendix C. Finally, once the log-law was fitted to each velocity profile, the bed shear stress at that location was calculated using Equation (2-8),  $\tau_b = \rho u_*^2$ .

By integrating the shear stress distribution along the wetted perimeter, the average shear stress was calculated for each experiment. This value was used to normalize the shear stress distributions so that comparisons could be drawn between the different experiments. It was also compared to the value obtained using Equation (2-7),  $\tau_a = \gamma RS$ , to verify that the shear velocities, and thus shear stresses, being calculated were at least of the correct magnitude. The specific weight was assumed to be  $9806 \text{ N/m}^3$  and the hydraulic radius calculated from known geometric measurements. The average slope of the energy grade line was taken as the value previously determined in Chapter 4.1 for the standard step method. The average shear stress for each of the experiments can be found in Table 4-8. Agreement between the integrated and theoretical values was fair with some experiments closer than others; however, all were of the same magnitude.

**Table 4-8: Average Shear Stresses (Pa)**

<b>Exp.</b>	<b>1</b>	<b>2</b>	<b>3</b>	<b>4</b>	<b>5</b>	<b>6</b>	<b>7</b>	<b>8</b>	<b>9</b>	<b>10</b>
<b>γRS</b>	0.29	0.32	0.37	0.10	1.13	0.36	0.32	1.43	0.87	2.23
<b>Integrated</b>	0.25	0.31	0.31	0.06	1.00	0.25	0.28	1.47	0.70	2.35

The shear stress distributions for Experiments 1-3 are illustrated in Figure 4-38 and are shown for illustrative purposes only.  $\tau_b/\tau_a$  values are read from the axis that are the same colour as the data points and begin at zero from the surface they correspond to. Further, the scale of each axis is identical to better show the relative magnitude of the shear stress along the wetted perimeter. The Base Experiment will be discussed in comparisons with Experiments 4 – 10 in the text that follows. Figures showing  $\tau_b/\tau_a$  distributions for all experiments in the same manner as Figure 4-38 can be found in Appendix C.

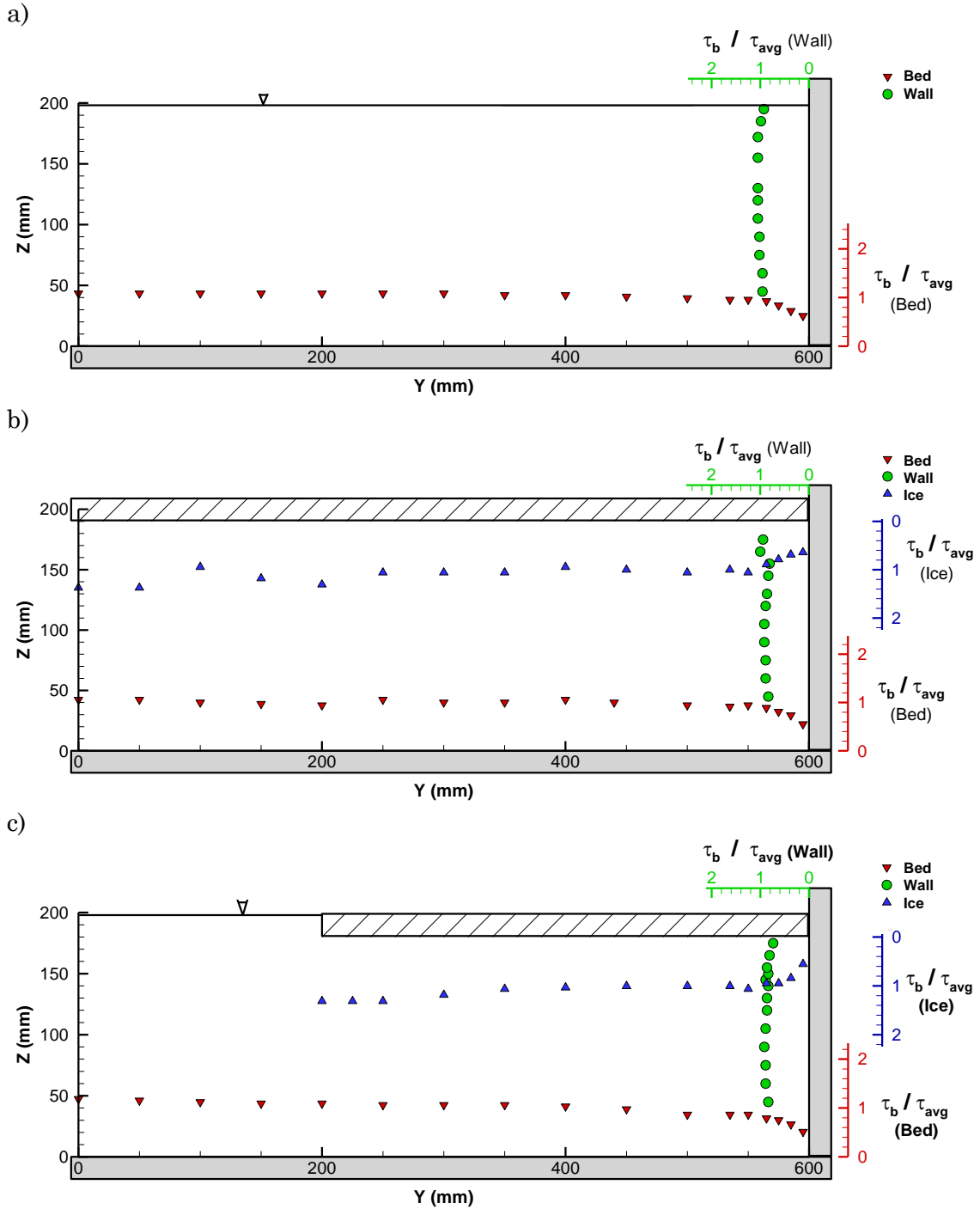


**Figure 4-38: Dimensionless shear stress distributions for the a) Open Channel, b) Covered Channel, and c) Base Experiments.**

A comparison of the  $\tau_b/\tau_a$  distributions in Experiments 3-5 (Figure 4-39) reveals the effect of the Froude Number. Along the bed, the distributions exhibited similar attributes of the relative average velocity distributions. Namely, in the open water

section, the value of  $\tau_b/\tau_a$  was higher for low Froude numbers than for high ones. In the wall affected section of the bed the trend reverses. However, beneath the majority of the covered section they were all approximately the same magnitude. Additionally, while Low Froude and Base Experiments had peak shear stress at the centre of the channel, the High Froude experiment peaked at the edge of the ice cover. The peak  $\tau_b/\tau_a$  magnitudes on the bed for the Low Froude, Base, and High Froude experiments were 1.25, 1.18, and 1.13, respectively. Along the vertical side wall, higher Froude numbers yielded higher  $\tau_b/\tau_a$  values. Otherwise, all three experiments had the same distribution shape: minima near the corners and a maximum near mid depth. Beneath the cover the peak value of  $\tau_b/\tau_a$  for all distributions was approximately 1.3. For both the Base and High Froude Experiments, this occurred directly beneath the edge of the ice. The Low Froude Experiment, however, peaked just beneath the cover from the edge. The reason for this is unknown. Generally, the experiments with higher Froude numbers exhibited a tendency to have less variable distributions on all surfaces while the Low Froude experiment experienced a greater variability in  $\tau_b/\tau_a$ .

While overall sediment transport is likely to increase from increased Froude numbers because of an absolute increase in shear stresses the erosion and deposition patterns, may change. With higher Froude numbers there would be a decreased tendency for sediment transport in the open water region and an increased tendency near the wall which has negative implications for bank erosion and stability. With respect to frazil accumulation, the higher relative shear stresses near the edge of the ice cover indicate frazil, if present, would be more likely to accumulate beneath the cover closer to the wall than at the leading edge.

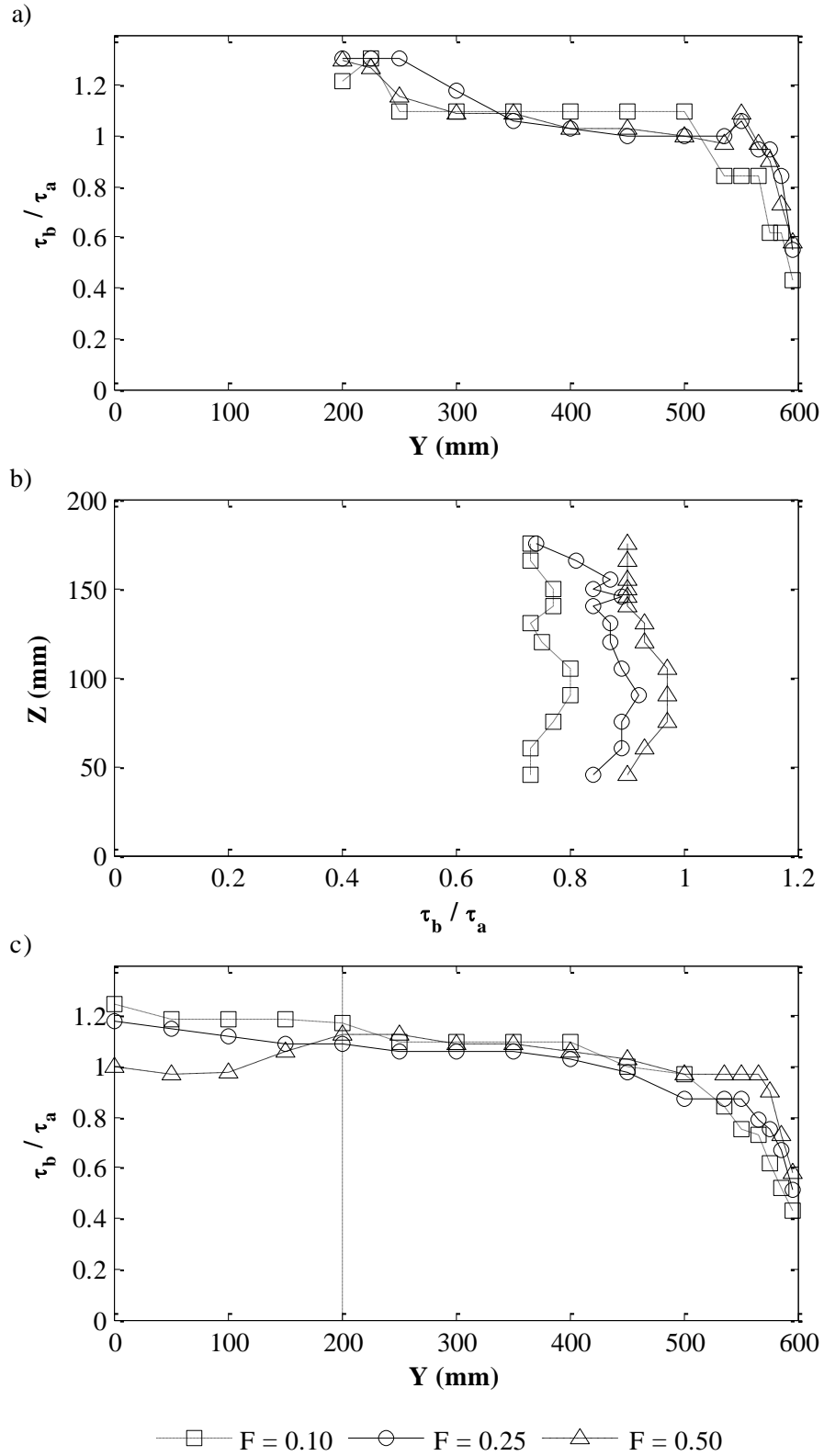


**Figure 4-39: Dimensionless shear stress distribution comparison Experiments 3 ( $F = 0.25$ ), 4 ( $F = 0.10$ ), and 5 ( $F = 0.50$ ) along a) the underside of the ice, b) the vertical side wall, and c) the bed. Vertical line indicates edge of ice cover above the bed.**

As the amount of coverage increased in a channel, so too did the maximum shear stress acting on the ice cover. This is illustrated in Figure 4-40a. For the cases examined, it can be seen that larger encroachments of border ice have higher  $\tau_b/\tau_a$  values at the edge of the cover. Additionally, for areas of the cross section that were covered in multiple experiments, (e.g.  $Y = 300$  to  $Y = 450$  was covered by both Experiment 3 and 7 but not 6), the dimensionless shear stress distributions follow similar trends. Interestingly, while the distributions from the experiments with smaller coverages always had higher magnitudes of  $\tau_b/\tau_a$  for the same location in the channel, their shear stresses were always lower. For frazil ice, this suggests that accumulation is more likely beneath the whole width of small coverages than wider ones. As the cover widens, there will be a higher shear stress at the edge acting to dampen further accumulation.

Along the vertical side wall there was no trend in the order of the distributions. However, they all had the same general shape; minima at the corners and a maximum near mid depth. Along the bed, the  $\tau_b/\tau_a$  distributions were all quite similar (Figure 4-40c). While there was an increase in shear stress beneath the edge of the 25% Coverage Experiment similar increases had occurred in the same position for the higher coverages as well. This suggests the change was not a result of the termination of the ice cover. For the 50% Coverage Experiment, the shear stress decreased in the open water area of the channel the same way the depth-averaged velocity had. As a result, the peak  $\tau_b/\tau_a$  of 1.15 occurs beneath the edge of the ice rather than at the centreline of the channel with the 25% and 67% coverage tests which had maxima of 1.24 and 1.18 respectively. Therefore, it cannot be concluded that the amount of coverage has an effect on the  $\tau_b/\tau_a$  distribution along the bed.

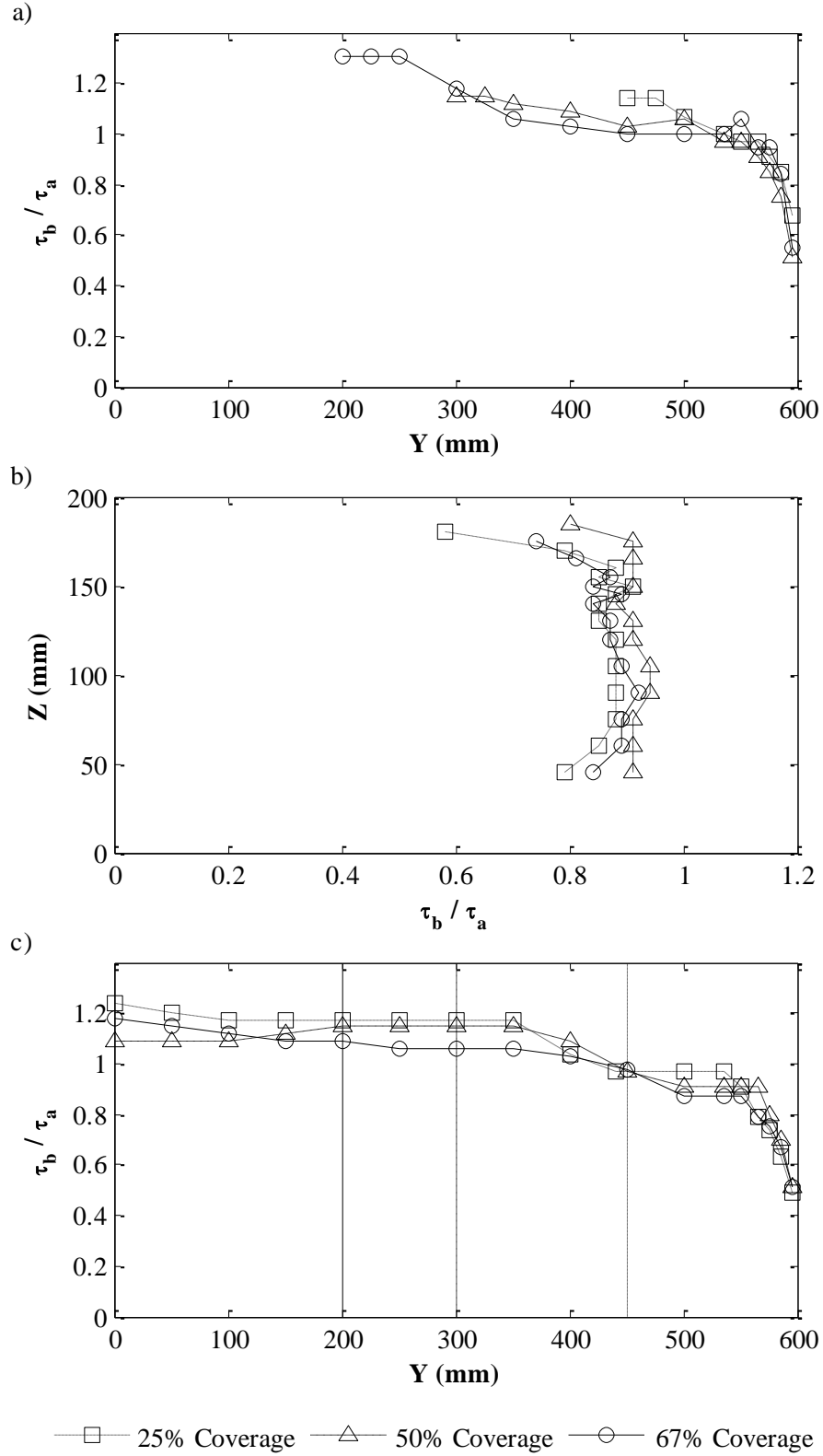


**Figure 4-40: Dimensionless shear stress distribution comparison Experiments 3 (67% coverage), 6 (25% coverage), and 7 (50% coverage) along a) the underside of the ice, b) the vertical side wall, and c) the bed. Vertical lines indicate respective edges of ice cover above the bed.**

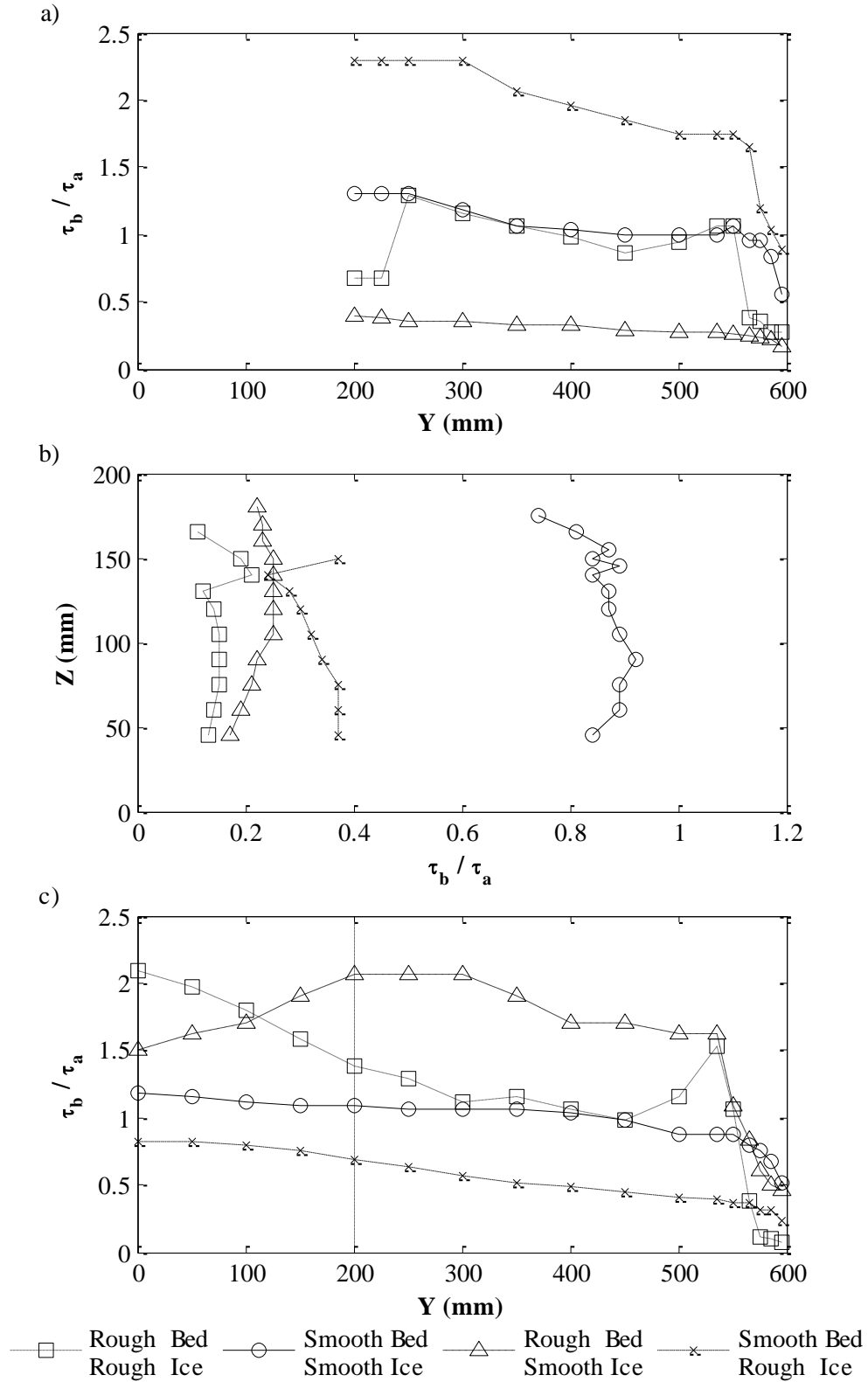


Figure 4-41: Dimensionless shear stress distribution comparison Experiments 3 (smooth bed - smooth ice), 8 (rough bed - smooth ice), 9 (smooth bed - rough ice), and 10 (rough bed - rough ice) along a) the underside of the ice, b) the vertical side wall, and c) the bed. Vertical line indicates edge of ice cover above the bed.

Figure 4-41 illustrates the effects of different roughness regimes on the  $\tau_b/\tau_a$  distribution. Along the underside of the cover the roughened ice experiment had the highest magnitude of  $\tau_b/\tau_a$ , as expected. The experiments with equal bed and ice roughness were approximately equal in magnitude, except at the edge of the ice and in the corner near the side wall. Here, the distribution from the experiment with both bed and ice roughness elements was significantly lower. The Rough Bed Experiment had the lowest magnitude. Intuitively this makes sense; in asymmetrically rough channels, the rougher surface will have a higher shear stress relative to its average than the smooth surface. Additionally, when the surfaces are equal in roughness, they should all have magnitudes that are closer to the average. The Base, Rough Bed, and Rough Ice Experiments followed the trend of most experiments and had peak  $\tau_b/\tau_a$  values directly under the edge of the ice. The values were approximately 1.3, 0.4, and 2.3 respectively. For the Rough Bed – Rough Ice Experiment, the peak shear stress did not occur at the edge of the ice, it was offset by 12.5% of the distance beneath the cover. The magnitude before its sudden decline was the same as the Base Experiment (1.3). Directly beneath the edge, the value was nearly halved, at 0.7. The reason for this sharp decrease is unknown.

On the vertical side wall (Figure 4-41b) there were marked differences in the  $\tau_b/\tau_a$  distributions from experiment to experiment. Regarding magnitude, it can be seen that distributions can be ranked by the amount of wetted perimeter that had been roughened. The Base Experiment, where all surfaces were the same roughness, had the highest magnitude and was closest to the average. Contrarily, Experiment 10, where the bed and ice had been roughened but the wall remained smooth, had the lowest magnitude. The Rough Bed Experiment, which had less of its wetted

perimeter roughened than the Rough Bed – Rough Ice Experiment, had a higher magnitude, and the Rough Ice Experiment, with even less roughened surface, was higher still. With respect to the shapes of the shear stress distribution, the minima of each experiment were still located in the corners; however, the maximum did not always occur at the same location. As with all previous experiments, when the bed and ice were the same roughness the maximum wall shear occurred at approximately mid depth. When the roughness was asymmetrical the maximum was displaced towards the smoother surface. In all cases it appeared that the maximum shear stress coincided with the location of maximum velocity.

The shear stress distributions along the bed (Figure 4-41c) exhibited different characteristics for each of the experiments. The Rough Ice Experiment had the lowest magnitude, as expected, and was similar in shape to the Base Experiment. Beside magnitude, the other main difference between these two experiments was that the Rough Ice Experiment had a steadier and relatively larger increase toward the centreline than the Base Experiment which appeared to plateau closer to the wall. Both experiments increased monotonically to peak  $\tau_b/\tau_a$  values at the centreline of approximately 0.8 and 1.2, respectively. For the Rough Bed Experiment the peak  $\tau_b/\tau_a$  value did not occur at the centreline. Instead, the maximum occurred beneath the edge of the ice cover with a magnitude of 2.06 compared to 1.5 at the centre. The reason for the decrease is unknown but is similar to the observed decrease in depth-averaged velocity. The Rough Bed – Rough Ice Experiment, unlike all other partial cover experiments, displayed two local maxima in the bed shear stress distribution. The global maximum, 2.1, was still located at the centreline and the other was located near the edge of the wall affected zone with a magnitude of

1.5. Between the two, the magnitude reduced to nearly equivalent to the Base Experiment. Only near the edge of the ice did it start to increase again.

Along the bed it should be expected to see locally higher sediment transport in the centre of the channel for equivalent or ice-dominated roughness regimes, while when bed roughness dominates the most movement should be expected near the edge of the ice cover. Similar trends exist for frazil accumulation beneath the cover as with previously mentioned experiments, i.e. more likely to occur near the bank than the ice edge. The exception was when both surfaces had been roughened where the results suggest frazil would be more likely to accumulate beneath the cover near the bank and leading edge of the ice than between them in the middle of the ice cover.

It is important to bear in mind that the results presented above for all the  $\tau_b/\tau_a$  distributions describe whether or not a location in the cross section is more or less likely to experience sediment transport or frazil deposition than another point in the same cross section. Whether or not sediment transport or frazil deposition manifests itself will depend on the absolute magnitude of the shear stress in the channel. It is not necessarily the case that because it is more likely for sediment transport or frazil deposition to occur that it actually will.

#### **4.5. Turbulence Intensities**

Important aspects of turbulence include its ability to exchange and dissipate momentum and heat through mixing. In the context of channels with border ice, this means there are implications for the growth rate of the ice itself through effects on heat exchange and erosion at the leading edge as well as for the likelihood of frazil production in the open water section and deposition beneath the ice. Furthermore,

there could be impacts on water quality through changes to the mixing of wastewater, be it biological or thermal, oxygen dissolution, and the concentration of suspended material. Therefore, understanding how turbulence intensity is affected by border ice is required to be able to develop accurate models for the design and analysis processes.

Another way to look at the effect of turbulence intensities is to combine the individual components into an aggregate value. This value is known as the turbulent kinetic energy (TKE). TKE is calculated as one half of the sum of the squares of the component turbulence intensities Equation (4-14). This section examines only the three orthogonal components of turbulence intensity and does not provide any results explicitly for TKE.

$$TKE = \frac{(u'^2 + v'^2 + w'^2)}{2} \quad (4-14)$$

As with analyzing secondary circulation, examining the turbulence intensities was not without issue. The Vectrino+ ADV in the up-looking orientation yielded turbulence intensities that generally had a higher magnitude than the Vectrino Profiler. This effect was observed for all three components, though spanwise turbulence intensity was affected the most. However, the Vectrino+ was able to capture the trend of the data for all components. Turbulence intensity values in the top 20% of the flow where data was collected with the Vectrino+ were examined skeptically and the trend was treated as more important than the magnitude.

The streamwise turbulence intensity distribution for the Open Channel Experiment is shown in Figure 4-42. The distribution was split along the interface of the regions

that were sampled by each ADV as indicated by the horizontal dashed line. It is not the intention that turbulence intensity values should be able to be read from the figures, nor is it guaranteed that the magnitude of each contour level matches between subareas or between experiments. The figures are provided solely to illustrate the trends in turbulence intensity within a single cross section.

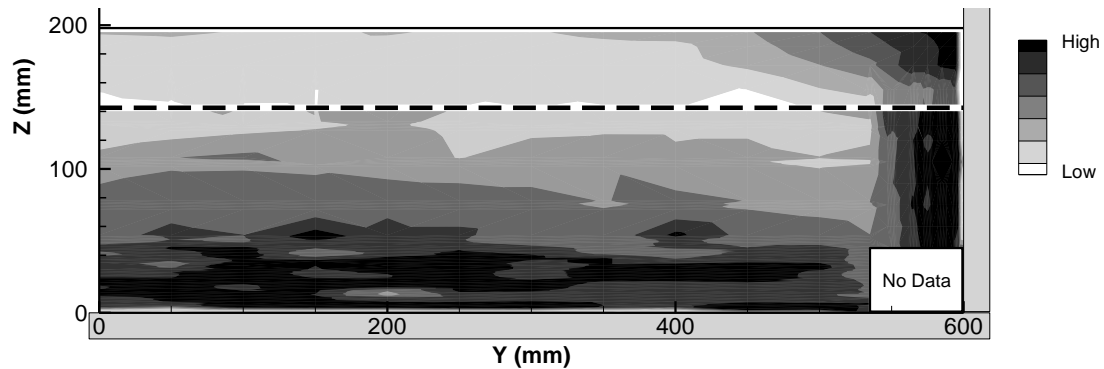


**Figure 4-42: Streamwise turbulence intensity distribution for the Open Channel Experiment.**

It can be seen from Figure 4-42 that in open channel flow the turbulence intensities were highest near the boundaries and decreased towards the surface and centre of the channel. This is in agreement with the theory as described in Chapter 2, where the turbulence intensity profiles are described by exponential decay equations. The equations for open channels, developed by Nezu & Nakagawa (1993), were already presented as Equations (2-4), (2-5), and (2-6). Figure 4-43 shows the turbulence intensity profiles for the centreline of the Open Channel Experiment. In panels a) and c) the discrepancy in magnitude between the data produced by each of the ADVs can be seen. Ignoring these points, the data fits well with Equations (2-4) and (2-6) having mean percent differences of -0.5% and 2.3% respectively. The vertical turbulence intensity, shown in panel b), does not follow Equations (2-5) when

$Z/D < 0.2$  as well as the other components followed their respective equations.

However, over the remainder of the profile, visually there is still good agreement.

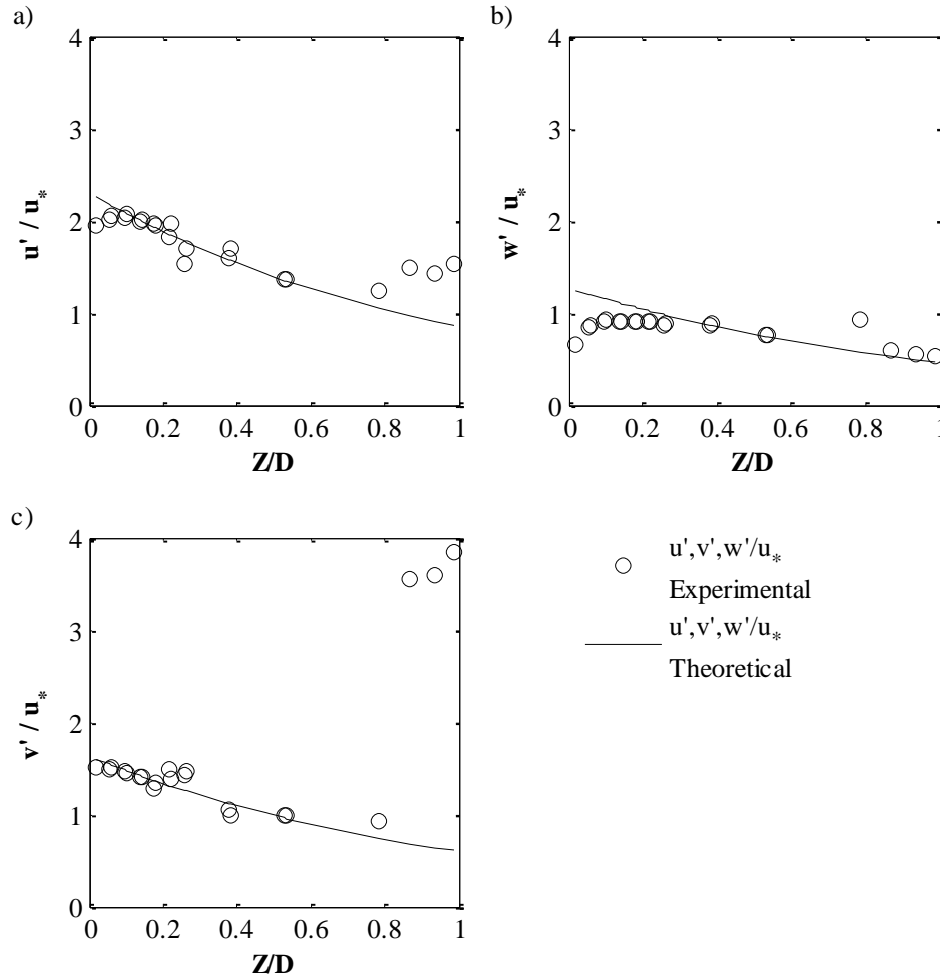


**Figure 4-43: Turbulence intensity profiles for the Open Channel Experiment at  $Y = 0$ .**

The streamwise turbulence intensity distribution of the Covered Channel Experiment is illustrated in Figure 4-44. It can be seen that the minimum turbulence intensity occurred at approximately mid-depth through the cross section. The relative maximum values were near the boundaries. Both observations are consistent with what was discussed in Chapter 2.

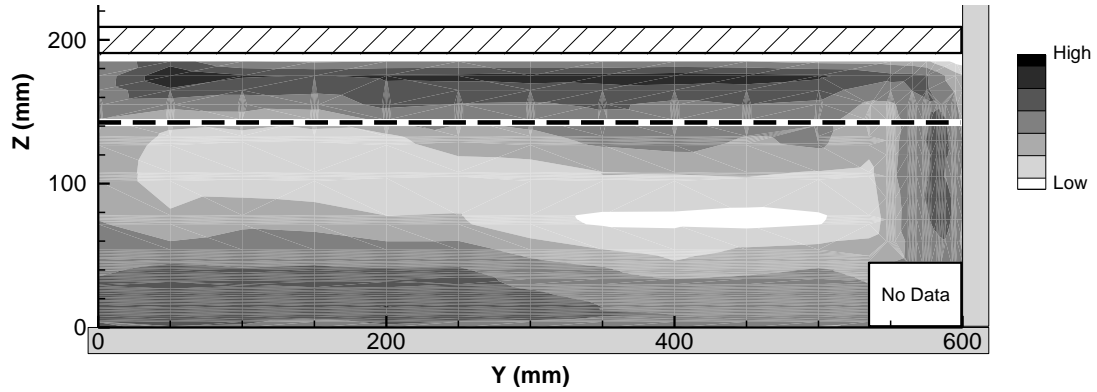


**Figure 4-44: Streamwise turbulence intensity distribution for the Covered Channel Experiment.**

Parthasarathy & Muste (1994) proposed a piecewise application of Equations (2-4), (2-5), and (2-6) for determining turbulence intensity profiles in covered channels. For this method, the flow is split at the plane of zero Reynolds shear stress,  $z_0$ , and turbulence intensities are normalized by the streamwise shear velocity of the boundary in their region. Equations for the bed-affected and ice-affected zones are given by Equation (4-15) and Equation (4-16), respectively.

$$\frac{u', v', w'}{u_{*,bed}} = C_{u,v,w} \exp\left(-\frac{z}{z_0}\right) \quad \text{for } 0 < z < z_0 \quad (4-15)$$

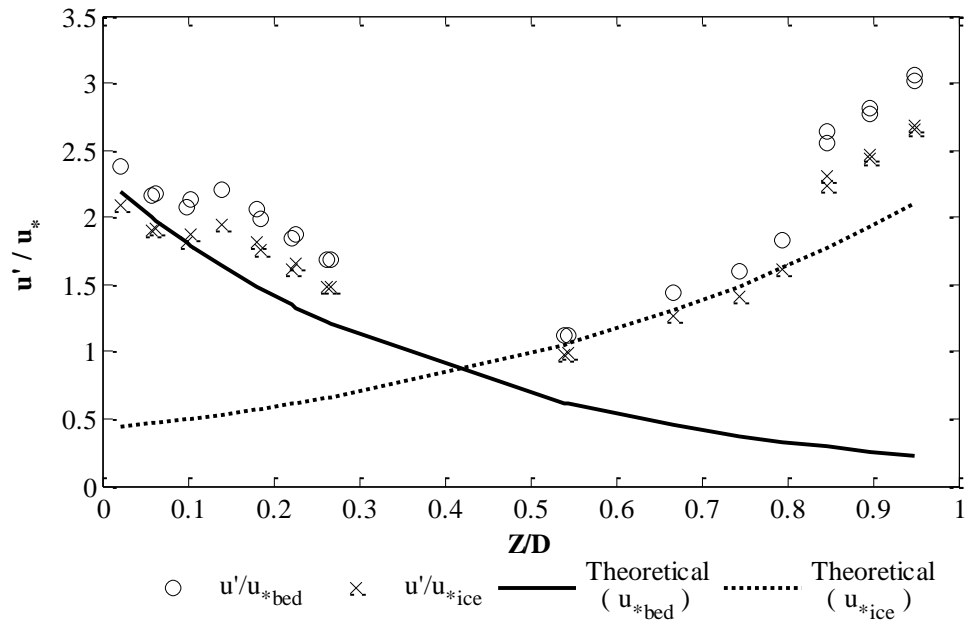
$$\frac{u', v', w'}{u_{*,ice}} = C_{u,v,w} \exp\left(-\frac{D-z}{D-z_0}\right) \quad \text{for } z_0 < z < D \quad (4-16)$$

where

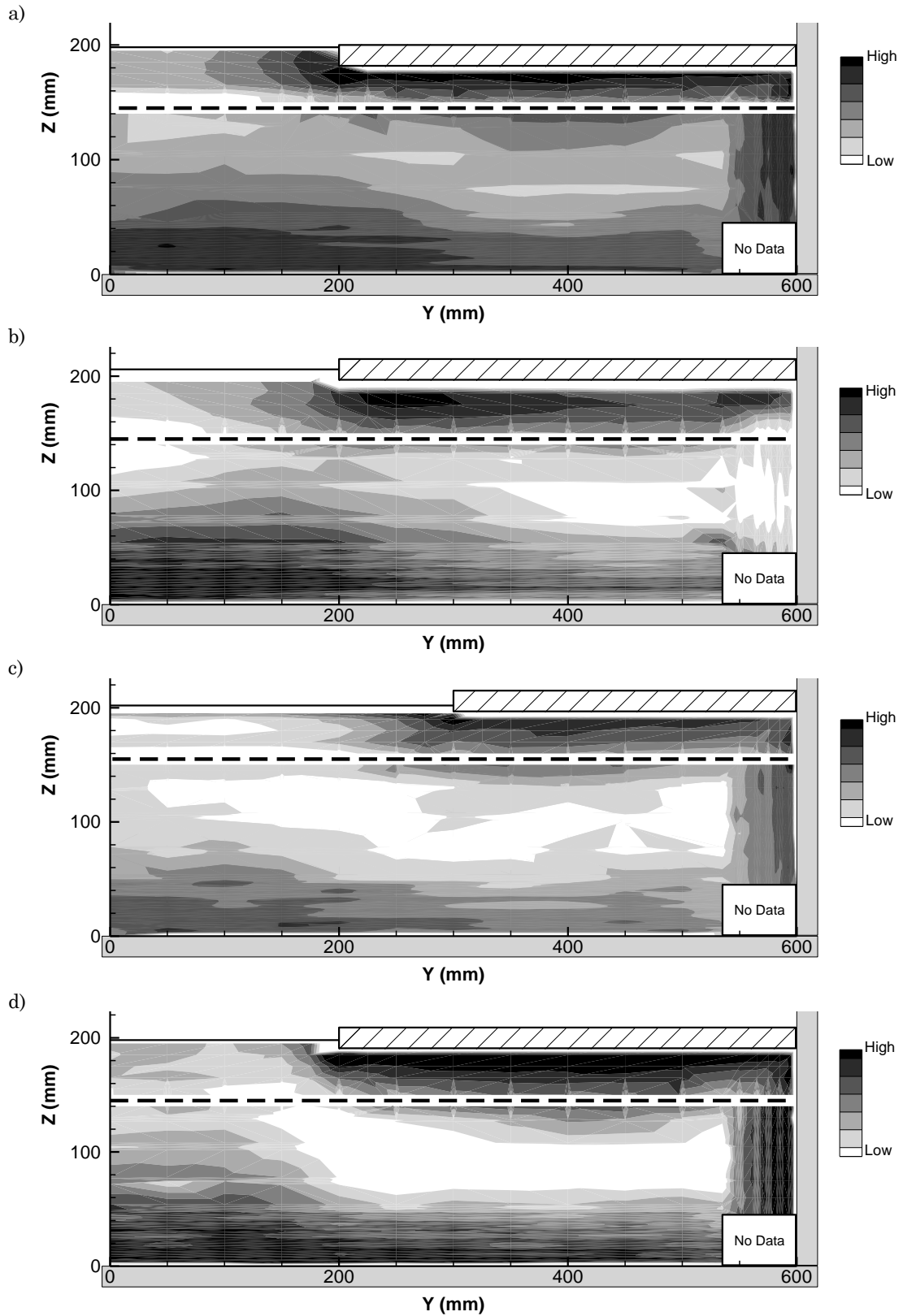
$$C_{u,v,w} = \text{coefficients from Eqns. (2-4), (2-5), and (2-6) } [ - ]$$

Figure 4-45 shows the application of these equations to the centreline profile from the Covered Channel Experiment. The solid line represents Equation (4-15) while the dashed line represents Equation (4-16). In practice, the lines terminate where they intersect but they have been shown in their entirety below for illustrative purposes. Additionally, to the left of the intersection only the data represented by the circular points are valid and only the crosses are valid to the right. Both have

been shown to illustrate the effect of accounting for the different shear velocities for each boundary. Interestingly, in this case the crosses provide a better fit through the whole depth of flow than using the circles where appropriate. One possible explanation is this may be a result of the subjective nature of determining the shear velocities. In either case, the trend is the same and the data agrees reasonably well with Equations (4-15) and (4-16).



**Figure 4-45: Streamwise turbulence intensity profile for the Covered Channel Experiment at  $Y = 0$ .**



**Figure 4-46: Streamwise turbulence intensity distribution for the a) Base, b) Rough Bed – Rough Ice, c) 50% Coverage, and d) High Froude Experiments.**

As with the streamwise velocity distribution, the turbulence intensity distribution in channels with border ice possesses characteristics of both open channels and covered channels. It can be seen in Figure 4-46 that beneath the cover there is a local minimum turbulence intensity that is generally located at approximately mid-depth and higher turbulence intensities along the boundaries. This was observed throughout the cross section in Figure 4-44 for the Covered Channel Experiment. Additionally, in the open water area, the turbulence intensity can be seen decreasing in magnitude as it approaches the surface, the same as in Figure 4-42 for the Open Channel Experiment. However, the turbulence intensity does not decrease monotonically from the bed to the surface through the entire open water section. The reason for this will be discussed further on. Streamwise turbulence intensity distributions for all experiments can be found in Appendix C.

When applied to the data from the partial ice cover experiments, Equations (4-15) and (4-16) performed reasonably well over the width of the cross section. The exception was in the region primarily affected by the vertical side-wall where agreement was poor. For most experiments in this study, the shape of the profiles in the covered region agreed with observations made by Muste et al., (2000), Robert & Tran, (2012), and Sukhodolov et al., (1999). Figure 4-47 provides an illustration of the typical fit for streamwise turbulence intensity profiles in the covered area of the channel for four different experiments. The average percent differences from Equations (4-15) and (4-16) for the experiments shown below when the up-looking data was excluded are 6.9%, -11.9%, 13.3%, and 9% for panels a) through d), respectively.

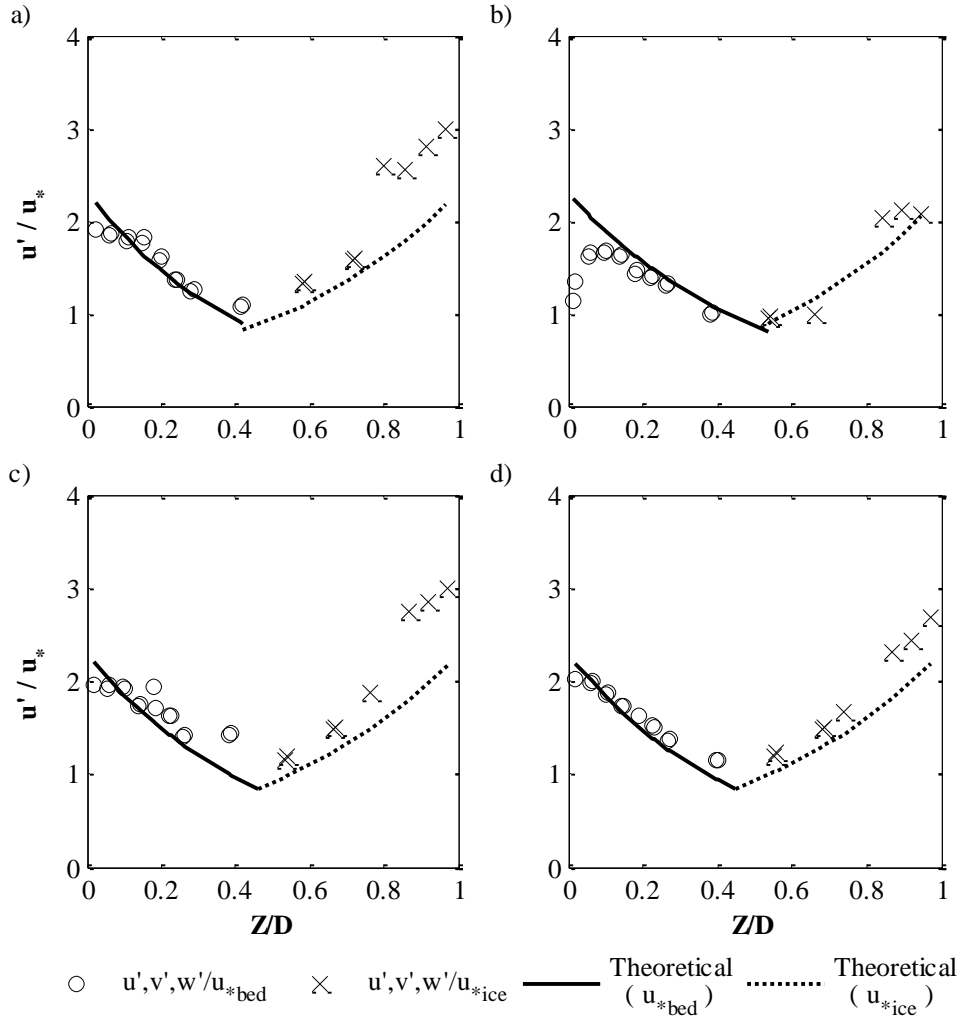


**Figure 4-47: Streamwise turbulence intensity profiles for the a) Base, b) Rough Bed – Rough Ice, c) 50% Coverage, and d) High Froude Experiments under the partial ice cover at  $Y = 400$**

However, beneath the cover, in Experiments 8 and 9 where the roughnesses of the bed and ice were asymmetrical, Equations (4-15) and (4-16) do not produce a good fit when applied in the manner directed. As illustrated in Figure 4-48, the best fit was achieved by using only the equation that corresponded to the roughest boundary.

For the Rough Ice Experiment this meant using Equation (4-16) and using Equation (4-15) for the Rough Bed Experiment. The equations for each experiment that did not apply should be disregarded, and are only shown in Figure 4-48 for illustrative purposes. The data points from the incorrect boundary are also shown to illustrate

the large difference in magnitude between the two. It is possible that the difference in roughness between the two surfaces was so large that the zone affected by the smooth boundary was suppressed into a depth that could not be measured with the current instrumentation.

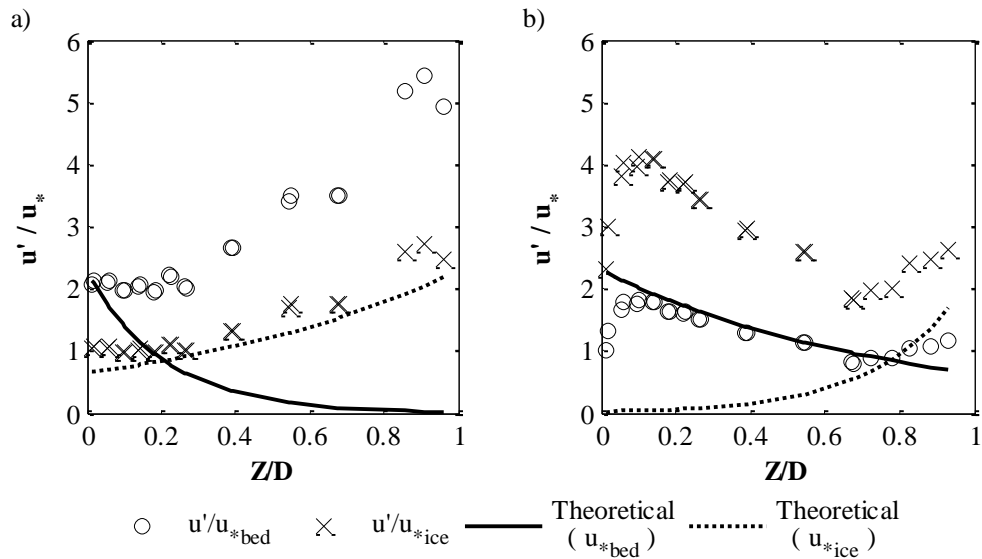


**Figure 4-48: Streamwise Turbulence intensity profiles for the a) Rough Ice, and b) Rough Bed Experiments beneath the partial ice cover at Y = 400**

In the open water region it was important to still consider the location of zero shear stress and not to automatically use the open channel turbulence intensity equations. In the zone where streamwise velocity profiles were transitional there was a better fit between the calculated data and the empirical equations if both Equations (4-15) and (4-16) were used along with the location of zero shear stress rather than just using the equations for an open channel, even though there was a free surface. Figure 4-49 shows all three turbulence intensities from a profile in the transitional zone of the 50% Coverage Experiment and is a general representation for the turbulence intensity profiles of the transition zones of all experiments. Since all three turbulence intensities increased toward the surface rather than decreasing

monotonically from the bed, continued use of both equations represented the shape of the turbulence intensity profile better than if the equations for an open channel had been used. In these cases, the shear velocity for the surface region was taken as the greater of the value from the bed or the edge of the ice cover.

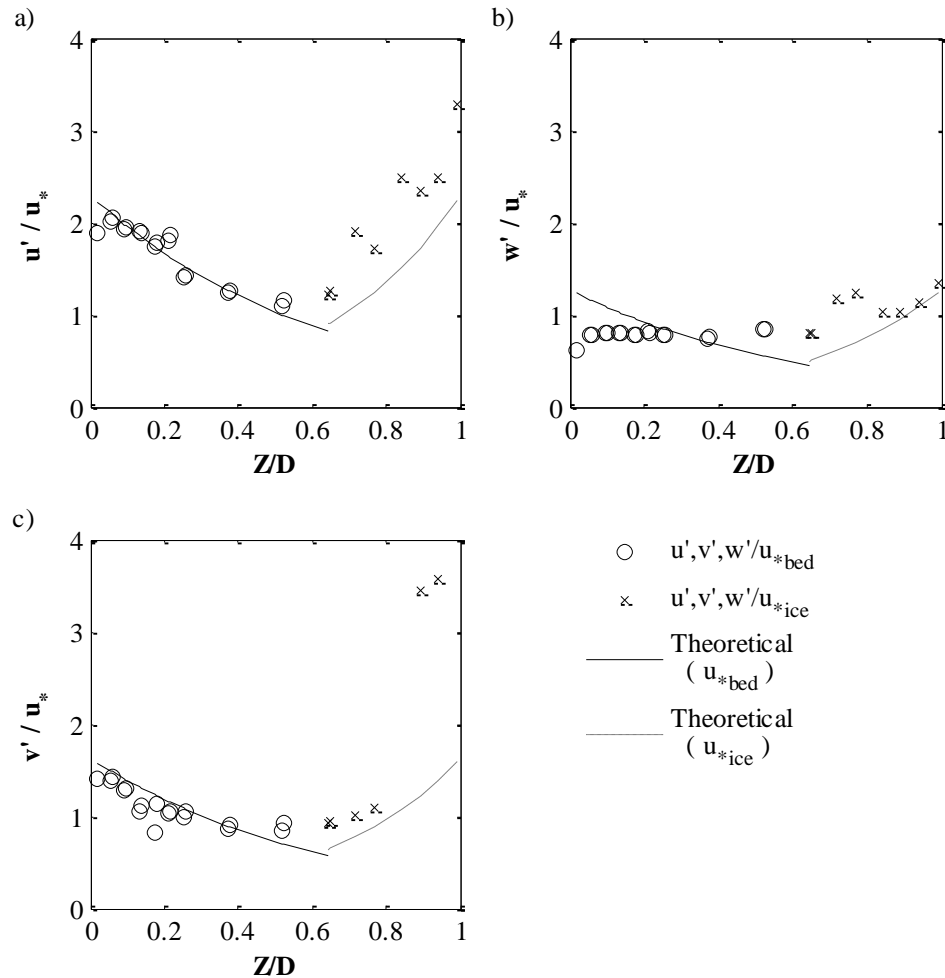


**Figure 4-49: Turbulence intensity profiles from the transition zone ( $Y = 250$ ) of the 50% Coverage Experiment.**

When the streamwise velocity profiles had been classified as open, Equations (2-4), (2-5), and (2-6) most often provided the better fit of the two methods. This was not altogether unexpected. When a profile was classified as open, the maximum velocity and plane of zero shear stress were located at or near the surface which would simplify Equation (4-15) into the Nezu & Nakagawa (1993) equations. However, this

did not apply to all experiments. As shown in Figure 4-50a and b, for some experiments the location of zero Reynolds shear stress was still depressed in the open water section, requiring the use of Equation (4-15). Similar to when there was asymmetrical roughness between the bed and the cover though, use of Equation (4-16) was not necessary to represent the shape of the profile near the surface and should therefore be disregarded. Figure 4-50c and d show examples of when the open channel equations were used as directed. As mentioned previously, the discrepancy in magnitude for points in the top 20% of the depth is likely due to the data having been collected with the Vectrino+ ADV.

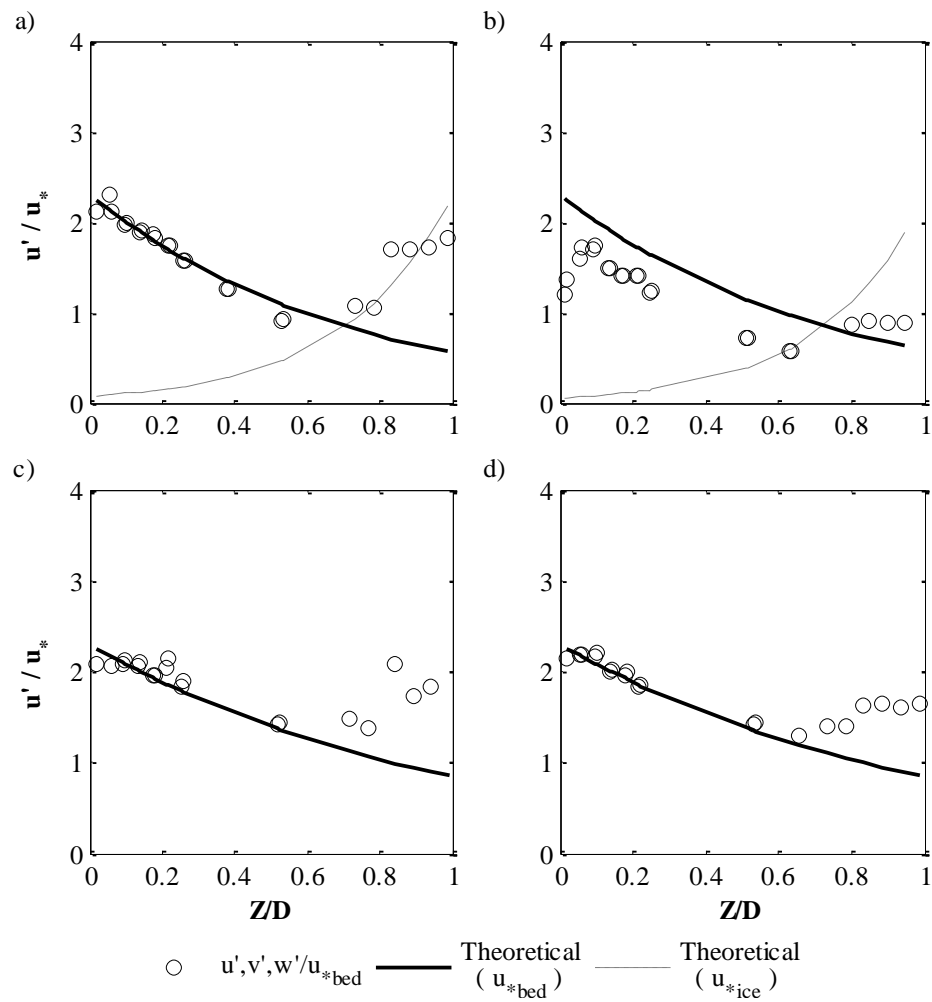


**Figure 4-50: Streamwise turbulence intensity profiles for the a) Base, b) Rough Bed - Rough Ice, c) 50% Coverage, and d) High Froude Experiments at  $Y = 0$ .**

When the cross sections were examined as a whole, it was found that all three components of turbulence intensities were locally higher at the edge of the ice cover. An example of this phenomenon is given in Figure 4-51. Note that the area of the cross section beneath  $Z = 160$  has been left blank and compressed. When the ice was rough, the local maximum turbulence intensity was located slightly beneath the cover rather than right at the edge. Given that this effect was limited to the two experiments where roughness elements were installed on the underside of the ice it is likely that their presence is the primary reason for this difference.

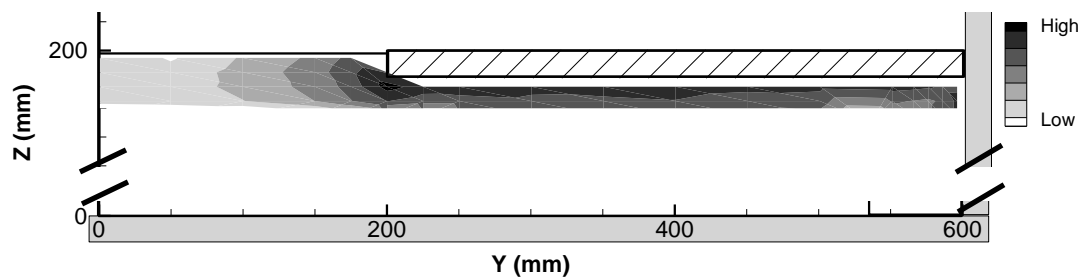


**Figure 4-51: Streamwise turbulence intensity near border ice: Experiment 3.**

The presence of this local maximum of turbulence intensity could have a significant impact on the progression of the leading edge of border ice. Higher turbulence intensities would cause higher heat transfer between the water and the ice. This would promote more rapid cooling of the water and encourage the formation of additional border ice. However, higher turbulence intensities are also more erosive and able to destroy the delicate ice crystals attempting to grow into the channel. With further research into turbulence intensities at the leading edge of border ice, relationships where the growth or erosion rate of border ice under different turbulence intensity levels for given water and air temperatures could be quantified. This data could be used to improve existing border ice growth models, such as the one developed by Matousek (1984), or to develop new ones entirely.

## 5. Conclusions and Recommendations

Understanding border ice formation and the impact of its presence on discharge, velocity, and turbulence intensity patterns can help to fill current knowledge gaps. It can also improve existing numerical models, especially since comprehensive, two dimensional river ice models now exist. The improved capability to model ice processes could help to reduce the impact of large spring floods through better planning and management of river ice as well as to reduce ice related energy losses, and ensuing financial losses, experienced at northern hydroelectric generating stations.

While many studies have been conducted in channels that are fully open or entirely covered with ice, little has been examined in channels with border ice. To begin filling this knowledge gap, experiments were conducted in the Hydraulics Research Testing Facility at the University of Manitoba in a 1.2 m wide, 14 m long flume to assess the impact of Froude number, coverage ratio and bed-to-ice roughness ratio on the hydraulic characteristics of channels with border ice cover. Acoustic Doppler velocimetry was used to collect detailed 3D velocity data over a cross section of the flume. This facilitated the analysis of velocity and turbulence intensity fields as well as the shear stress distribution. The data collected thus far represents the most complete experimental dataset of measured water velocities in a channel with a border ice cover, from which several conclusions may be drawn.

## 5.1. Conclusions

Through analyzing changes to the water surface profile, the effects of each parameter group were quantified and several methods of determining the composite roughness of the channel were evaluated. It was found that for different Froude numbers and amounts of coverage in the channel, the Manning's roughness of the channel did not change appreciably from the open water to the partially covered condition. The increase in upstream water surface elevation had therefore resulted from the increase in wetted perimeter added by the partial ice cover, rather than an increase in Manning's roughness. Having unequal roughness between the bed and underside of the ice cover did change the composite Manning's roughness of the channel. The Krishnamurthy and Christensen method performed the best of the methods evaluated. However, its use requires knowledge of, or the willingness to assume, the location of maximum velocity beneath the cover. Using the incorrect location reduced the performance of the method. Another method that performed almost as well was a simple perimetric weighting of the individual roughness components. The linear weighting method requires less information and represents a more practical approach. Additionally, in all methods examined, it was generally better to exclude the effect of the vertical side wall of the flume when determining the composite roughness of the channel.

It can be seen from the 2D streamwise velocity distributions and difference plots that the presence of border ice causes a redistribution of flow from beneath the cover into the open water region. This is in agreement with the conclusions made by Tsang (1970), Majewski and Baginska (1988), and Miles (1993). It was observed that the reduced velocity in the area of the cross section replaced with additional border ice

was compensated for with higher velocities in the open water region. The impact of asymmetric bed and ice roughness was as expected, with flow forced to the smoother boundary, increasing the velocity in that area. Additionally, when one or both surfaces were roughened, there was a greater redistribution of flow from beneath the cover to the open water portion of the channel than when the channel was entirely smooth. This was likely due to the resistance of the free surface remaining unchanged, with the net effect of increased flow preference for the open water section. The greatest impact on flow redistribution was realized when the ice had been roughened and the bed remained smooth. This was due to the greater enhancement of the preferential flow path. When both surfaces had been roughened, the changes to velocity occurred along the boundary of the covered section and in the open water area. Meanwhile, the velocity beneath the cover, within approximately  $\pm 40$  mm of mid-depth ( $\pm 20\%$  D), did not change significantly.

The streamwise velocity profiles from the partial ice cover experiments were compared to the Open Channel and Covered Channel profiles for the same locations across the cross section. Analysis revealed that beneath the covered section, streamwise velocity profiles exhibit the same shape at their locations as if the channel were completely covered. This effect extended up to and including beneath the leading edge of the ice. It occurred regardless of the Froude number or the amount of the channel that was covered. In the open water section, the streamwise velocity profiles did not always resemble those of either the Open Channel Experiment; some had a transitional shape. It was found that higher Froude numbers and channels with a rough bed reduced the amount of the open water section that was required for transitioning from one type of profile to the other.

Consequently, low Froude numbers and channels with a rough ice cover had increased transition zone widths. Further, the width of the transition zone may expand to encompass the entire open water section at low Froude numbers with a large amount of coverage. This was also the case in channels with sufficiently rough ice cover. Lastly, for the same Froude number, the same percentage of the open section of the channel was in transition under different amounts of coverage.

Through examination of the depth-averaged velocity distribution, it was found that there is a greater redistribution of flow for channels with lower Froude numbers than channels with higher Froude numbers. This is reflected by the higher relative average velocities in the open water section for the Low Froude Experiment compared to the Base Experiment. Additionally, both the Low Froude and Base Experiments were higher than the High Froude Experiment. Accordingly, the High Froude Experiment had a higher relative average velocity than the other two experiments beneath the cover. There was no clear trend observed for different amounts of coverage, and, the roughness of the ice appears to have a greater influence on the relative average velocity distribution than the roughness of the bed.

Unlike with the streamwise velocity, no firm conclusions could be drawn about the characteristics of secondary circulation in channels with border ice. This was due, in part, to the large amount of measurement uncertainty relative to the magnitude of the transverse and spanwise velocities. Further, small misalignments in the probe head of the ADV could have also caused errors through the translation of streamwise velocity into one or both of the secondary components. However, in spite of these complications, two things were apparent. First, it seemed as though each half of the channel possessed two secondary circulation cells, though not always in

the same configuration, relative magnitude, or direction. Secondly, the pattern of the secondary circulation was more similar to that of an open channel than a covered channel, even in the covered region.

The methods proposed by Shen & Ackermann (1980) for predicting the cumulative and transverse discharge distributions in a channel were compared to the results of these experiments. For the cumulative discharge distribution it was found that the Shen and Ackermann method consistently underpredicted discharge by approximately 2% on average. The maximum error was as high as 4% and usually located beneath the edge of the cover. Higher Froude numbers produced a greater amount of error than lower ones and results were most accurate for channels where the ice had been roughened. The transverse discharge distribution, meanwhile, was found to underpredict near the wall of the flume and overpredict in the open water. The most accurate region for the transverse discharge distribution equation was beneath the cover.

Regarding the shear stress distribution of channels with border ice cover, the distribution along the bed resembled, for the most part, that of an open channel. The minimum shear stress was in the corners and the maximum shear stress was in the centre of the channel. The High Froude, 50% Coverage, and Rough Bed Experiments did not follow this trend and instead had a local minimum value at the centreline and their respective maximums were located approximately beneath the edge of the ice. The overall pattern resembled the theoretical distribution for the shear stress in a completely covered channel. It is unknown why those three experiments differed from the others, especially since the Covered Channel Experiment did not exhibit that distribution. Lower Froude numbers produced higher normalized shear stresses

along the bed of the channel while coverage did not appear to have a clear effect. Shear stress has practical implications for the transport of sediment and frazil ice. While higher Froude numbers may produce more sediment transport due to higher shear stresses overall, the shape of the shear stress distribution, and therefore erosion and deposition patterns, may change. With higher Froude numbers there would be a decreased tendency for sediment transport in the open water region and an increased tendency near the wall which has negative implications for bank erosion and stability. The amount of coverage did not appear to affect the shear stress distribution along the bed. Beneath the ice cover the peak shear stress almost always occurred at the leading edge, regardless of Froude number, amount of coverage, or which surface was rougher. The Low Froude and Rough Bed – Rough Ice Experiments did not follow that trend. For the Low Froude Experiment there was a slight decrease immediately at the edge of the ice while for the Rough Bed – Rough Ice Experiment the decrease occurred slightly farther beneath the cover. The reason for this discrepancy is currently unknown. With respect to frazil accumulation, the higher relative shear stresses near the edge of the ice cover indicates frazil, if present, would be more likely to accumulate beneath the cover closer to the wall than at the leading edge.

The shape of turbulence intensity profiles in a channel with border ice cover was found to be estimated well by the dual layer flow method as proposed by Parthasarathy & Muste (1994). However, it is important that throughout the cross section, including the open water region, the location of zero shear stress is used as directed in the equations. In the area of the cross section where the streamwise velocity profiles had transitional shapes, the turbulence intensities also behaved in a

transitional manner. Here the location of the minimum turbulence intensity gradually moved towards the surface with increasing distance from the edge of the cover. As a portion of the open water section is in transition, to automatically use the open water turbulence intensity equations in the open water section could produce incorrect results. There is a local maximum turbulence intensity for all three components beneath the edge of the ice. This could affect the progression of the leading edge of border ice. Higher turbulence intensities would cause higher heat transfer between the water and the ice which would promote more rapid cooling of the water and encourage the formation of additional border ice. However, higher turbulence intensities are also more erosive and more able to destroy the delicate ice crystals attempting to grow into the channel.

## **5.2. Recommendations for Future Work**

The data collected for these experiments represents a good first step in attempting to further our understanding of the effects of border ice on the hydraulic characteristics in a channel. There are still, however, many potential avenues of research to explore that will strengthen and deepen our knowledge on the topic. There are also further insights to be gained from the experiments conducted thus far. The following list outlines some potential future areas of focus and suggestions for improving upon the process of study.

1. Further quantify the effects of different amounts of coverage and roughness by increasing the number of conditions examined.
2. Quantify the effect of different parameter sets, such as the channel aspect ratio, cross sectional geometry (e.g. trapezoidal channel), and asymmetrical ice coverage, on the hydraulic characteristics of channels with border ice.

3. Increase the density of data collection in the transition zone to enable more accurate characterization of how the width is affected by each of the parameters and how the shape of the velocity profiles change throughout.
4. Many challenges were encountered in studying secondary flow in these experiments. Future researchers should consider developing a more comprehensive plan for executing data collection if secondary flows are continued to be studied.
5. Take advantage of further advances in technology and utilize stereoscopic particle image velocimetry to collect velocity data. This technology would allow for nonintrusive measurement of all three velocity components over an entire cross section simultaneously.
6. Compare the results of these and future experiments with 3D numerical turbulence models.
7. Lastly, once a more complete understanding of these data sets is obtained, the results of these and future experiments should be considered for incorporation into comprehensive numerical river ice models.

## 6. Works Cited

- Absi, R. (2011). An ordinary differential equation for velocity distribution and dip-phenomenon in open channel flows. *Journal of Hydraulic Research*, 49(1), 82–89. <http://doi.org/10.1080/00221686.2010.535700>
- Arisz, H., Davar, K. S., & Tang, T. C. C. (1988). Flow resistance for partially ice-covered channels: A laboratory simulation study. In *Proceedings of the 9th International Symposium on Ice* (pp. 131–141). Sapporo, Japan: International Association of Hydro-Environment Engineering and Research.
- Ashton, G. D. (1986). *River and lake ice engineering*. Highlands Ranch, CO., USA: Water Resources Publications.
- Beltaos, S. (2013). *River Ice Formation*. Edmonton, AB: Committee on River Ice Processes and the Environment.
- Brunner, G. (2010). *HEC-RAS River Analysis System Hydraulic Reference Manual*. Davis, CA.
- Chow, V. Te. (1959). *Open Channel Hydraulics*. New York, NY: McGraw-Hill Book Company, Inc.
- Dolgoplova, E. (1998). Velocity distribution in ice-covered flow. In *Ice in Surface Waters: Proceedings of the 14th International Symposium on Ice* (pp. 123–129). Potsdam, NY: International Association of Hydro-Environment Engineering and Research.

- Durand, Z. (2014). *Experimental Study of Tailwater Level and Asymmetry Ratio Effects on Three-Dimensional Offset Jets*. University of Manitoba.
- Engel, P., Lau, Y. L., Hicks, F. E., & Steffler, P. M. (1996). Estimation of Mean Flow Velocity in Ice-Covered Channels. *Journal of Hydraulic Engineering*, 474–477.
- Gogus, M., & Tatinclaux, J. C. (1980). Characteristics of flow beneath a rough floating cover. In *Proceedings from the 1st Workshop on Hydraulics of Ice Covered Rivers* (pp. 122–142). Burlington, Ontario: Canadian Geophysical Union - Committee on River Ice Processes and the Environment.
- Goring, D. G., & Nikora, V. I. (2002). Despiking Acoustic Doppler Velocimeter Data. *Journal of Hydraulic Engineering*, 128(January), 117–126.
- Guo, J. (2014). Modified log-wake-law for smooth rectangular open channel flow. *Journal of Hydraulic Research*, 52(1), 121–128.  
<http://doi.org/10.1080/00221686.2013.818584>
- Guo, J., & Julien, P. (2008). Application of the modified log-wake law in open-channels. *Journal of Applied Fluid Mechanics*, 1(2), 17–23. Retrieved from [http://ascelibrary.org/doi/abs/10.1061/40856\(200\)200](http://ascelibrary.org/doi/abs/10.1061/40856(200)200)
- Hanjalic, K., & Launder, B. (1972). Fully developed asymmetric flow in a plane channel. *Journal of Fluid Mechanics*, 51, 301–335.
- Haresign, M., Toews, J. S., & Clark, S. (2011). Comparative Testing of Border Ice Growth Prediction Methods. In *Proceedings from the 16th Workshop on River*

- Ice* (pp. 400–413). Winnipeg, MB: Canadian Geophysical Union - Committee on River Ice Processes and the Environment.
- Hirayama, K. (1986). Growth of ice cover in steep and small rivers. In *Proceedings of the 8th International Symposium on Ice* (pp. 451–464). Iowa City, IA: International Association of Hydro-Environment Engineering and Research.
- Khodashenas, S. R., Abderrezzak, K. E. K., & Paquier, A. (2008). Boundary shear stress in open channel flow: A comparison among six methods. *Journal of Hydraulic Research*, 46(5), 598–609. <http://doi.org/10.3826/jhr.2008.3203>
- Knight, D. W., Demetriou, J. D., & Hamed, M. E. (1984). Boundary Shear in Smooth Rectangular Channels, 110(4), 405–422.
- Larsen, P. (1969). Head Losses Caused by an Ice Cover on Open Channels. *Journal of the Boston Society of Civil Engineers*, 56(1), 45–67.
- Lassabatere, L., Pu, J., Bonakdari, H., Joannis, C., & Larrarte, F. (2012). Velocity Distribution in Open Channel Flows: Analytical Approach for the Outer Region. *Journal of Hydraulic Engineering*, (January), 37–43. [http://doi.org/10.1061/\(ASCE\)HY.1943-7900.0000609](http://doi.org/10.1061/(ASCE)HY.1943-7900.0000609).
- Leonardi, S., Orlandi, P., & Antonia, R. a. (2005). A method for determining the frictional velocity in a turbulent channel flow with roughness on the bottom wall. *Experiments in Fluids*, 38(6), 796–800. <http://doi.org/10.1007/s00348-005-0975-7>

- Leonardi, S., Orlandi, P., Smalley, R. J., Djenidi, L., & Antonia, R. a. (2003). Direct numerical simulations of turbulent channel flow with transverse square bars on one wall. *Journal of Fluid Mechanics*, 491, 229–238.  
<http://doi.org/10.1017/S0022112003005500>
- Majewski, W. (1990). River Ice Hydraulics. In *Proceedings of the 10th International Symposium on Ice* (pp. 29–47). Espoo, Finland: International Association of Hydro-Environment Engineering and Research.
- Majewski, W. (1992). Laboratory Investigation of the Flow in Open Channels with Partial Ice Cover. In *Proceedings of the 11th International Symposium on Ice* (pp. 335–345). Banff, AB: International Association of Hydro-Environment Engineering and Research.
- Majewski, W. (1994). Flow Characteristics in Open Channels with Floating Ice Cover. In *Proceedings of the 12th International Symposium on Ice*. Trondheim, Norway: International Association of Hydro-Environment Engineering and Research.
- Majewski, W., & Baginska, M. (1988). Hydraulic Conditions in open channels with ice cover. In *Proceedings of the 9th International Symposium on Ice* (pp. 112–121). Sapporo, Japan: International Association of Hydro-Environment Engineering and Research.
- Matousek, V. (1984). Regularity of the Freezing-up of the Water Surface and Heat Exchange between Water Body and Water Surface. In *Proceedings of the 7th*

- International Symposium on Ice* (pp. 187–200). Hamburg, Germany:  
International Association of Hydro-Environment Engineering and Research.
- Michel, B., Marcotte, N., Fonseca, F., & Rivard, G. (1982). Formation of Border Ice in the Ste. Anne River. In *Proceedings of the 2nd Workshop on Hydraulics of Ice Covered Rivers* (pp. 38–61). Edmonton, AB: Canadian Geophysical Union - Committee on River Ice Processes and the Environment.
- Miles, T. M. (1993). *A Study of Border Ice Growth on the Burntwood River*.  
University of Manitoba.
- Munson, B. R., Young, D. F., & Okiishi, T. H. (2006). *Fundamentals of Fluid Mechanics* (5th ed.). John Wiley & Sons, Inc.
- Muste, M., Braileanu, F., & Ettema, R. (2000). Flow and sediment transport measurements in a simulated ice-covered channel. *Water Resources Research*, *36*(9), 2711–2720. <http://doi.org/10.1029/2000WR900168>
- Newbury, R. (1968). *The Nelson River: A Study of Subarctic River Processes*. John Hopkins University.
- Nezu, I., & Nakagawa, H. (1993). *Turbulence in Open-Channel Flows*. Rotterdam, Netherlands: A.A. Balkema.
- Nortek. (2004). Vectrino Velocimeter User Guide.
- Nortek. (2012). Vectrino profiler user guide. Boston, MA.
- Nortek. (2013). Midas Data Acquisition Software Users Guide. Boston, MA.

- Parthasarathy, R., & Muste, M. (1994). Velocity measurements in asymmetric turbulent channel flows. *Journal of Hydraulic Engineering*. Retrieved from [http://ascelibrary.org/doi/abs/10.1061/\(ASCE\)0733-9429\(1994\)120:9\(1000\)](http://ascelibrary.org/doi/abs/10.1061/(ASCE)0733-9429(1994)120:9(1000))
- Pratte, B. D. (1979). Review of flow resistance of consolidated smooth and rough ice covers. In *Canadian Hydrology Symposium* (pp. 52–92). Vancouver, BC: National Research Council.
- Pu, J. (2013). Universal Velocity Distribution for Smooth and Rough Open Channel Flows. *Journal of Applied Fluid Mechanics*, 6(3), 413–423. Retrieved from [http://198.55.49.74/En/VEWSSID/J\\_pdf/112520130314.pdf](http://198.55.49.74/En/VEWSSID/J_pdf/112520130314.pdf)
- Robert, A., & Tran, T. (2012). Mean and turbulent flow fields in a simulated ice-covered channel with a gravel bed: some laboratory observations. *Earth Surface Processes and Landforms*, 37(9), 951–956. <http://doi.org/10.1002/esp.3211>
- Shen, H. T., & Ackermann, N. L. (1980). Wintertime Flow Distribution in River Channels. *Journal of the Hydraulics Division*, 805–817.
- SonTek. (2001). SonTek ADVField Acoustic Doppler Velocimeter Technical Documentation.
- Sturm, T. W. (2010). *Open Channel Hydraulics* (2nd ed.). McGraw-Hill.
- Sukhodolov, A., Thiele, M., Bungartz, H., & Engelhardt, C. (1999). Turbulence structure in an ice-covered, sand-bed river. *Water Resources Research*, 35(3), 889–894. <http://doi.org/10.1029/1998WR900081>

- Teal, M., Ettema, R., & Walker, J. (1994). Estimation of mean flow velocity in ice-covered channels. *Journal of Hydraulic Engineering*, *120*(12), 1385–1400. Retrieved from [http://ascelibrary.org/doi/abs/10.1061/\(ASCE\)0733-9429\(1994\)120:12\(1385\)](http://ascelibrary.org/doi/abs/10.1061/(ASCE)0733-9429(1994)120:12(1385))
- Tsai, W., & Ettema, R. (1994). Modified eddy viscosity model in fully developed asymmetric channel flows. *Journal of Engineering Mechanics*, *120*(4), 720–732. Retrieved from [http://ascelibrary.org/doi/abs/10.1061/\(ASCE\)0733-9399\(1994\)120:4\(720\)](http://ascelibrary.org/doi/abs/10.1061/(ASCE)0733-9399(1994)120:4(720))
- Tsang, G. (1970). Change of Velocity Distribution in a Cross-Section of a Freezing River and the Effect of Frazil Ice Loading on Velocity Distribution. In *Proceedings of the 1st International Symposium on Ice* (pp. 1–11). Reykjavik, Iceland: International Association of Hydro-Environment Engineering and Research.
- Uzuner, M. S. (1975). The composite roughness of ice covered streams. *Journal of Hydraulic Research*, *13*(1), 79–102. Retrieved from <http://www.tandfonline.com/doi/pdf/10.1080/00221687509499721>
- Yang, S., Tan, S., & Lim, S. (2004). Velocity distribution and dip-phenomenon in smooth uniform open channel flows. *Journal of Hydraulic Engineering*, *130*(12), 1179–1186. Retrieved from [http://ascelibrary.org/doi/abs/10.1061/\(ASCE\)0733-9429\(2004\)130:12\(1179\)](http://ascelibrary.org/doi/abs/10.1061/(ASCE)0733-9429(2004)130:12(1179))

## **Appendix A: Rationale behind ADV Settings**

When conducting experiments it is important to select instrument settings that are appropriate to the task being performed and time efficient. This section outlines the rationale for the selection of the ADV settings that were used during data collection. For determining which setting would converge fastest the percent error of the “true value” was used. The “true value” was assumed to have been reached after 30 minutes of sampling and all statistics calculated based on the full time series are assumed to be, for the purposes of this analysis, accurate and free of error.

The presented percent error for a statistic at a given time was calculated using the following procedure. For time  $t_i$  the percent error was taken as the maximum absolute percent error for times  $t_i$  through to  $t_n$ , where  $n$  is the last time in the series. The reasoning being, at time  $t_i$ , it is still possible that up to that maximum error could occur between then and the “true value” at  $t_n$ ; just because the percent error at  $t_i$  might happen to be  $x\%$  this time does not guarantee that it will be the same value in every subsequent run.

Statistics were analyzed for the cell 5 cm from the transducer as this is the sweet spot of the instrument and will be assumed to represent the true value. The other cells in the profile were later analyzed to determine which cells should be included in the calculation of which statistics. Vertical and spanwise velocity errors are given as percentage of the mean streamwise velocity.

## A.1 Ping Algorithm

ADV's function by sending out pulses of sound and calculating the velocity from the Doppler shift in the return signal. Each of these pulses is called a ping. The velocity given for one sampling interval is the average of the results of many pings. Three options exist when selecting how the Vectrino Profiler sends out pings, each of which has a different intended result (Nortek, 2013).

The first option is to use the maximum interval algorithm. This algorithm produces pings at intervals such that the ambiguity velocity is matched to the selected velocity range resulting in the longest duration between pings. This method is most appropriate for smooth flows (Nortek, 2013). The second option is to use the minimum interval algorithm. This algorithm produces pings as quickly as possible and is most appropriate for highly turbulent flows (Nortek, 2013). The third option is to use an adaptive interval algorithm. This algorithm measures the initial return signals and changes the length of the interval between pings so as to reduce the interference from the reflections of previous pulses. This acoustic interference can create regions of the velocity profile where significant errors are possible (Nortek, 2013). For this reason, it is advantageous to pre-emptively reduce or eliminate these weak-spots to improve overall data quality.

Measurements were collected using all three ping interval methods both near the bed and in the free stream region. No ping algorithm outperformed any other for either of these regions. Furthermore, the size of the 95% confidence interval is unaffected by the algorithm used except in a small number of cases where the maximum interval algorithm produced a larger 95% confidence interval. As expected, the adaptive interval algorithm had reduced the occurrence of weak spots

in the velocity profiles. Use of the adaptive ping interval was selected for the remainder of the experiments.

## **A.2 Frequency**

The Vectrino II profiling ADV is capable of recording velocity readings at frequencies up to 100 Hz. Velocity profiles were collected near the wall and in the free stream at frequencies of 25, 50 and 100 Hz. The data was analyzed to determine whether the sampling frequency had an impact on the amount of time required for the flow characteristics calculated to reach convergence and the relative size of the confidence intervals for the calculated values.

From the graphs in Figure A-1, one can see in the free stream velocity region that frequency did not have an appreciable effect on the time required for convergence to within a reasonable tolerance of the true value. The  $-\overline{uv}$  figure being the exception where the 50 Hz data contains markedly more error than the other two frequencies. This can be explained by a smaller calculated magnitude for the true  $-\overline{uv}$  value at 50 Hz, relative to 25 and 100 Hz, exaggerating the amount of error. Similarly, in the near bed region, frequency did not provide significant influence over the time required for convergence to a value within a reasonable tolerance of the true value.

Using a frequency of 100 Hz becomes preferable when considering the size of the confidence interval. For the same sampling time, the number of measurements taken at 100 Hz was 2 and 4 times greater than those taken for 50 and 25Hz, respectively. This means 100 Hz produces the smallest confidence interval regardless of the statistic being examined or the position of the measurement in the velocity profile.

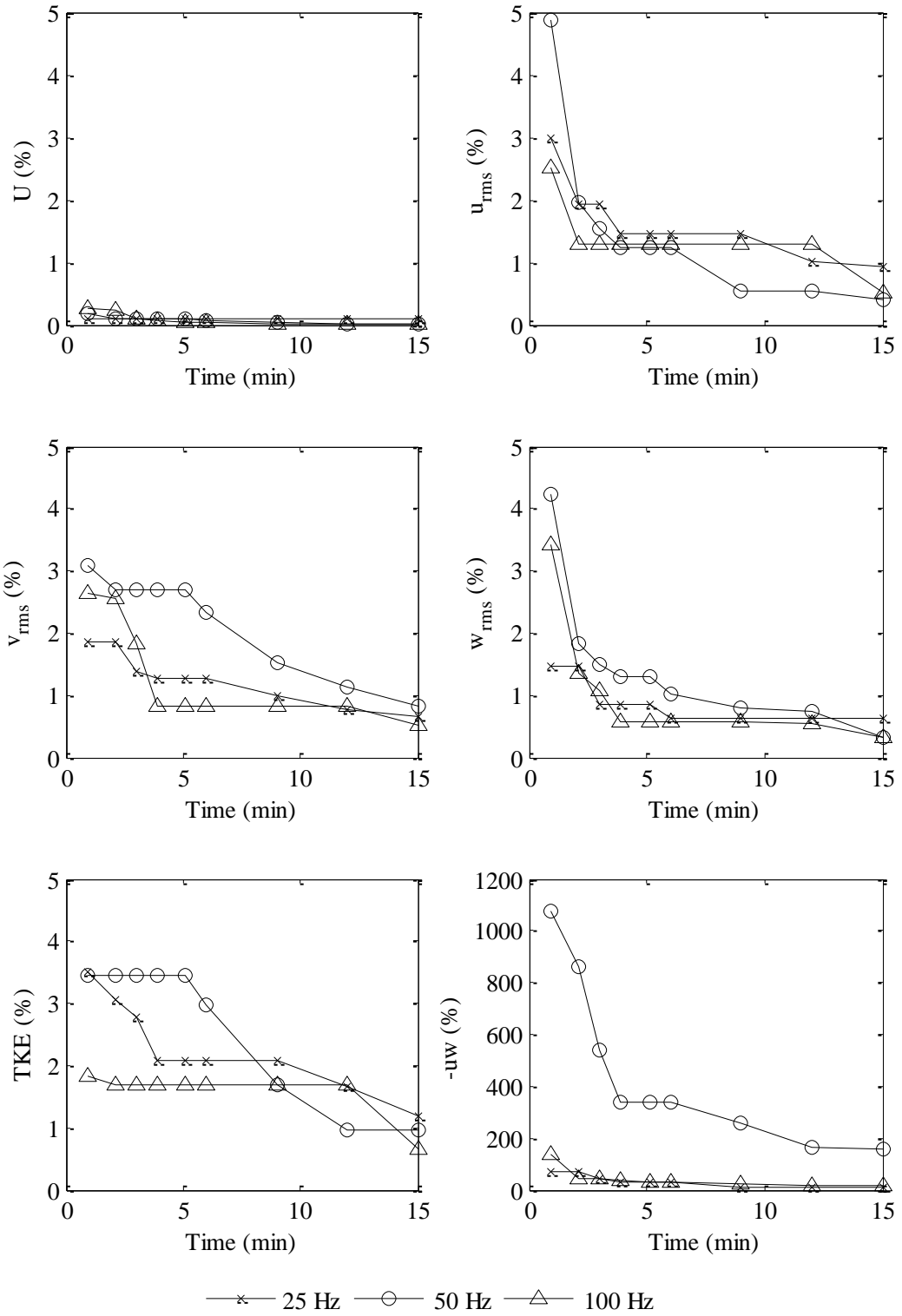


**Figure A-1: Comparison of the effect of sampling frequency on convergence in the free stream velocity region.**

### A.3 Time to convergence (for 100 Hz Adaptive Interval)

The parameters selected for analyzing the time to convergence and use in all subsequent testing were a frequency of 100Hz and an adaptive ping interval for their smaller confidence interval and ability to reduce weak spots respectively.

#### A.3.1 Free Stream

The results of the convergence test for the free stream region, shown in Figure A-2, indicate that it takes approximately 3 minutes for the greatest reductions in percent error to be realized. The data in Figure A-2 is also summarized in Table A-1.

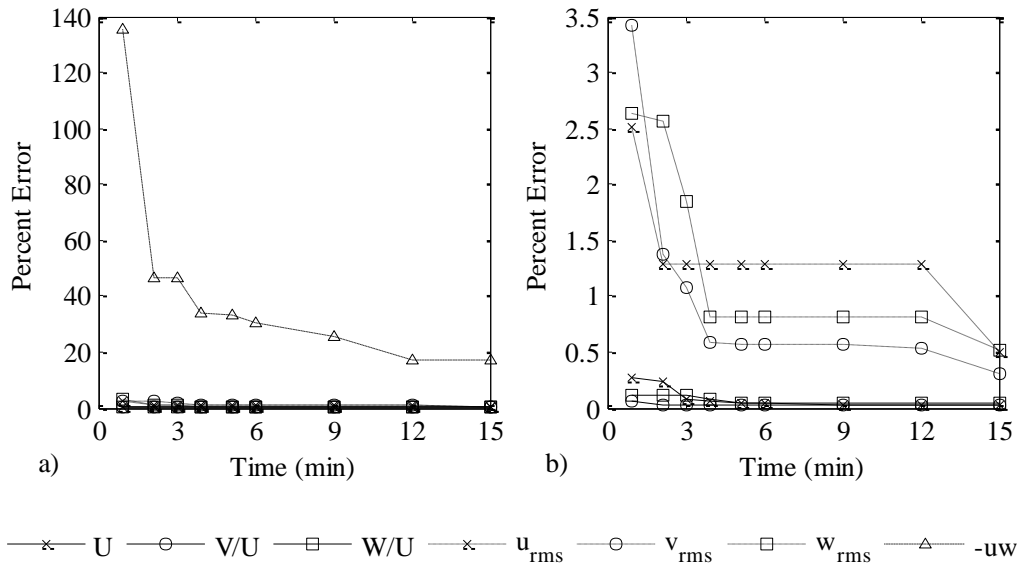


Figure A-2: Convergence test in free stream (a) including  $-\bar{u}\bar{v}$ ; (b) excluding  $-\bar{u}\bar{v}$

Mean velocities in all directions converged to under 0.5% error after less than one minute of sampling. Likewise, all turbulence intensities and the turbulent kinetic energy converged fairly quickly with less than 3% error after 2 minutes and less than 2% after 3 minutes. Contrarily, the shear stress took a significant amount of time for the value to converge. After 2 minutes the error was 46.5% and did not

decrease further until 4 minutes when it reduced to 34%. After 15 minutes of sampling the percent error of the 30 minute true value is 17%. Practically, the value of  $-\overline{uv}$  in the free stream is on the order of  $1E-5$  to  $1E-6$ , so any fluctuations in the percent error at this point were greatly amplified due to the small value of the denominator. The actual value was not changing significantly and inspection of the percent error in  $-\overline{uv}$  versus time suggests that the value stabilized after 3-4 minutes.

**Table A-1: Percent error for flow statistics in the free stream region.**

Time (min)	U	V	W	V/U	W/U	$u_{rms}$	$v_{rms}$	$w_{rms}$	TKE	-uw
0.9	0.3	12.8	1.6	0.1	0.1	2.5	2.6	3.4	1.8	135
2.1	0.2	12.8	0.9	0.1	0	1.3	2.6	1.4	1.7	46.5
3	0.1	11.8	0.9	0.1	0	1.3	1.8	1.1	1.7	46.5
3.9	0.1	9.6	0.9	0.1	0	1.3	0.8	0.6	1.7	33.8
5.1	0	4.7	0.9	0	0	1.3	0.8	0.6	1.7	33.4
6	0	4.7	0.9	0	0	1.3	0.8	0.6	1.7	30.4
9	0	4.7	0.7	0	0	1.3	0.8	0.6	1.7	25.9
12	0	4.7	0.7	0	0	1.3	0.8	0.5	1.7	17
15	0	4.3	0.7	0	0	0.5	0.5	0.3	0.7	17

Note: values have been rounded to the nearest 0.1%; values of 0.0% do not represent zero error.

### A.3.2 Near Boundary

In the near wall region the previous assumption that the “true value” is located 5 cm from the transducer is inherently flawed because of the known logarithmic velocity profile. Near the boundary the convergence will be examined on a cell by cell basis for each of the statistics. Due to elimination of data for quality control reasons, data was not available in the first 3 mm from the bed.

The results of the convergence test for the near bed region, shown in Figure A-3, indicate that it took approximately 3 minutes for the greatest reductions in percent error to be realized. The data in Figure A-3 is also summarized in Table A-2.

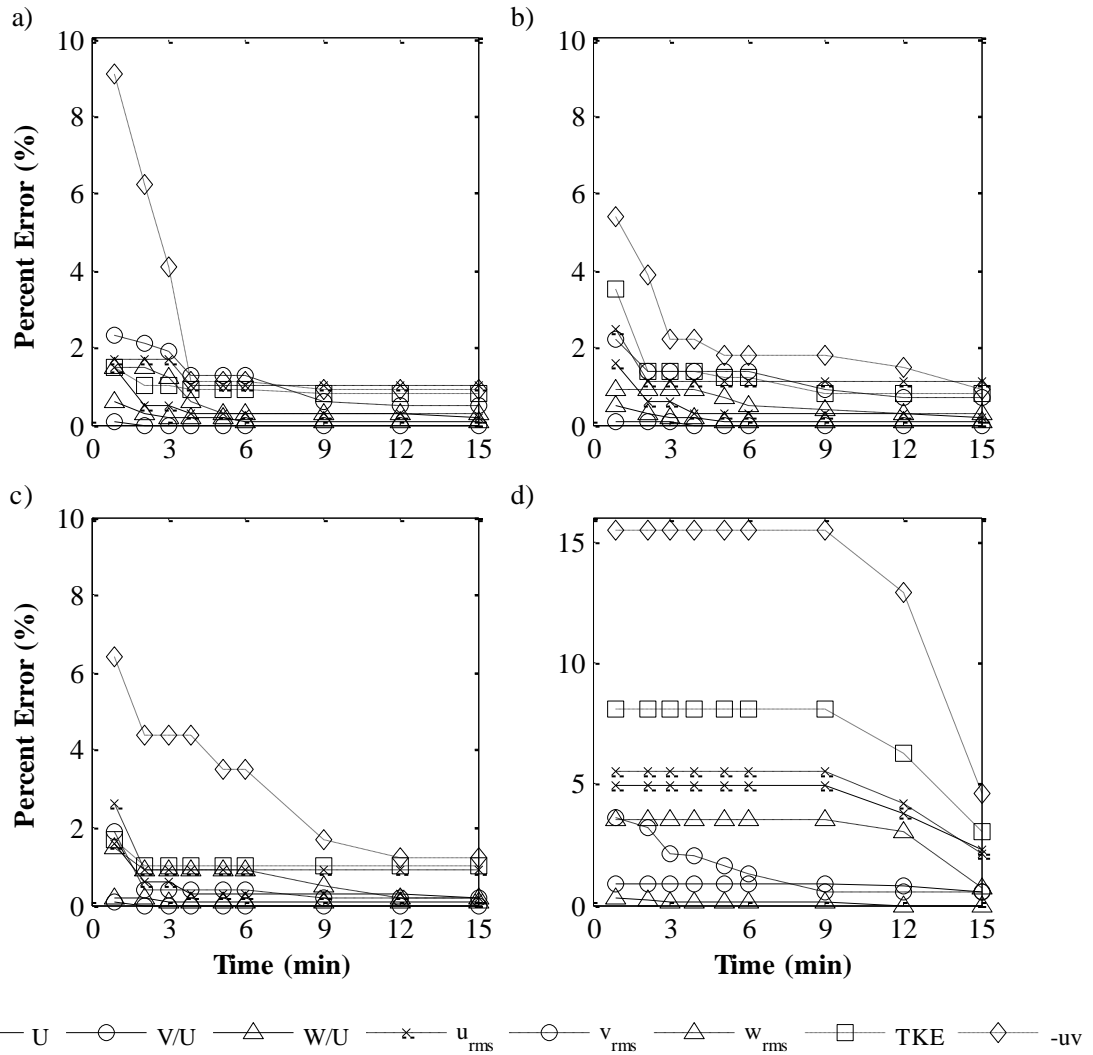


Figure A-3: Convergence test (a) 7 mm, (b) 6 mm, (c) 5 mm, and (d) 4 mm from the bed

As in the free stream region, the bulk mean velocities all converged fairly quickly to low percent errors. In the cells 5mm away and further the percent error after 1 minute was 1.5% and 0.5% after 2 minutes. The error was slightly greater in the 4 mm cell (5%) but took significantly longer to yield lower errors (>10 minutes). The turbulence intensities and turbulent kinetic energy also did not take long to converge. After 1 minute the percent errors were within 3% (except at 4 mm, 5%) and reduced to <1.5% after 4 minutes even at 4 mm from the wall. The  $-\overline{uv}$  statistic

had a more marked convergence point than the other statistics. In nearly all cases  $-\overline{uv}$  reached an asymptote around 4-5 minutes with between 1% and 4% error. Prior to then the error was often 6% or even as much as 12%. The exception, as with all the other statistics, was the cell located 4mm from the wall. Here,  $-\overline{uv}$  had a relatively higher percent error (16%) and did not converge to a lower value until after 10 minutes of sampling, and only after 15 minutes of sampling the percent error is less than 5%.

**Table A-2: Percent error for flow statistics in cells near a boundary.**

<b>7 mm from the bed</b>										
<b>Time (min)</b>	U	V	W	V/U	W/U	urms	vrms	wrms	TKE	-uw
<b>0.9</b>	1.5	182.7	3.5	0.6	0.1	1.7	2.3	1.5	1.5	9.1
<b>2.1</b>	0.5	91.4	1.5	0.3	0.0	1.7	2.1	1.5	1	6.2
<b>3.0</b>	0.5	73.7	1.5	0.2	0.0	1.7	1.9	1.2	1	4.1
<b>3.9</b>	0.3	73.7	1.3	0.2	0.0	1.0	1.3	0.6	0.9	1.1
<b>5.1</b>	0.3	62	1.3	0.2	0.0	1.0	1.3	0.3	0.9	1.1
<b>6.0</b>	0.3	39.3	1.3	0.1	0.0	1.0	1.3	0.3	0.9	1.1
<b>9.0</b>	0.3	26.5	1.0	0.1	0.0	1.0	0.6	0.3	0.8	0.9
<b>12</b>	0.3	26.5	0.8	0.1	0.0	1.0	0.5	0.3	0.8	0.9
<b>15</b>	0.2	26.5	0.6	0.1	0.0	1.0	0.5	0.3	0.8	0.9
<b>6 mm from the bed</b>										
<b>Time (min)</b>	U	V	W	V/U	W/U	urms	vrms	wrms	TKE	-uw
<b>0.9</b>	1.6	367.6	3.4	0.5	0.1	2.5	2.2	0.9	3.5	5.4
<b>2.1</b>	0.6	254.8	2.0	0.3	0.1	1.1	1.4	0.9	1.4	3.9
<b>3.0</b>	0.6	147.5	2.0	0.2	0.1	1.1	1.4	0.9	1.4	2.2
<b>3.9</b>	0.3	133.6	1.0	0.2	0.0	1.1	1.4	0.9	1.4	2.2
<b>5.1</b>	0.3	112	1.0	0.1	0.0	1.1	1.4	0.7	1.2	1.8
<b>6.0</b>	0.3	93.9	1.0	0.1	0.0	1.1	1.4	0.5	1.2	1.8
<b>9.0</b>	0.3	93.9	1.0	0.1	0.0	1.1	0.9	0.4	0.8	1.8
<b>12</b>	0.3	93.9	1.0	0.1	0.0	1.1	0.7	0.3	0.8	1.5
<b>15</b>	0.2	93.9	0.7	0.1	0.0	1.1	0.7	0.3	0.8	0.9

<b>5 mm from the bed</b>										
<b>Time (min)</b>	<b>U</b>	<b>V</b>	<b>W</b>	<b>V/U</b>	<b>W/U</b>	<b>u<sub>rms</sub></b>	<b>v<sub>rms</sub></b>	<b>w<sub>rms</sub></b>	<b>TKE</b>	<b>-uw</b>
<b>0.9</b>	1.6	94.0	2.4	0.2	0.1	2.6	1.9	1.5	1.7	6.4
<b>2.1</b>	0.6	70.6	1.8	0.2	0.0	0.9	0.4	0.9	1.0	4.4
<b>3.0</b>	0.6	51.0	1.8	0.1	0.0	0.9	0.4	0.9	1.0	4.4
<b>3.9</b>	0.3	51.0	1.5	0.1	0.0	0.9	0.4	0.9	1.0	4.4
<b>5.1</b>	0.3	51.0	1.5	0.1	0.0	0.9	0.4	0.9	1.0	3.5
<b>6.0</b>	0.3	51.0	1.5	0.1	0.0	0.9	0.4	0.9	1.0	3.5
<b>9.0</b>	0.3	51.0	1.5	0.1	0.0	0.9	0.2	0.5	1.0	1.7
<b>12.0</b>	0.3	48.6	0.6	0.1	0.0	0.9	0.2	0.2	1.0	1.2
<b>15.0</b>	0.2	37.8	0.3	0.1	0.0	0.9	0.2	0.2	1.0	1.2
<b>4 mm from the bed</b>										
<b>Time (min)</b>	<b>U</b>	<b>V</b>	<b>W</b>	<b>V/U</b>	<b>W/U</b>	<b>u<sub>rms</sub></b>	<b>v<sub>rms</sub></b>	<b>w<sub>rms</sub></b>	<b>TKE</b>	<b>-uw</b>
<b>0.9</b>	4.9	244	130	0.3	0.9	5.5	3.6	3.5	8.1	15.5
<b>2.1</b>	4.9	130	130	0.2	0.9	5.5	3.2	3.5	8.1	15.5
<b>3.0</b>	4.9	102	130	0.1	0.9	5.5	2.1	3.5	8.1	15.5
<b>3.9</b>	4.9	96.9	130	0.1	0.9	5.5	2.0	3.5	8.1	15.5
<b>5.1</b>	4.9	59.4	130	0.1	0.9	5.5	1.6	3.5	8.1	15.5
<b>6.0</b>	4.9	47.9	130	0.1	0.9	5.5	1.3	3.5	8.1	15.5
<b>9.0</b>	4.9	43.8	130	0.1	0.9	5.5	0.5	3.5	8.1	15.5
<b>12.0</b>	3.8	38.1	114	0.0	0.8	4.2	0.5	3.0	6.3	12.9
<b>15.0</b>	2.3	24.0	68.0	0.0	0.5	2.1	0.5	0.7	3.0	4.6

#### **A.4 Summary**

Through the tests and analysis described above the following decisions were made:

1. The adaptive ping algorithm will be used for all further testing owing to its ability to reduce or eliminate the presence of weak cells
2. The sampling frequency will be set to 100 Hz because no time savings would be realized by changing it. Additionally, 100 Hz is the maximum frequency the Vectino II ADV can sample so it will provide greater resolution of the time series and produce the tightest confidence intervals about the mean.
3. Samples will be collected for a duration of 3 minutes.

## Appendix B: Symmetry Analysis

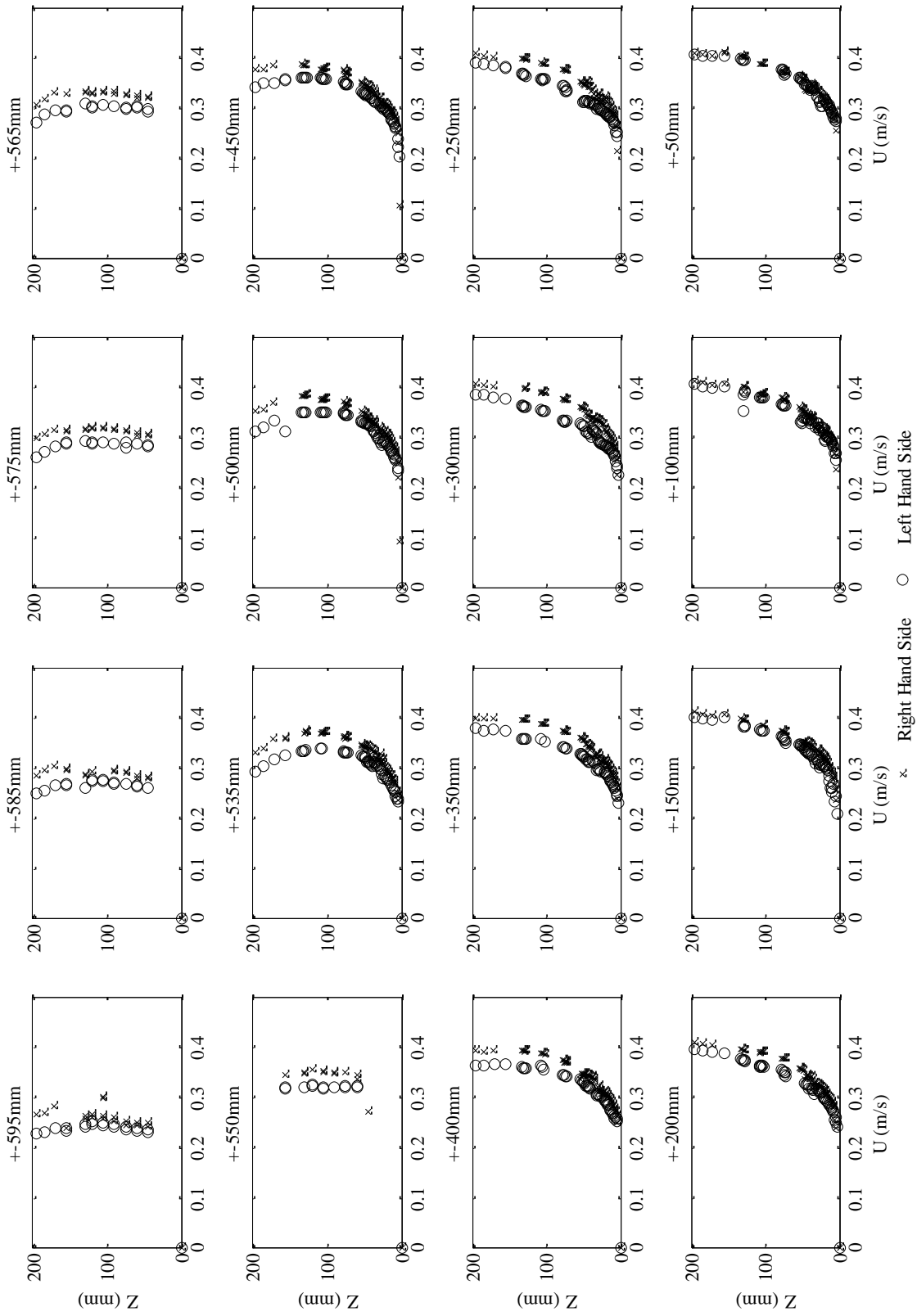


Figure B-1: Open Channel Symmetry Analysis: Streamwise Velocity

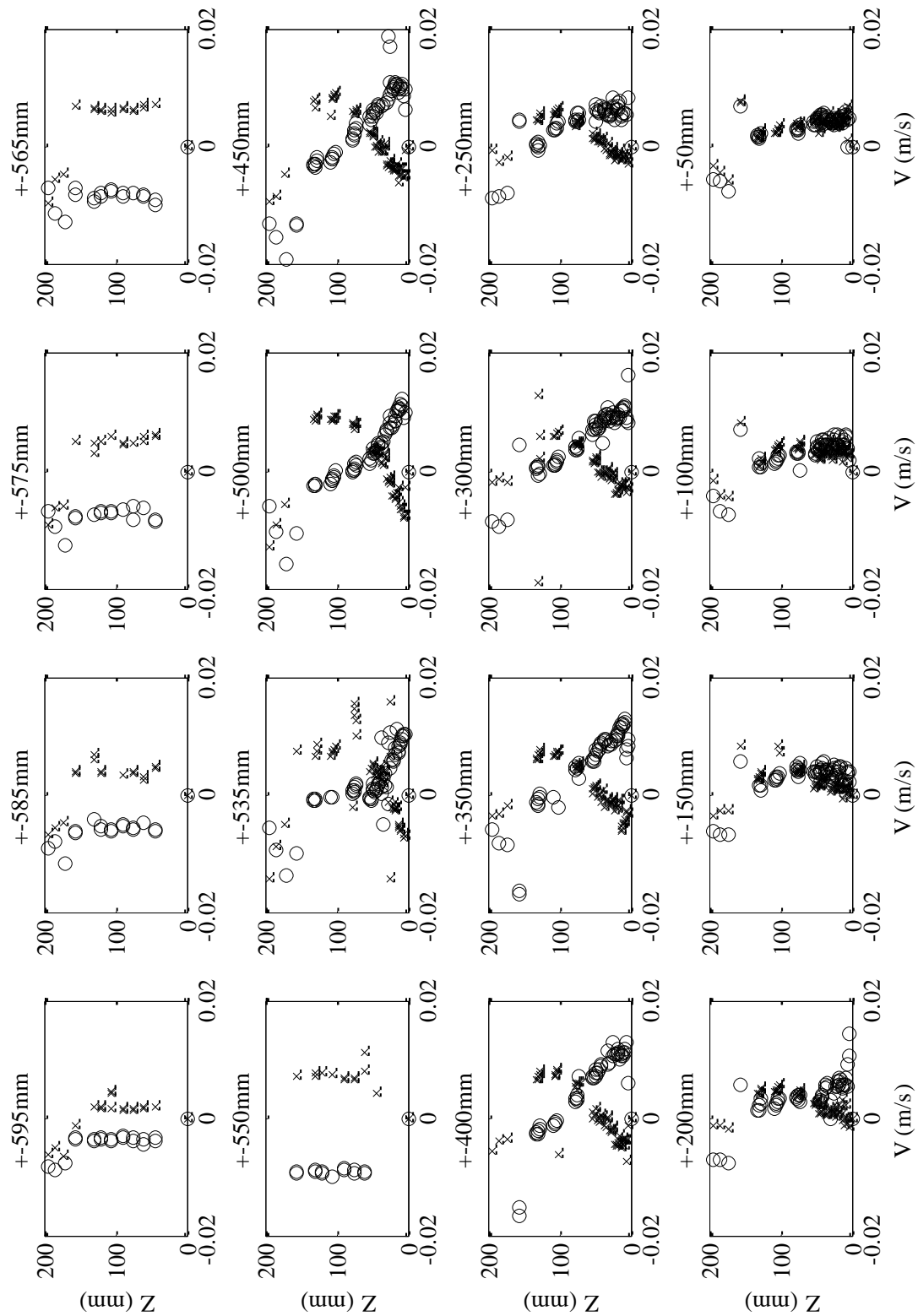


Figure B-2: Open Channel Symmetry Analysis: Spanwise Velocity

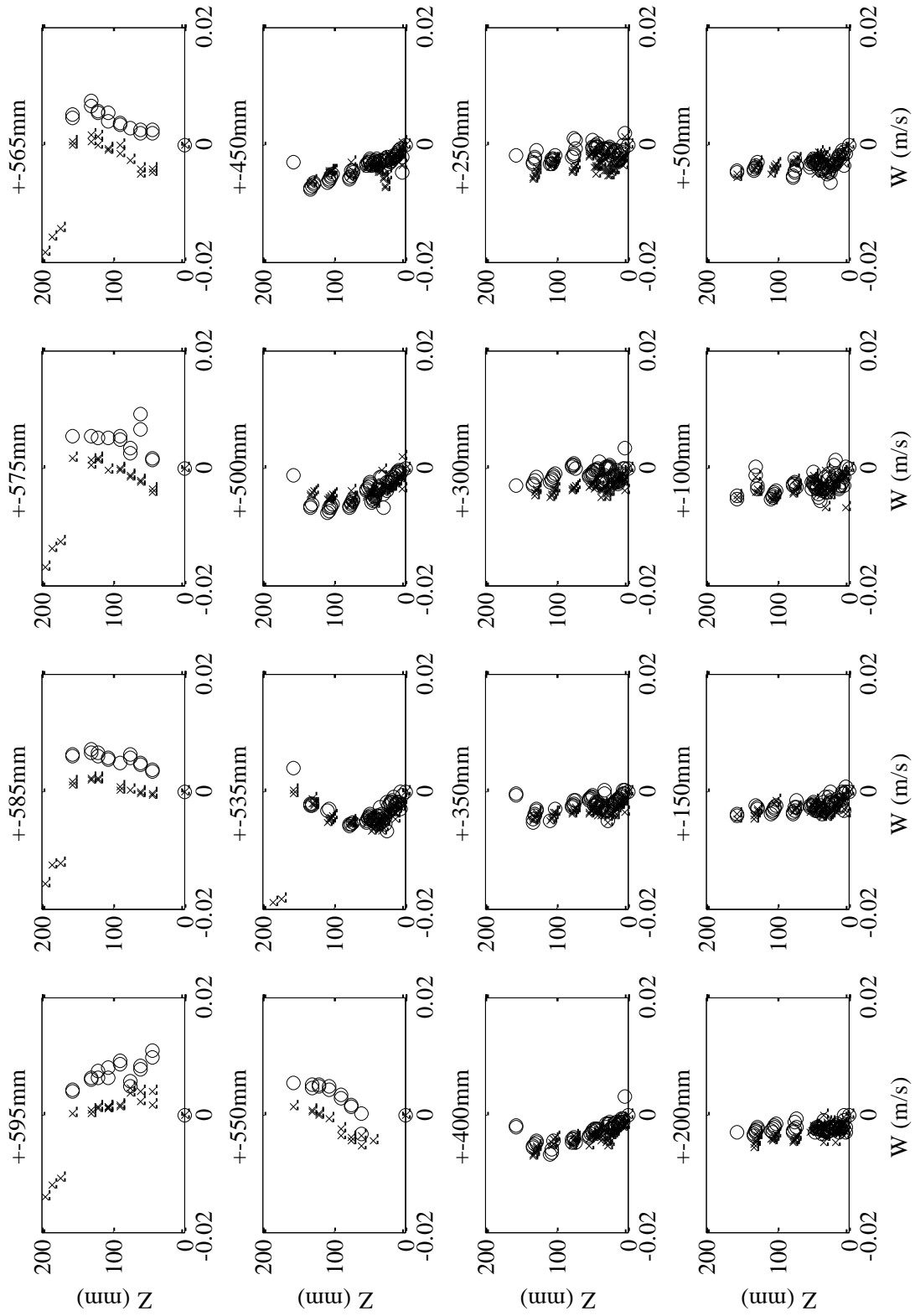


Figure B-3: Open Channel Symmetry Analysis: Vertical Velocity

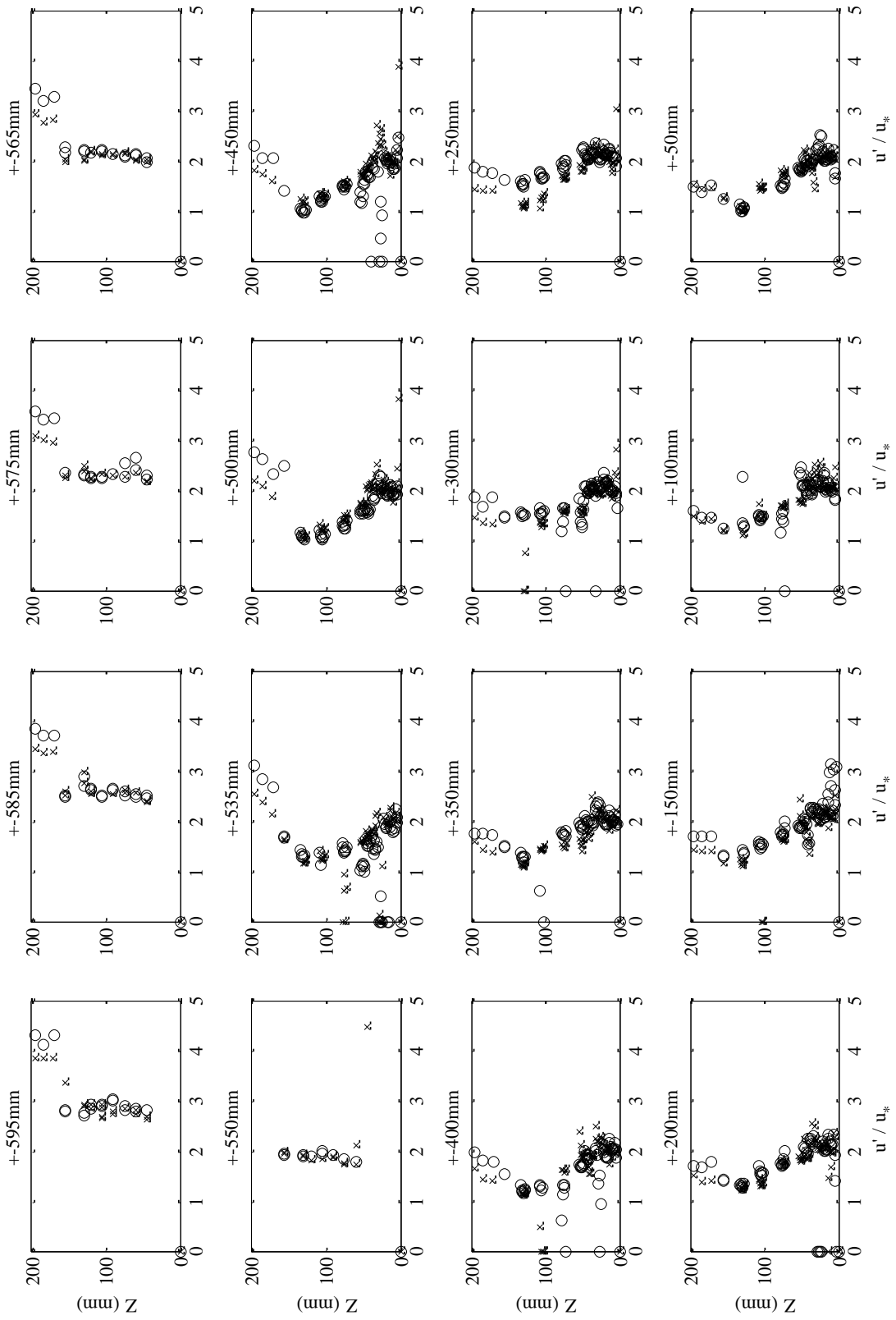


Figure B-4: Open Channel Symmetry Analysis: Streamwise Turbulence Intensity

x Right Hand Side    o Left Hand Side

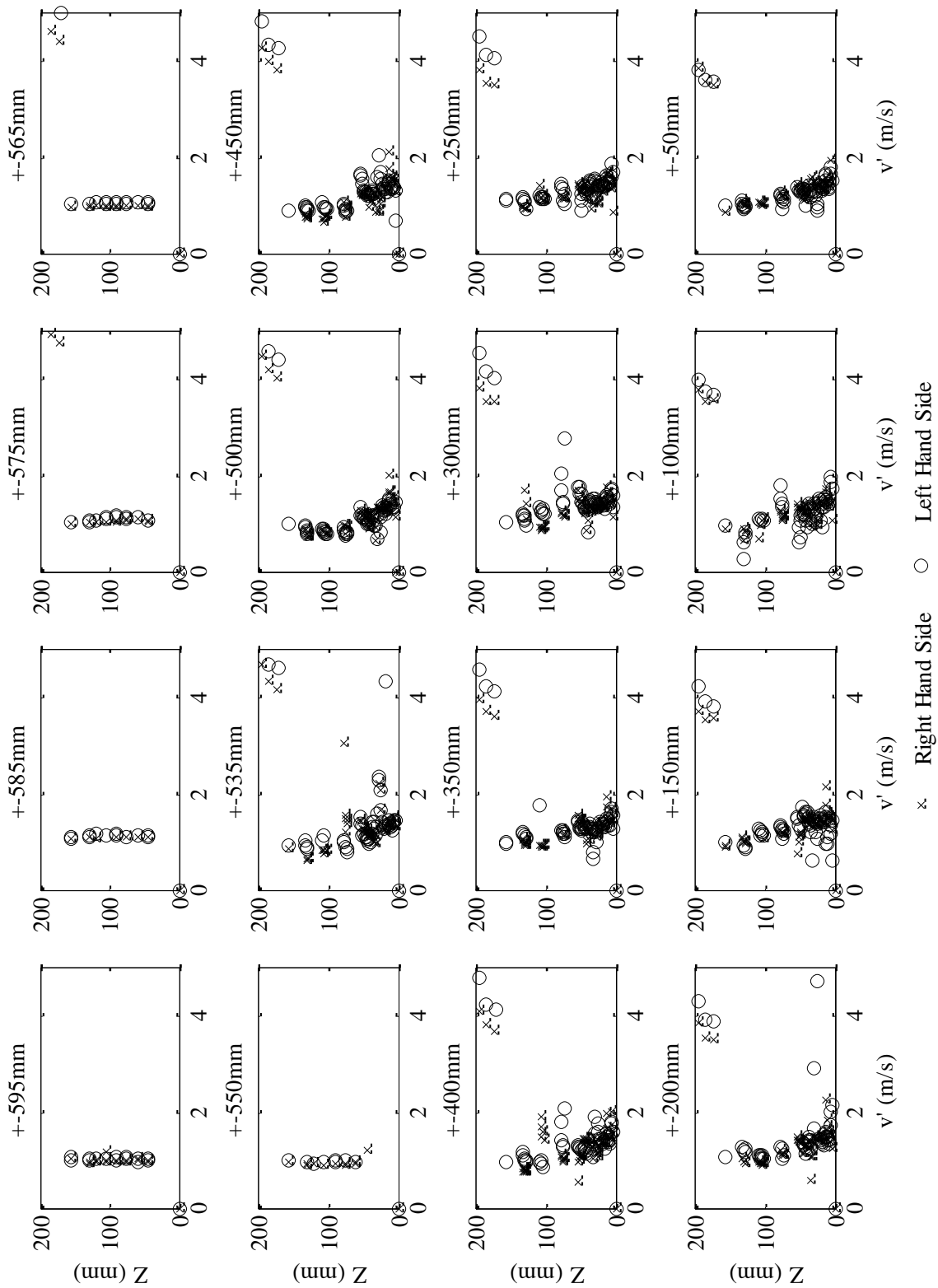


Figure B-5: Open Channel Symmetry Analysis: Spanwise Turbulence Intensity

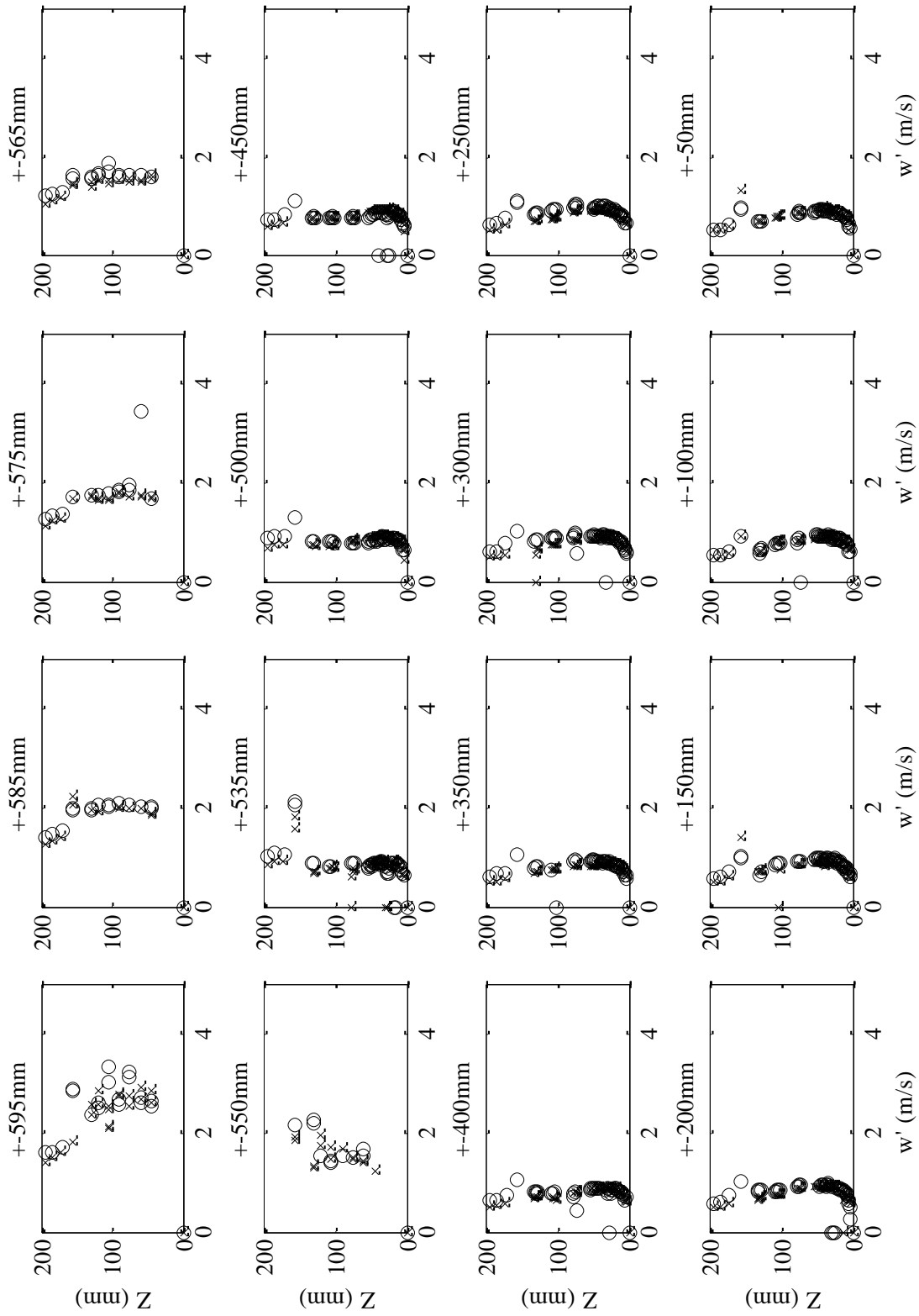
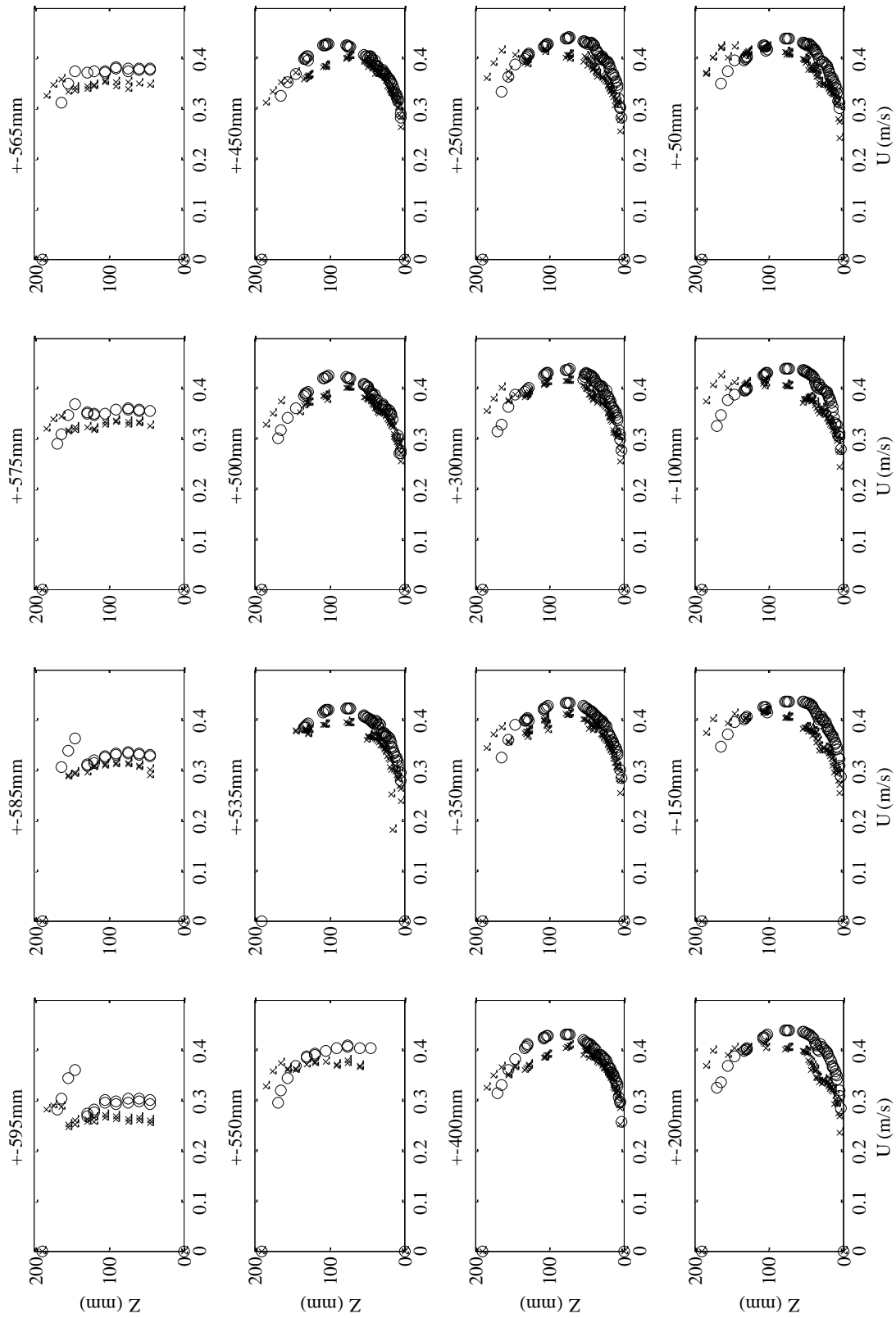


Figure B-6: Open Channel Symmetry Analysis: Vertical Turbulence Intensity



**Figure B-7: Covered Channel Symmetry Analysis: Streamwise Velocity**  
 x Right Hand Side    o Left Hand Side

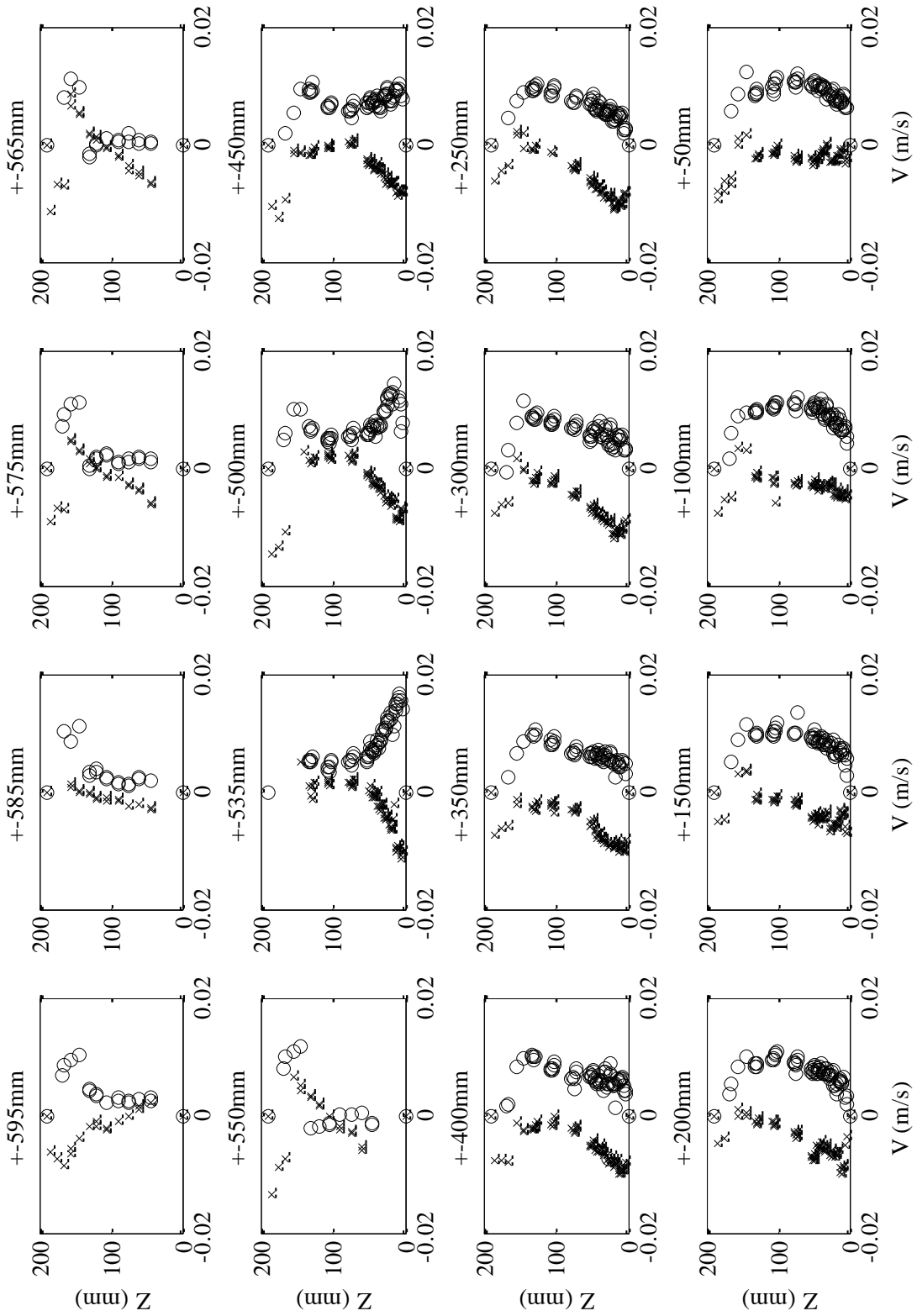


Figure B-8: Covered Channel Symmetry Analysis: Spanwise Velocity

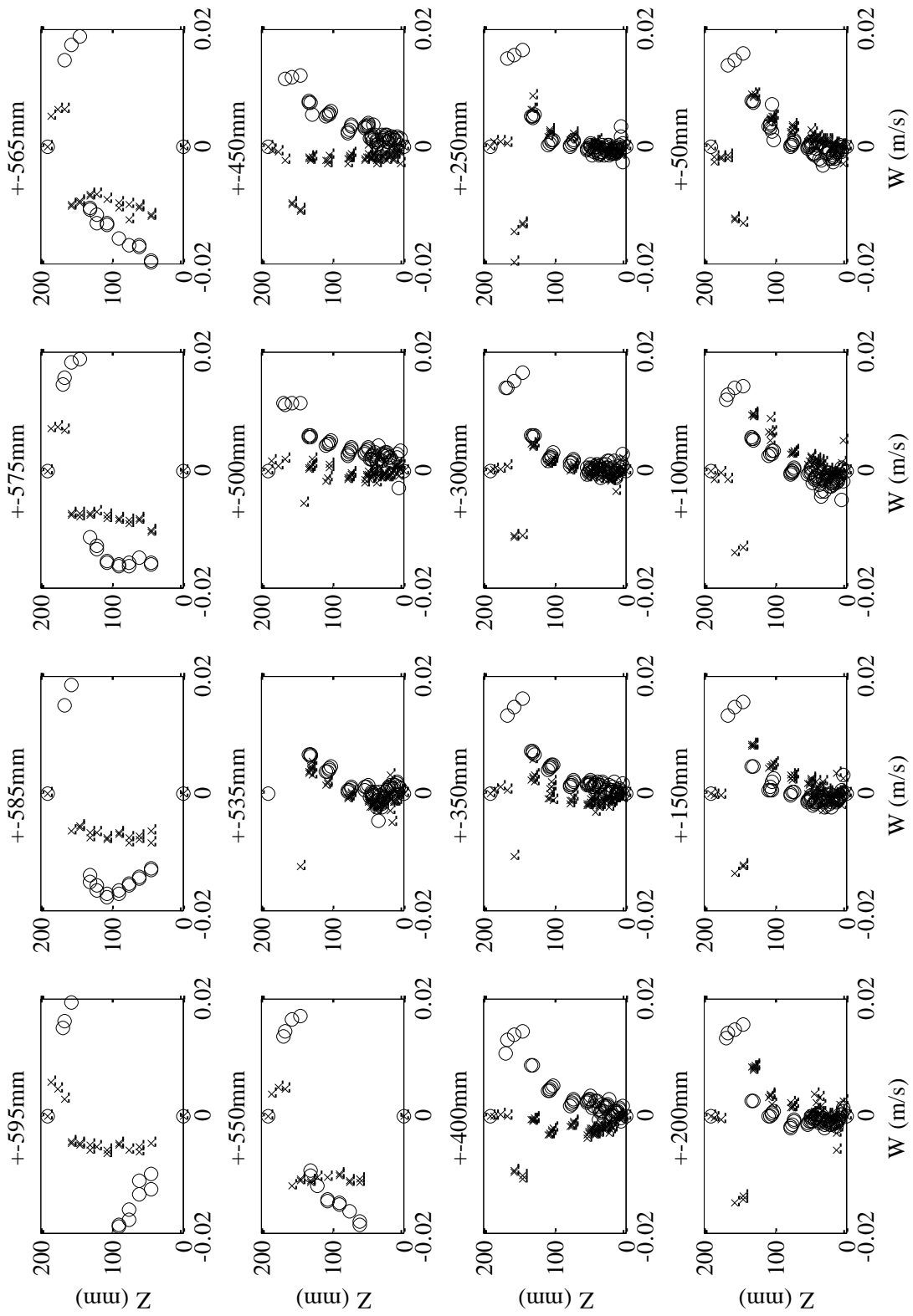
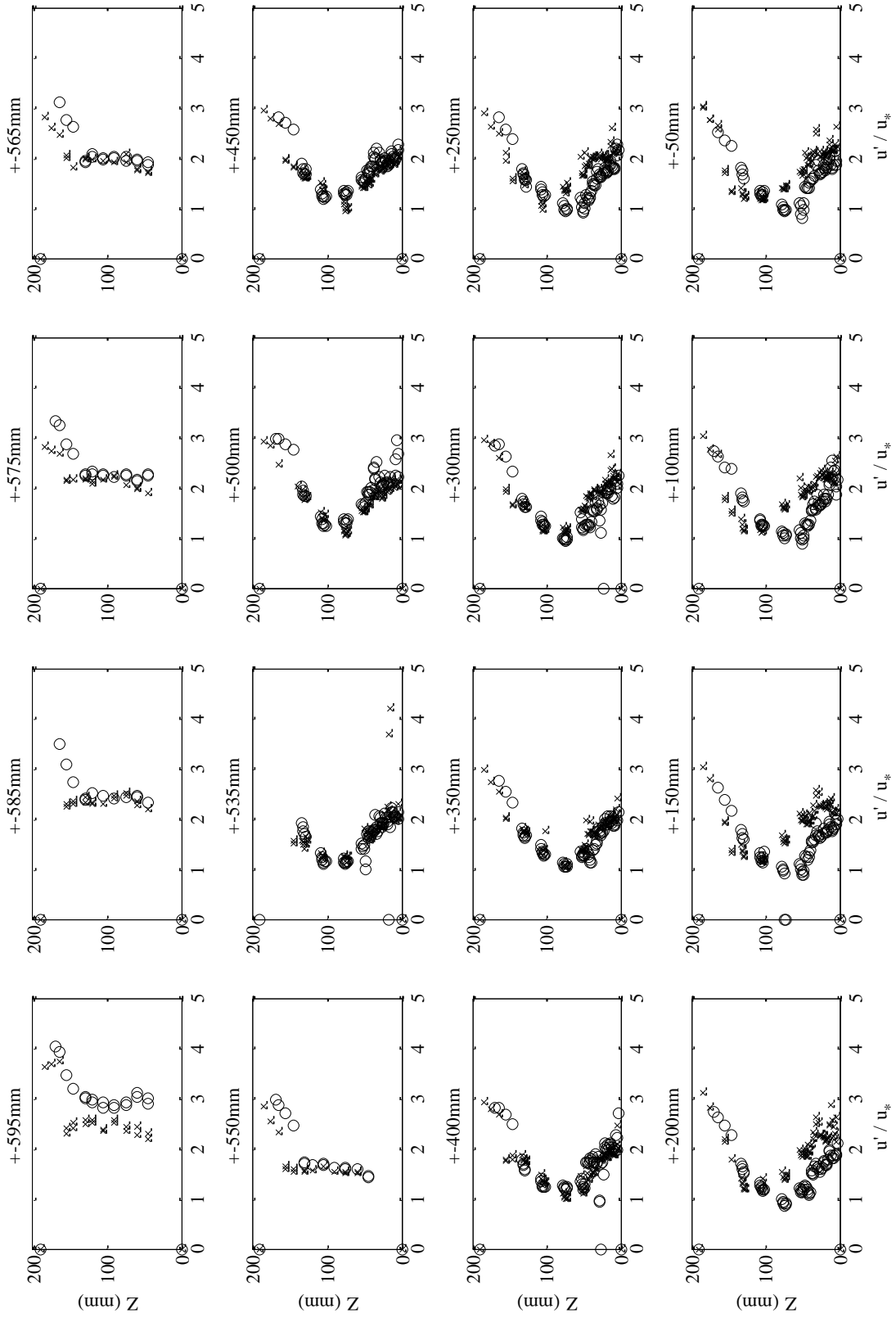


Figure B-9: Covered Channel Symmetry Analysis: Vertical Velocity



**Figure B-10: Covered Channel Symmetry Analysis: Streamwise Turbulence Intensity**

x Right Hand Side    o Left Hand Side

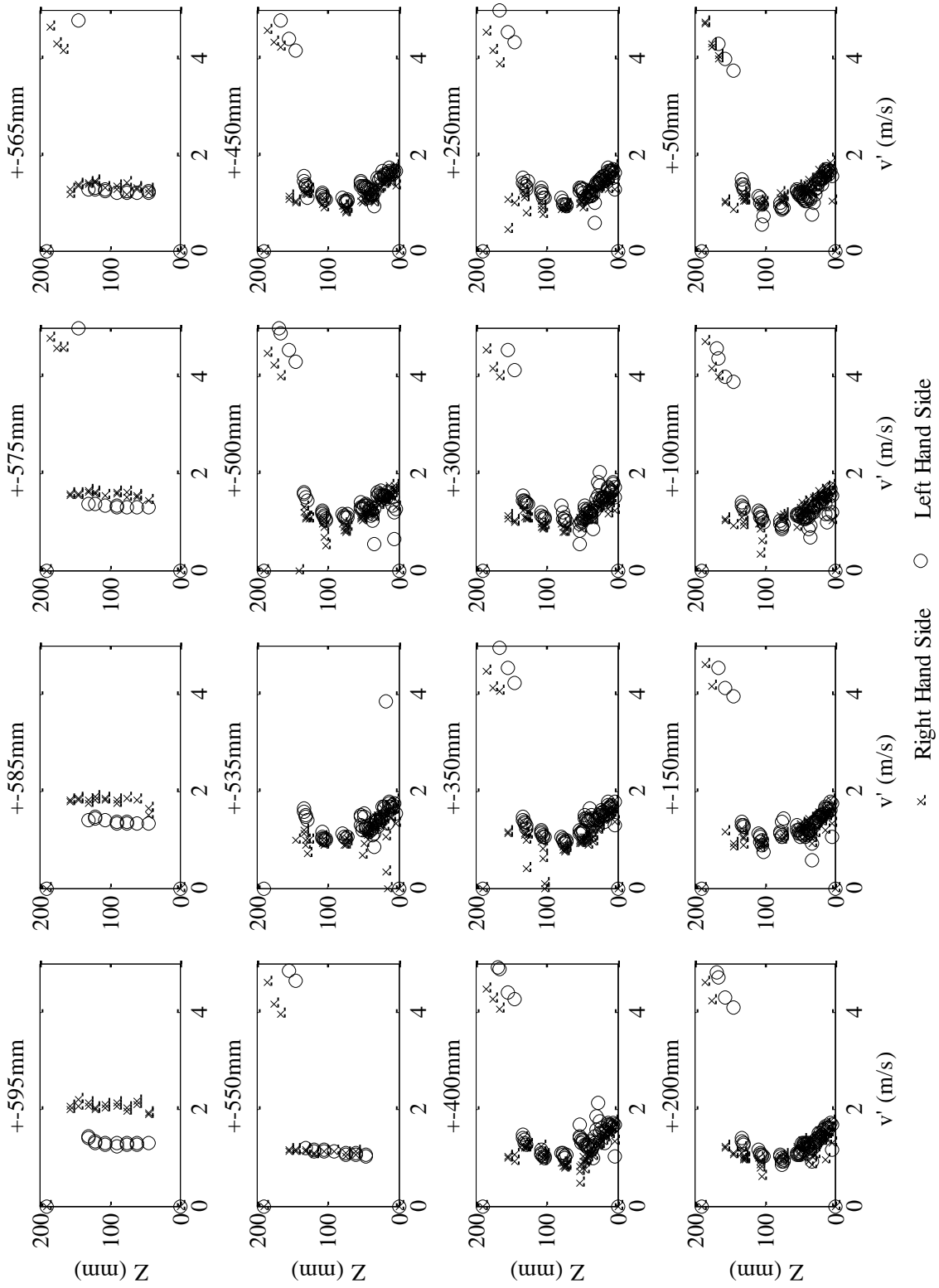


Figure B-11: Covered Channel Symmetry Analysis: Spanwise Turbulence Intensity

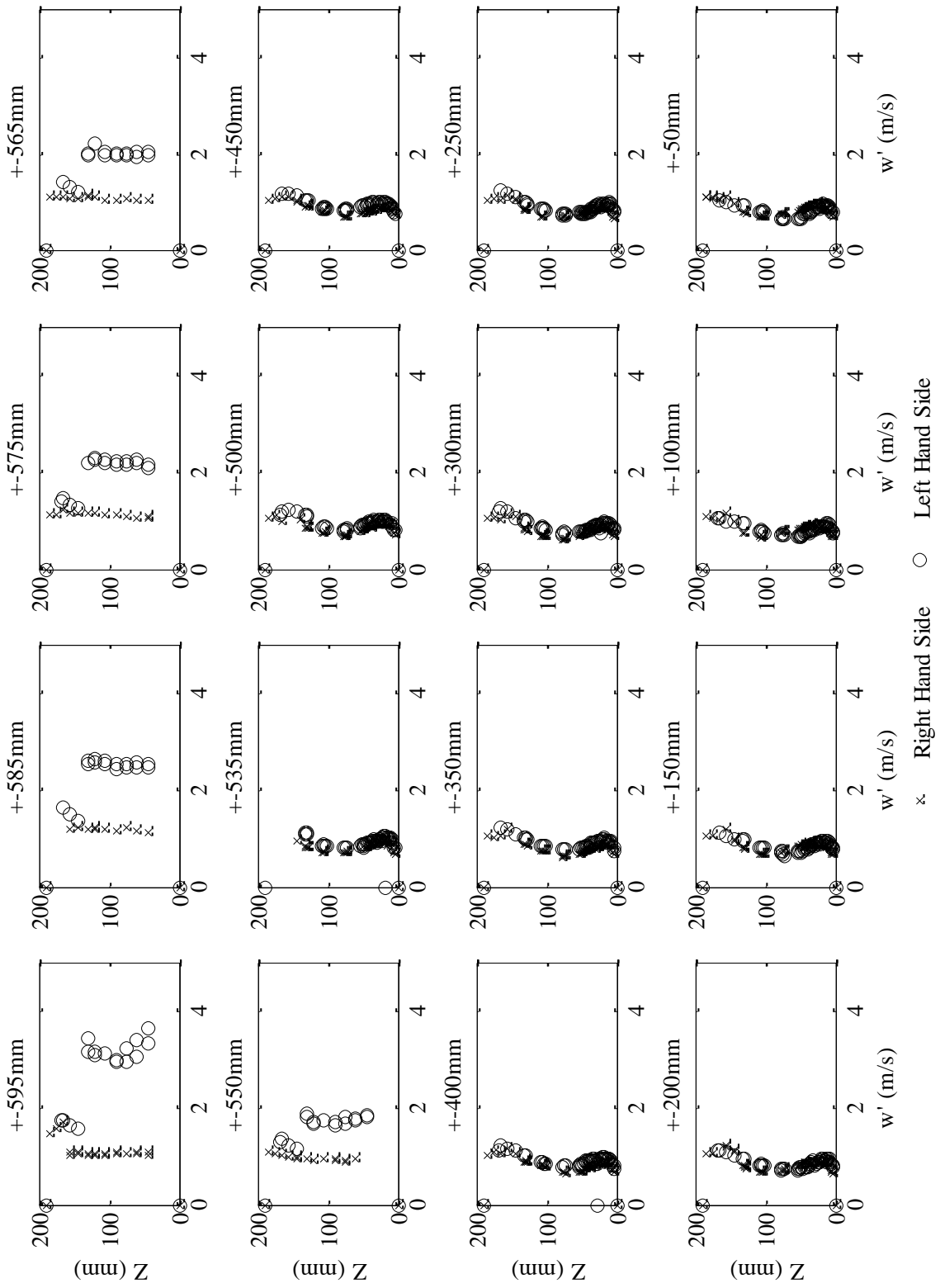


Figure B-12: Covered Channel Symmetry Analysis: Vertical Turbulence Intensity

## Appendix C: Supplemental Results Figures

### C.1 Water Surface Profiles

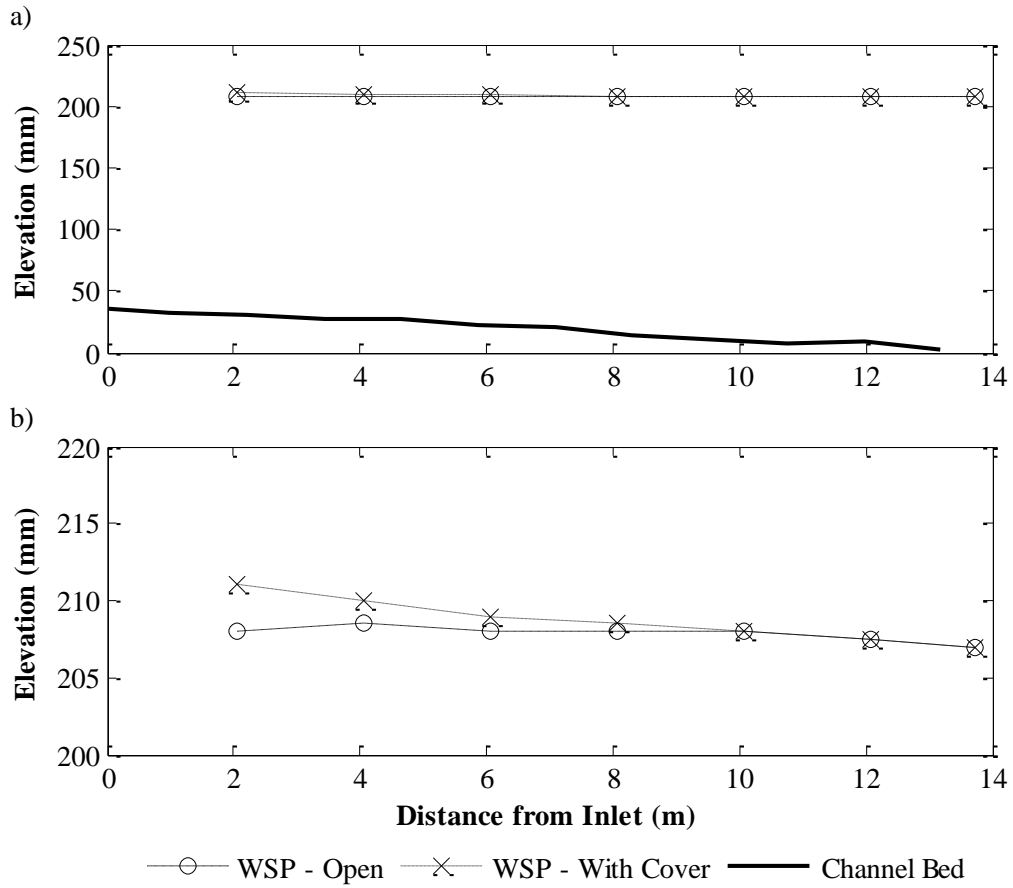
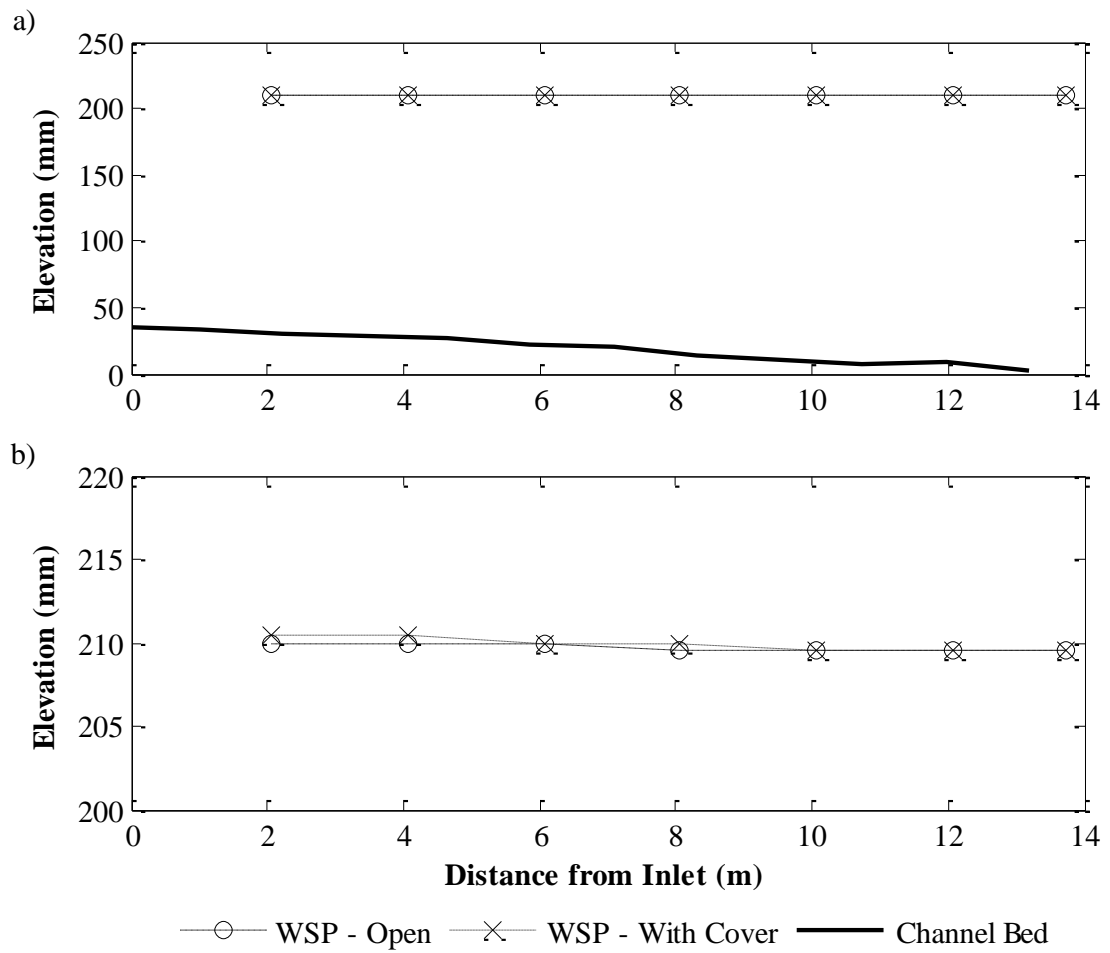


Figure C-1: Water surface profiles from the Base Experiment showing a) bed included, b) water surface profiles only.



**Figure C-2: Water surface profiles from the Low Froude Experiment showing a) bed included, b) water surface profiles only.**

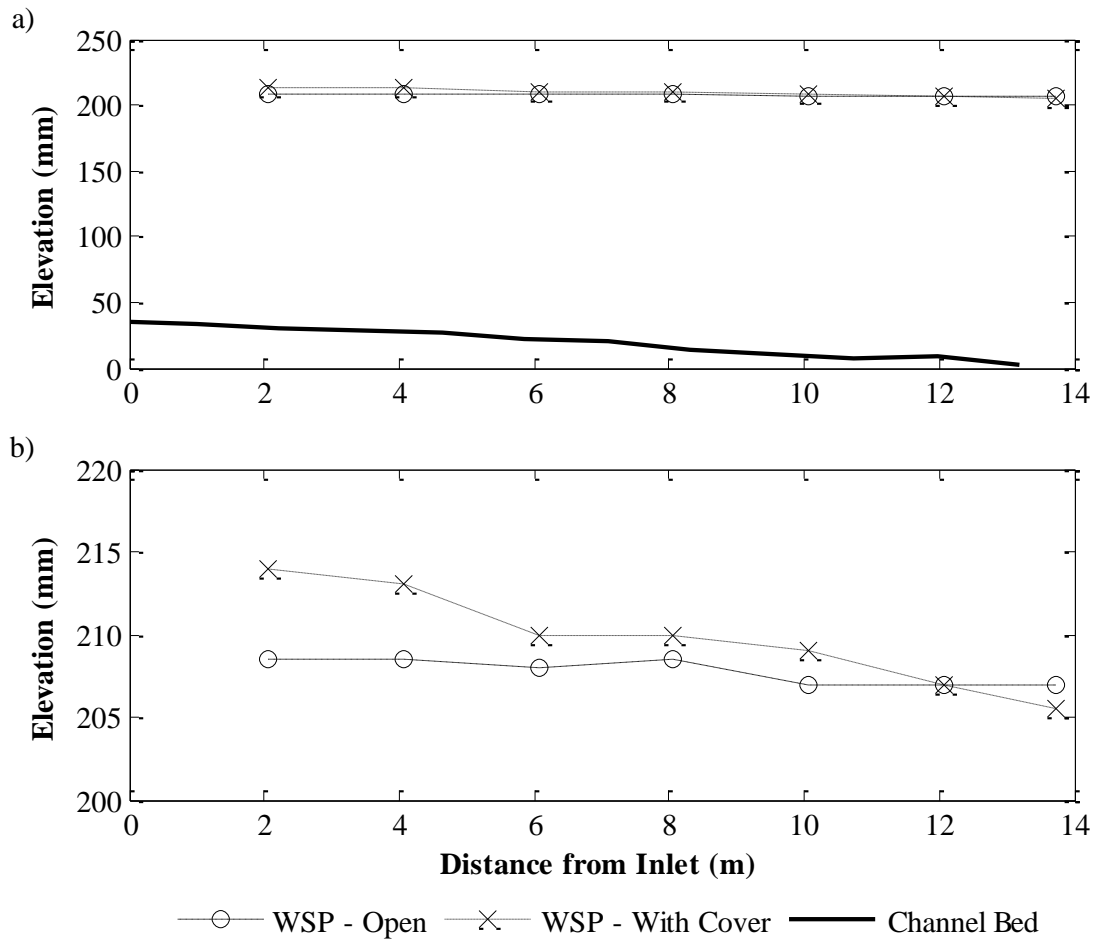


Figure C-3: Water surface profiles from the High Froude Experiment showing a) bed included, b) water surface profiles only.

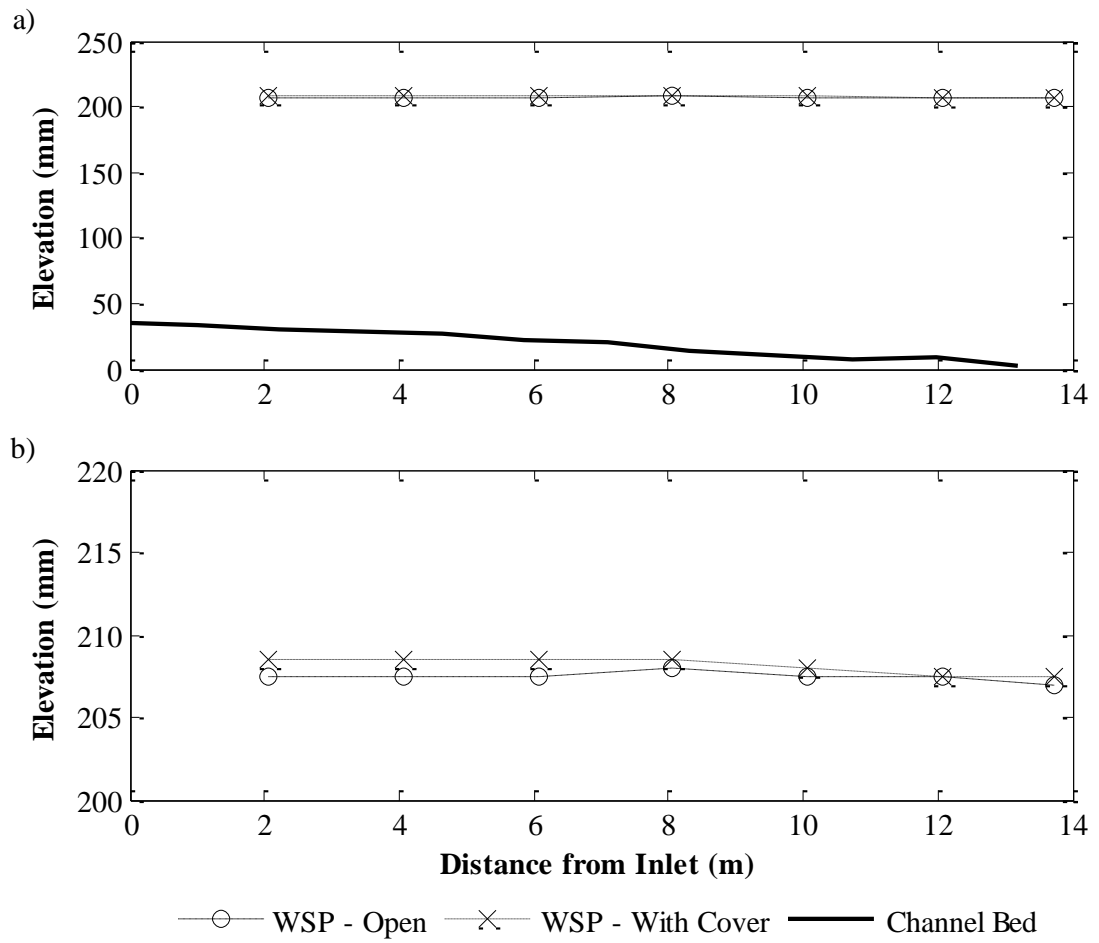


Figure C-4: Water surface profiles from the 25% Coverage Experiment showing a) bed included, b) water surface profiles only.

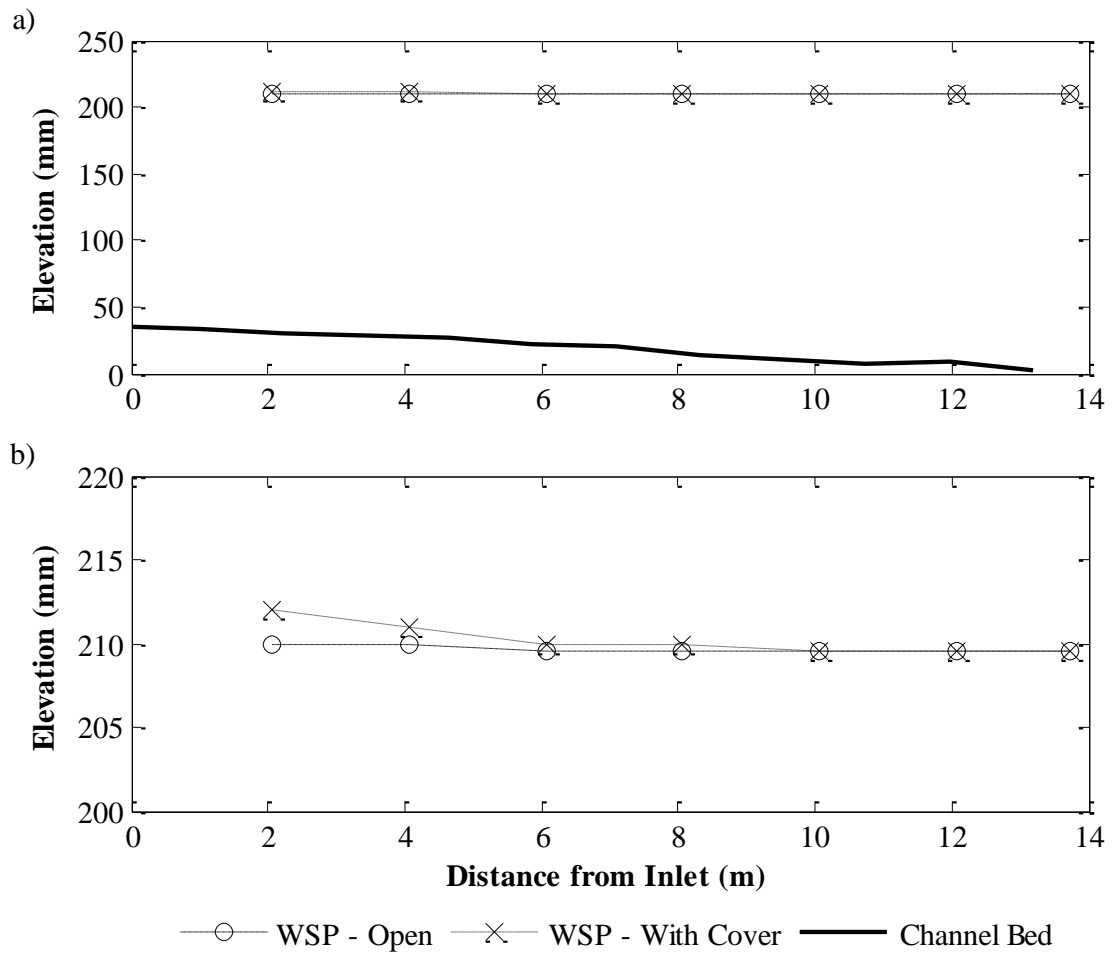


Figure C-5: Water surface profiles from the 50% Coverage Experiment showing a) bed included, b) water surface profiles only.

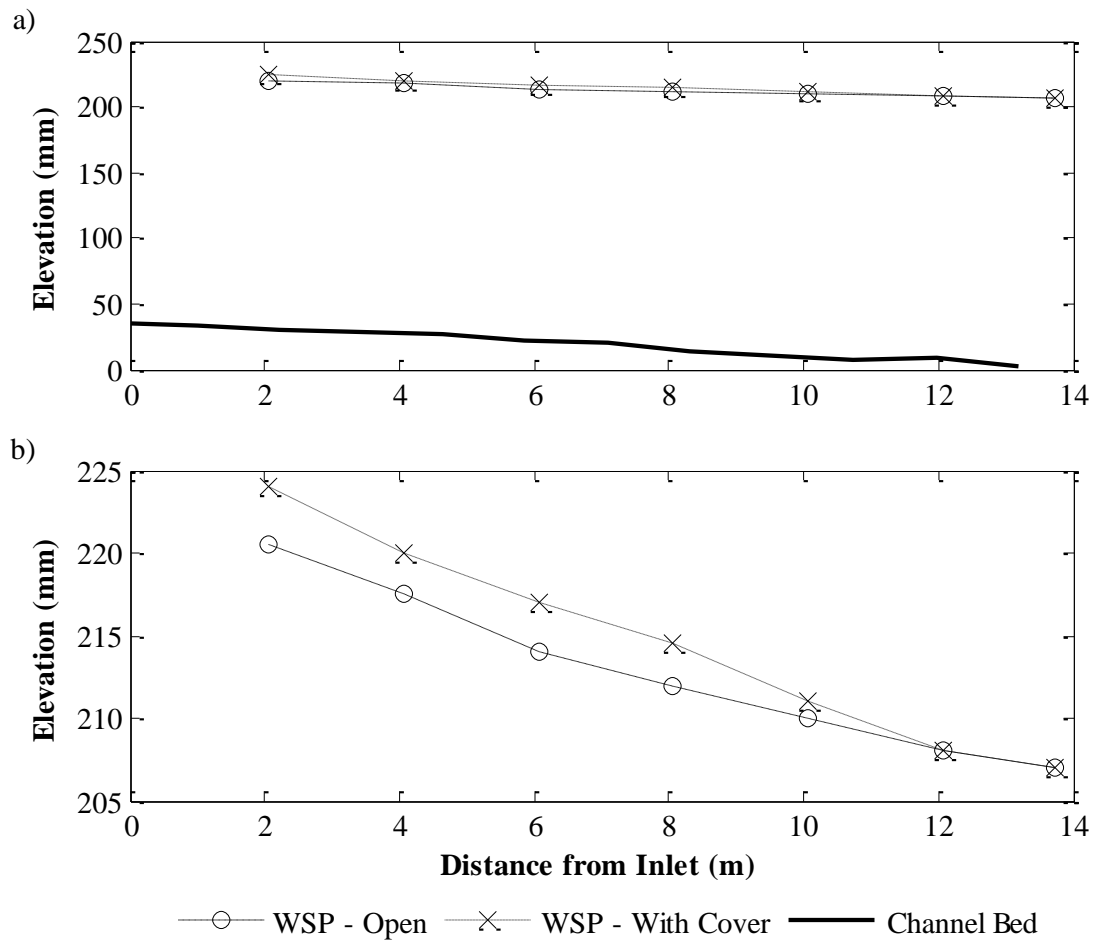


Figure C-6: Water surface profiles from the Rough Bed Experiment showing a) bed included, b) water surface profiles only.

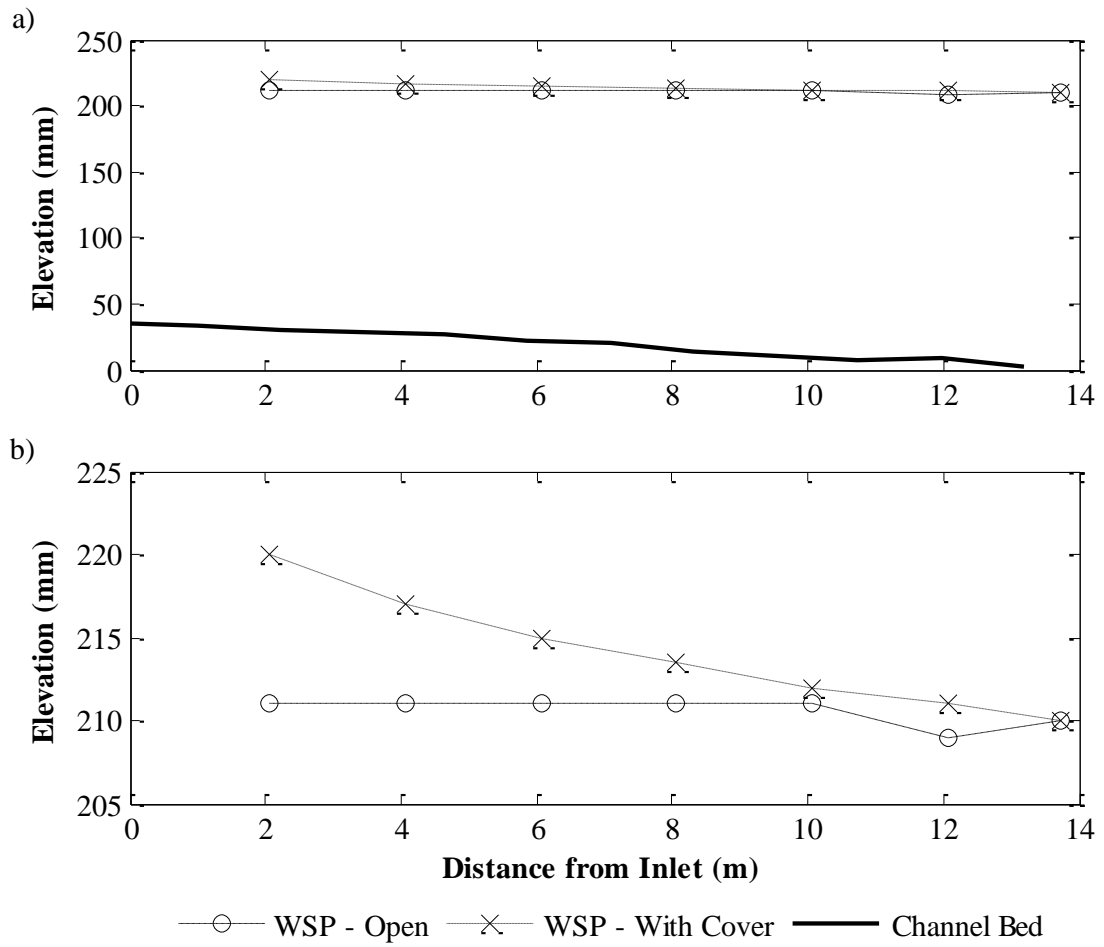


Figure C-7: Water surface profiles from the Rough Ice Experiment showing a) bed included, b) water surface profiles only.

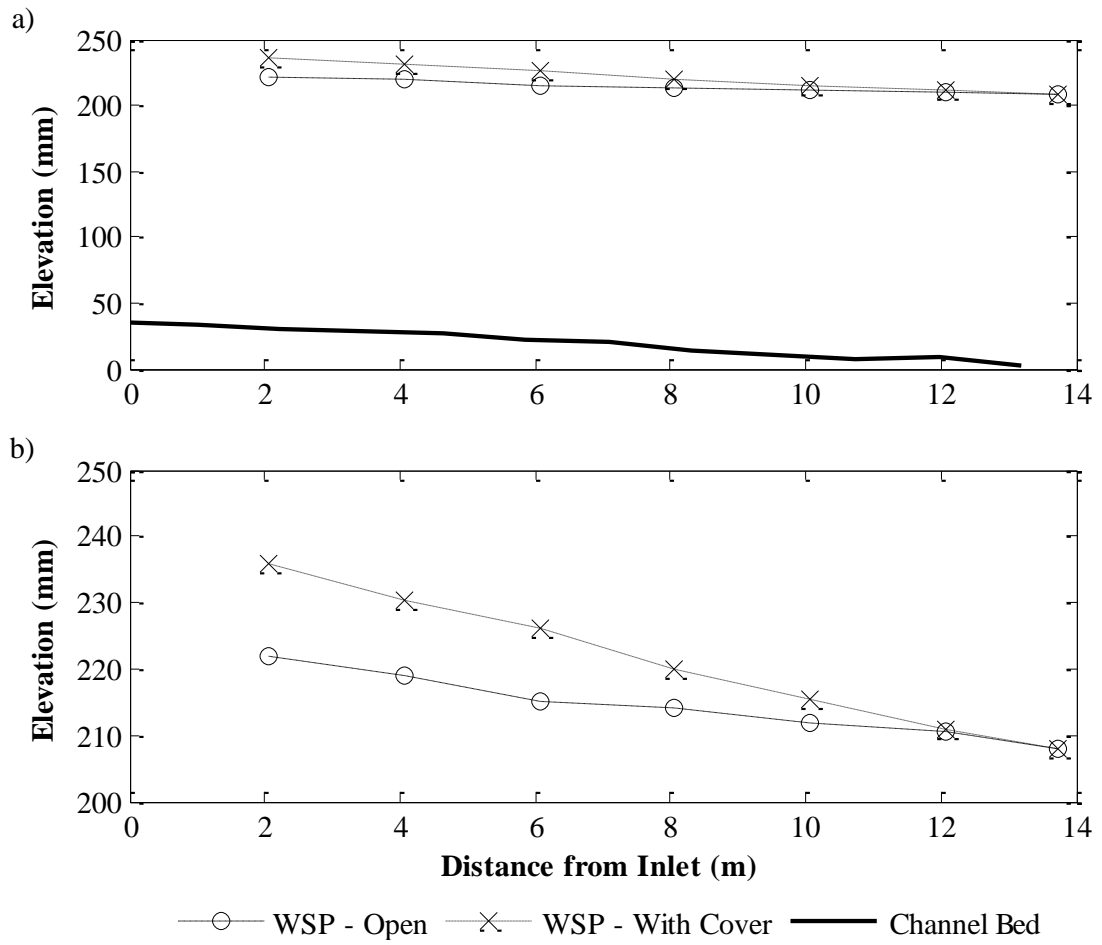


Figure C-8: Water surface profiles from the Rough Bed - Rough Ice Experiment showing a) bed included, b) water surface profiles only.

## C.2 Secondary Circulation

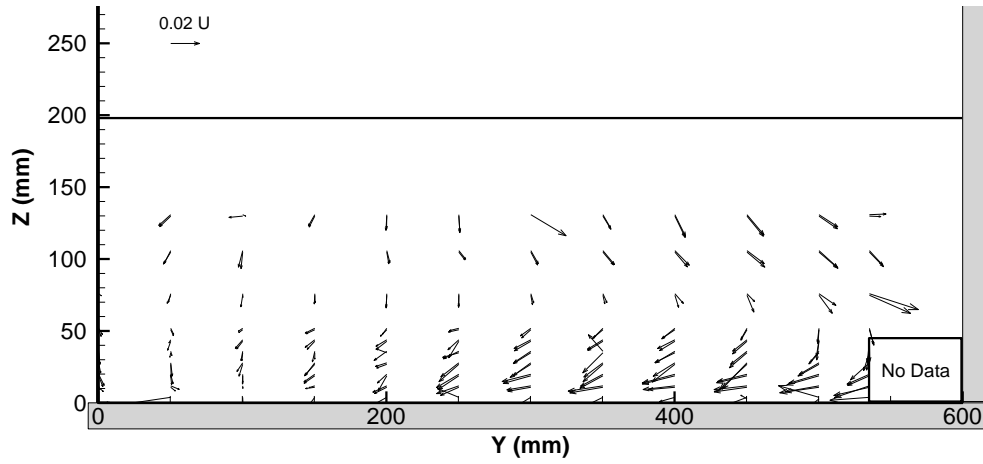


Figure C-9: Secondary circulation vectors for the Open Channel Experiment.

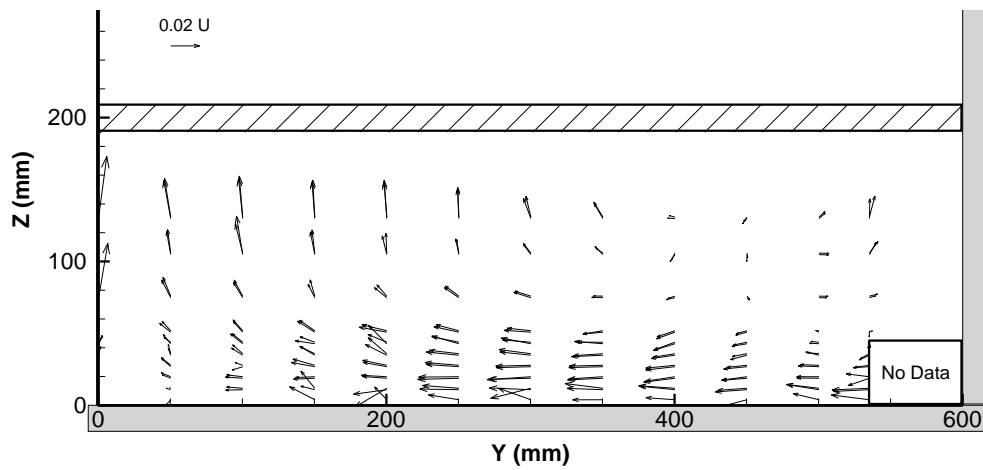


Figure C-10: Secondary circulation vectors for the Covered Channel Experiment.

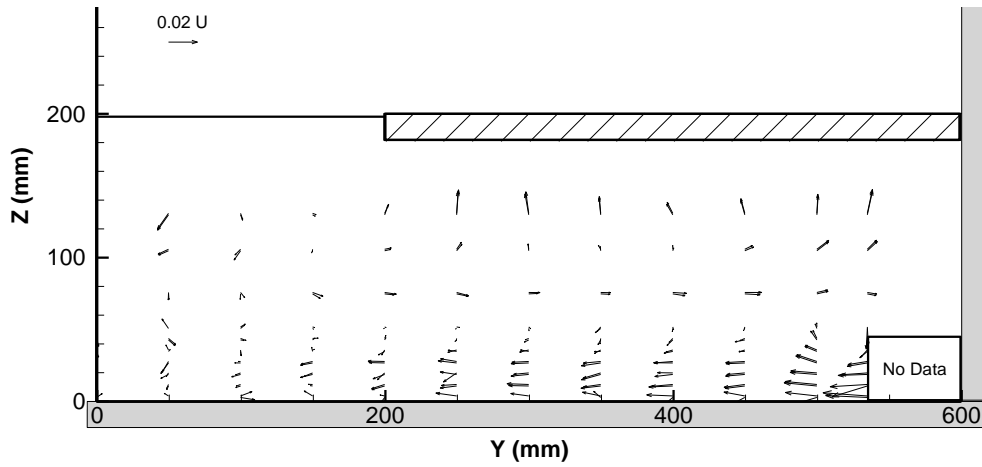


Figure C-11: Secondary circulation vectors for the Base Experiment.

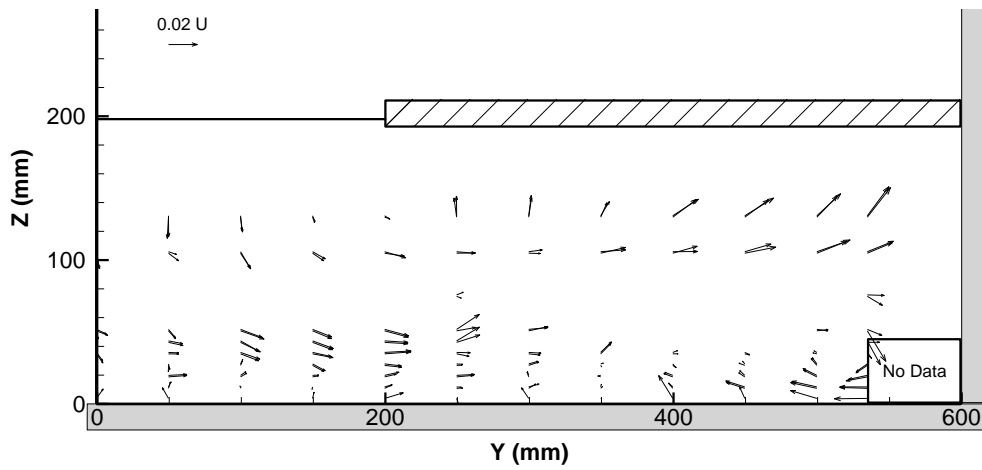


Figure C-12: Secondary circulation vectors for the Low Froude Experiment.

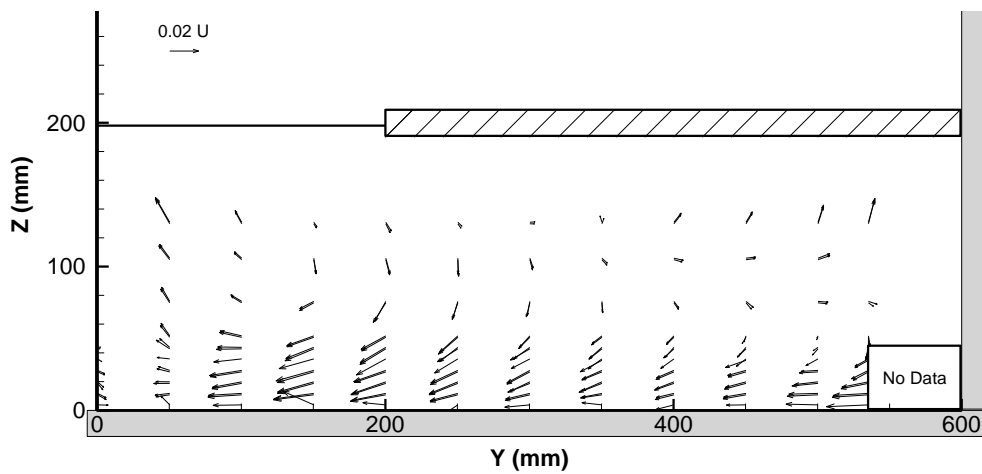


Figure C-13: Secondary circulation vectors for the High Froude Experiment.

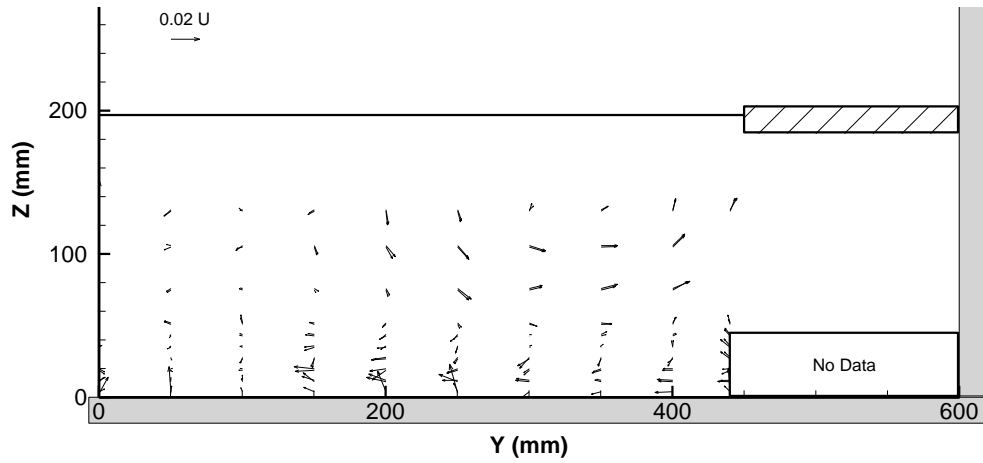


Figure C-14: Secondary circulation vectors for the 25% Coverage Experiment.

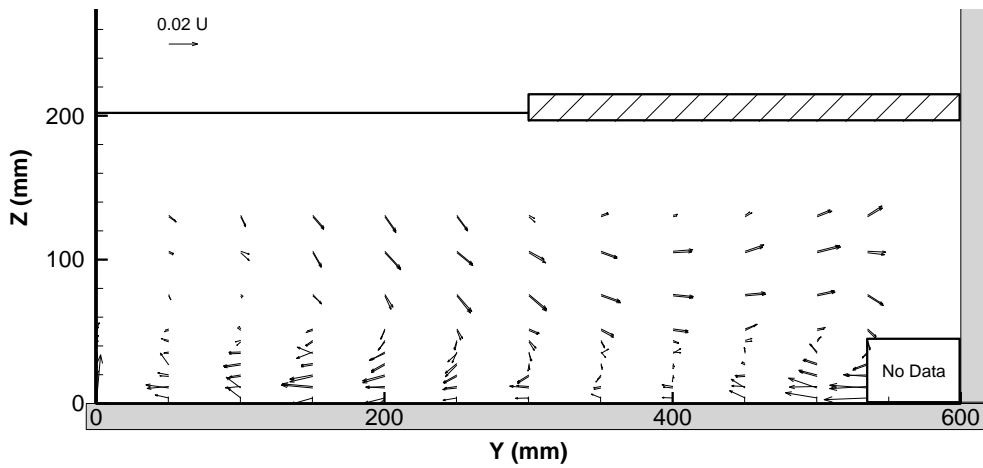


Figure C-15: Secondary circulation vectors for the 50% Coverage Experiment.

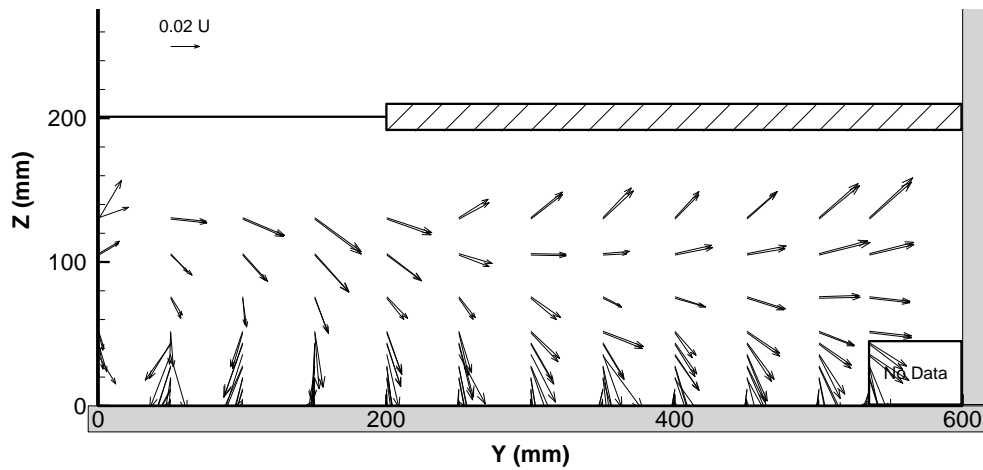


Figure C-16: Secondary circulation vectors for the Rough Bed Experiment.

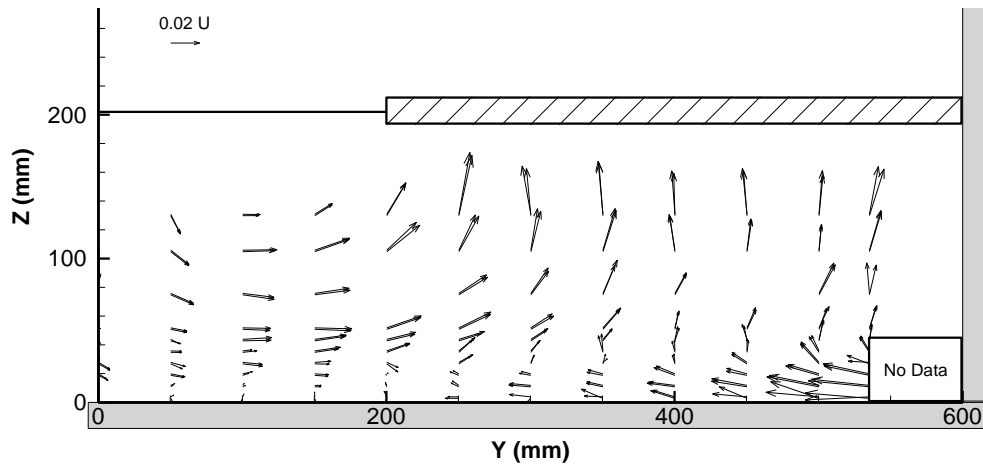


Figure C-17: Secondary circulation vectors for the Rough Ice Experiment.

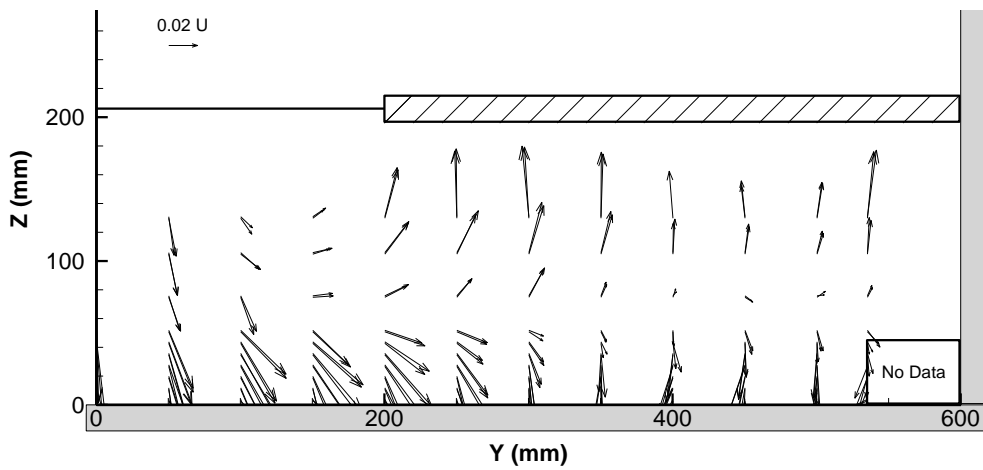


Figure C-18: Secondary circulation vectors for the Rough Bed - Rough Ice Experiment.

### C.3 Discharge Distribution - Cumulative

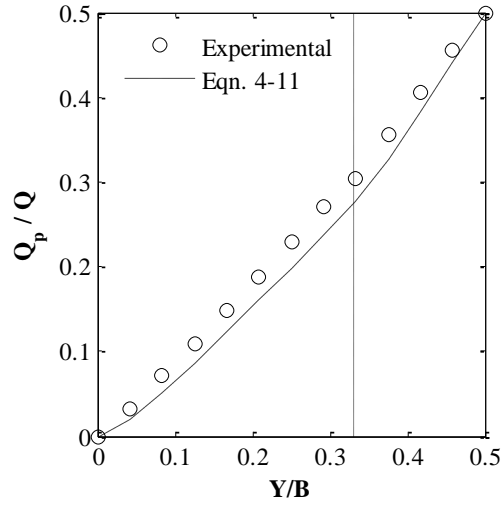


Figure C-19: Cumulative discharge distribution for the Base Experiment.

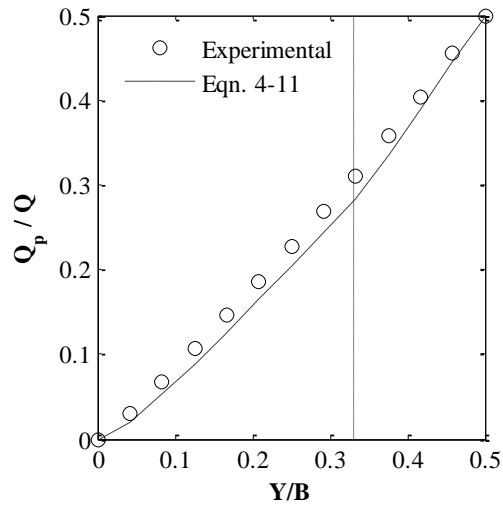


Figure C-20: Cumulative discharge distribution for the Low Froude Experiment.

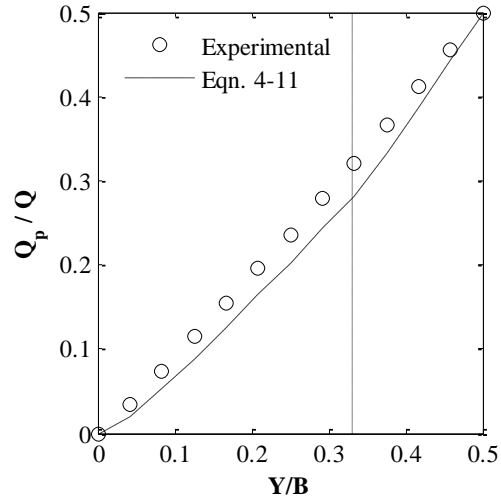


Figure C-21: Cumulative discharge distribution for the High Froude Experiment.

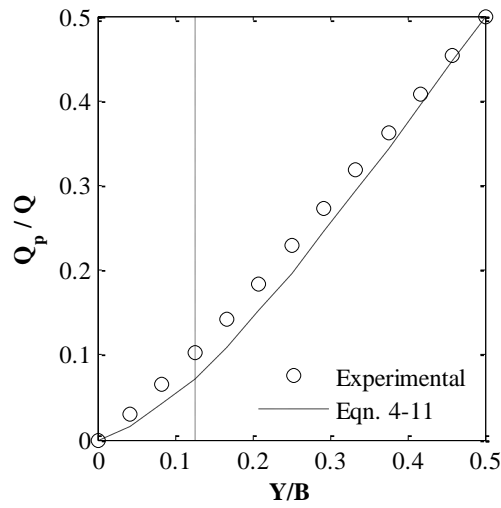


Figure C-22: Cumulative discharge distribution for the 25% Coverage Experiment.

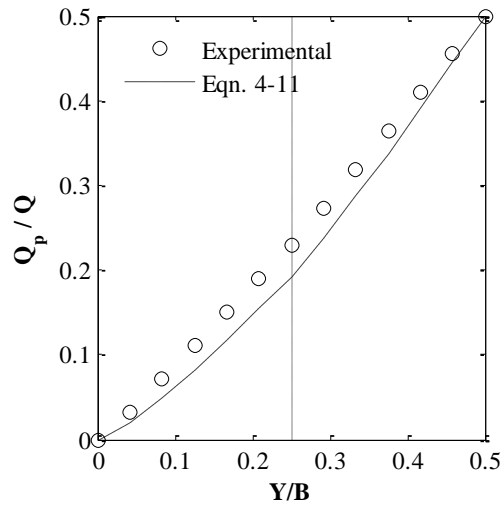


Figure C-23: Cumulative discharge distribution for the 50% Coverage Experiment.

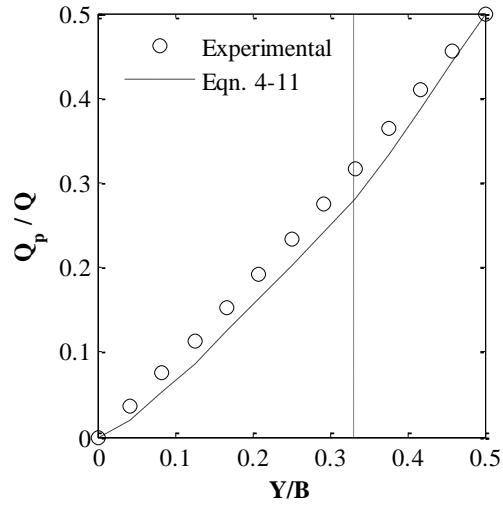


Figure C-24: Cumulative discharge distribution for the Rough Bed Experiment.

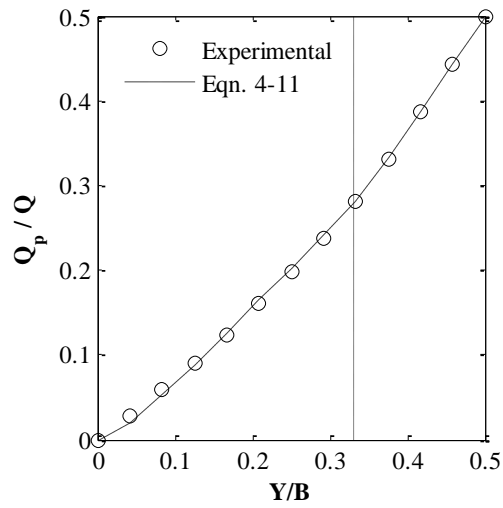


Figure C-25: Cumulative discharge distribution for the Rough Ice Experiment.

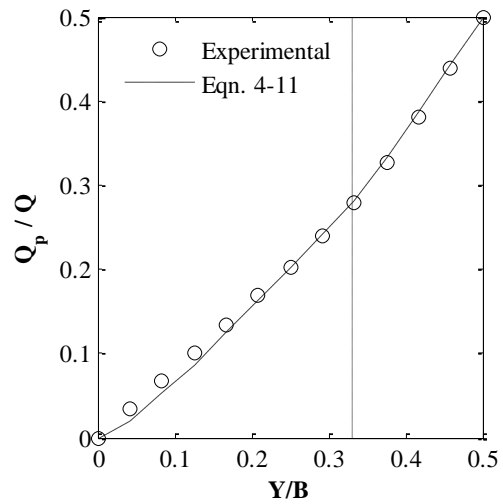


Figure C-26: Cumulative discharge distribution for the Rough Bed - Rough Ice Experiment.

## C.4 Discharge Distribution – Transverse

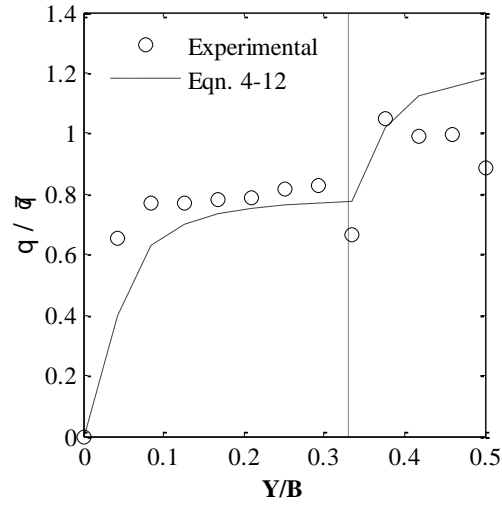


Figure C-27: Transverse discharge distribution for the Base Experiment.

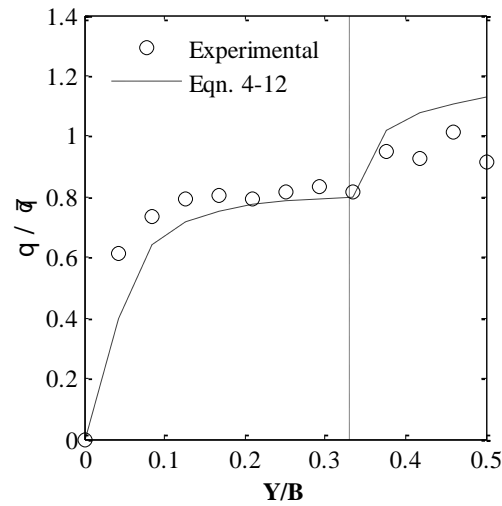


Figure C28: Transverse discharge distribution for the Low Froude Experiment.

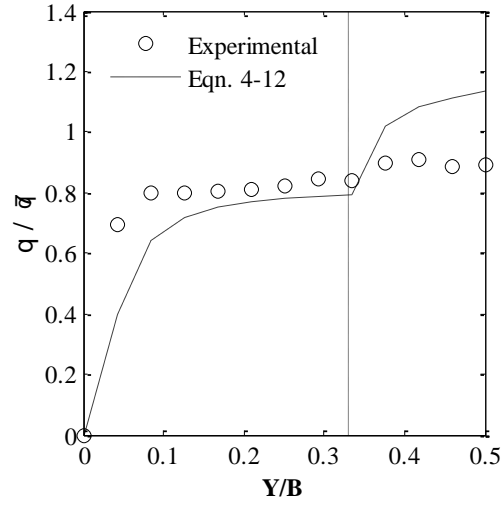


Figure C29: Transverse discharge distribution for the High Froude Experiment.

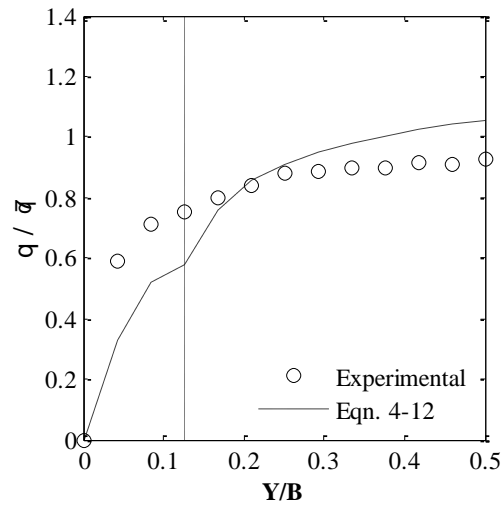


Figure C30: Transverse discharge distribution for the 25% Coverage Experiment.

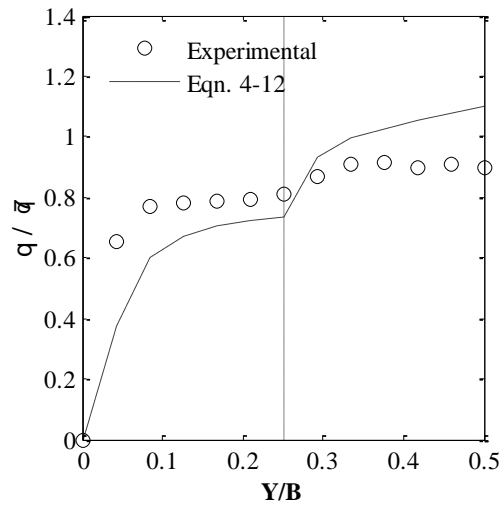


Figure C31: Transverse discharge distribution for the 50% Coverage Experiment.

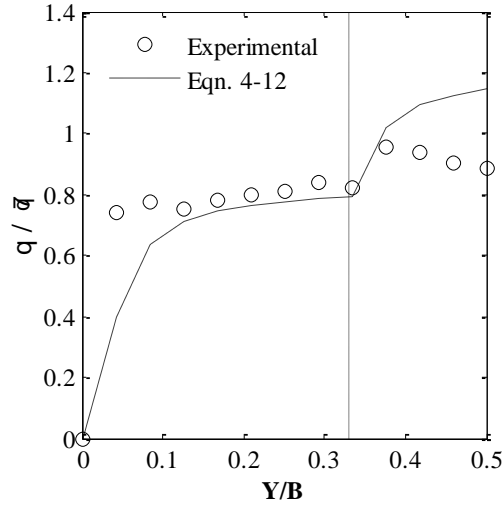


Figure C32: Transverse discharge distribution for the Rough Bed Experiment.

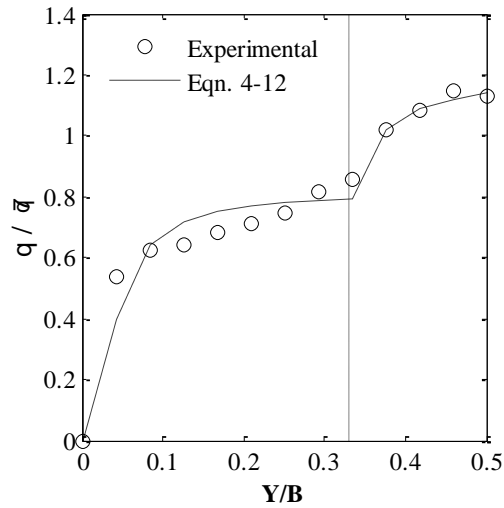


Figure C33: Transverse discharge distribution for the Rough Ice Experiment.

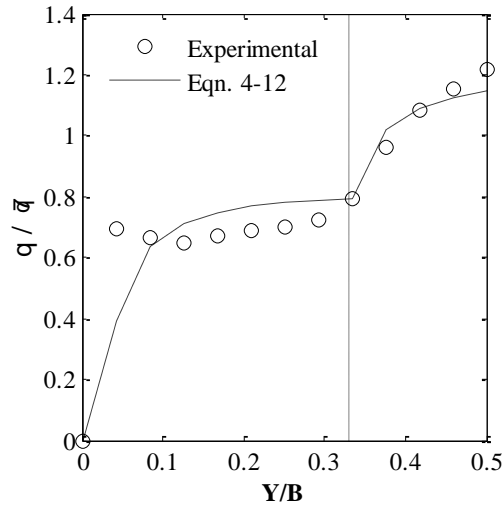


Figure C34: Transverse discharge distribution for the Rough Bed - Rough Ice Experiment.

## C.5 Log-law Velocity Profiles

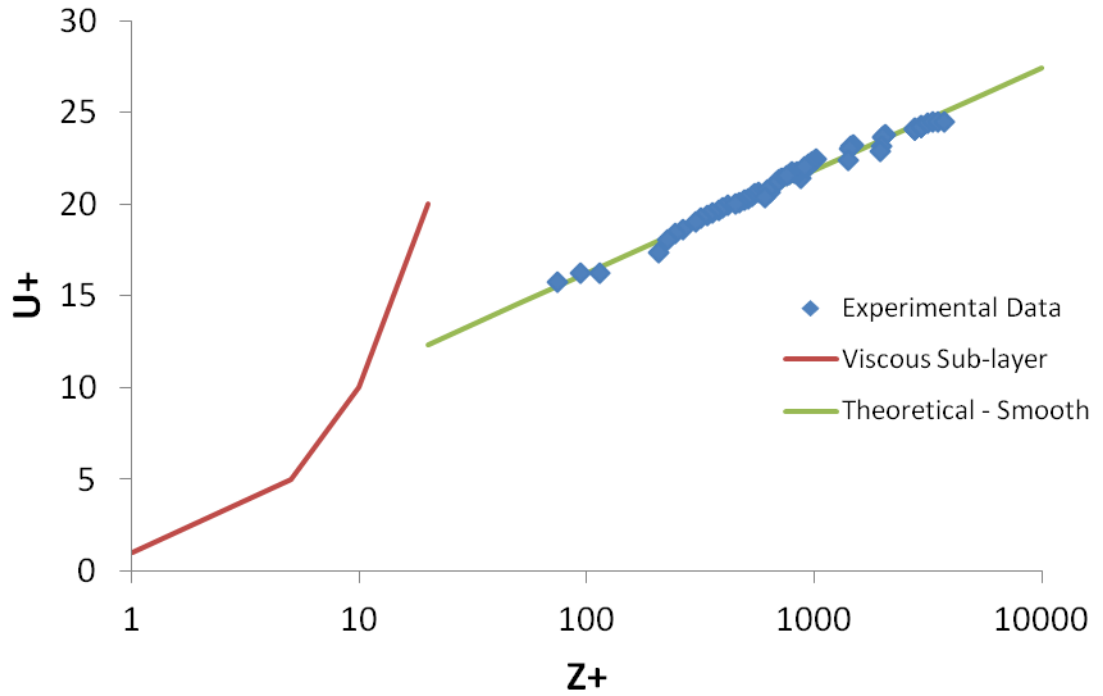


Figure C-35: Fit of experimental data in the bed affected zone to the log-law at  $Y = 0$  mm for the Base Experiment with  $u_* = 0.019$  m/s.

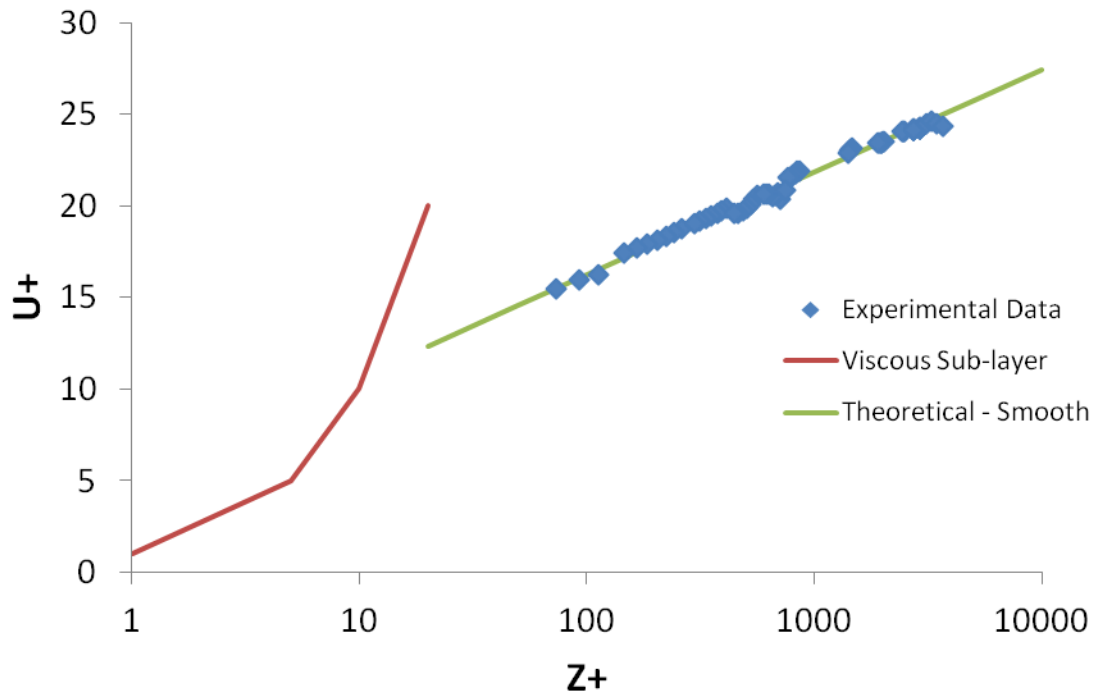


Figure C-36: Fit of experimental data in the bed affected zone to the log-law at  $Y = 50$  mm for the Base Experiment with  $u_* = 0.01875$  m/s.

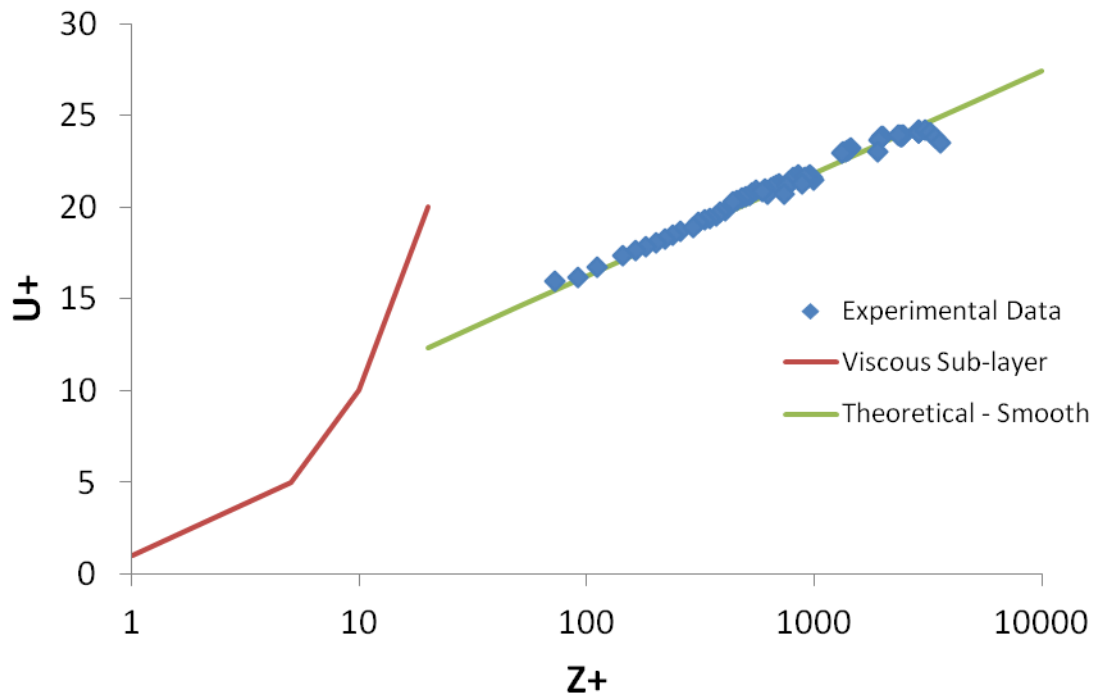


Figure C-37: Fit of experimental data in the bed affected zone to the log-law at  $Y = 100$  mm for the Base Experiment with  $u_* = 0.0185$  m/s.

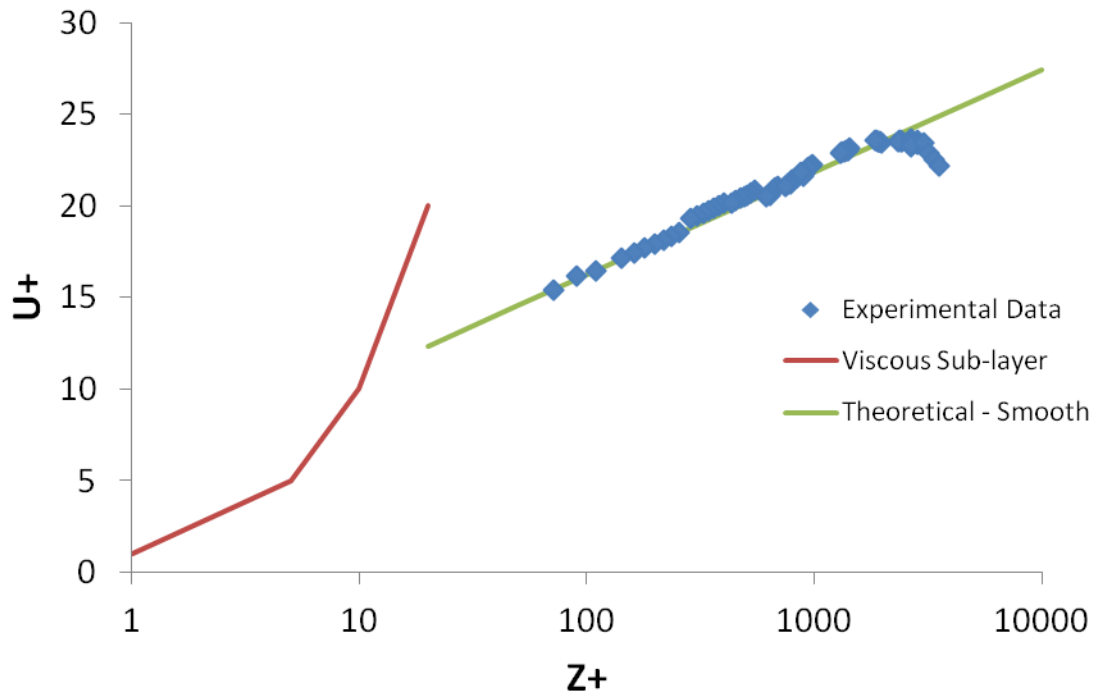


Figure C-38: Fit of experimental data in the bed affected zone to the log-law at  $Y = 150$  mm for the Base Experiment with  $u_* = 0.01825$  m/s.

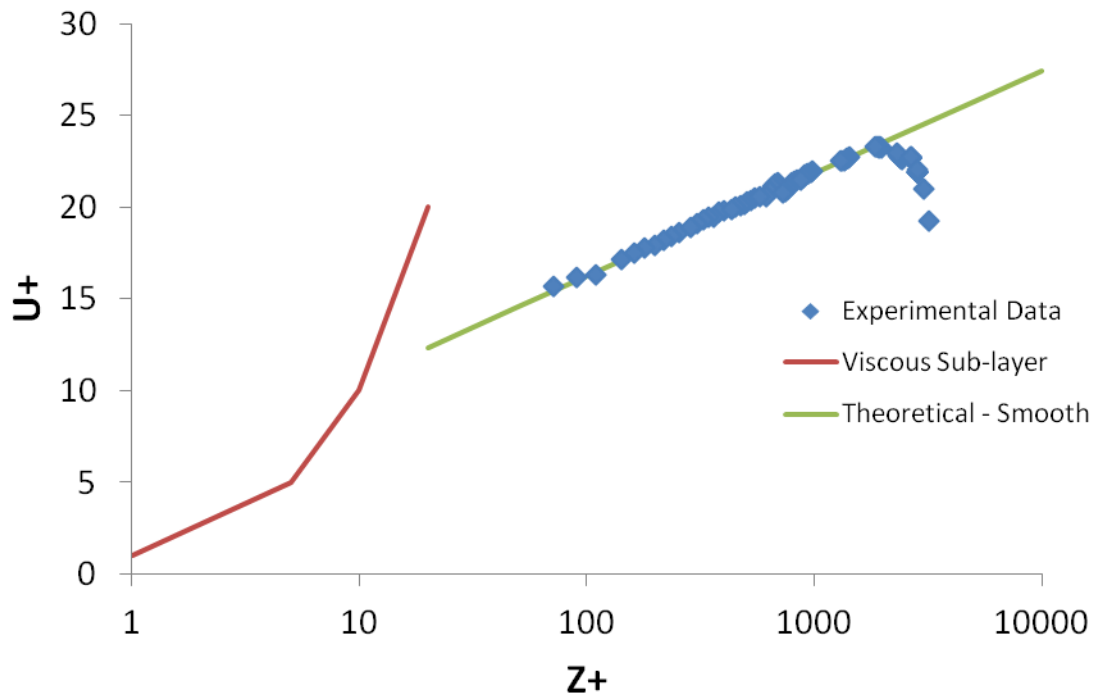


Figure C-39: Fit of experimental data in the bed affected zone to the log-law at  $Y = 200$  mm for the Base Experiment with  $u_* = 0.01825$  m/s.

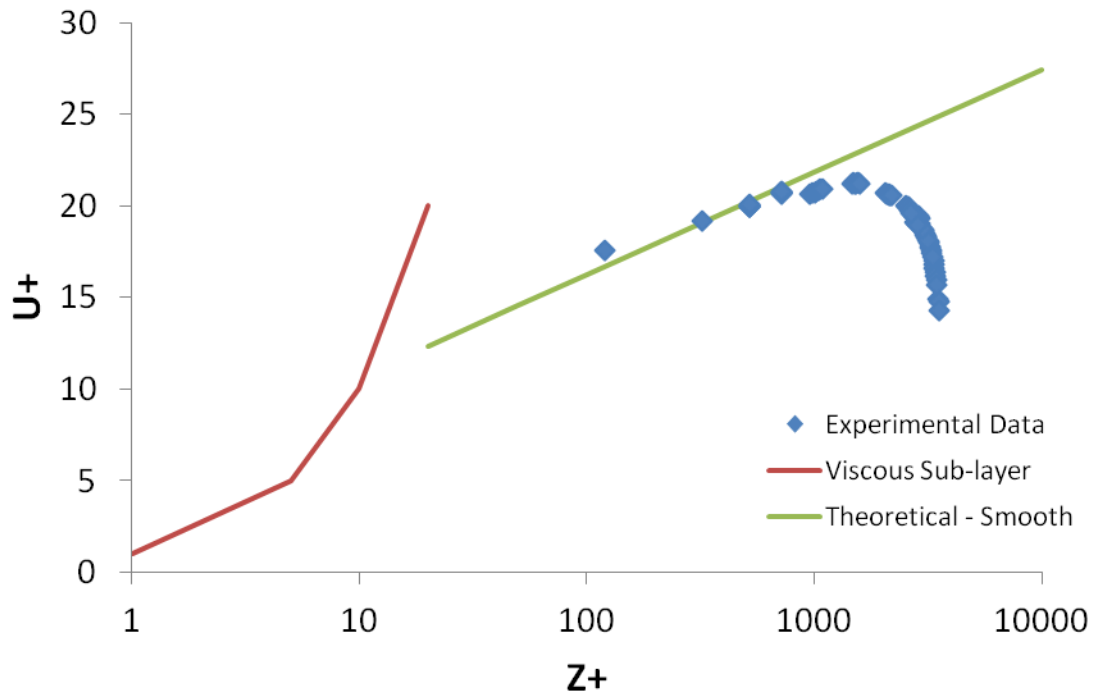


Figure C-40: Fit of experimental data in the ice affected zone to the log-law at  $Y = 200$  mm for the Base Experiment with  $u_* = 0.02$  m/s.

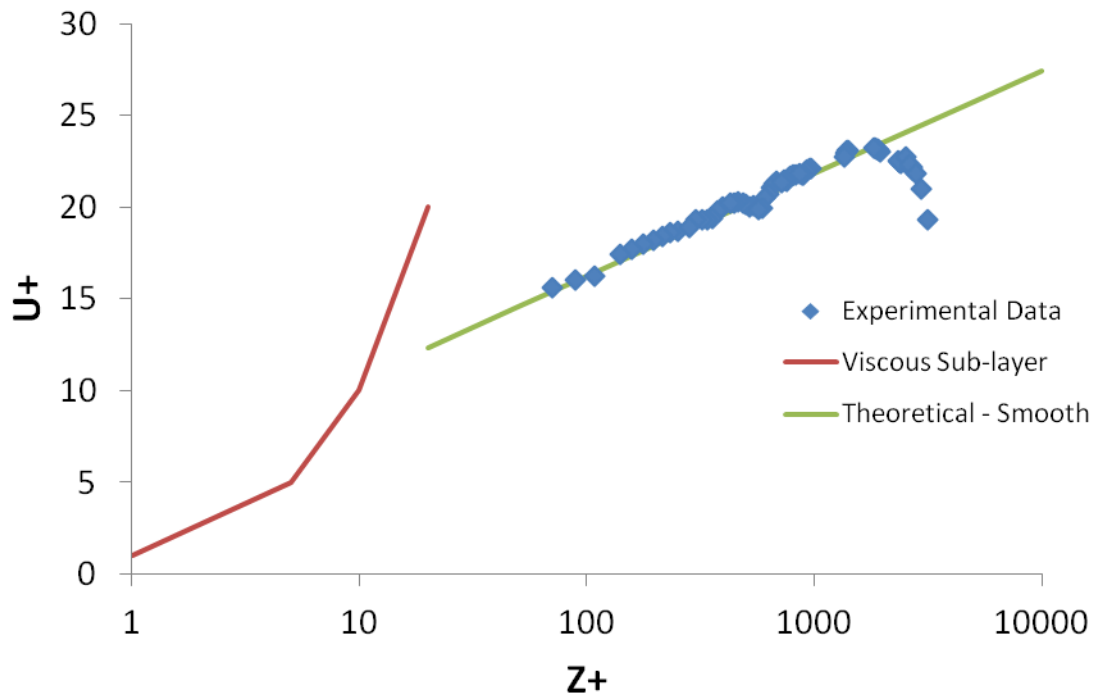


Figure C-41: Fit of experimental data in the bed affected zone to the log-law at  $Y = 250$  mm for the Base Experiment with  $u_* = 0.018$  m/s.

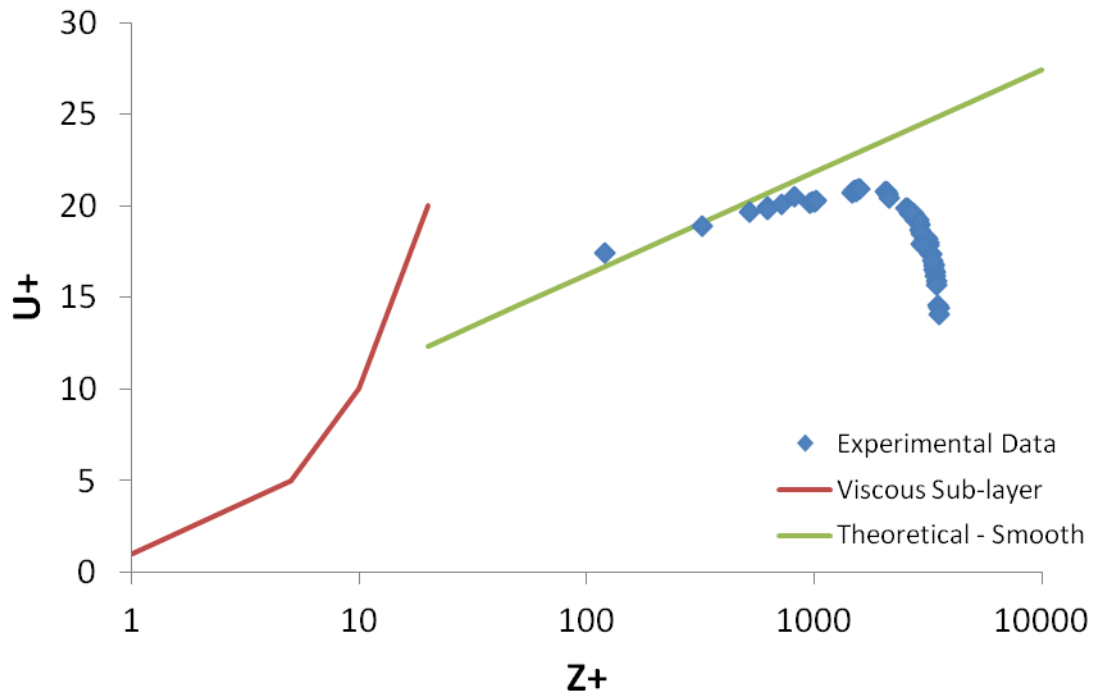


Figure C-42: Fit of experimental data in the ice affected zone to the log-law at  $Y = 250$  mm for the Base Experiment with  $u_* = 0.02$  m/s.

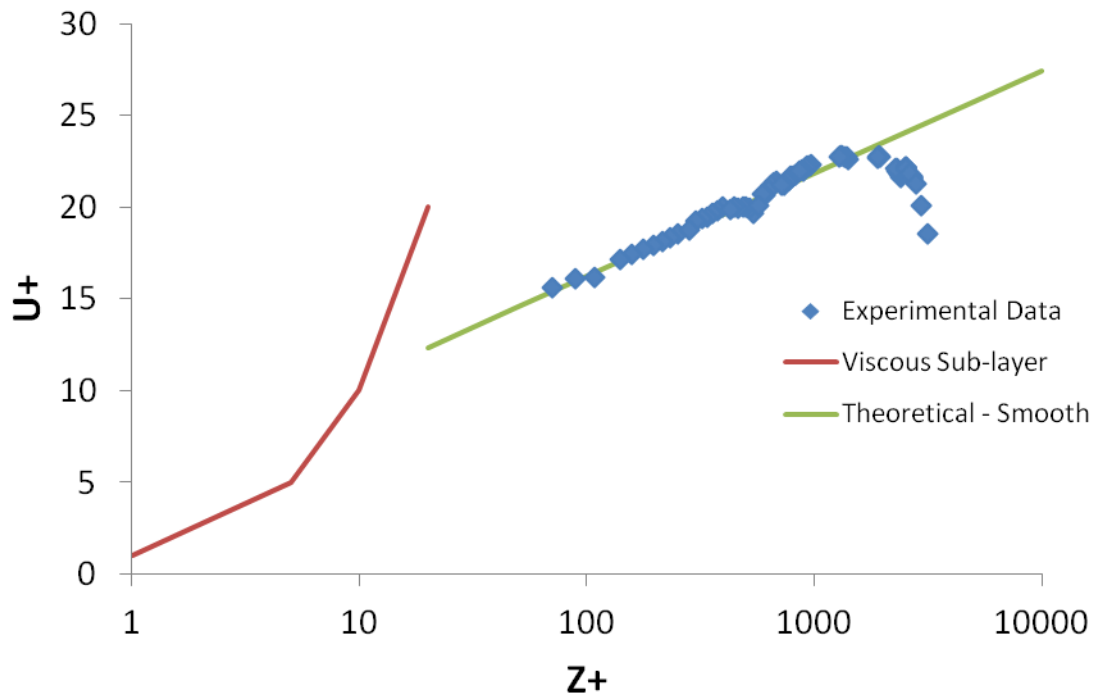


Figure C-43: Fit of experimental data in the bed affected zone to the log-law at  $Y = 300$  mm for the Base Experiment with  $u_* = 0.018$  m/s.

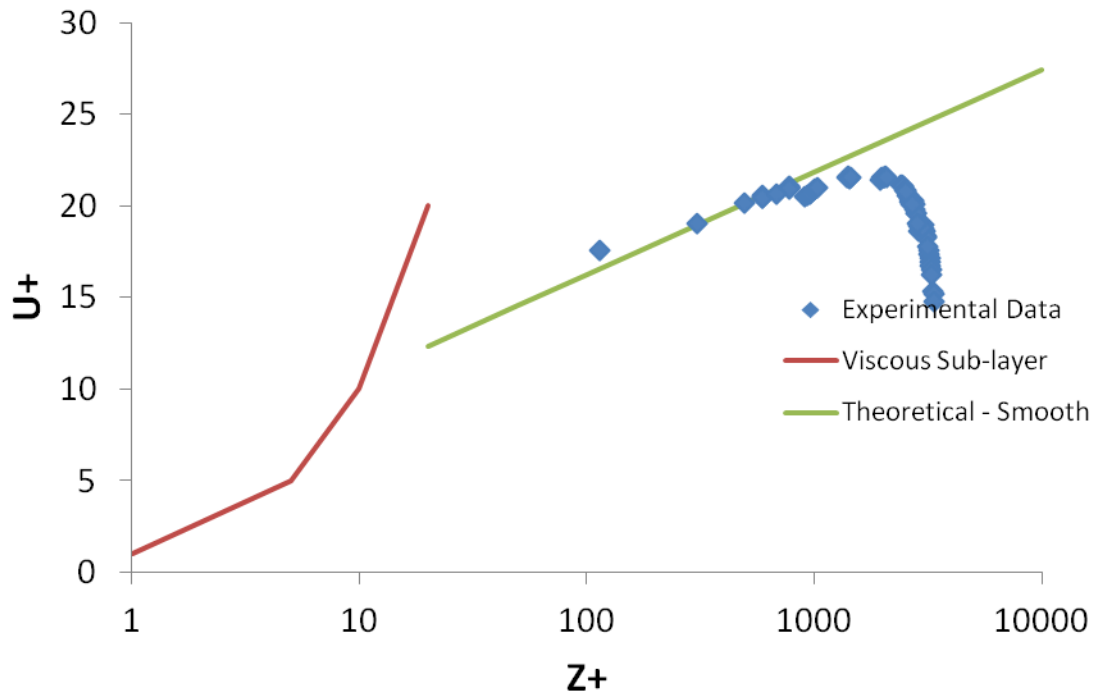


Figure C-44: Fit of experimental data in the ice affected zone to the log-law at  $Y = 300$  mm for the Base Experiment with  $u_* = 0.019$  m/s.

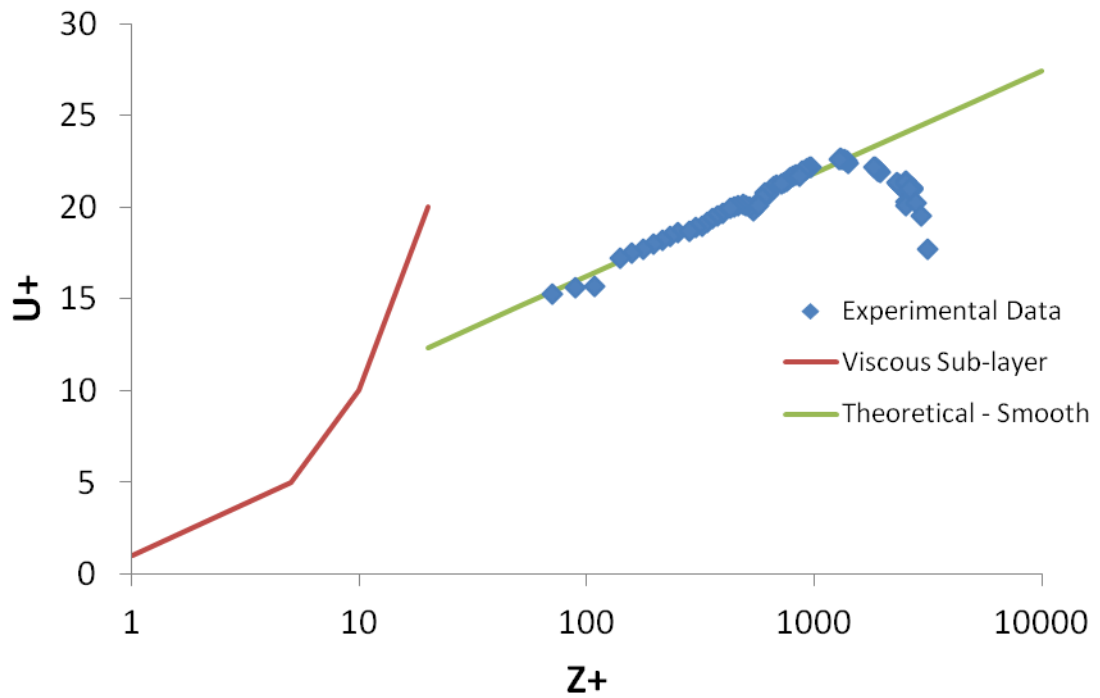


Figure C-45: Fit of experimental data in the bed affected zone to the log-law at  $Y = 350$  mm for the Base Experiment with  $u_* = 0.018$  m/s.

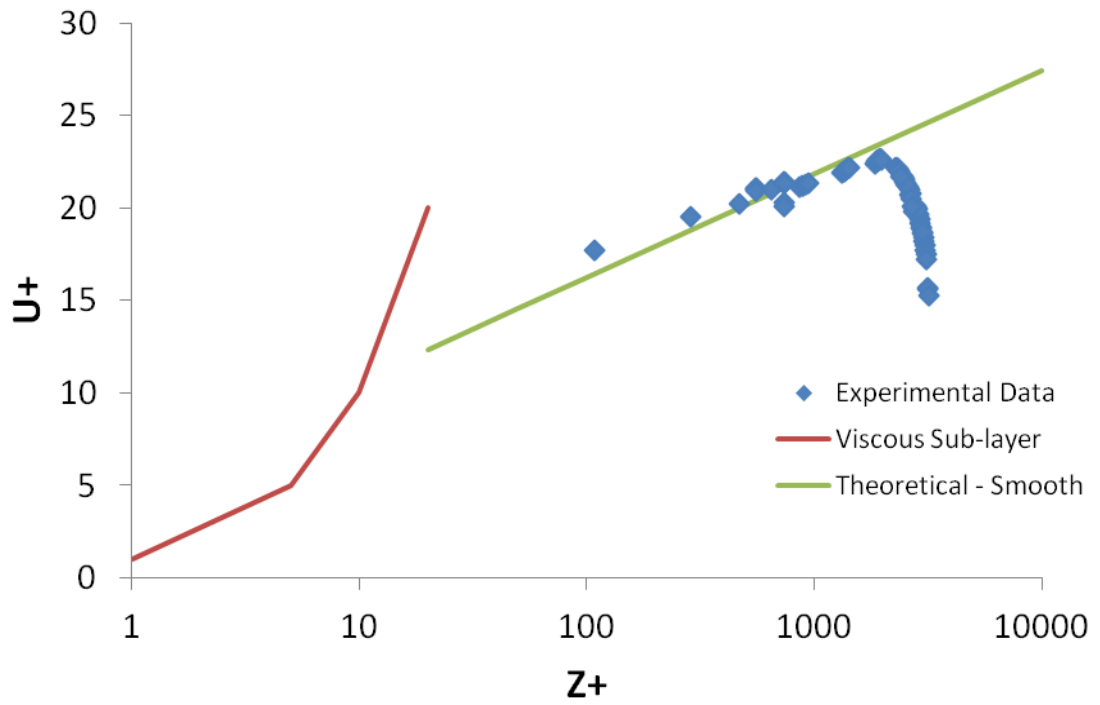


Figure C-46: Fit of experimental data in the ice affected zone to the log-law at  $Y = 350$  mm for the Base Experiment with  $u_* = 0.018$  m/s.

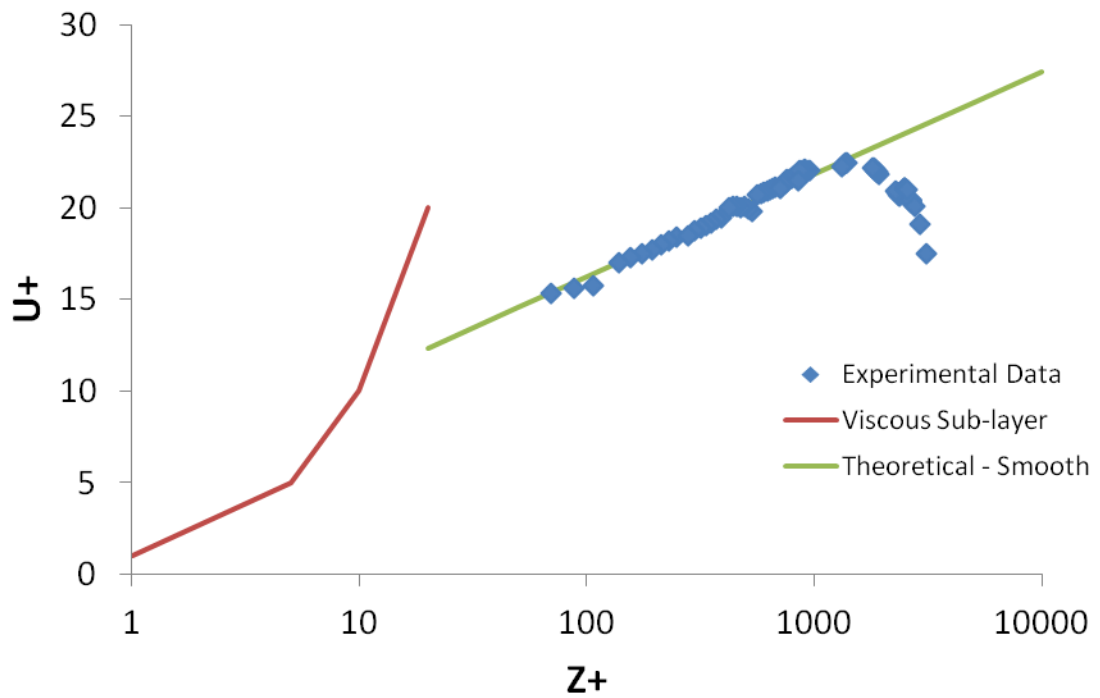


Figure C-47: Fit of experimental data in the bed affected zone to the log-law at  $Y = 400$  mm for the Base Experiment with  $u_* = 0.01775$  m/s.

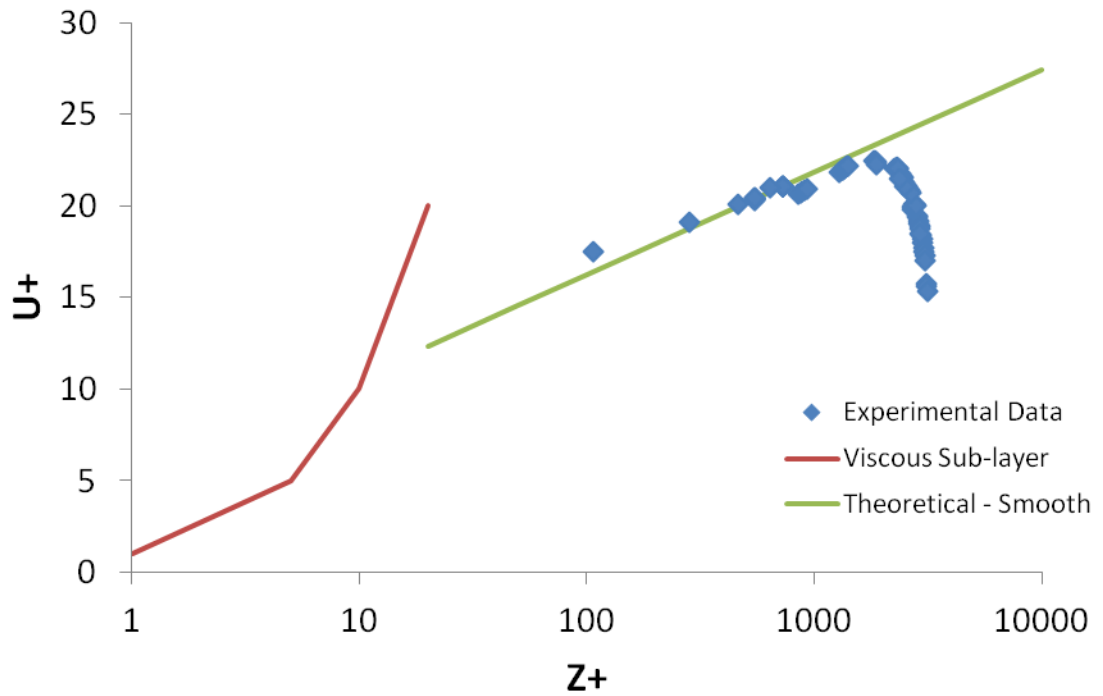


Figure C-48: Fit of experimental data in the ice affected zone to the log-law at  $Y = 400$  mm for the Base Experiment with  $u_* = 0.01775$  m/s.

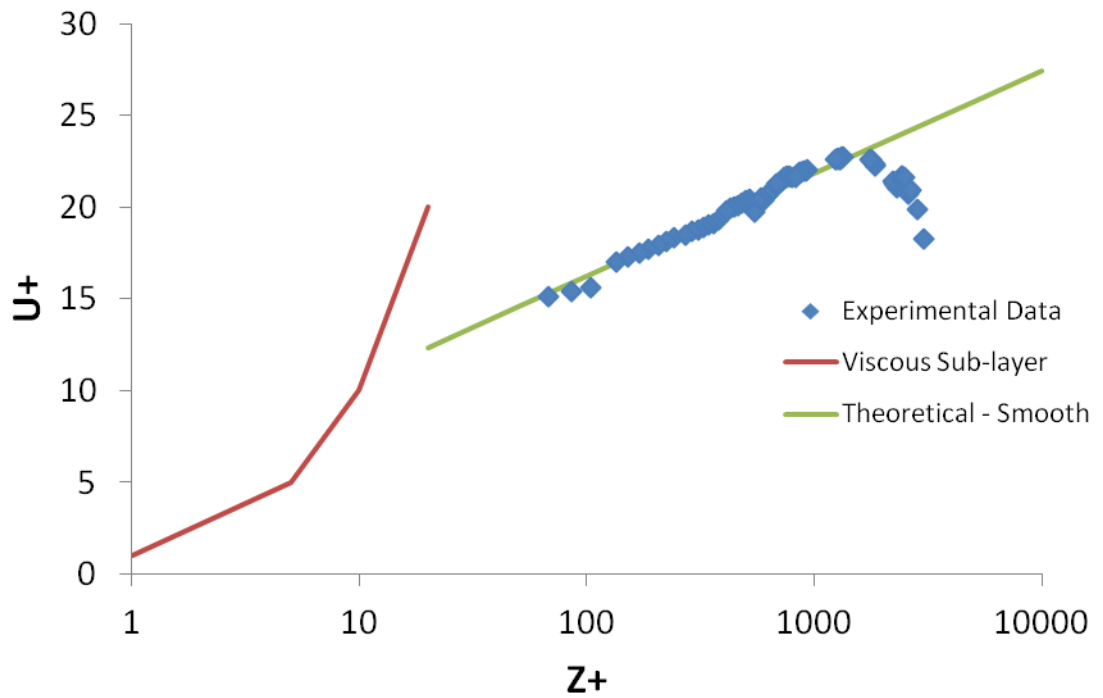


Figure C-49: Fit of experimental data in the bed affected zone to the log-law at  $Y = 450$  mm for the Base Experiment with  $u_* = 0.01725$  m/s.

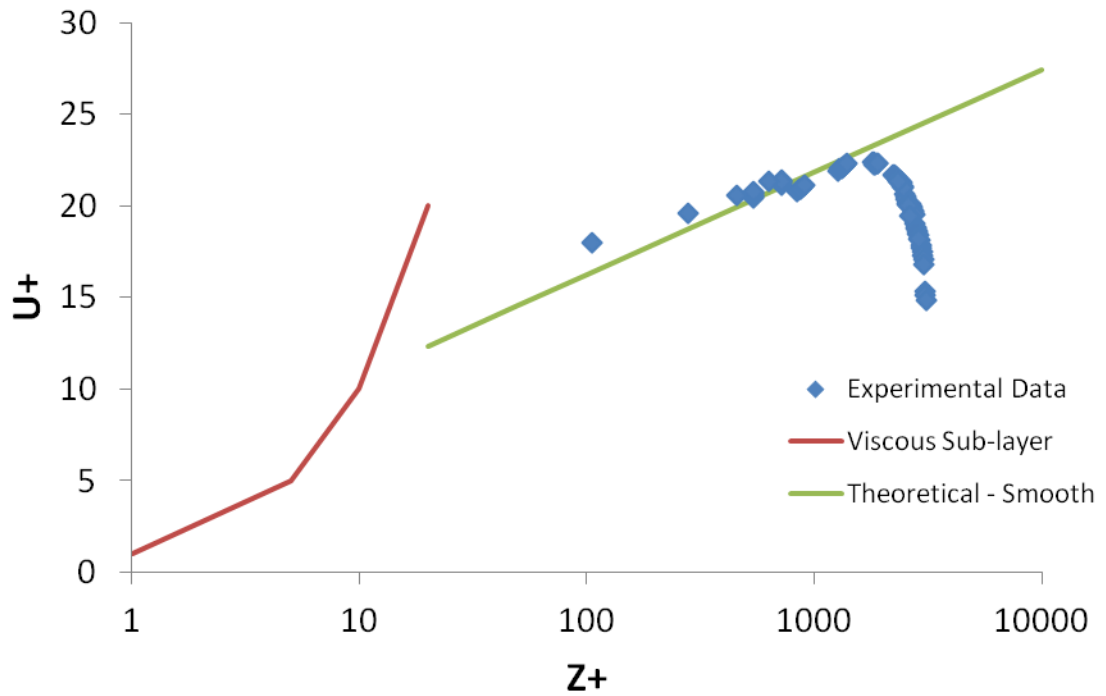


Figure C-50: Fit of experimental data in the ice affected zone to the log-law at  $Y = 450$  mm for the Base Experiment with  $u_* = 0.0175$  m/s.

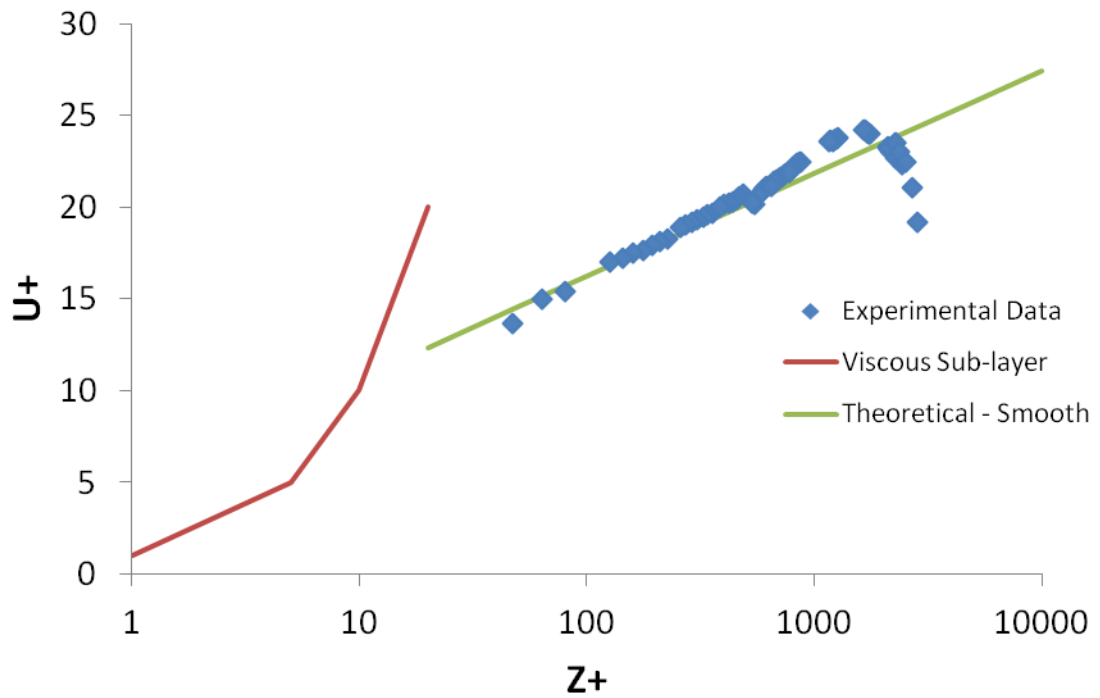


Figure C-51: Fit of experimental data in the bed affected zone to the log-law at  $Y = 500$  mm for the Base Experiment with  $u_* = 0.01625$  m/s.

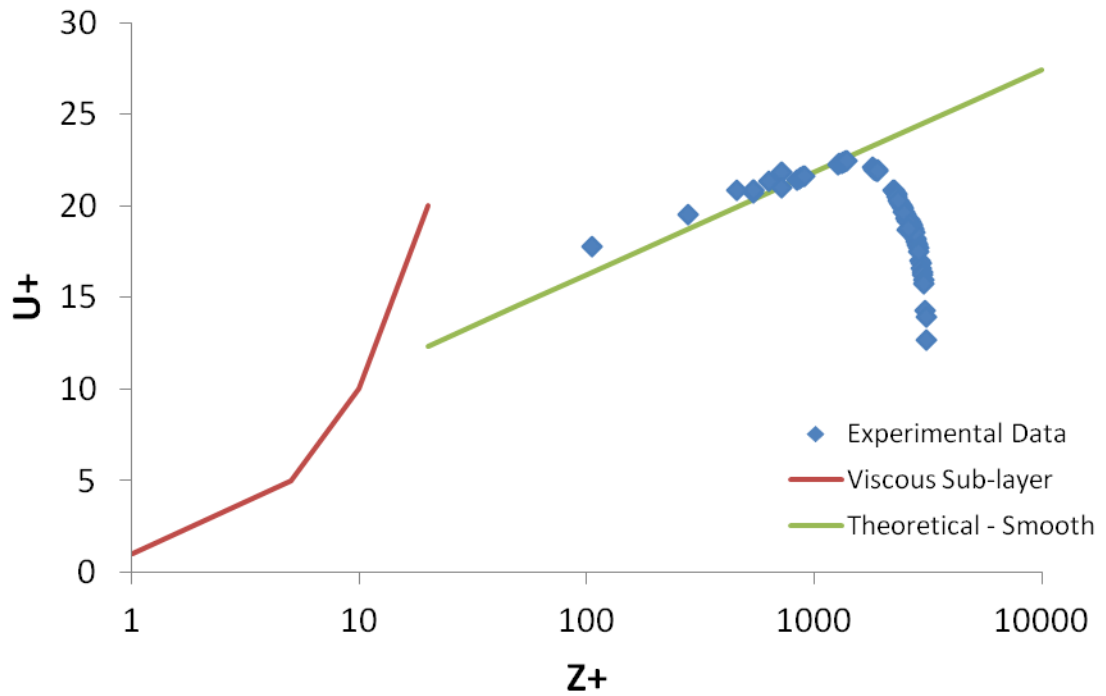


Figure C-52: Fit of experimental data in the ice affected zone to the log-law at  $Y = 500$  mm for the Base Experiment with  $u_* = 0.0175$  m/s.

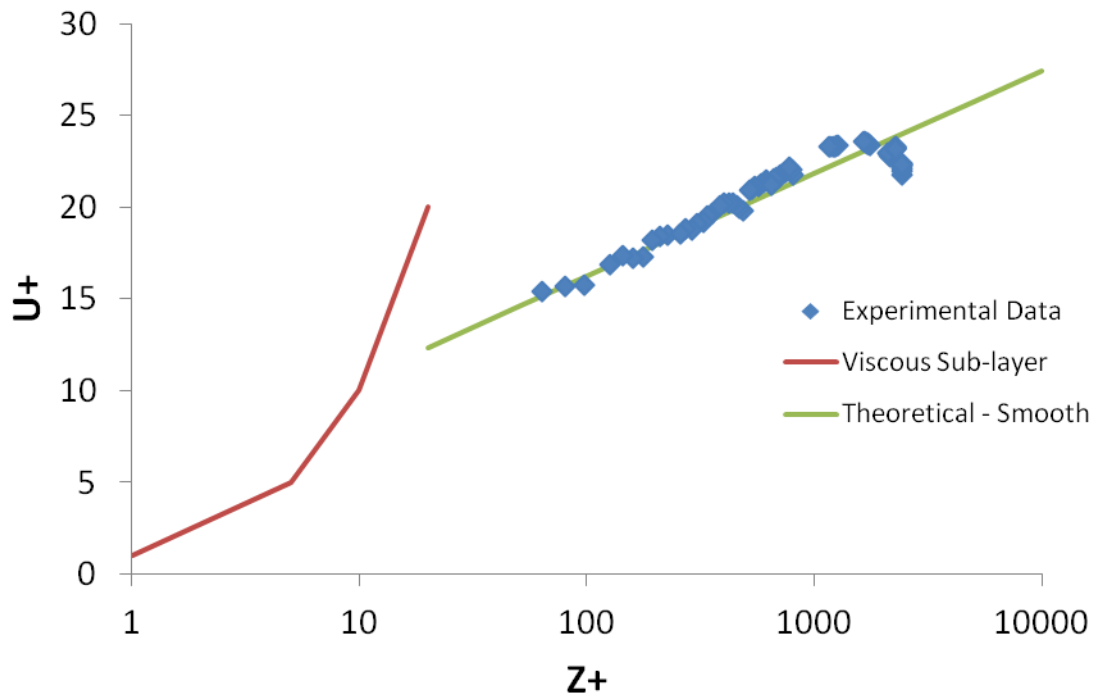


Figure C-53: Fit of experimental data in the bed affected zone to the log-law at  $Y = 535$  mm for the Base Experiment with  $u_* = 0.01625$  m/s.

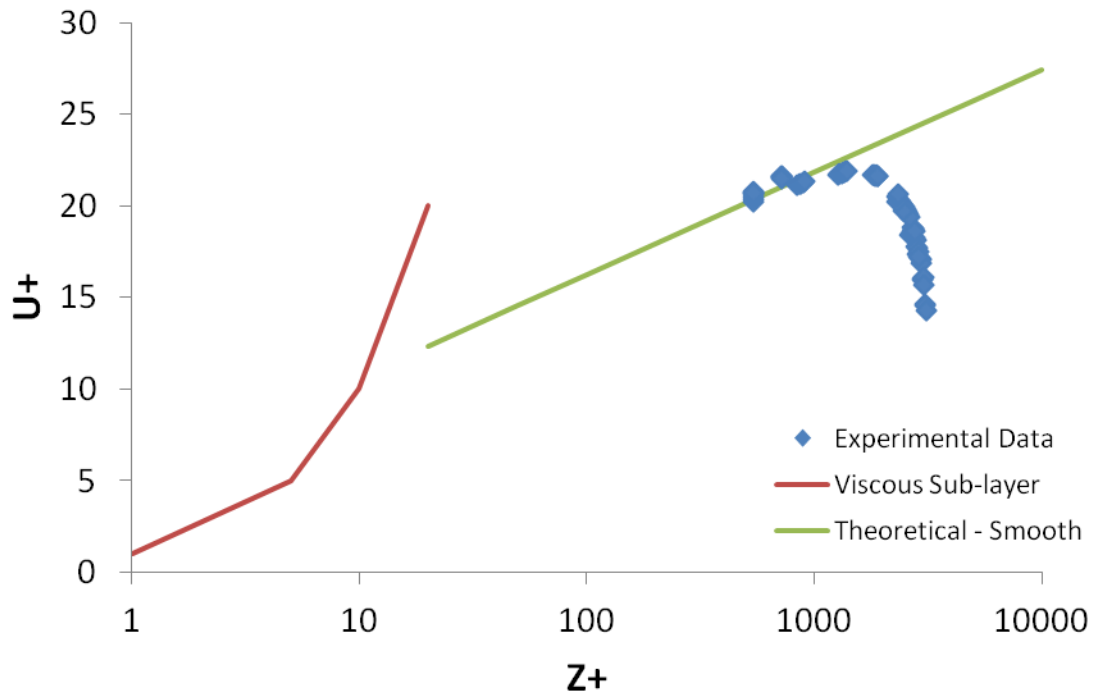


Figure C-54: Fit of experimental data in the ice affected zone to the log-law at  $Y = 535$  mm for the Base Experiment with  $u_* = 0.0175$  m/s.

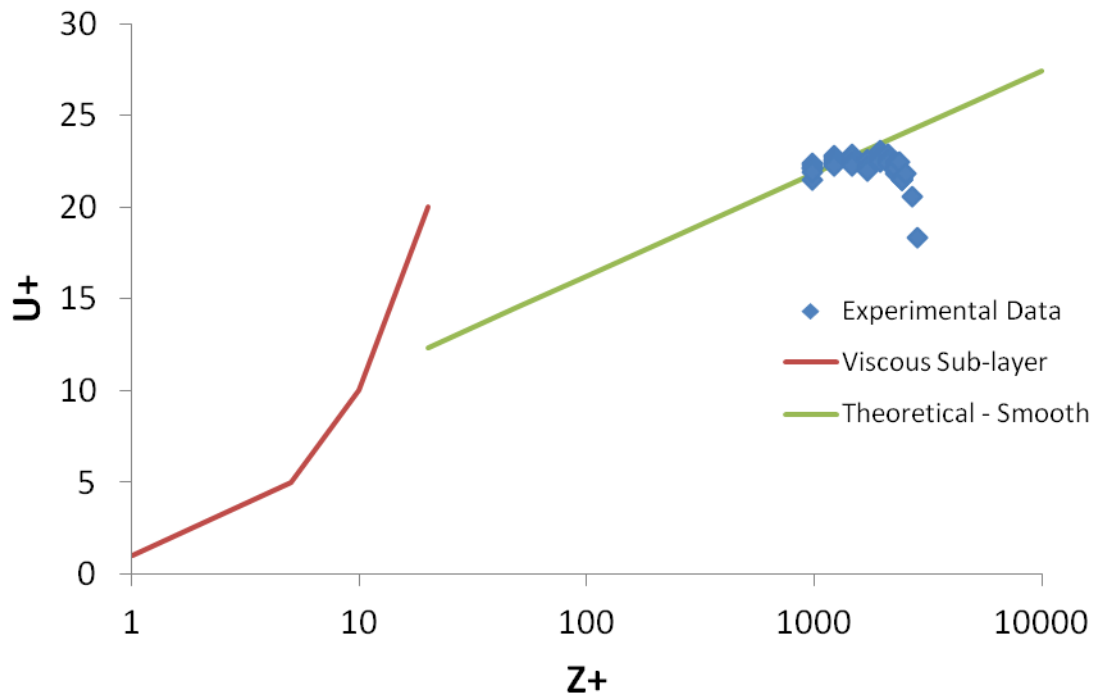


Figure C-55: Fit of experimental data in the bed affected zone to the log-law at  $Y = 550$  mm for the Base Experiment with  $u_* = 0.01625$  m/s.

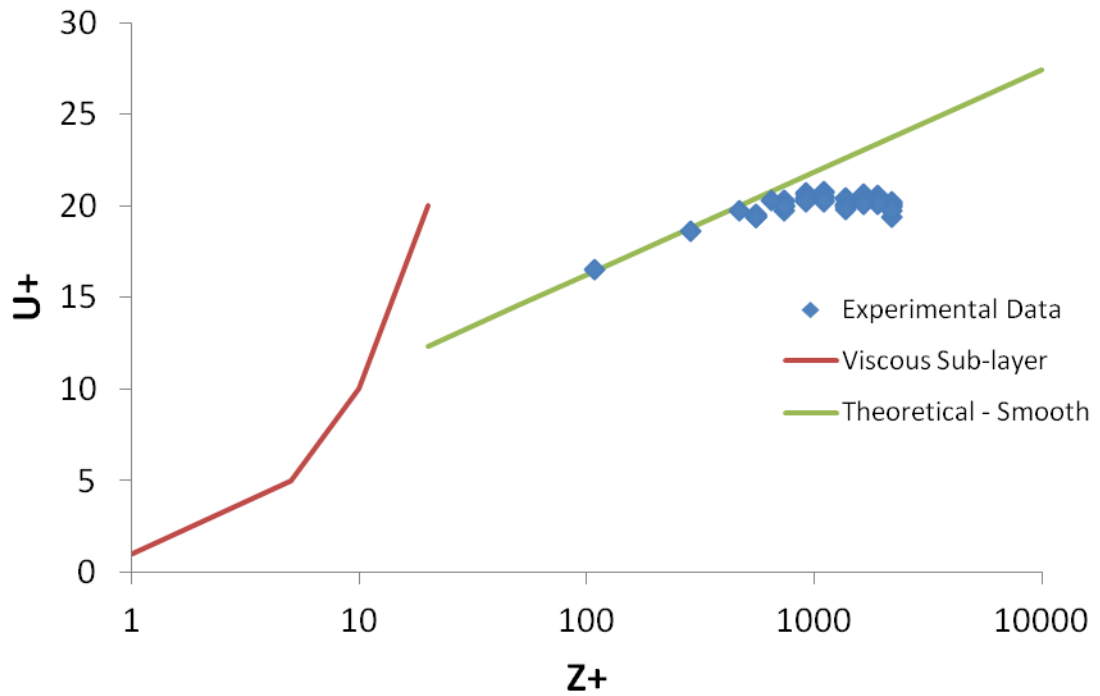


Figure C-56: Fit of experimental data in the ice affected zone to the log-law at  $Y = 550$  mm for the Base Experiment with  $u_* = 0.018$  m/s.

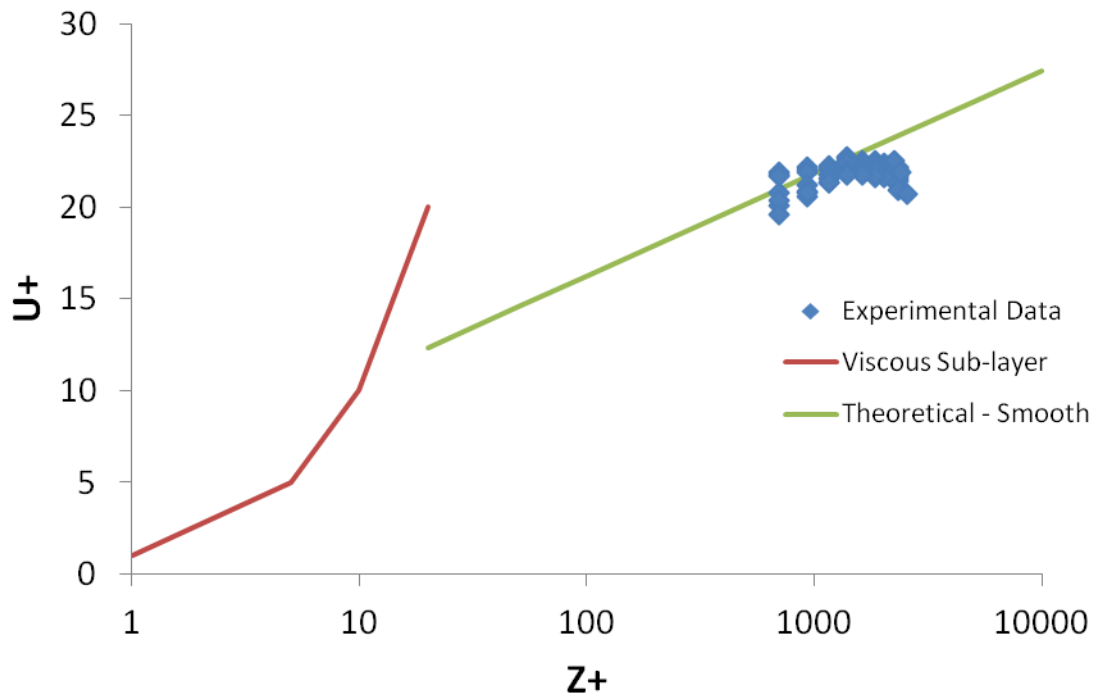


Figure C-57: Fit of experimental data in the bed affected zone to the log-law at  $Y = 565$  mm for the Base Experiment with  $u_* = 0.0155$  m/s.

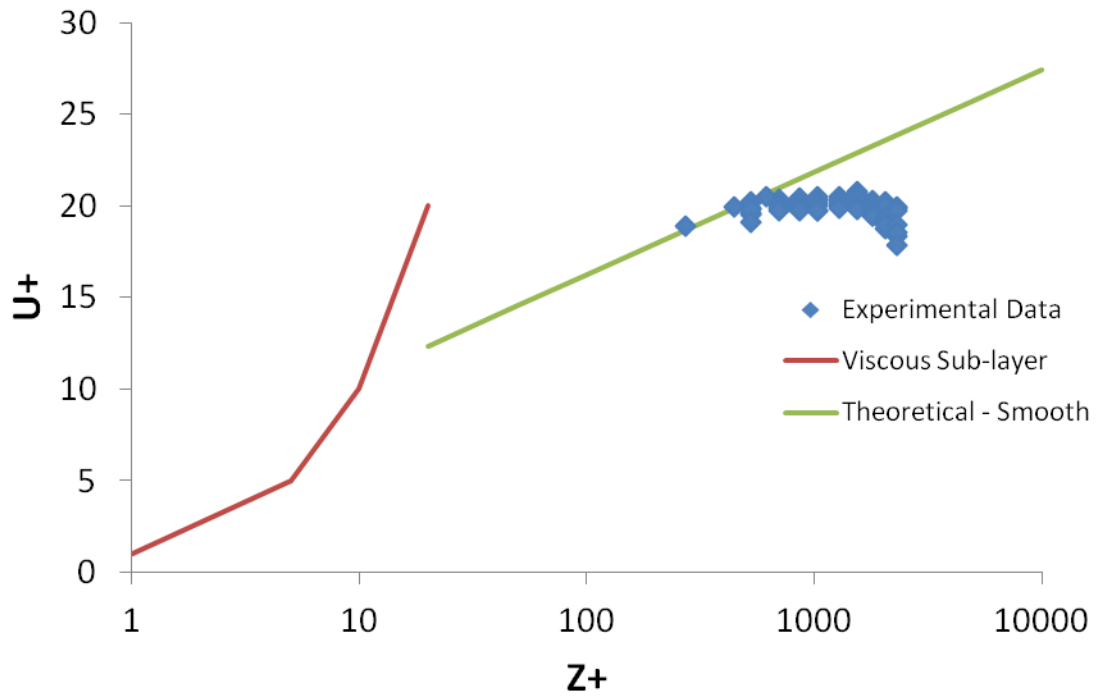


Figure C-58: Fit of experimental data in the ice affected zone to the log-law at  $Y = 565$  mm for the Base Experiment with  $u_* = 0.017$  m/s.

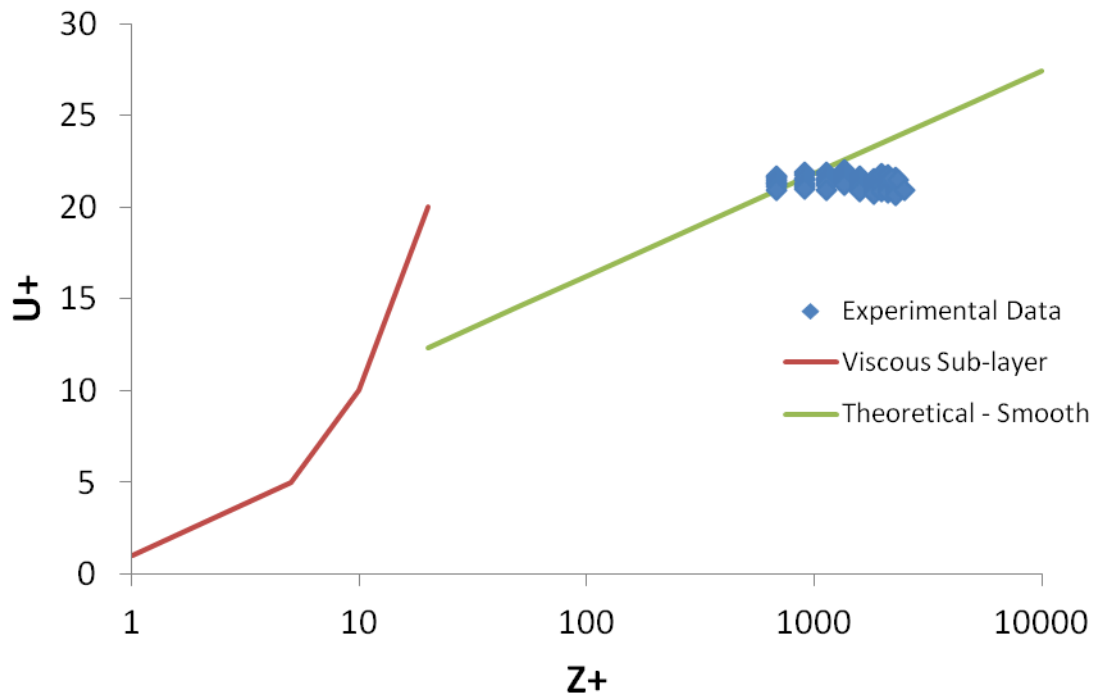


Figure C-59: Fit of experimental data in the bed affected zone to the log-law at  $Y = 575$  mm for the Base Experiment with  $u_* = 0.01515$  m/s.

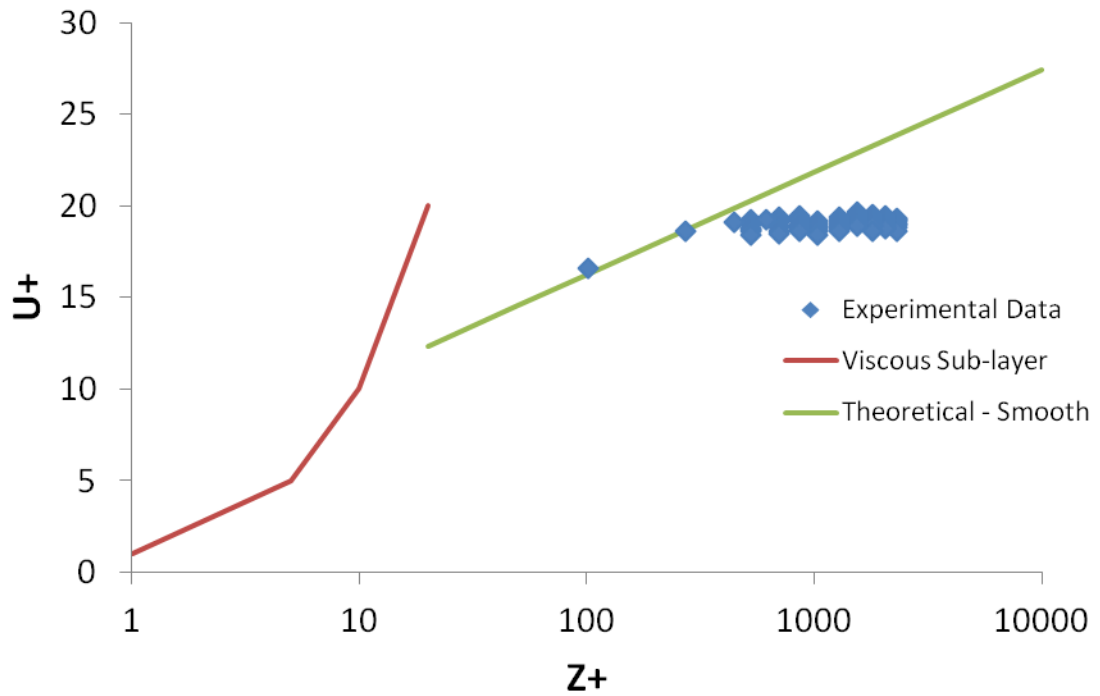


Figure C-60: Fit of experimental data in the ice affected zone to the log-law at  $Y = 575$  mm for the Base Experiment with  $u_* = 0.017$  m/s.

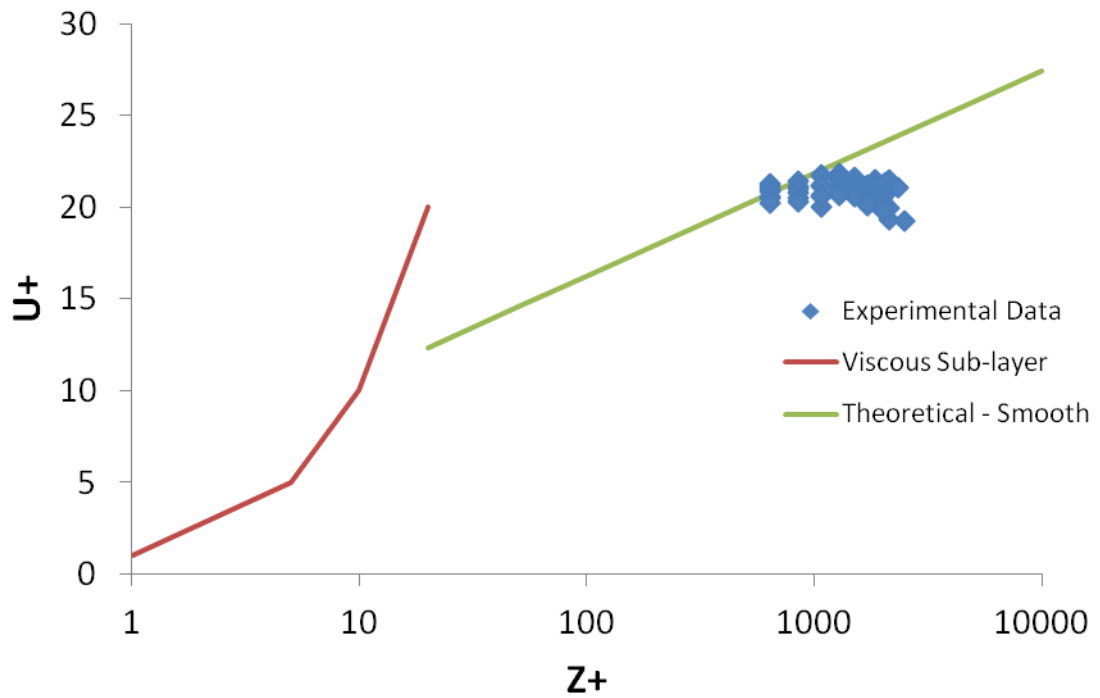


Figure C-61: Fit of experimental data in the bed affected zone to the log-law at  $Y = 585$  mm for the Base Experiment with  $u_* = 0.01425$  m/s.

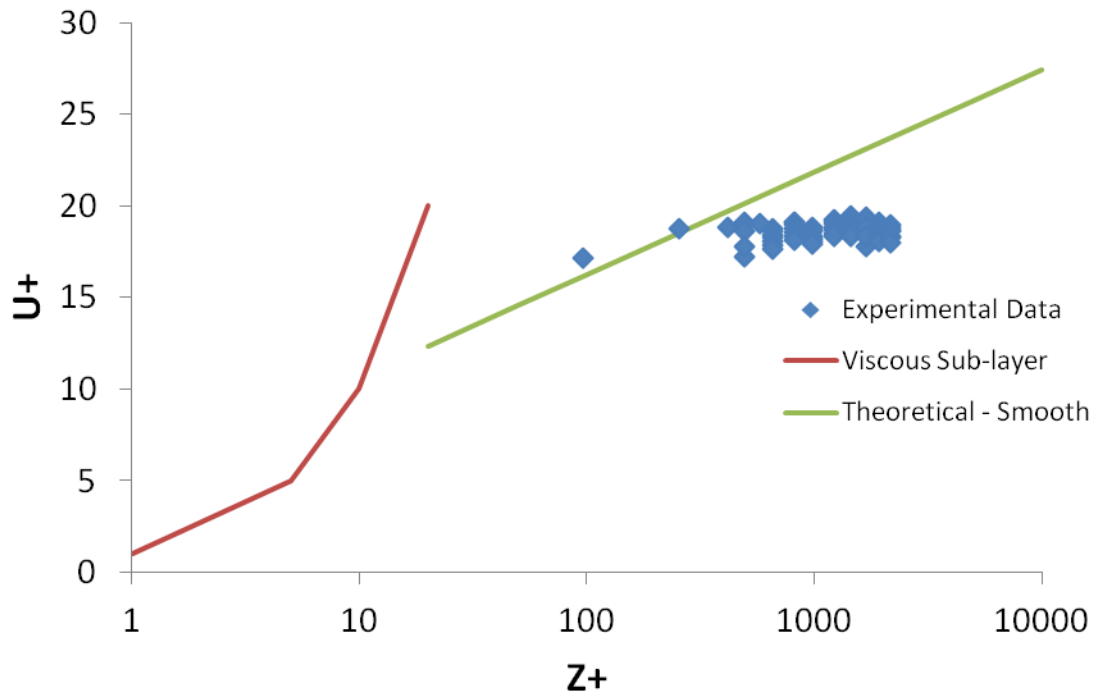


Figure C-62: Fit of experimental data in the ice affected zone to the log-law at  $Y = 585 \text{ mm}$  for the Base Experiment with  $u_* = 0.016 \text{ m/s}$ .

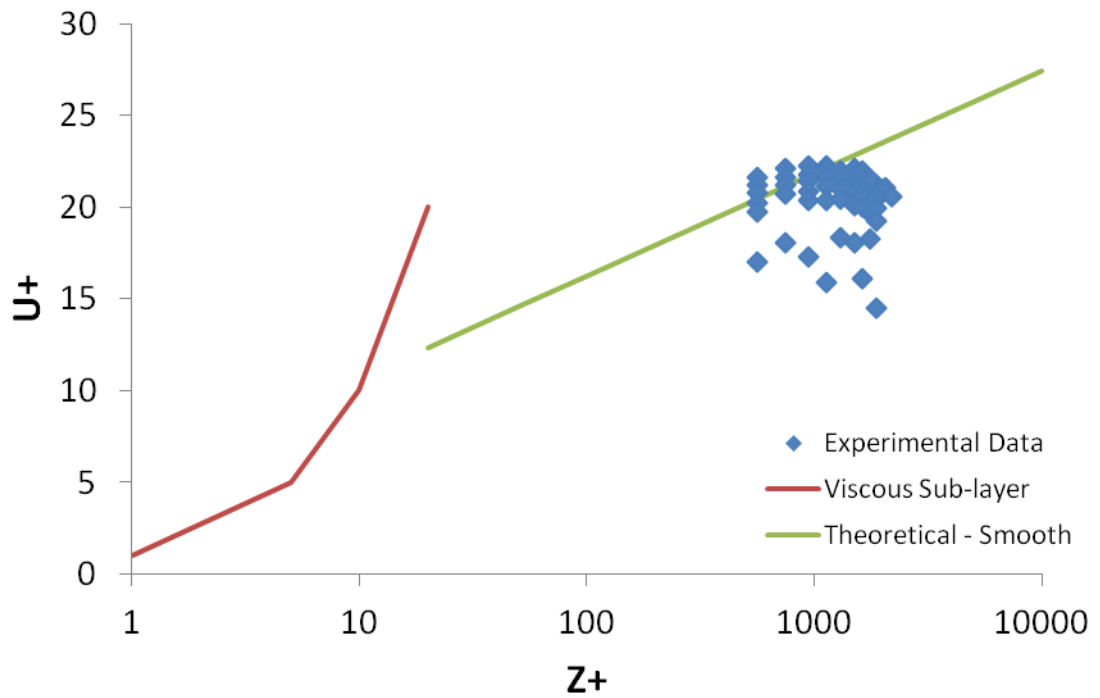


Figure C-63: Fit of experimental data in the bed affected zone to the log-law at  $Y = 595 \text{ mm}$  for the Base Experiment with  $u_* = 0.0125 \text{ m/s}$ .

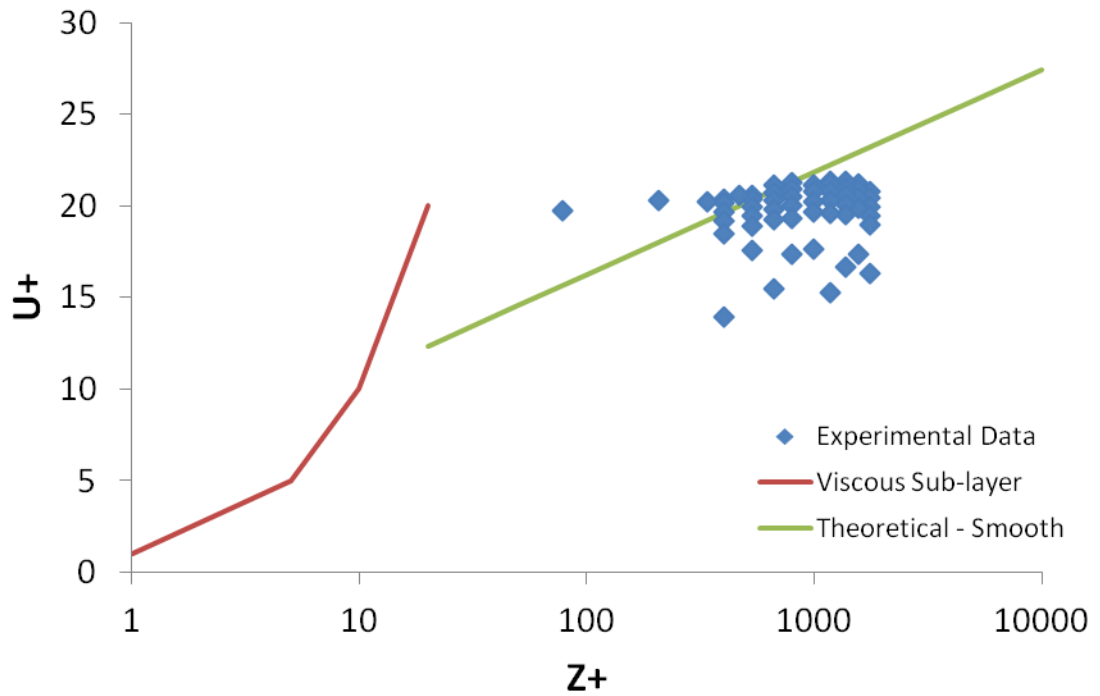


Figure C-64: Fit of experimental data in the ice affected zone to the log-law at  $Y = 595$  mm for the Base Experiment with  $u_* = 0.013$  m/s.

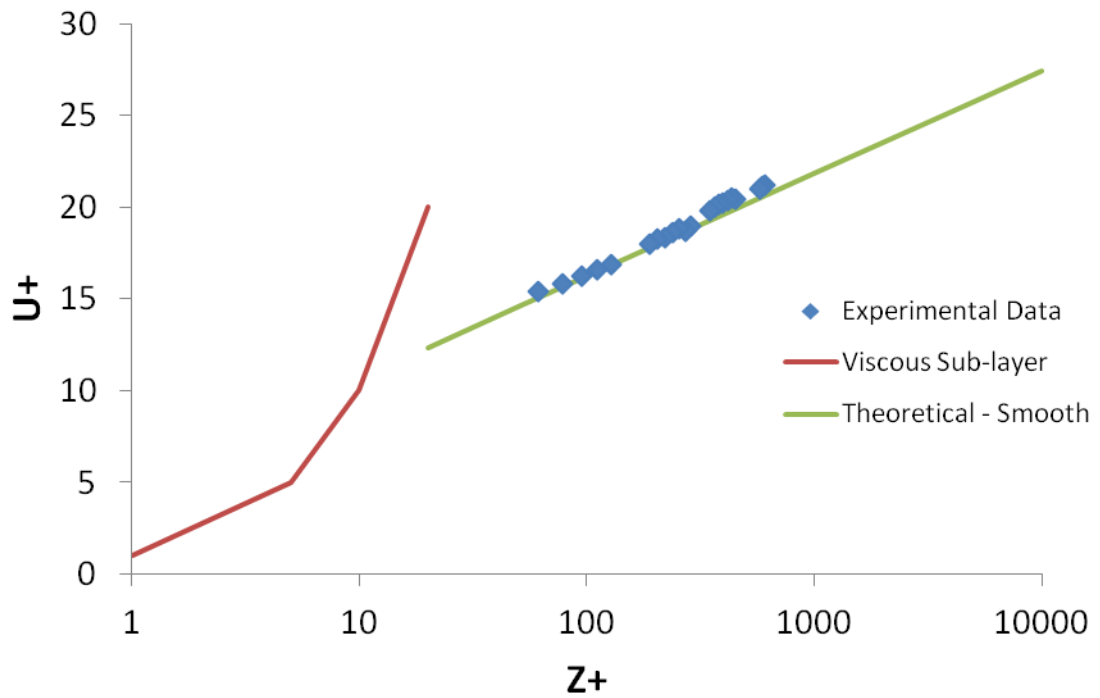


Figure C-65: Fit of experimental data in the wall affected zone to the log-law at  $Z = 45$  mm for the Base Experiment with  $u_* = 0.016$  m/s.

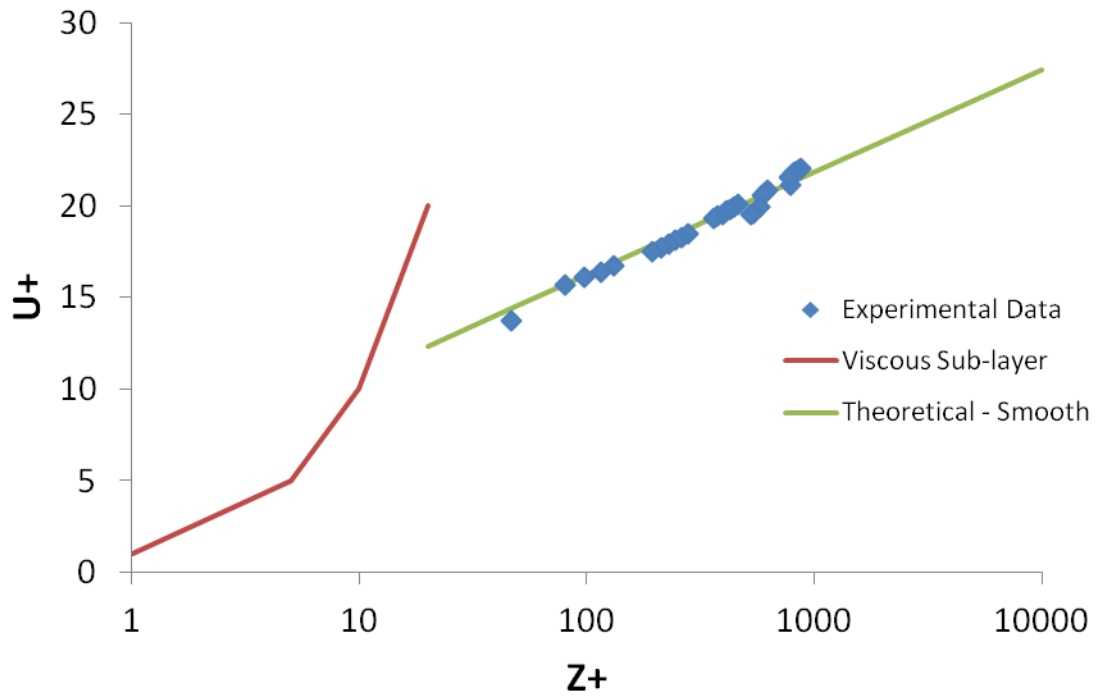


Figure C-66: Fit of experimental data in the wall affected zone to the log-law at  $Z = 60$  mm for the Base Experiment with  $u_* = 0.0165$  m/s.

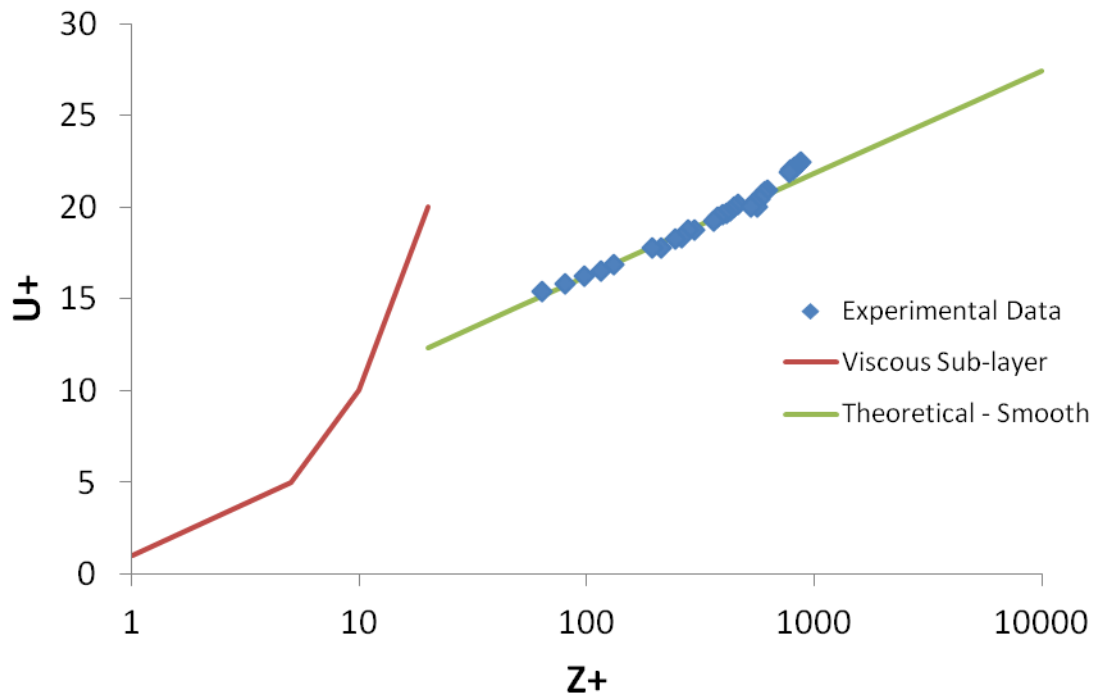


Figure C-67: Fit of experimental data in the wall affected zone to the log-law at  $Z = 75$  mm for the Base Experiment with  $u_* = 0.0165$  m/s.

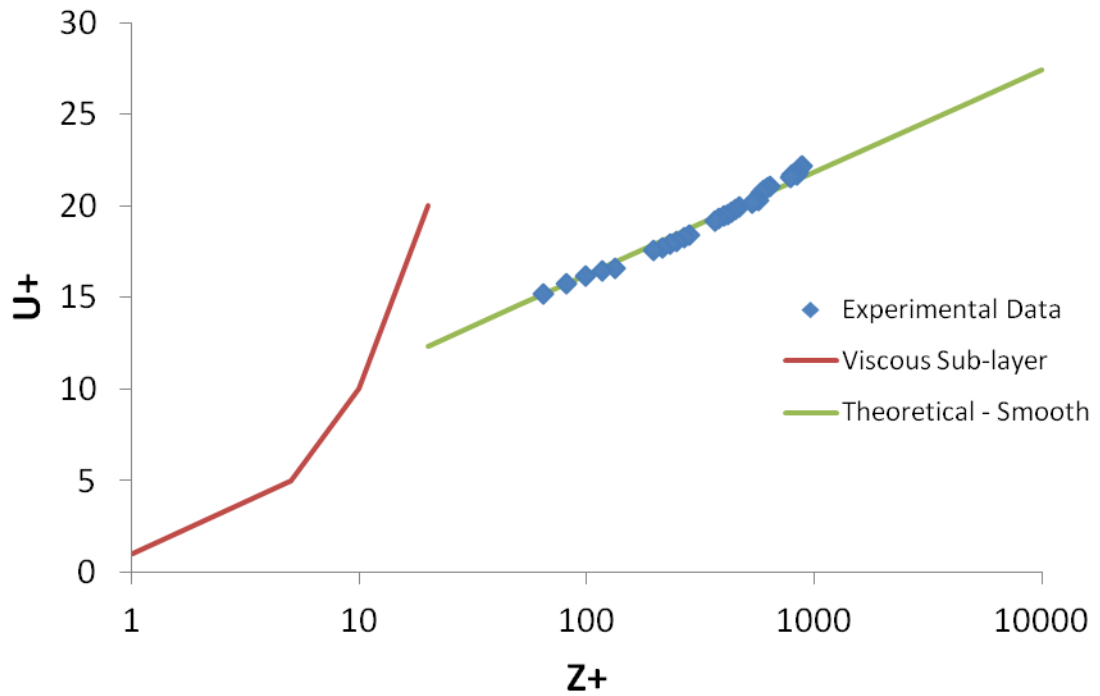


Figure C-68: Fit of experimental data in the wall affected zone to the log-law at  $Z = 90$  mm for the Base Experiment with  $u_* = 0.01675$  m/s.

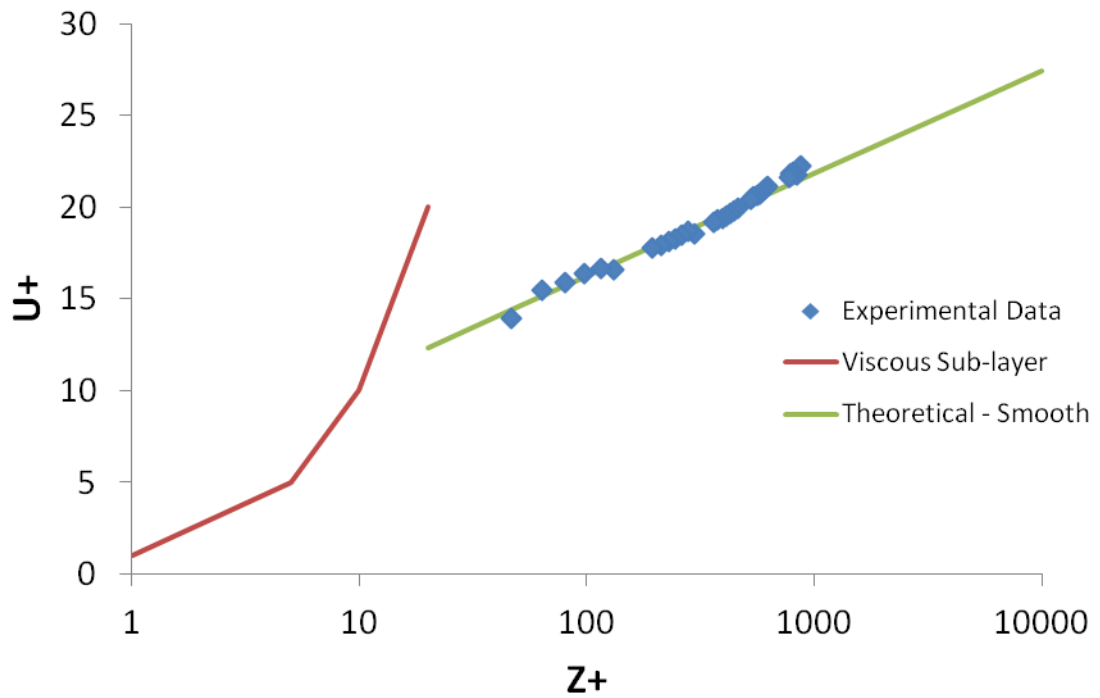


Figure C-69: Fit of experimental data in the wall affected zone to the log-law at  $Z = 105$  mm for the Base Experiment with  $u_* = 0.0165$  m/s.

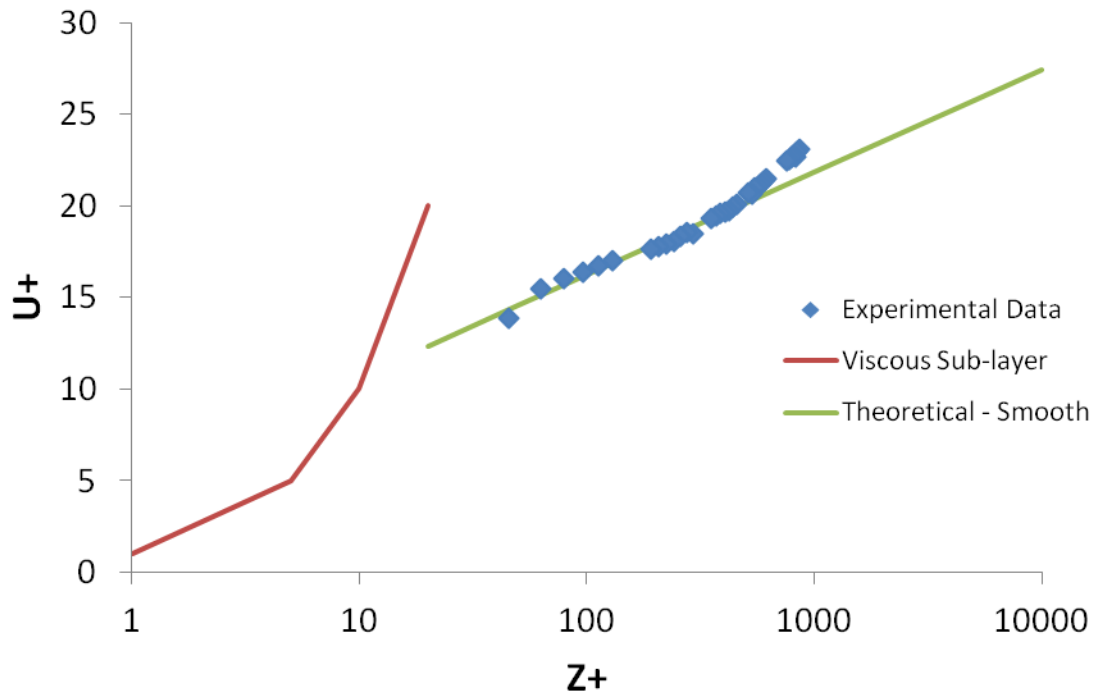


Figure C-70: Fit of experimental data in the wall affected zone to the log-law at  $Z = 120$  mm for the Base Experiment with  $u_* = 0.01625$  m/s.

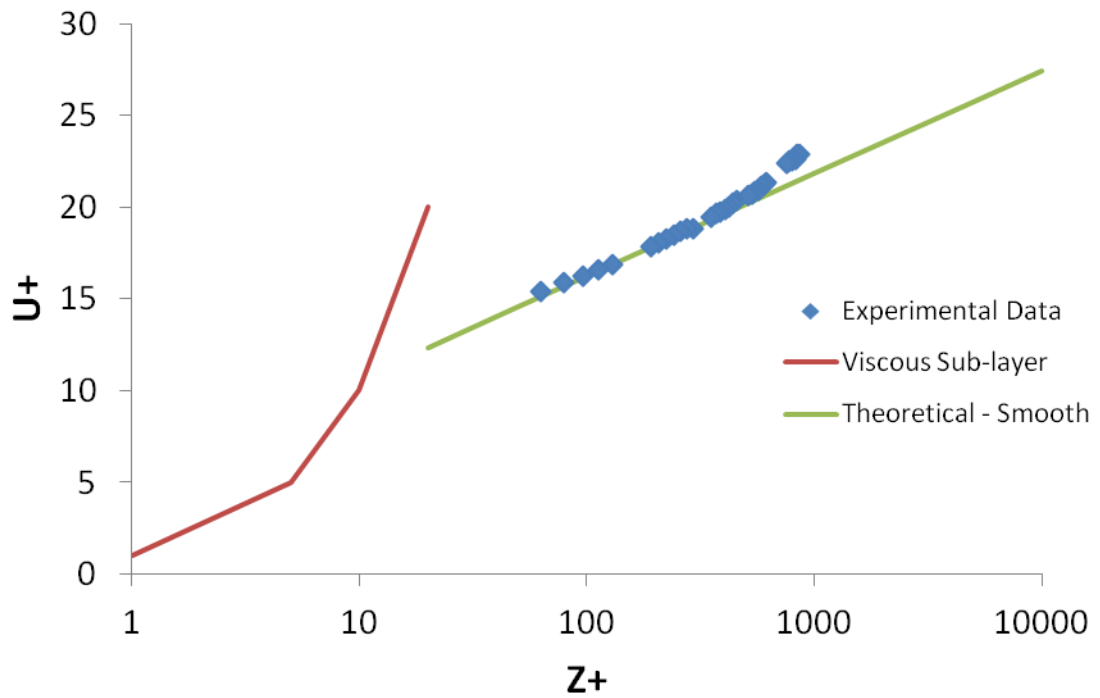


Figure C-71: Fit of experimental data in the wall affected zone to the log-law at  $Z = 130$  mm for the Base Experiment with  $u_* = 0.01625$  m/s.

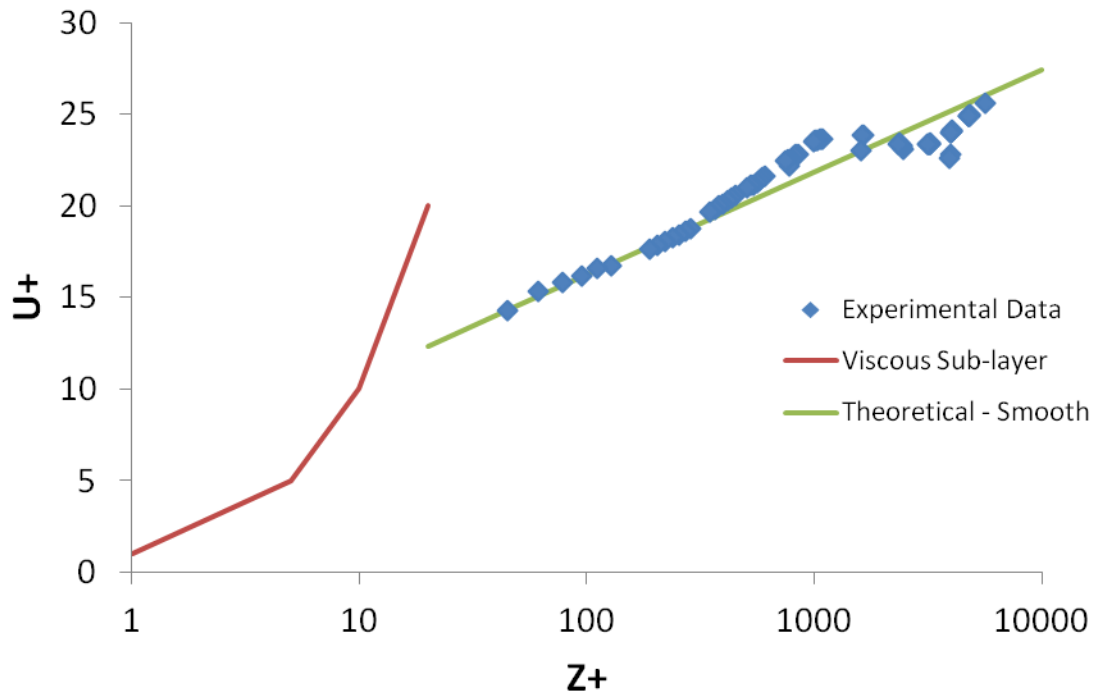


Figure C-72: Fit of experimental data in the wall affected zone to the log-law at  $Z = 140$  mm for the Base Experiment with  $u_* = 0.016$  m/s.

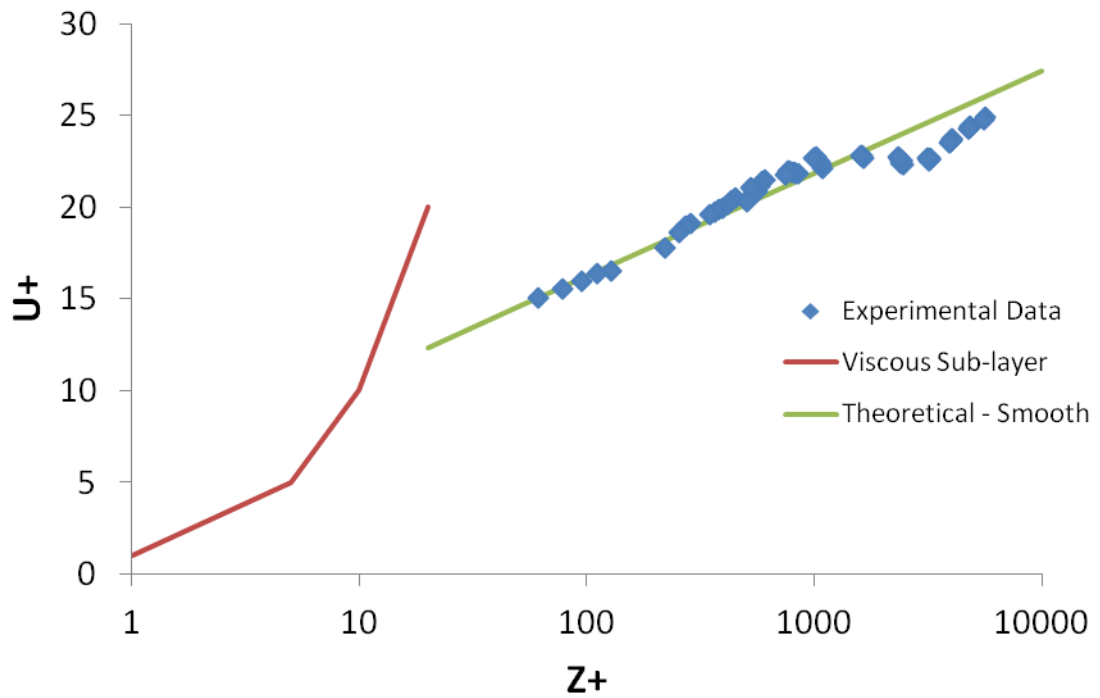


Figure C-73: Fit of experimental data in the wall affected zone to the log-law at  $Z = 150$  mm for the Base Experiment with  $u_* = 0.016$  m/s.

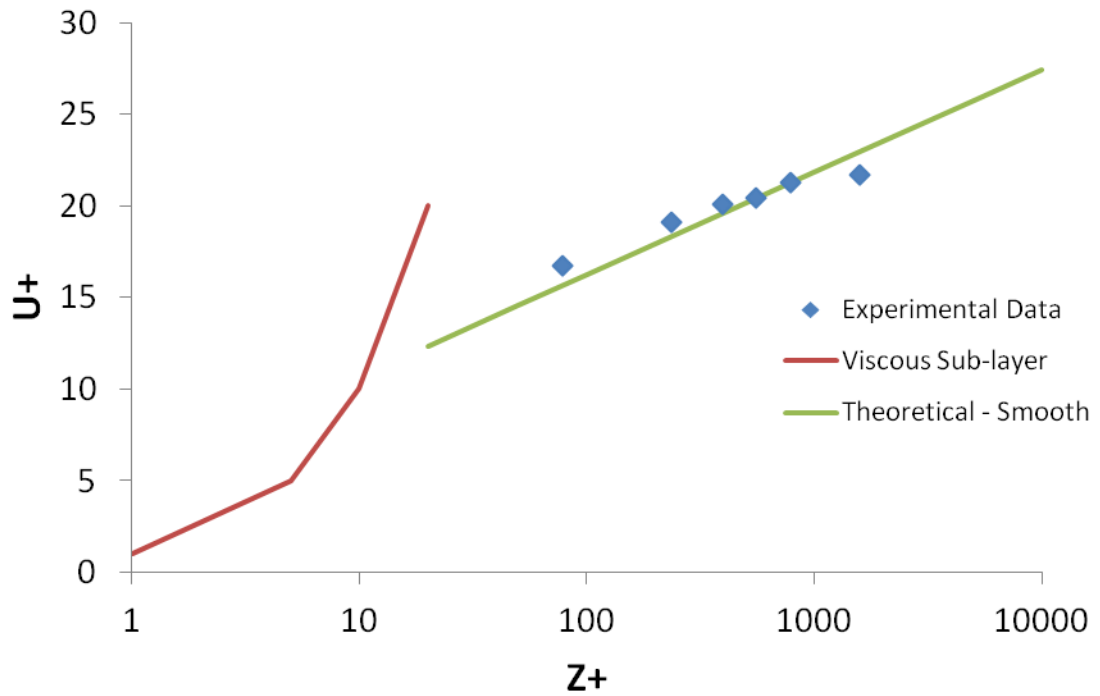


Figure C-74: Fit of experimental data in the wall affected zone to the log-law at  $Z = 165$  mm for the Base Experiment with  $u_* = 0.01575$  m/s.

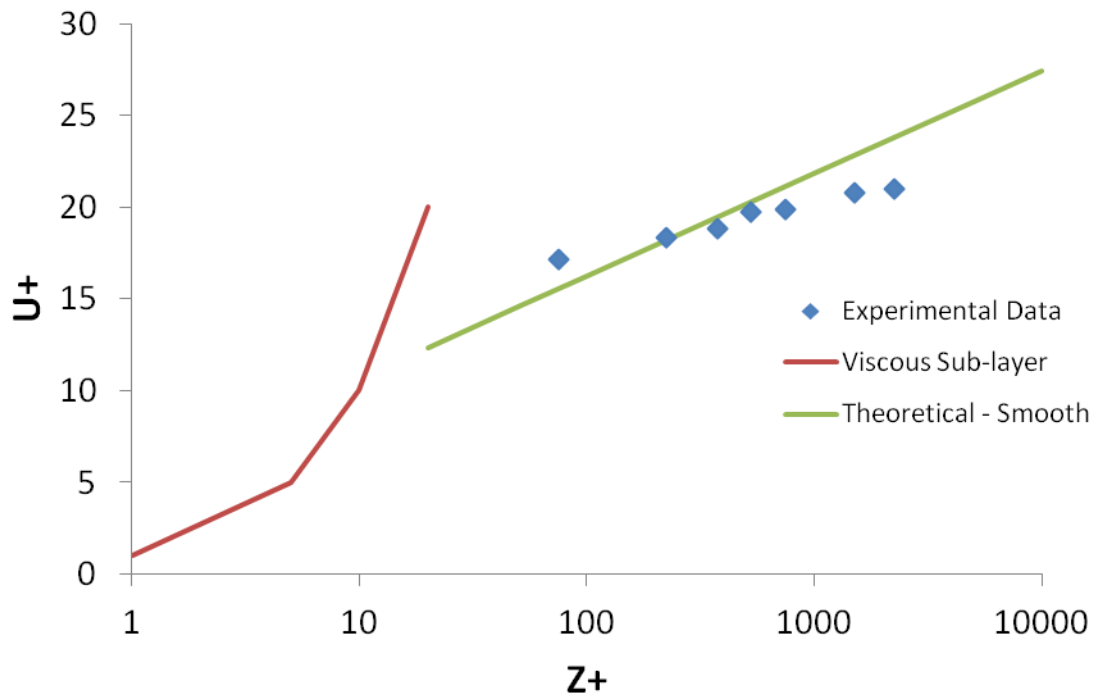


Figure C-75: Fit of experimental data in the wall affected zone to the log-law at  $Z = 175$  mm for the Base Experiment with  $u_* = 0.015$  m/s.

## C.6 Shear Stress Distributions

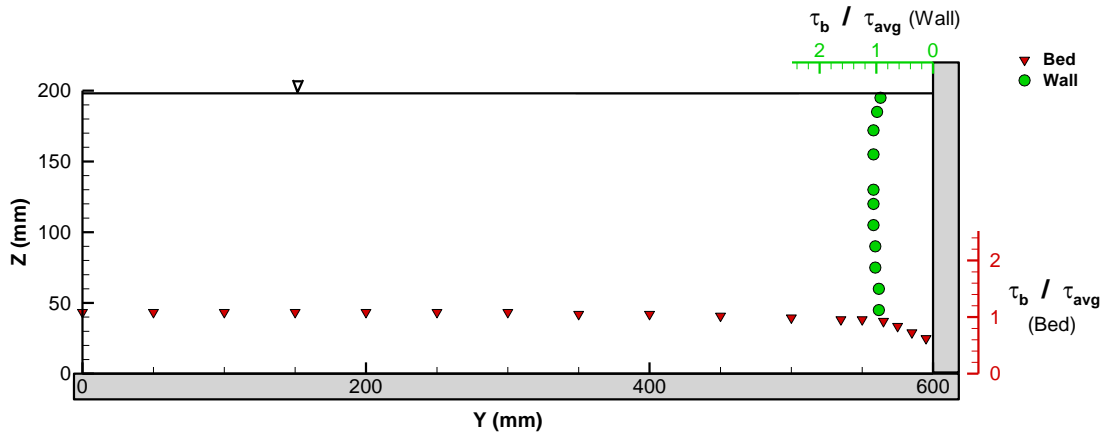


Figure C-76: Shear stress distribution for the Open Channel Experiment.

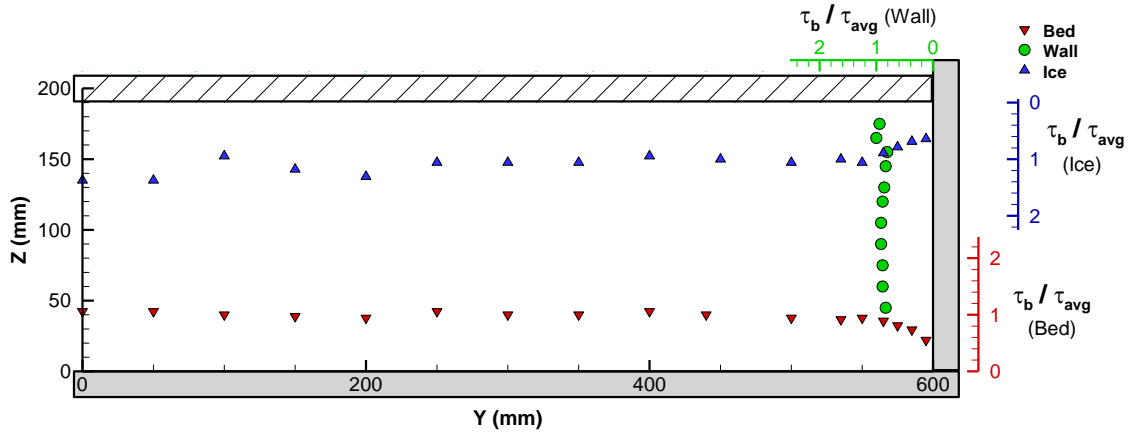


Figure C-77: Shear stress distribution for the Covered Channel Experiment.

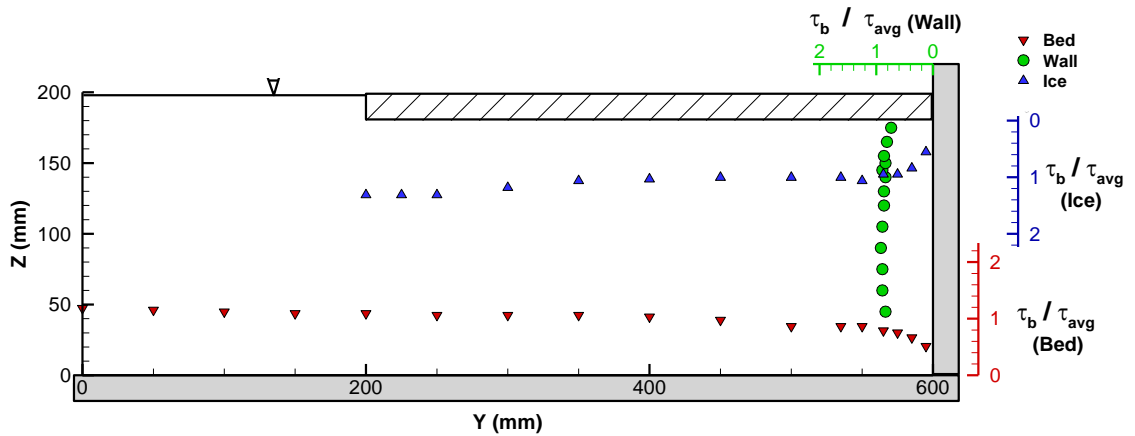


Figure C-78: Shear stress distribution for the Base Experiment.

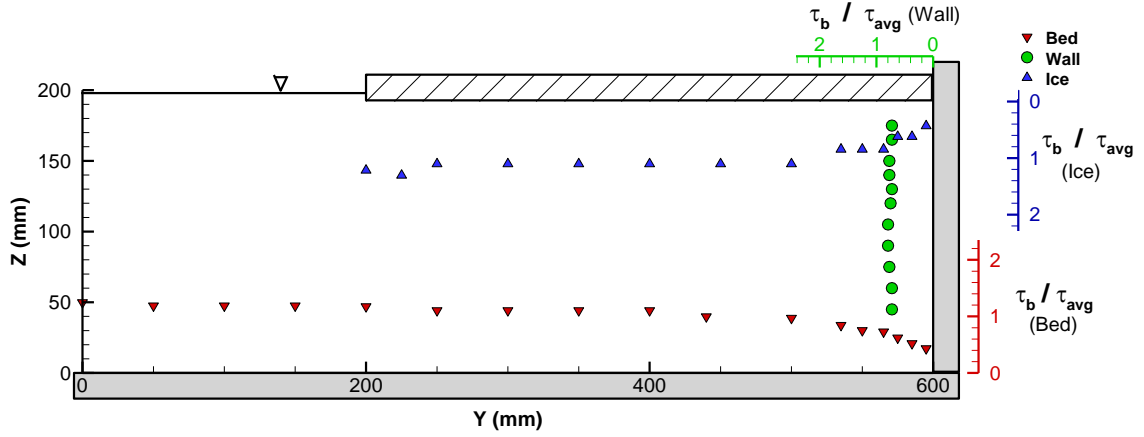


Figure C-79: Shear stress distribution for the Low Froude Experiment.

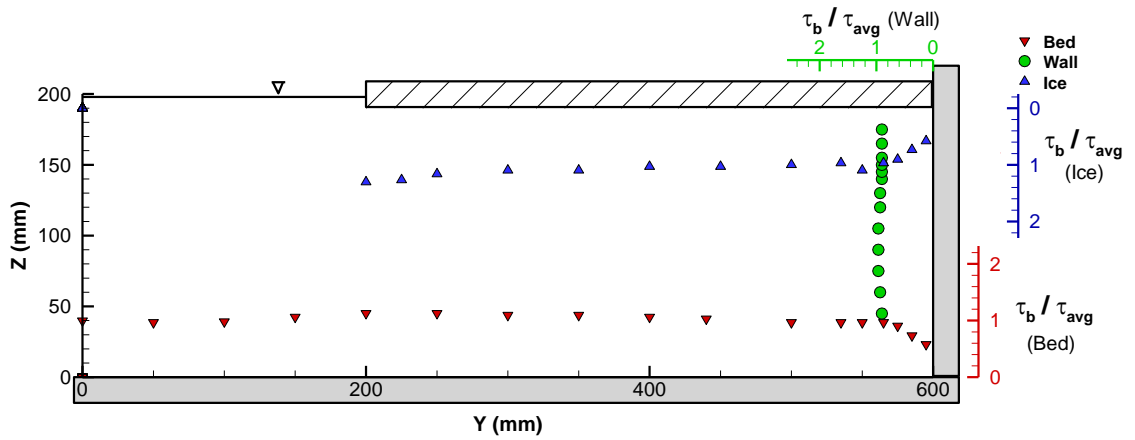


Figure C-80: Shear stress distribution for the High Froude Experiment.

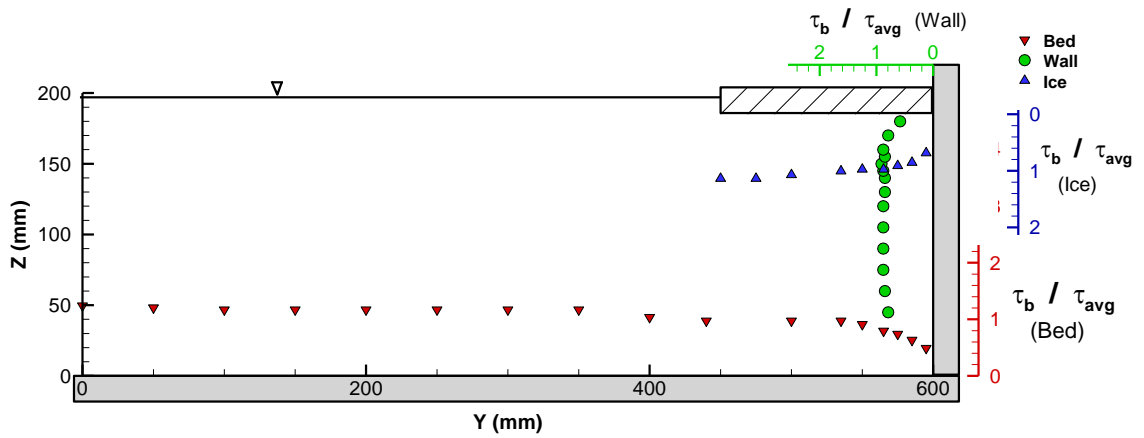


Figure C-81: Shear stress distribution for the 25% Coverage Experiment.

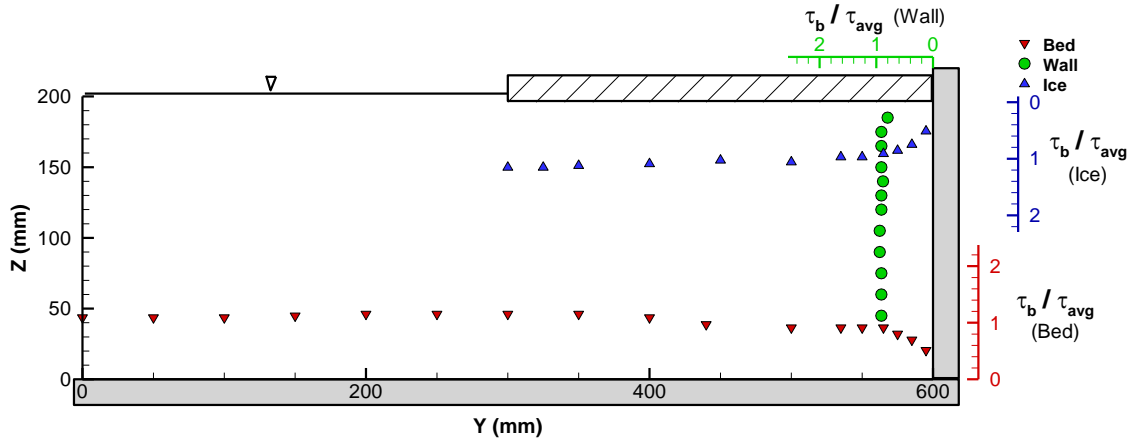


Figure C-82: Shear stress distribution for the 50% Coverage Experiment.

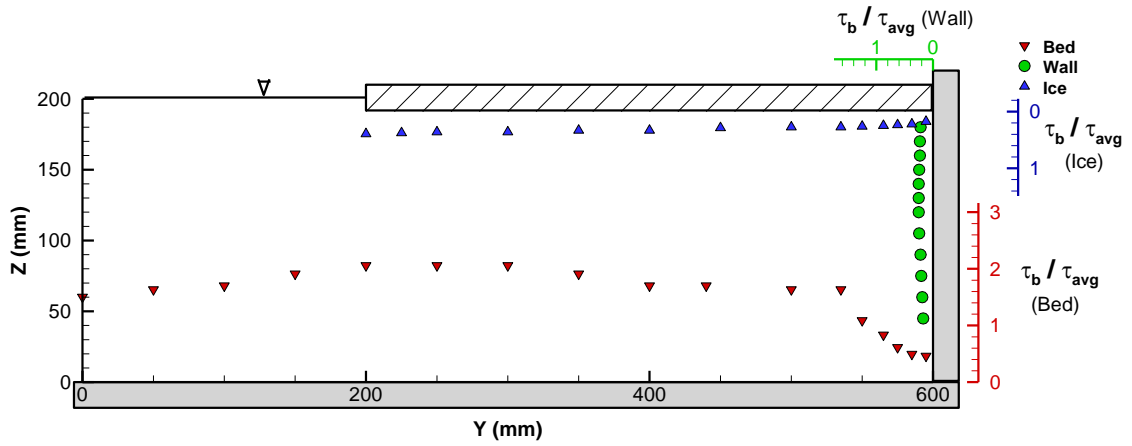


Figure C-83: Shear stress distribution for the Rough Bed Experiment.

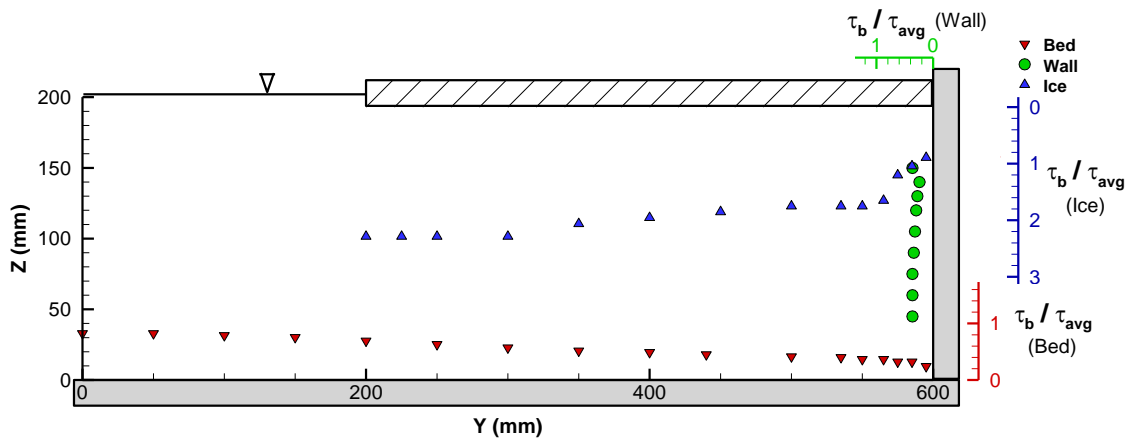


Figure C-84: Shear stress distribution for the Rough Ice Experiment.

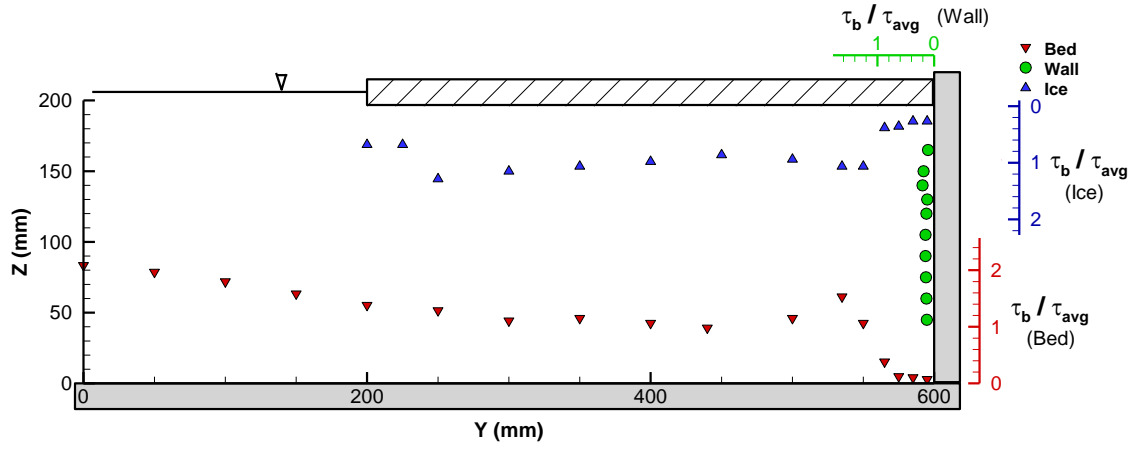


Figure C-85: Shear stress distribution for the Rough Bed - Rough Ice Experiment.

## C.7 Streamwise Turbulence Intensity Distributions

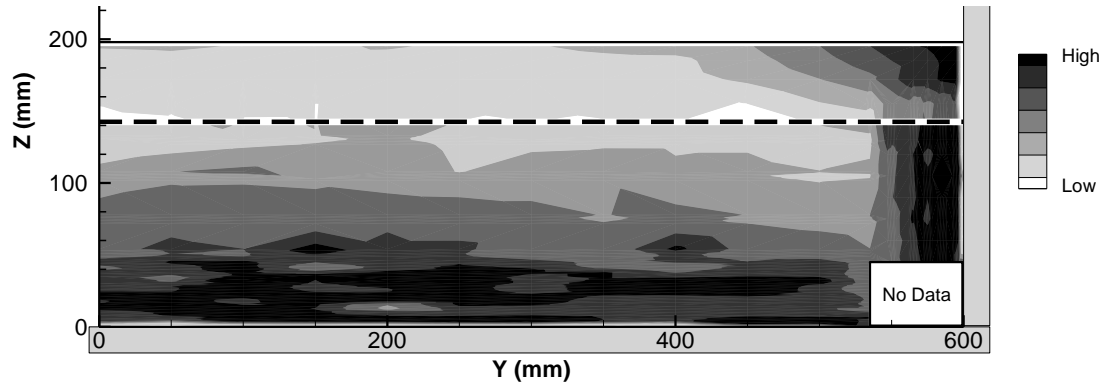


Figure C-86: Streamwise turbulence intensity distribution for the Open Channel Experiment.

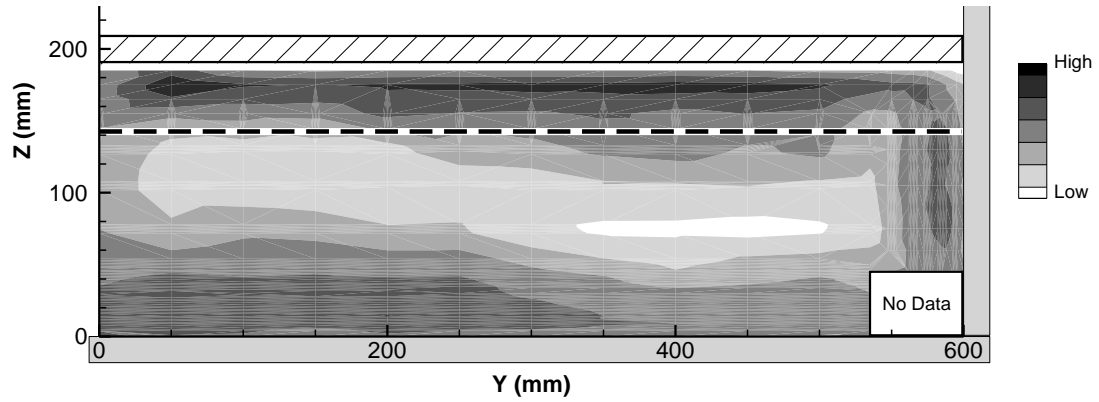


Figure C-87: Streamwise turbulence intensity distribution for the Covered Channel Experiment.

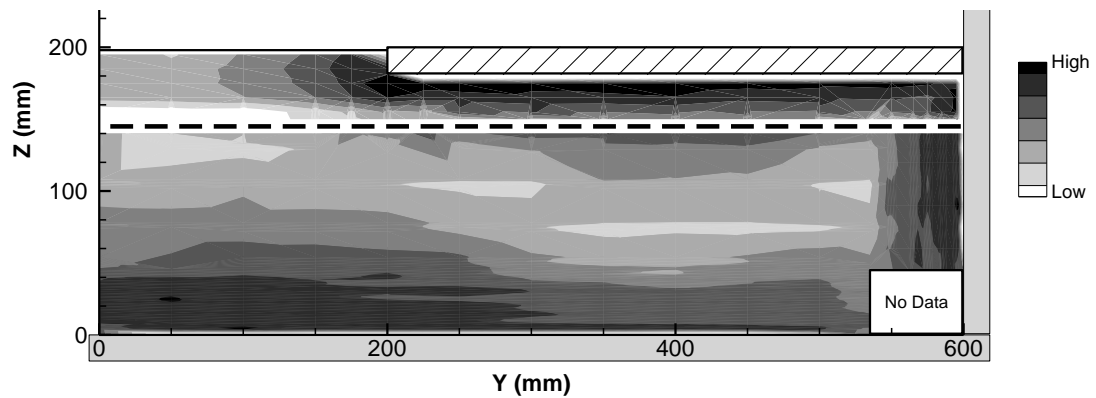


Figure C-88: Streamwise turbulence intensity distribution for the Base Experiment.

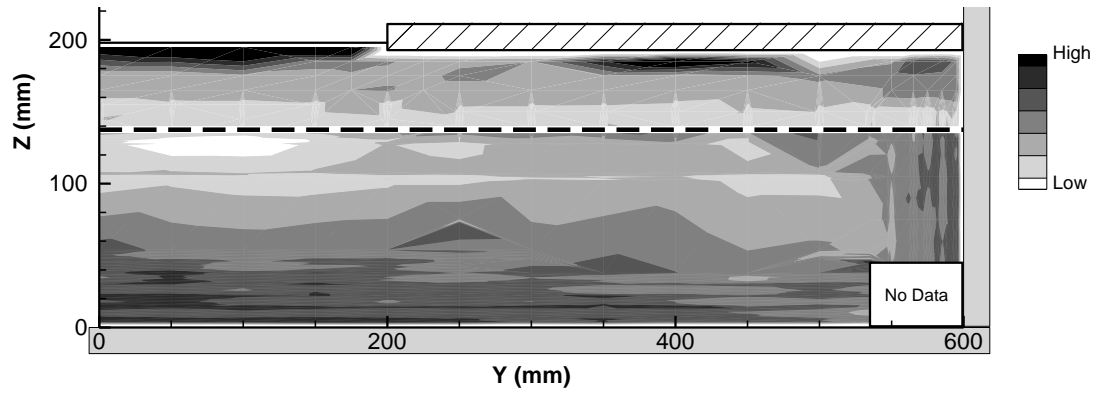


Figure C-89: Streamwise turbulence intensity distribution for the Low Froude Experiment.

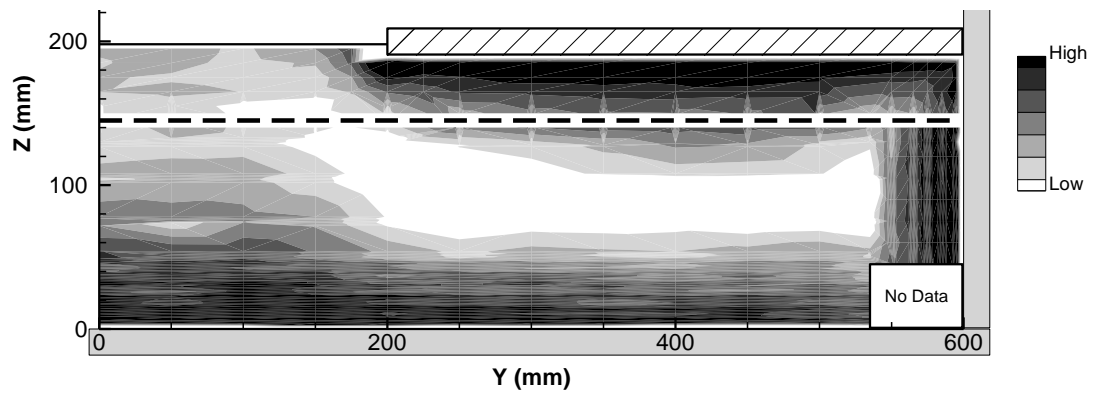


Figure C-90: Streamwise turbulence intensity distribution for the High Froude Experiment.

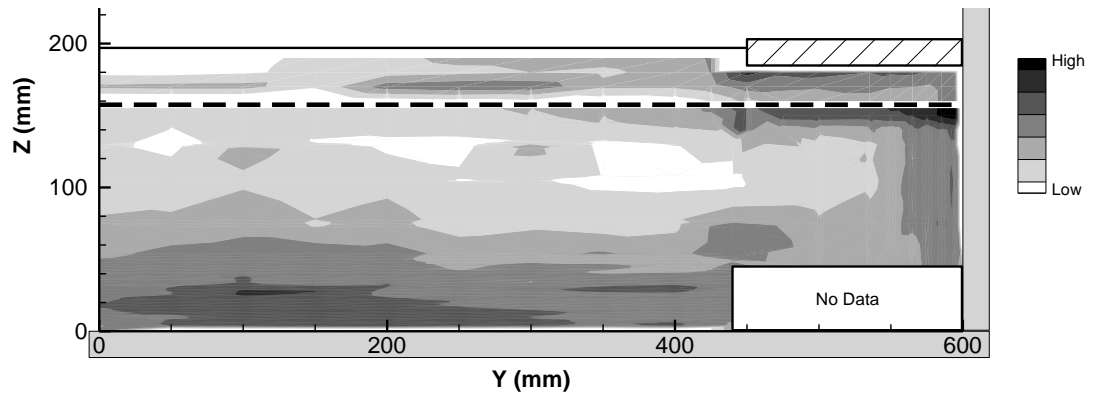
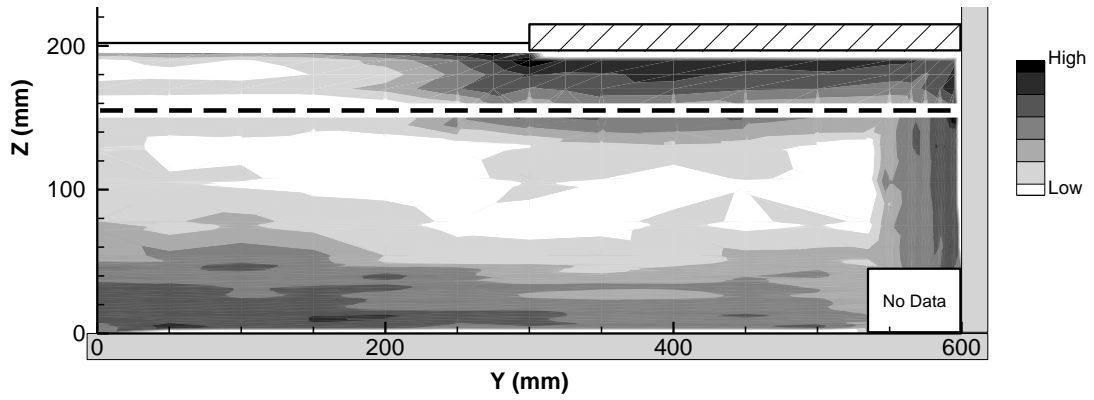
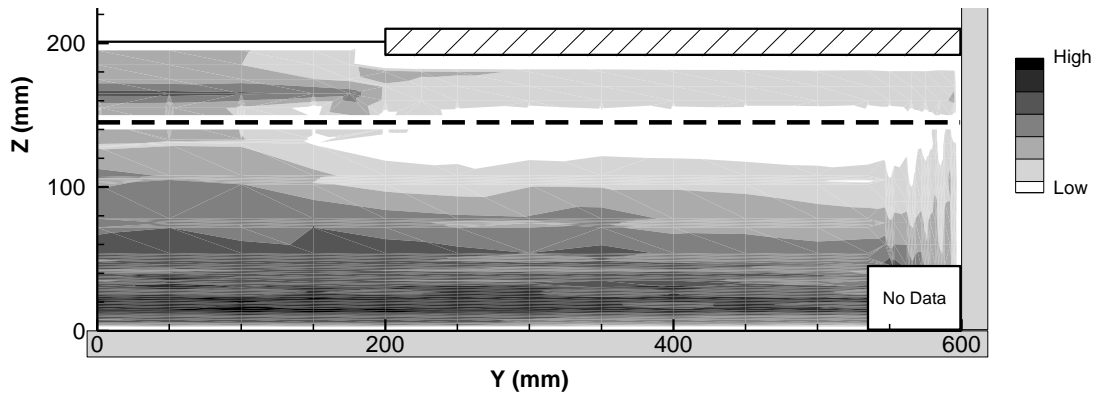


Figure C-91: Streamwise turbulence intensity distribution of the 25% Coverage Experiment.



**Figure C-92: Streamwise turbulence intensity distribution for the 50% Coverage Experiment.**



**Figure C-93: Streamwise turbulence intensity distribution for the Rough Bed Experiment.**

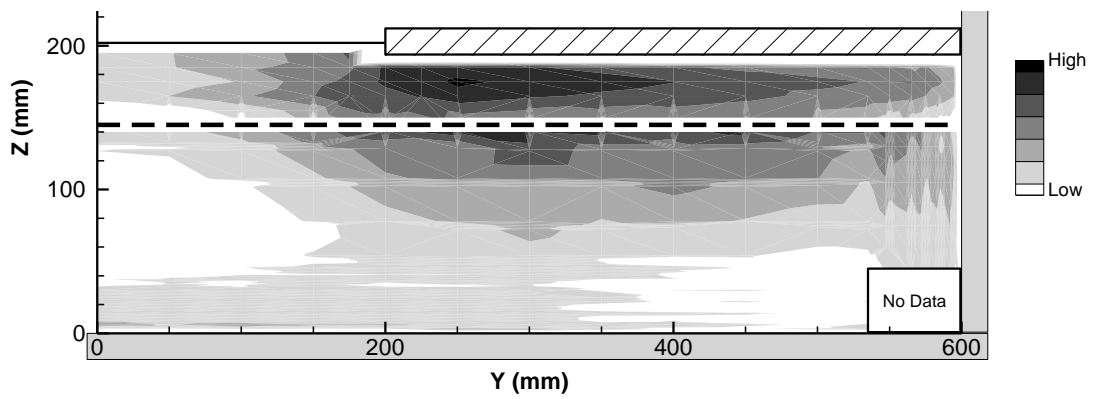


**Figure C-94: Streamwise turbulence intensity distribution for the Rough Ice Experiment.**

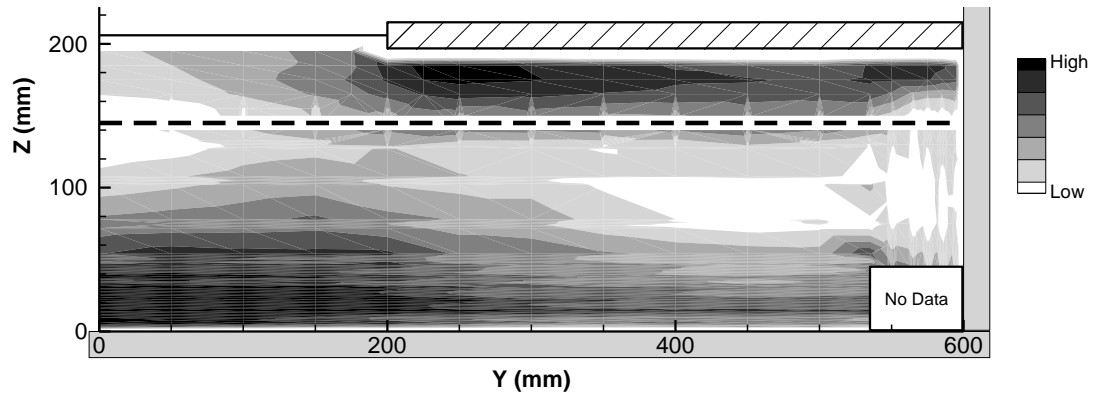


**Figure C-95: Streamwise turbulence intensity distribution for the Rough Bed - Rough Ice Experiment.**